

Theory of Coulomb induced signatures in two dimensional spectroscopy of colloidal quantum dots

vorgelegt von
Master of Science
Anke Ginter

an der Fakultät II – Mathematik und Naturwissenschaften
der Technischen Universität Berlin
zur Erlangung des akademischen Grades

Doktor der Naturwissenschaften
— Dr. rer. nat. —

genehmigte Dissertation

Promotionsausschuss:

- Vorsitzende: Prof. Dr. rer. nat. Birgit Kanngießer
1. Gutachter: Prof. Dr. rer. nat. Andreas Knorr
2. Gutachter: Dr. rer. nat. Benjamin Fingerhut
3. Gutachter: Prof. Dr. rer. nat. Marten Richter

Tag der wissenschaftlichen Aussprache: 26. Februar 2019

Berlin 2019

To my three A's

Abstract

In this thesis, the interplay between the Brownian motion of colloidal quantum dots (QDs) and the position-dependent Coulomb coupling is investigated. The Coulomb interaction plays an important role since it changes the optical and electrical properties of nanostructures such as colloidal QDs, even in the case of non-overlapping electron wave functions. Due to the Coulomb coupling, the individual characteristics of the single QDs are modified and new delocalized exciton states are formed. Coulomb coupled colloidal QDs diffuse in the solvent and thus, they frequently change their spatial positionings and their angular orientations. The Brownian motion represents a simple approximative way for describing this stochastic motion of the QDs.

Since the Coulomb coupling is determined by the distance between the QDs and their relative dipole orientation, the strength of the coupling is influenced by the spatial arrangement of the colloidal QDs. Accordingly, the diffusion of the colloidal QDs determines the strength of the Coulomb coupling. In general, the calculation of the Coulomb coupling requires the evaluation of a six dimensional integral. Therefore, it presents a limiting factor in quantum mechanical calculations, if the size or the complexity of the model system increases. Therefore, the Poisson Green's function method for an efficient numerical calculation of a high number of Coulomb coupling elements is introduced. The method reduces the number of integrals in real space without being restricted to specific symmetry conditions or an explicit Coulomb Green's function. Furthermore, the method naturally includes an arbitrarily spatial-dependent dielectric permittivity, as is needed for colloidal QDs with varying spatial arrangements caused by the diffusion.

Since the signatures in the multidimensional coherent spectroscopy are directly induced by the interaction processes between the QDs, the double quantum coherence spectroscopy allows an analysis of the averaged positions of the QDs to be done without influencing the motion of the QDs. Thus, the two dimensional (2d) coherent spectroscopy is used for the visualization and investigation of the Coulomb coupling. The position-dependent Coulomb interaction as well as the excitation transfers between the colloidal QDs cause characteristic shifts and signatures in the 2d spectra. Since the motion of colloidal QDs in the solvent, induced by the diffusion, changes the strength of the Coulomb coupling, the characteristic signatures in the 2d spectra can be used for investigating the arrangement specific Coulomb coupling. Accordingly, the 2d spectroscopy enables an analysis of the interplay between the Brownian motion of the colloidal QDs and the strength of the Coulomb coupling to be done.

Furthermore, the spectroscopic signatures of millions of QDs arrangements are averaged to get stochastically converged signatures providing information on the characteristics of the Brownian motion. The averaged spectroscopic signatures are calculated for varying QD concentrations. The different averaged distances and orientations of the colloidal QDs, determining the strength of the Coulomb coupling, induce specific signatures in the 2d spectra. If the QDs are densely arranged in mean, the Coulomb coupling, which decreases with the distance, forms delocalized exciton states and QD clusters arise. For a decreasing concentration of the colloidal QDs, the influences of the Coulomb coupling decreases and the colloidal QDs appear more and more as localized single QDs. Hence, an analysis of the interplay between the Brownian motion of the colloidal QDs and the Coulomb coupling provides information on the QD concentration using the characteristic averaged signatures in the 2d spectra.

Zusammenfassung

In dieser Dissertation wird das Zusammenspiel zwischen der Brownschen Bewegung kolloidaler Quantenpunkte (QP) und der positionsabhängigen Coulomb-Kopplung untersucht. Die Coulomb-Wechselwirkung spielt eine wichtige Rolle, da sie die optischen und elektrischen Eigenschaften von Nanostrukturen wie kolloidale QP ändert, selbst wenn die elektronischen Wellenfunktionen nicht überlappen. Durch die Coulomb-Wechselwirkung werden die individuellen Eigenschaften von einzelnen QPn modifiziert und neue delokalisierte Exziton-Zustände gebildet. Coulomb-gekoppelte kolloidale QP diffundieren im Lösungsmittel und ändern deshalb regelmäßig ihre räumlichen Positionen und ihre Winkelorientierungen. Die Brownsche Bewegung stellt eine einfache Möglichkeit zur Beschreibung dieser stochastischen Bewegung der QP dar.

Da die Coulomb-Wechselwirkung durch die Distanz zwischen den QPn und ihrer relativen Dipolorientierung bestimmt wird, ist die Stärke der Kopplung abhängig von der räumlichen Anordnung der kolloidalen QP. Dementsprechend bestimmt die Diffusion der kolloidalen QP die Stärke der Coulomb-Wechselwirkung. Im Allgemeinen erfordert die Berechnung der Coulomb-Wechselwirkung die Auswertung eines sechsdimensionalen Integrals. Dieses stellt somit einen limitierenden Faktor in quantenmechanischen Berechnungen dar, sobald Größe oder Komplexität des Modellsystems erhöht werden. Aus diesem Grund wird eine Methode, die auf der Darstellung der Lösung der Poissongleichung mittels Greenscher Funktionen basiert, für eine effiziente Berechnung einer großen Anzahl an Coulomb-Kopplungselementen eingeführt. Diese Methode reduziert die Anzahl der Integrale im Realraum ohne auf bestimmte Symmetriebedingungen oder eine explizite Form der Greenschen Funktion beschränkt zu sein. Darüber hinaus beinhaltet die Methode direkt den Einfluss einer beliebigen ortsabhängigen Permittivität, wie sie auch für kolloidale QP mit diffusionsbedingten räumlich veränderlichen Anordnungen benötigt wird.

Da die Signaturen in der multidimensionalen kohärenten Spektroskopie direkt von den Wechselwirkungsprozessen zwischen den QPn beeinflusst werden, erlaubt es die doppelte Quantenkohärenzspektroskopie eine Analyse der gemittelten Positionen der QP durchzuführen, ohne die Bewegung der QP zu beeinflussen. Aus diesem Grund wird die zweidimensionale (2d) kohärente Spektroskopie für die Visualisierung und Untersuchung der Coulomb-Kopplung verwendet. Die ortsabhängige Coulomb-Wechselwirkung sowie der Anregungstransfer zwischen kolloidalen QPn verursachen charakteristische Signaturen und Verschiebungen in den 2d Spektren. Da die Bewegung der kolloidalen QP, welche durch die Diffusion hervorgerufen wird, die Stärke der Coulomb-Kopplung verändert, können diese charakteristischen Signaturen in den 2d Spektren verwendet werden, um die anordnungsspezifische Coulomb-Kopplung zu untersuchen. Aus diesem Grund ermöglicht es die 2d Spektroskopie, eine Analyse des Zusammenspiels zwischen der Brownschen Bewegung der kolloidalen QP und der Stärke der Coulomb-Kopplung durchzuführen.

Weiterhin werden spektroskopische Signaturen von Millionen Quantenpunktanordnungen gemittelt um stochastisch konvergente Signaturen zu erhalten, welche dann Informationen über die Charakteristiken der Brownschen Bewegung bereitstellen. Die gemittelten spektroskopischen Signaturen werden für verschiedene Quantenpunktkonzentrationen berechnet. Die unterschiedlichen mittleren Distanzen und Ausrichtungen der kolloidalen QP, die die Stärke der Coulomb-Kopplung festlegen, rufen spezifische Signaturen in den 2d Spektren hervor. Wenn die QP im Mittel dicht beieinander liegen, bildet die Coulomb-Wechselwirkung, welche mit zunehmender Distanz abgeschwächt wird, Exziton-Zustände aus und Quantenpunktcluster entstehen. Für eine sinkende Konzentration der kolloidalen QP sinkt auch der Einfluss der Coulomb-Kopplung und die gekoppelten QP erscheinen mehr und mehr als lokalisierte einzelne QP. Demzufolge stellt eine Analyse des Zusammenspiels zwischen der Brownschen Bewegung der kolloidalen QP und der Coulomb-Kopplung, anhand der charakteristischen gemittelten Signaturen in den 2d Spektren, Informationen bezüglich der Quantenpunktkonzentration bereit.

Contents

Abstract	iv
Zusammenfassung	v
List of Figures	ix
1 Introduction	1
1.1 Main idea	1
1.2 Motivation	1
1.3 Structure of the thesis	3
2 Physical concepts	5
2.1 Colloidal quantum dots	5
2.1.1 Model system and material parameters	5
2.1.2 The free particle Hamiltonian and the confinement potential	8
2.2 Interaction Hamiltonian	10
2.2.1 Coulomb Hamiltonian	10
2.2.2 Electron-light interaction	12
2.2.3 The total Hamiltonian	13
2.3 Exciton basis	14
2.3.1 Localized exciton states and Hamiltonian	14
2.3.2 Delocalized exciton states	18
2.3.3 Transforming the dipole operator into the delocalized basis	19
2.4 Rotation of three dimensional objects	21
2.4.1 Euler angles	21
2.4.2 Quaternions	22
2.4.3 Rotation on a grid	25
3 Calculation of Coulomb coupling elements	29
3.1 Poisson Green's function method	30
3.1.1 Concepts in the literature	30
3.1.2 Approach of the PGF method	32
3.1.3 Applications of the method	34
3.2 Calculation of different orders in the Coulomb coupling	36
3.2.1 Taylor series of the Green's function	36
3.2.2 Monopole-monopole coupling elements	38
3.2.3 Dipole-dipole coupling elements	39
3.3 Position dependent Coulomb coupling of colloidal QDs	42
3.3.1 Distance dependence	42
3.3.2 Influence of the angular orientation	44

3.4	Spatially dependent dielectric permittivity	47
3.4.1	Solvent induced dielectric mismatch	48
3.4.2	Size effects and core/shell structure of colloidal QDs	50
3.4.3	Homogeneous dielectric environment	54
3.5	Point-dipole approximation	57
3.5.1	Taylor series of the free space Coulomb potential	58
3.5.2	Coulomb coupling approximation	59
3.5.3	Statical macroscopic quadrupole-quadrupole correction terms	61
3.5.4	Förster elements in the point-dipole approximation	62
3.6	Conclusion	64
4	Arrangement dependent signatures in 2d spectra	67
4.1	Double quantum coherence spectroscopy	68
4.1.1	Heterodyne detection	68
4.1.2	Feynman diagrams and spectroscopic signatures	69
4.2	Fully calculated 2d spectra with a dielectric permittivity	71
4.2.1	Signatures depending on the QD arrangements	72
4.2.2	Variation of size and shape of the colloidal QDs	77
4.3	2d spectra based on point-dipole approximation	78
4.3.1	Comparison with the fully calculated signatures	79
4.3.2	Rotation around the cartesian axis	82
4.3.3	Polarization and dephasing	85
4.4	Conclusion	87
5	Brownian motion analyzed by averaged 2d spectra	89
5.1	Brownian Motion	90
5.1.1	Translational motion	90
5.1.2	Rotational motion	92
5.2	Implementation of the Brownian motion of colloidal QDs	93
5.2.1	Simulation box with periodic boundary conditions	94
5.2.2	Trajectory including positions and angular orientations	95
5.2.3	Convergence of the QD positions	98
5.3	Averaged spectra of QDs showing Brownian motion	101
5.3.1	Influence of the particle concentration	102
5.3.2	Influence of the solvent's viscosity	106
5.4	Conclusion	109
6	Conclusion	111
6.1	Summary	111
6.2	Outlook	112
	Appendices	115
A	Coulomb Hamiltonian	117
A.1	Coulomb coupling elements determining the Hamiltonian	117
A.1.1	Monopole-monopole Coulomb Hamiltonian	117
A.1.2	Dipole-dipole Coulomb Hamiltonian	119
A.2	Hamiltonian matrix in the local exciton basis	120
A.2.1	Local single exciton basis	121
A.2.2	Local double exciton basis	122

B Calculation of the Coulomb potential	123
B.1 Multidimensional Taylor expansion	123
B.2 Calculate mixed Coulomb terms	124
B.3 Free particle Coulomb potential	126
B.3.1 Calculate terms of the dipole-dipole approximation	126
B.3.2 Calculate quadrupole-quadrupole correction terms	128
C Formalism of the coherent optical spectroscopy	131
D Mode of the program	135
Danksagung	137
Bibliography	137

List of Figures

1.1	Model of moving Coulomb coupled colloidal QDs	2
2.1	Model system of two Coulomb coupled QDs	6
2.2	Two Coulomb coupled QDs moving on schematically illustrated trajectories.	7
2.3	Confinement potential of CdSe/ZnTe core/shell QDs	8
2.4	Core/shell QD types	9
2.5	Four local bright exciton states	14
2.6	The monopole-monopole Coulomb coupling elements	15
2.7	The dipole-dipole Coulomb coupling elements	16
2.8	Six local bright double exciton states	17
2.9	Rotation of a body on a discrete grid	25
2.10	Approximating the rotation on a discrete grid	26
2.11	Exciton energies from the rotation on a discrete grid	27
3.1	Schema of the PGF method for increased numerical efficiency	32
3.2	Scale separation including unit cells	37
3.3	Interdot and intradot monopole-monopole interaction	38
3.4	Interdot and intradot dipole-dipole interaction	40
3.5	Sketch of Coulomb coupling elements	42
3.6	Monopole elements depending on distance between QDs.	43
3.7	Dipole elements depending on distance between QDs.	44
3.8	Initial dipole orientations	44
3.9	Rotation angles for two QDs	45
3.10	Monopole elements as function of orientation.	45
3.11	Dipole elements as function of rotation starting with parallel dipole moments.	46
3.12	Dipole elements depending on rotation starting from orthogonal dipole moments.	47
3.13	Coupling elements for different solvent's permittivities	48
3.14	Influence of solvent's permittivities on intradot dipole and monopole coupling	49
3.15	Influence of the QD's size on monopole-monopole coupling elements	50
3.16	Influence of the QD's size on Förster coupling elements	51
3.17	Monopole-monopole coupling elements of CdS/ZnSe QDs	51
3.18	Förster elements of CdS/ZnSe QDs	52
3.19	Monopole elements of QDs with $r = 3.0$ nm with and without core/shell structures	53
3.20	Influence of the QD's size and the core/shell structure on Förster elements	53
3.21	Influence of the shell thickness on Förster elements	54
3.22	Monopole coupling fully calculated and in different homogeneous environments.	55
3.23	Comparing monopole element rotation fully calculated with homogeneous medium	55
3.24	Förster elements fully calculated and in different homogeneous environments	56
3.25	Comparing fully calculated Förster elements with homogeneous environment	57

3.26	Scale separations of the spatial operator	58
3.27	Distance dependance of Förster elements in dipole approximation	62
3.28	Förster elements in dipole orientation depending on angular orientation	63
3.29	Comparing fully calculated Förster elements with dipole approximation	63
4.1	Pulse sequence of the heterodyne detection	68
4.2	Feynman diagrams and exciton states of DQCS	70
4.3	DQCS for different QD distances and orientations influenced by the permittivity	73
4.4	Exciton energies for different QD distances and orientations fully calculated	74
4.5	DQCS for different QD distances and orientations calculated for $\epsilon_{\text{hom}} = 6$	76
4.6	Influence of the size and core/shell structure	77
4.7	Comparing exciton energies as function of distances and orientations	80
4.8	DQCS for different QD distances and orientations in the point-dipole approximation	81
4.9	Exciton energies for the rotations around the three cartesian axis	82
4.10	DQCS for rotations around cartesian axis	84
4.11	DQCS for varying polarization directions	85
4.12	DQCS for an increased dephasing rate	86
5.1	Colloidal QDs diffusing in water	92
5.2	Two QDs in a periodic simulation box	94
5.3	Box size determines QD concentration	95
5.4	Distribution of the distance vector	96
5.5	Histogram of distance distribution	97
5.6	Distance-dependent changes in the spectra	98
5.7	Convergence of the angular orientations	99
5.8	Convergence behavior of the translational positions	100
5.9	Deviation of 20 million steps from 100M steps	101
5.10	DQCS and real and imaginary parts for different sized boxes	103
5.11	Diagonal cuts for different box sizes	104
5.12	Cuts through DQCS	105
5.13	Extrema and cuts through 2d spectra for different sized boxes.	106
5.14	DQCS and real and imaginary parts for different viscosities with $b = 30$ nm	107
5.15	DQCS and real and imaginary parts for different viscosities with $b = 50$ nm	108
5.16	Cuts through 2d spectra for varying viscosities	109
D.1	Two QDs in a periodic simulation box	136
D.2	Sketch of the program mode	136

Chapter 1

Introduction

1.1 Main idea

In this thesis, the interplay between the diffusion of colloidal quantum dots (QDs) and the position-dependent Coulomb coupling is investigated. The multidimensional coherent spectroscopy allows an analysis of the averaged QD positions to be done without influencing their motion. In the two dimensional (2d) spectroscopy, the signatures are directly induced by the interaction processes between the QDs [1]. Thus, they can be used for visualizing and analyzing the spatial-dependent couplings and excitation transfers between the colloidal QDs [2]. Since the Coulomb coupling is determined by the distance between the QDs and their relative dipole orientations [3,4], the diffusion of the colloidal QDs changes the strength of the coupling. In the 2d spectra, the Coulomb induced exciton shifts [5,6] cause characteristic signatures for the different spatial QD arrangements. Therefore, the 2d spectra provide information on the Brownian motion of the colloidal QDs induced by the spatial-dependent Coulomb coupling.

1.2 Motivation

Colloidal QDs have been in the focus of research for many years, since their tunable size and shape, manipulatable by the synthesis process [7,8], strongly influence their optical and electronic properties [9,10]. With the developments in the chemical synthesis of colloidal nanocrystals [11–13], a selective control of the size, the shape and the dimensionality of the colloidal QDs becomes possible [14]. Therefore, the size-dependence of the electron band gap [14,15] and the related exciton energies [16] presents one of the most important topics in the colloidal semiconductor research [17]. Moreover, in colloidal core/shell nanostructures [18,19] two or more semiconductor materials are combined forming new materials with adapted properties such as a high emission rate [11,13].

Since the colloidal QDs diffuse in the solvent, they change their spatial positioning and their angular orientation frequently. The manipulatable brightness and photostability of the colloidal QDs make them excellent markers for the visualization of biological processes [20,21]. The Brownian motion represents a simple approximative way for describing the stochastic motion of the QDs. Following the fluctuation-dissipation theorem [22], the Brownian motion determines the dynamics including the random positions and the averaged velocity of a microscopic particle immersed in a fluid. Therefore, an analysis of the Brownian motion is of particular interest since the motion is directly related to the transport of molecules and cells in biological systems [23–25].

In assemblies of colloidal QDs [26,27], the optical and electrical properties are changed due to the Coulomb interaction between the QDs [4,28]. Even in the case of non-overlapping electron wave functions, the Coulomb interaction plays an important role, since the individual characteris-

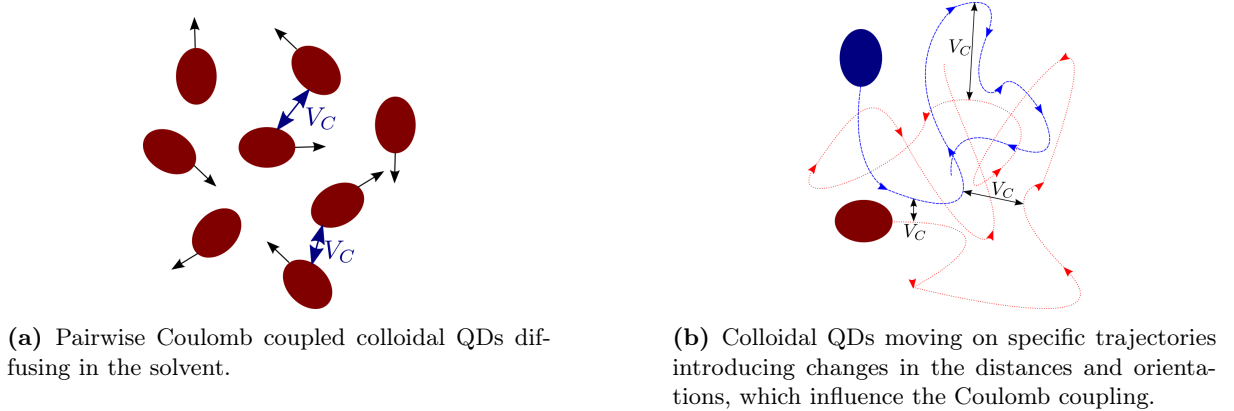


Figure 1.1 Coulomb coupled colloidal QDs diffuse in the solvent and thus, they frequently change their spatial positions and angular orientations. The motion influences the strength of the coupling. For investigating the motion of the colloidal QDs, arrangement specific 2d spectra are used.

tics of the QDs are modified and new delocalized exciton energy states are formed [4, 16, 29]. The coupling includes the electrostatic monopole-monopole Coulomb coupling between electrons and holes respectively [30], and the Förster dipole-dipole coupling [31, 32] as nonradiative resonant energy transfer between the QDs [33]. Therefore, the Coulomb coupling, which is determined by the Brownian motion of the colloidal QDs, induces characteristic exciton energy shifts [5, 6] and excitation transfers [34, 35].

A microscopic analysis of the Coulomb coupling is essential for the understanding of several physical processes in condensed matter such as the scattering of charge carriers [36, 37] or the formation of collective states as excitons and biexcitons [38, 39]. Therefore, the Coulomb coupling as a many particle interaction plays an important role in a variety of systems such as nanostructures as QDs or wells [36], coupled nanotubes [40, 41], bulk semiconductors [37, 42], graphene [43, 44] as well as atomic structures and molecular systems [45, 46]. In this thesis, semiconductor QDs are investigated, which are of great interest for the fundamental physic and for novel device applications [10]. For instance, the resonance energy transfer is important in the context of quantum computations and quantum dot lasers [3].

In general, the calculation of the Coulomb coupling requires the evaluation of a six dimensional integral [47, 48]. For numerical efficient calculations, the Poisson Green's function (PGF) method [49] is introduced for reducing the number of integrals in real space. The fast computation of Coulomb coupling elements may be important in electronic structure calculations [46, 50] and for quantum dynamics [28, 51] and efficient density matrix calculations using many-body correlation expansions [52, 53]. Following the approach of the PGF method [49], the monopole and the Förster coupling elements are calculated microscopically. The method enables the influence of the dielectric environment of the two colloidal QDs diffusing in the solvent to be included. The results of the full microscopical calculation of the Coulomb coupling are compared to the typically used point-dipole approximation, which offers the possibility of a very fast calculation of the Coulomb coupling for homogeneous media [54, 55].

Since the Coulomb coupling is determined by the distance between the QDs and their relative dipole orientation [3, 4], the strength of the coupling is influenced by the spatial arrangement of the colloidal QDs in the solvent. For detecting and analyzing the spatial-dependent coupling and excitation transfers, the 2d coherent optical spectroscopy is used [1, 2]. The position-dependent Coulomb coupling causes characteristic shifts and shape transformation of the optical signatures in the 2d spectra. Since the motion of colloidal QDs in the solvent, induced by the diffusion, changes the strength of the Coulomb coupling, the characteristic signatures in the 2d spectra

can be used for investigating the arrangement specific Coulomb coupling. Accordingly, the 2d spectroscopy is used for analyzing the interplay between the Brownian motion of the colloidal QDs in the solvent and the strength of the Coulomb coupling.

For investigating the characteristic spectra according the QD positions, first the Coulomb coupling between QDs with varying positions and orientations needs to be calculated. Therefore, the motion of colloidal QDs is given by characteristic trajectories, which are represented by specific positions and orientations of the dots to each other. Thus, each of these snapshots of the motion require the calculation of the Coulomb coupling elements to determine the corresponding 2d spectroscopic signature. Therefore, the fast model of the point-dipole approximation is used for the calculation of the Coulomb coupling elements in the Brownian motion of two colloidal QDs. All single position signatures resulting from one trajectory are added together into an averaged 2d spectra providing information of the motion and the averaged distances between the QDs.

1.3 Structure of the thesis

This thesis is composed of a part introducing the fundamental physical concepts, three main parts and a conclusion.

After this introduction, the second chapter briefly introduces the model system as well as the main physical concepts used in the following chapters. This includes the properties of the colloidal QDs together with the connected Hamiltonian, the Coulomb induced exciton states, and the realization of rotations in three dimensions.

For investigating the relation between the coupling processes and the motion of the colloidal QDs, firstly the position-dependent Coulomb coupling needs to be calculated. Thus, in the third chapter, the numerical efficient Poisson Green's function method is defined and adapted to the model of the colloidal QDs. In the approach of the method, the QD's arrangement-specific strength of the monopole-monopole and dipole-dipole Coulomb coupling elements is investigated. Furthermore, the influence of the spatial-dependent dielectric permittivity is included. Finally, the results are compared with the point-dipole approximation for a very fast calculation of the interdot Coulomb coupling.

In the fourth chapter the formalism of the double quantum coherence spectroscopy (DQCS) is presented and 2d spectra for varying QD arrangements are calculated. Using the results of chapter three, the position-dependent signatures resulting from the full calculation of the Coulomb coupling are compared with the signatures in the point-dipole approximation. Furthermore, the influence of the QD's size, the polarization of the excitation pulses and the dephasing rate on the spectroscopic signatures is demonstrated.

In chapter five, the concepts of the Brownian motion of the colloidal QDs are introduced. The formalism of the 2d spectroscopy given in chapter four, together with the results of the Coulomb coupling from chapter three, are used to calculate averaged 2d spectra consisting of millions of single QD signatures. The implementation of the approach together with a convergence analysis are given in the fifth chapter. Then the signatures in the averaged 2d spectra are analyzed concerning the influence of the QD concentration as well as the influence of the solvent's parameters.

Finally, in the brief conclusion the main results are summarized and a short outlook for further investigations is given.

Chapter 2

Physical concepts

While in the main part of this thesis, the Coulomb coupling between diffusing colloidal QDs will be used to investigate the motion of the QDs in the approach of a multidimensional spectroscopy, in this chapter, the fundamental physical concepts needed for the description are briefly introduced. Firstly, the model system of colloidal QDs and the concerning material parameters are presented. Then, the free particle Hamiltonian together with the confinement potential of colloidal core/shell QDs are introduced. In the following, the interaction Hamiltonian is defined, which determines the Coulomb coupling between the colloidal QDs and the electron-light interaction. Furthermore, the exciton basis as a result of the Coulomb interaction between the colloidal QDs is given and the pure electronic Hamiltonian is formulated in this basis. A description in the eigenstate of this Hamiltonian allows other observables, such as the dipole operator, to be formulated in the simple three band exciton model directly including the influence of the Coulomb interaction. Finally, the rotation of three dimensional objects based on the quaternion as well as the Euler angle description is introduced.

2.1 Colloidal quantum dots

QDs are nanocrystals which are sized smaller than the Bohr radius [56] in all three dimensions. Accordingly, the excitons (electron-hole pairs) are confined in all directions and the QD is experienced as a 0-dimensional object [57]. In this thesis, colloidal QDs are investigated, which are synthesized in a solvent [7,8] and thus they diffuse freely in their surrounding medium. Typical diameters of colloidal QDs occur in a range from 1 to 10 nanometers [17].

Colloidal CdSe QDs have been in the focus of research for many years, and therefore, they are extensively studied as a prototypical colloidal QD [58]. Due to developments in the synthesis process of colloidal QDs, the size and shape of the colloidal QDs are manipulatable [11–13]. Therefore, the optical as well as the electronic properties are tunable [9,10]. The resulting size-dependence of the electron band gap and the related exciton energies presents one of the most important topics in the colloidal semiconductor research [17]. In the following section, the model system used in this thesis, which consists of two Coulomb coupled colloidal QDs, is presented together with its characteristic material parameters. Then, the confinement potential and the free particle Hamiltonian are introduced.

2.1.1 Model system and material parameters

In this thesis, colloidal core/shell QDs pairwise coupled via Coulomb interaction were analyzed, as schematically depicted in Fig.2.1. Since the Brownian motion of the QDs in the solvent is considered, both QDs frequently change their spatial positions and dipole orientations due to

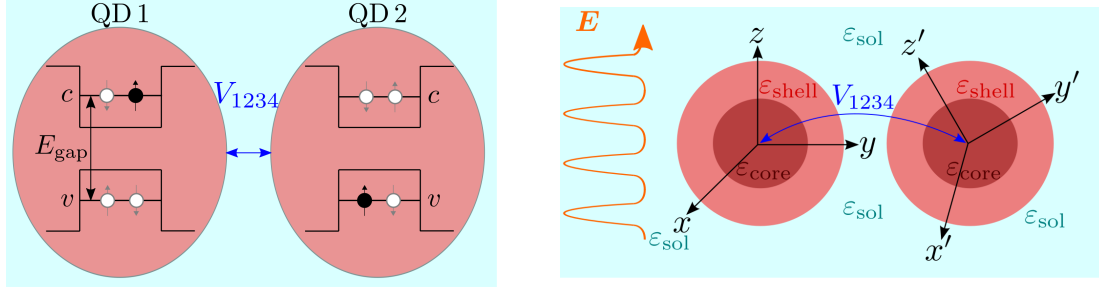


Figure 2.1 Two Coulomb coupled colloidal QDs. Each QD can be described by a two level-systems consisting of a valance band v and a conduction band c with two spin configurations respectively. The two Coulomb coupled core/shell CdSe/ZnTe QDs in water change their spatial positions and orientations due to the diffusion. For investigating the coupling processes, the QDs are excited with a sequence of laser pulses.

the diffusion. The Brownian motion used to describe such a diffusion will be shortly introduced in Chap. 5. The orientation of the spherical QDs is given by the orientation of the permanent transition dipole moment which is induced by the orientation of the crystal axes [59]. As it will be calculated in Chap. 3, the Coulomb coupling, which influences the electronic properties [28], is determined by the QD arrangements. To investigate the influence of the QD's positioning on the Coulomb coupling [4], the system is excited with a sequence of laser pulses and the 2d spectra are detected [2]. The double quantum coherence spectroscopy together with its spatial-dependent signatures will be introduced in Chap. 4.

In contrast to bulk materials, carriers in semiconductor QDs are confined in all spatial dimensions [56, 60] and therefore, they show discrete energy states [56, 61, 62]. Since we investigate the energy of the direct excitons, the QD model is given by a two-level system, which is composed of the highest valence band v and the lowest conduction band c separated by the energy of the band gap E_{gap} , as depicted in Fig. 2.1. The resulting two-level model system is characterized by the bandindex $\lambda \in \{v, c\}$, the QD number $n \in \{1, 2\}$, and the spin configuration $\sigma \in \{\uparrow, \downarrow\}$. The large range of the size variation of colloidal QDs over tens of nanometers according to the synthesis process results in manipulable changes in the density of the electronic states [57]. The band gap increases with decreasing size of the nanocrystal.

The optical spectra as well as the electronic properties of the colloidal QDs are influenced by the Coulomb coupling [4, 28]. Even if the wave functions of the QDs do not overlap, the Coulomb coupling between the QDs may have a significant impact. The Coulomb interaction between two QDs contains the direct electrostatic monopole-monopole coupling between the electrons and the holes of the two QDs [30] and dipole-dipole coupling such as the non-radiative Förster energy transfer [31, 32] inducing exciton energy shifts [5, 6] and excitation transfer between the QDs [34, 35].

The QDs are excited with a sequence of circular polarized light for investigating the influence of the motion of the colloidal QDs, which is determined by specific trajectories, as schematically depicted in Fig. 2.2 and calculated in Chap. 5, on the Coulomb coupling. In order to get a systematically analysis of the influence of the QD arrangement on the strength of the Coulomb coupling (Chap. 3) and on the spectroscopic signatures (Chap. 4), the distances and the angular orientations are varied. The material parameters for describing different core/shell QDs are listed in Tab 2.1. These parameters are used of all the numerical calculations based on the model of the pairwise Coulomb coupled colloidal QDs.

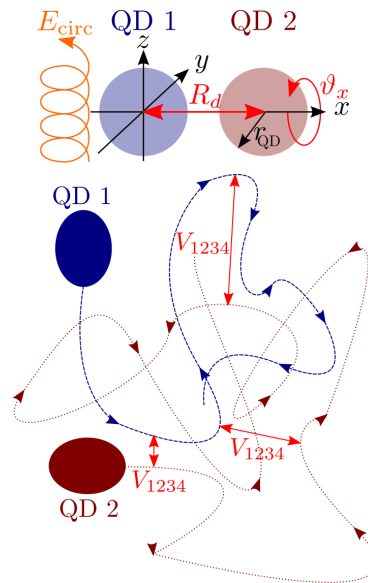


Figure 2.2 Two colloidal QDs moving on characteristic trajectories. The movement of the QDs changes their distance \mathbf{R}_d and their relative dipole orientation. Both influence the strength of the Coulomb coupling between the QDs. To analyze the interplay between the movement of the colloidal QDs and the Coulomb coupling, the 2d spectroscopy can be used. Therefore, the QDs are excited by an external circular polarized electrical field E_{circ} .

Table 2.1 Material parameters used for the different core/shell QDs and the parameters of water H_2O used as a solvent. These parameters include the effective electron m_e^* and hole m_h^* mass in units of the free electron mass m_0 . Furthermore, the permittivity ε of the different materials is listed. These parameters are used of all the numerical calculations of the model system of the two Coulomb coupled colloidal QDs.

material	$m_e^*[m_0]$	$m_h^*[m_0]$	ε	references
CdSe	0.13	0.30	6.23	[10, 15, 17]
ZnTe	0.13	0.56	7.28	[17, 63, 64]
H_2O	1.0	1.0	1.78	[65]
CdS	0.18	0.60	5.50	[18, 65]
ZnSe	0.14	0.52	5.90	[18, 64]

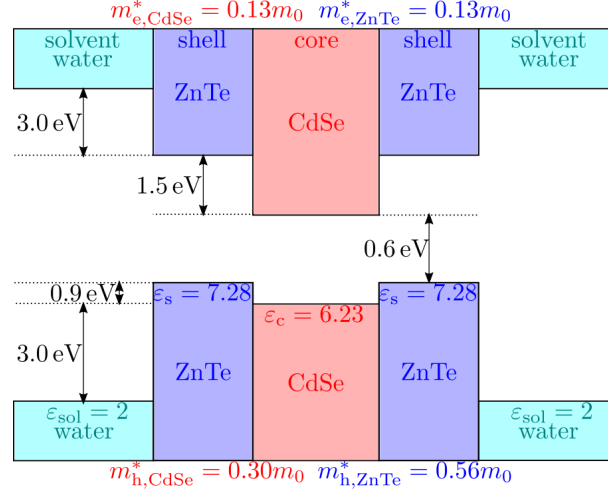


Figure 2.3 The confinement potential of CdSe/ZnTe core/shell QDs surrounded by water [33]. At the bottom the confinement potential of the holes is given, while at the top the electron potential well resulting from the different materials is plotted.

2.1.2 The free particle Hamiltonian and the confinement potential

The Hamiltonian of a system of Coulomb coupled QDs excited by an external light field consists of three parts: the free electronic part H_0 , the part of the Coulomb interaction H_C and the coupling to the excitation field H_{e-1} . The free particle Hamiltonian reads

$$H_0 = \sum_{\lambda,n,\sigma} \varepsilon_{\lambda\sigma} a_{\lambda n\sigma}^\dagger a_{\lambda n\sigma}. \quad (2.1)$$

Here, $a_{\lambda n\sigma}^{(\dagger)}$ denotes the annihilation (creation) operator of an electron in the band λ of the n th QD and with the spin configuration σ . The connected single particle energy is given by $\varepsilon_{\lambda\sigma}$. Following the envelope function description, the electron wave functions $\phi(\mathbf{r})$ are written as a product of an envelope function $\xi(\mathbf{r})$ and a lattice periodic Bloch part $u(\mathbf{r})$ [41,55]. For evaluating the eigenfunctions of the material system, the stationary Schrödinger equation

$$H_0 \xi_{c/v}(\mathbf{r}) = \left(-\frac{\hbar^2}{2m^*} \Delta + V(\mathbf{r}) \right) \xi_{c/v}(\mathbf{r}) = E \xi_{c/v}(\mathbf{r}) \quad (2.2)$$

is solved by using the numerical eigenvalue solver SLEPc [66] for the electrons ξ_c and holes ξ_v respectively. The equation is determined by the free particle Hamiltonian H_0 including the confinement potential $V(\mathbf{r})$ which depends on the geometry as well as on the electronic structure of the model system [67]. Typically, the confinement potential of colloidal QDs is given by a three dimensional potential well for electrons and holes respectively. Fig. 2.3 gives the confinement potential of CdSe/ZnTe core/shell QDs surrounded by water. The confinement is determined by the material's composition and structure [57]. The large range of size variation over tens of nanometers induces changes in the density of electronic states and in the energy level separation. This results in an increase of the band gap with decreasing size of the nanocrystal and the formation of discrete energy levels in the range of the band edges [57]. Accordingly, the electronic and the optical properties of the colloidal QDs are strongly size and shape dependent and therefore, they are tunable by the synthesis process.

Since in the experimental setup the different materials are mixed at the interfaces, a softening of the function of the confinement potential $V(\mathbf{r})$ is introduced [67]. Accordingly, the rectangular-like potential wells of the specific material systems are softened by a weighting factor, which is

QDs can be used to reduce the overlap between the electron and hole wavefunctions still providing a non-zero overlap region. A change between those types of core/shell QDs can be achieved by varying the thickness of the shell material. Thus, the optical and electrical properties of colloidal QDs can be selectively manipulated by changing both core radius and shell width. This influences the overlap of electron and hole wave functions. Accordingly, for a large dimensionality of both core and shell structures, the electron and holes can be completely separated due to a vanishing overlap of the wave functions [18].

The core/shell structure of colloidal QDs is used for manipulating the electrical, optical and the chemical properties of the QDs. For instance, the shell passivates the core's surface and prevents it from leeching with the fluid molecules [25] influencing the motion of the colloidal QD. Furthermore, molecules can be arranged around the QD, which is called a ligand [25]. This monolayer of phospho-alkane ligands creates a barrier to the molecules of the solvent and therefore, the ligand strongly influences the QD-solvent interaction [69]. The composition and chemical interaction between the solvent molecules and the ligand chain length and the size of the QD [69] determine the influence of the ligand to the environment-QD coupling. A surrounding ligand of stabilizing molecules can be extended some nanometers out from the particle [20]. Therefore, the occurrence of a ligand influences the strength of distance-dependent interdot coupling such as the Coulomb interaction.

2.2 Interaction Hamiltonian

If the Coulomb coupled colloidal QDs which diffuse in the solvent are excited with a sequence of laser pulses, the interaction Hamiltonian consists of two parts: the Coulomb Hamiltonian and the electron-light Hamiltonian. These parts of the interaction Hamiltonian are defined in this section. Finally, the total Hamiltonian describing the model system of the colloidal QDs coupled by the Coulomb interaction and interacting with an external laser field is summarized.

2.2.1 Coulomb Hamiltonian

In this thesis, the influence of the frequently changing positions of the colloidal QDs in the solvent on the Coulomb coupling will be investigated. For calculating the strength as well as the QD arrangements dependence of the Coulomb coupling, first the Coulomb Hamiltonian needs to be defined. Thus, the Hamiltonian of the Coulomb interaction is derived for a spatial-dependent medium characterized by $\varepsilon(\mathbf{r})$ [70]. In analogy to the approach of the Poisson Green's function method, which will be introduced in Sec. 3.1, for the derivation of the Hamiltonian a Green's function representation of a Poisson equation is used. The method as well as parts of this section are published in [49], ©2016 American Physical Society.

The inhomogeneous Maxwell equations describe electromagnetic fields, including free charges ρ and currents \mathbf{j} as source terms [71]. To solve the Maxwell equations in material, we use the vector potential \mathbf{A} in a generalized Coulomb gauge [71, 72]: $\nabla_{\mathbf{r}} \cdot (\varepsilon(\mathbf{r})\mathbf{A}(\mathbf{r})) = 0$. Following the approach of Ref. [73], in semiclassical description, the longitudinal part of the dielectric displacement is defined as $\mathbf{D}_L(\mathbf{r}) = -\varepsilon_0\varepsilon(\mathbf{r})\nabla_{\mathbf{r}}\Phi(\mathbf{r})$ with the scalar potential Φ . Therefore, the Coulomb field energy is given by:

$$H_C = \frac{1}{2} \int d^3r \frac{\mathbf{D}_L(\mathbf{r}) \cdot \mathbf{D}_L(\mathbf{r})}{\varepsilon_0\varepsilon(\mathbf{r})}. \quad (2.3)$$

Inserting the definition of the longitudinal dielectric displacement \mathbf{D}_L in Eq. (2.3), the scalar

potential Φ appears:

$$H_C = -\frac{1}{2} \int d^3r \nabla_{\mathbf{r}} \Phi(\mathbf{r}) \cdot \mathbf{D}_L(\mathbf{r}). \quad (2.4)$$

After an integration by parts, the Maxwell equation $\nabla_{\mathbf{r}} \cdot \mathbf{D}_L(\mathbf{r}) = \rho(\mathbf{r})$ is used to include the free charge density ρ :

$$H_C = \frac{1}{2} \int d^3r \Phi(\mathbf{r}) \rho(\mathbf{r}). \quad (2.5)$$

In the Coulomb gauge, the scalar potential Φ satisfies the Poisson equation and the influence of a spatially inhomogeneous medium is represented by a dielectric function $\varepsilon(\mathbf{r})$ [73, 74]:

$$\nabla_{\mathbf{r}} \cdot (\varepsilon(\mathbf{r}) \nabla_{\mathbf{r}} \Phi(\mathbf{r})) = -\frac{\rho(\mathbf{r})}{\varepsilon_0}. \quad (2.6)$$

To express the solution of Eq. (2.6) for a spatially inhomogeneous medium, as is done in Ref. [73], a generalized Coulomb Green's function $G(\mathbf{r}, \mathbf{r}')$ is defined through:

$$\nabla_{\mathbf{r}} \cdot (\varepsilon(\mathbf{r}) \nabla_{\mathbf{r}} G(\mathbf{r}, \mathbf{r}')) = -\frac{1}{\varepsilon_0} \delta(\mathbf{r} - \mathbf{r}'). \quad (2.7)$$

Using the definition of the Green's function in Eq. (2.7), the scalar potential Φ as solution of the Poisson Eq. (2.6) is:

$$\Phi(\mathbf{r}) = \int d^3r' G(\mathbf{r}, \mathbf{r}') \rho(\mathbf{r}'). \quad (2.8)$$

The scalar potential in the Hamiltonian in Eq. (2.5) is replaced using Eq. (2.8) and the two-particle Coulomb Hamiltonian is obtained:

$$H_C = \frac{1}{2} \int d^3r \int d^3r' \rho(\mathbf{r}) G(\mathbf{r}, \mathbf{r}') \rho(\mathbf{r}'). \quad (2.9)$$

In second quantization, the charge density is given by the electron field operators expanded into electronic eigenstates. Thus, the Coulomb Hamiltonian is:

$$H_C = \frac{1}{2} \sum_{1234} V_{1234} a_1^\dagger a_2^\dagger a_3 a_4, \quad (2.10)$$

with 1,2,3 and 4 as multi-indices representing all quantum numbers states (e.g., band index, QD number, spin configuration) and a_i^\dagger (a_i) denoting the creation (annihilation) operators for electrons of the state i . The Coulomb coupling elements V_{1234} of a generalized Coulomb interaction potential $G(\mathbf{r}, \mathbf{r}')$ read [50, 75]:

$$V_{1234} = e^2 \int d^3r \int d^3r' \phi_1^*(\mathbf{r}) \phi_2^*(\mathbf{r}') G(\mathbf{r}, \mathbf{r}') \phi_3(\mathbf{r}') \phi_4(\mathbf{r}), \quad (2.11)$$

where $\phi_i(\mathbf{r})$ is the electron wave function of the state i . In general, Eq. (2.11) requires a numerical solution. The six dimensional space integral needs to be evaluated for calculating the two-particle Coulomb interaction. Accordingly, the calculation of the Coulomb coupling elements is numerically demanding, compared to three dimensional integrals, and constitutes a significant limitation factor in the calculation of complex problems. Since the colloidal QDs diffusing in the solvent frequently change their spatial positions and angular orientations, a high number of Coulomb coupling elements needs to be calculated. Therefore, the Poisson Green's function method for fast numerical calculations is necessary and will be introduced in Sec. 3.1 representing a general numerical procedure to reduce the computational cost of the calculation of the related coupling elements.

2.2.2 Electron-light interaction

For detecting and visualizing the influence of the QD arrangements on the Coulomb coupling, the multidimensional coherent spectroscopy will be used. Therefore, the colloidal QDs are excited with a sequence of well-defined laser pulses. The coupling of the electrons of the colloidal QDs to this external light field \mathbf{E} is given by a semiclassical dipole interaction and the Hamiltonian of the electron-light interaction as follows:

$$H_{e-l} = -\mathbf{d} \cdot \mathbf{E}. \quad (2.12)$$

In second quantization, the dipole operator \mathbf{d} is given by electron field operators $\psi^{(\dagger)}(\mathbf{r})$ for the annihilation (creation) of an electron at position \mathbf{r}

$$\mathbf{d} = e \int d^3r \psi^\dagger(\mathbf{r}) \mathbf{r} \psi(\mathbf{r}). \quad (2.13)$$

These electron field operators are expanded into electronic eigenmodes

$$\psi(\mathbf{r}) = \sum_{\lambda, n, \sigma} \phi_{\lambda n \sigma}(\mathbf{r}) a_{\lambda n \sigma}, \quad (2.14)$$

where $\phi_{\lambda n \sigma}(\mathbf{r})$ denotes the electron wave function of an electron with bandindex $\lambda \in \{v, c\}$, QD number $n \in \{1, 2\}$ and spin configuration $\sigma \in \{\uparrow, \downarrow\}$, and $a_{\lambda n \sigma}$ gives the annihilation of an electron in the corresponding quantum state. Using the effective mass and the envelope function approximation, the electron wave functions are assumed to be written as a product of the envelope function $\xi(\mathbf{r})$ and a lattice periodic Bloch part $u(\mathbf{r})$ [55]:

$$\phi_{\lambda n \sigma}(\mathbf{r}) = \xi_{\lambda n}(\mathbf{r}) u_{\lambda n \sigma}(\mathbf{r}). \quad (2.15)$$

Using Eq. (2.14) and Eq. (2.15), the dipole operator of the semiconductor QD reads

$$\mathbf{d} = e \int d^3r \sum_{\lambda_1, \lambda_2} \sum_{n_1, n_2} \sum_{\sigma_1, \sigma_2} \xi_{\lambda_1 n_1}^*(\mathbf{r}) u_{\lambda_1 n_1 \sigma_1}^*(\mathbf{r}) \mathbf{r} \xi_{\lambda_2 n_2}(\mathbf{r}) u_{\lambda_2 n_2 \sigma_2}(\mathbf{r}) a_{\lambda_1 n_1 \sigma_1}^\dagger a_{\lambda_2 n_2 \sigma_2}. \quad (2.16)$$

A scale separation of the space operator \mathbf{r} into the position of the i th unit cell \mathbf{R}_i and the variation inside the cell \mathbf{s}_i is conducted: $\mathbf{r} = \mathbf{R}_i + \mathbf{s}_i$ [41]. Under the assumption of a slowly varying envelope, the envelope function is treated to be constant on the size of the unit cell: $\xi(\mathbf{R}_i + \mathbf{s}_i) \approx \xi(\mathbf{R}_i)$. Using the periodicity of the Bloch functions: $u(\mathbf{R}_i + \mathbf{s}_i) = u(\mathbf{s}_i)$, the dipole operator is given by

$$\begin{aligned} \mathbf{d} = & e \sum_i \sum_{\lambda_1, \lambda_2} \sum_{n_1, n_2} \sum_{\sigma_1, \sigma_2} \xi_{\lambda_1 n_1}^*(\mathbf{R}_i) \xi_{\lambda_2 n_2}(\mathbf{R}_i) \\ & \cdot \left(\mathbf{R}_i \int d^3s_i u_{\lambda_1 n_1 \sigma_1}^*(\mathbf{s}_i) u_{\lambda_2 n_2 \sigma_2}(\mathbf{s}_i) + \int d^3s_i u_{\lambda_1 n_1 \sigma_1}^*(\mathbf{s}_i) \mathbf{s}_i u_{\lambda_2 n_2 \sigma_2}(\mathbf{s}_i) \right) a_{\lambda_1 n_1 \sigma_1}^\dagger a_{\lambda_2 n_2 \sigma_2}. \end{aligned} \quad (2.17)$$

The first term in the Eq. (2.17) corresponds to the intraband transitions, while the second term describes interband processes. In the following, the first term is neglected, since interband and intraband processes occur on different energy scales. Accordingly, in this thesis, only interband interactions are considered for the electron-light interaction. Therefore, the macroscopic dipole operator \mathbf{d} is determined by the microscopic dipole moments $\boldsymbol{\mu}_{\lambda_1 \lambda_2}^{n\sigma}$ for the interband electron transitions on the volume of the unit cells V_{uc} , which are defined through [34, 76]:

$$\boldsymbol{\mu}_{\lambda_1 \lambda_2}^{n\sigma} = \frac{e}{V_{uc}} \int_{V_{uc}} d^3s_i u_{\lambda_1 n \sigma}^*(\mathbf{s}_i) \mathbf{s}_i u_{\lambda_2 n \sigma}(\mathbf{s}_i). \quad (2.18)$$

Under the assumption that the unit cells are very close, the summation over the number of unit cells in Eq. (2.17) is transformed into an integration $\sum_i \rightarrow \frac{1}{V_{\text{uc}}} \int_{V_{\text{uc}}} d^3\mathbf{r}$ and therefore, the dipole operator is written as

$$\mathbf{d} = \sum_{\lambda_1, \lambda_2} \sum_{n, \sigma} \int d^3\mathbf{r} \xi_{\lambda_1 n}^*(\mathbf{r}) \xi_{\lambda_2 n}(\mathbf{r}) \boldsymbol{\mu}_{\lambda_1 \lambda_2}^{n\sigma} a_{\lambda_1 n \sigma}^\dagger a_{\lambda_2 n \sigma}. \quad (2.19)$$

Introducing the envelope overlap integral $\chi_{\lambda_1 \lambda_2}^n = \int d^3\mathbf{r} \xi_{\lambda_1 n}^*(\mathbf{r}) \xi_{\lambda_2 n}(\mathbf{r})$, which describes the spatial extension of the QDs, the dipole operator of a semiconductor QD consisting of a valence band v and a conduction band c is given by:

$$\mathbf{d} = \sum_{n, \sigma} \chi_{vc}^n \boldsymbol{\mu}_{vc}^{n\sigma} a_{vn\sigma}^\dagger a_{cn\sigma} + \chi_{cv}^n \boldsymbol{\mu}_{cv}^{n\sigma} a_{cn\sigma}^\dagger a_{vn\sigma}. \quad (2.20)$$

Due to the spin selection rules of the resonance energy transfer between QDs with a zinc-blende structure [3], the microscopic dipole transitions in Eq. (2.18), which depends on the spin of the involved system, can be written as follows:

$$\boldsymbol{\mu}_{cv}^{n\uparrow} = \frac{\mu_0}{\sqrt{2}} (\mathbf{e}_x + i\mathbf{e}_y) \quad \boldsymbol{\mu}_{vc}^{n\uparrow} = \frac{\mu_0}{\sqrt{2}} (\mathbf{e}_x - i\mathbf{e}_y) \quad (2.21a)$$

$$\boldsymbol{\mu}_{cv}^{n\downarrow} = \frac{\mu_0}{\sqrt{2}} (\mathbf{e}_x - i\mathbf{e}_y) \quad \boldsymbol{\mu}_{vc}^{n\downarrow} = \frac{\mu_0}{\sqrt{2}} (\mathbf{e}_x + i\mathbf{e}_y). \quad (2.21b)$$

Eqs. (2.21a) and (2.21b) show, that the microscopic transition dipole moments of QDs with a zinc-blende lattice are perpendicular to the crystal c -axis. Accordingly, if the QDs rotate, the angular orientation of the dipole moments changes too, which is particularly important for colloidal QDs freely diffusing in the solvent. For both, zinc-blende and wurtzite nanocrystals, the permanent dipole moment is linearly dependent on the radius of the colloidal QD [58]. Depending on the synthesis process, colloidal QDs like CdSe can be synthesized with a crystalline zinc-blende structure [12, 77]. Therefore, the orientation of microscopic dipole transitions of the colloidal QDs depends on the angular orientation of the QDs in the excitation field. The permanent dipole moment of colloidal CdSe QDs with a radius of $r_p = 1.5$ nm is $\mu_0 = 1$ enm [58]. If the size of the colloidal QDs increases, the value of the permanent dipole moment is enlarged. Thus, for bigger colloidal CdSe QDs with a radius of $r_p = 3$ nm a dipole moment of $\mu_0 = 2$ enm is used [78].

2.2.3 The total Hamiltonian

The total Hamiltonian used in this thesis, which describes the Coulomb coupled colloidal QDs interacting with an external light field, consists of three parts: the free electronic part H_0 , the part of the Coulomb interaction H_C and the coupling to the excitation field H_{e-1} :

$$H_0 = \sum_{\lambda, n, \sigma} \varepsilon_{\lambda\sigma} a_{\lambda n \sigma}^\dagger a_{\lambda n \sigma} \quad (2.22)$$

$$H_C = \frac{1}{2} \sum_{\lambda_1, \dots, \lambda_4} \sum_{n_1, \dots, n_4} \sum_{\sigma_1, \dots, \sigma_4} V_{1234} a_{\lambda_1 n_1 \sigma_1}^\dagger a_{\lambda_2 n_2 \sigma_2}^\dagger a_{\lambda_3 n_3 \sigma_3} a_{\lambda_4 n_4 \sigma_4} \quad (2.23)$$

$$H_{e-1} = -\hbar \sum_{n, \sigma} \left(\Omega_{cv}^{n\sigma} a_{cn\sigma}^\dagger a_{vn\sigma} + \Omega_{vc}^{n\sigma} a_{vn\sigma}^\dagger a_{cn\sigma} \right), \quad (2.24)$$

with the Coulomb coupling elements:

$$V_{1234} = e^2 \int d^3\mathbf{r} \int d^3\mathbf{r}' \phi_{\lambda_1 n_1 \sigma_1}^*(\mathbf{r}) \phi_{\lambda_2 n_2 \sigma_2}^*(\mathbf{r}') G(\mathbf{r}, \mathbf{r}') \phi_{\lambda_3 n_3 \sigma_3}(\mathbf{r}') \phi_{\lambda_4 n_4 \sigma_4}(\mathbf{r}), \quad (2.25)$$

and the Rabi frequency and the envelope overlap integral:

$$\Omega_{\lambda_1 \lambda_2}^{n\sigma} = \frac{1}{\hbar} \chi_{\lambda_1 \lambda_2}^n \boldsymbol{\mu}_{\lambda_1 \lambda_2}^{n\sigma} \cdot \mathbf{E} \quad \chi_{\lambda_1 \lambda_2}^n = \int d^3\mathbf{r} \xi_{\lambda_1 n}^*(\mathbf{r}) \xi_{\lambda_2 n}(\mathbf{r}). \quad (2.26)$$

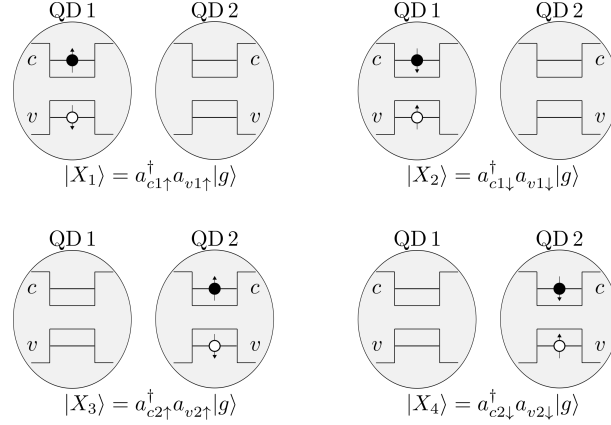


Figure 2.5 A system of two colloidal QDs includes four localized bright exciton states as eigenstates of the free particle Hamiltonian. While the local exciton states $|X_i\rangle$ are given in the electron-electron picture, in the schemes the electron-hole picture is illustrated.

2.3 Exciton basis

The Coulomb coupling between nanostructures induces the formation of collective particle states, such as excitons, biexcitons, or trions [36]. In this thesis, the single and double excitons as collective delocalized electronic excitations [79] determine the interaction processes of the system of two colloidal QDs. They provide information on the Coulomb coupling between carriers, such as exchanges and correlation effects [80]. For receiving a formalism directly including the influence of the Coulomb coupling, the pure electronic Hamiltonian, which includes the free particle Hamiltonian as well as the Coulomb-Hamiltonian, is formulated as a matrix in the exciton basis.

Even if the electron wave functions do not overlap, the Coulomb interaction between nanostructures causes a formation of new delocalized exciton states. Since the dipole-dipole Coulomb coupling induces off-diagonal elements, the Hamiltonian is diagonalized to get a description based on the delocalized exciton states as eigenstates of the pure Hamiltonian. Other variables and quantum dynamical equations are transformed into the new basis of delocalized exciton states for a consistent description based on the eigenstates of the electronic Hamiltonian. Therefore, the formalism directly includes the influence of the Coulomb coupling.

In the optical spectroscopy, the electron-light excitation processes determine the interaction processes. Therefore, the dipole operator, determining the electron-light Hamiltonian, is transformed into the exciton basis. This enables the whole formalism of the multidimensional spectroscopy to be introduced in the delocalized exciton states, which directly included the influence of the Coulomb coupling.

2.3.1 Localized exciton states and Hamiltonian

Colloidal QDs, as introduced in Sec. 2.1, can be viewed as a two-level system, which is composed of the highest valence band v and the lowest conduction band c separated by the energy of the band gap E_{gap} . Since the spin splitting of the electronic quantum states is included, each band with bandindex $\lambda \in \{v, c\}$ provides two spin levels $\sigma \in \{\uparrow, \downarrow\}$. In this thesis, a system consisting of two colloidal QDs is investigated. Thus, the Coulomb coupling as a two particle interaction occurs between the two QDs as interdot coupling or located in one QD as intradot coupling, given by the QD number $n \in \{1, 2\}$. The local single exciton states $|X_i\rangle$, which represent the

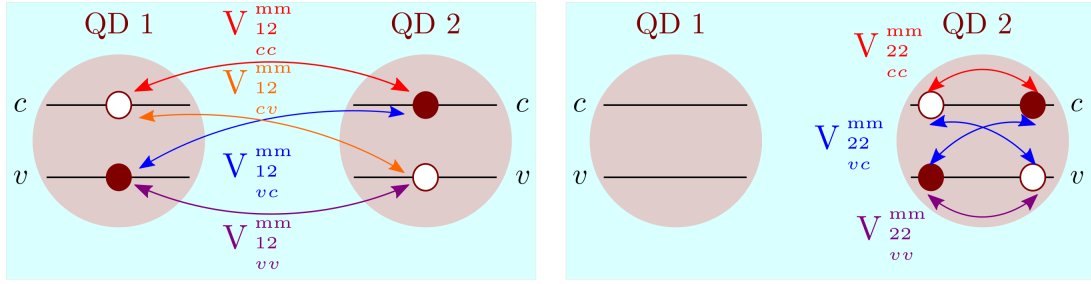


Figure 2.6 The interdot (left) and intradot (right) monopole-monopole Coulomb coupling elements. The electrostatic Coulomb coupling occurs between the electrons and holes of the colloidal QDs. The different coupling elements are determined by the band indices.

eigenstates of the free particle Hamiltonian H_0 , are generated from the ground state $|g\rangle$:

$$|X_i\rangle = a_{c n_i \sigma_i}^\dagger a_{v n_i \sigma_i'} |g\rangle. \quad (2.27)$$

Therefore, the local exciton states for a system of two coupled colloidal QDs, as depicted in Fig. 2.5, can be formulated. Respecting the bright states only, since the dark states are usually not excited due to the spin flip between electron and hole, the basis set of the localized single exciton states consists of four bright states:

$$|X_1\rangle = a_{c1\uparrow}^\dagger a_{v1\uparrow} |g\rangle, \quad (2.28a)$$

$$|X_2\rangle = a_{c1\downarrow}^\dagger a_{v1\downarrow} |g\rangle, \quad (2.28b)$$

$$|X_3\rangle = a_{c2\uparrow}^\dagger a_{v2\uparrow} |g\rangle \text{ and} \quad (2.28c)$$

$$|X_4\rangle = a_{c2\downarrow}^\dagger a_{v2\downarrow} |g\rangle. \quad (2.28d)$$

In the following, the Hamiltonian is formulated in the basis of localized bright exciton states. Since these exciton states result from the Coulomb interaction, the pure electronic Hamiltonian $H_{el} = H_0 + H_C$ is introduced. First, all elements of the pure electronic Hamiltonian resulting from the quantum numbers are identified. The Hamiltonian consists of multiple combinations of the two-particle electron-electron operators each weighted with a specific Coulomb coupling element, generally written as the sum in Eq. (2.10). All these elements are explicitly given in App. A.1. The Coulomb coupling between two colloidal QDs includes the monopole-monopole Coulomb coupling elements, given in App. A.1.1 as well as the dipole-dipole coupling elements in App. A.1.2, both occurring as intradot and interdot coupling. The monopole-monopole coupling elements, depicted in Fig. 2.6, represent the electrostatic Coulomb coupling between electrons and holes. The dipole-dipole coupling includes a spin-sensitive excitation energy transfer between the QDs as well as an intradot coupling, as schematically illustrated in Fig. 2.7.

For further calculations, the pure electronic Hamiltonian H_{el} needs to be expressed in the basis of the local exciton states, represented in a matrix formula. Starting with the single exciton basis defined in Eq. (2.28), the calculations are conducted in App. A.2.1 for the example of two Coulomb coupled colloidal QDs. In this notation, terms resulting from the free particle Hamiltonian H_0 (cf. Eq. (2.1)) as well as shifts caused by the direct monopole-monopole Coulomb coupling occur on

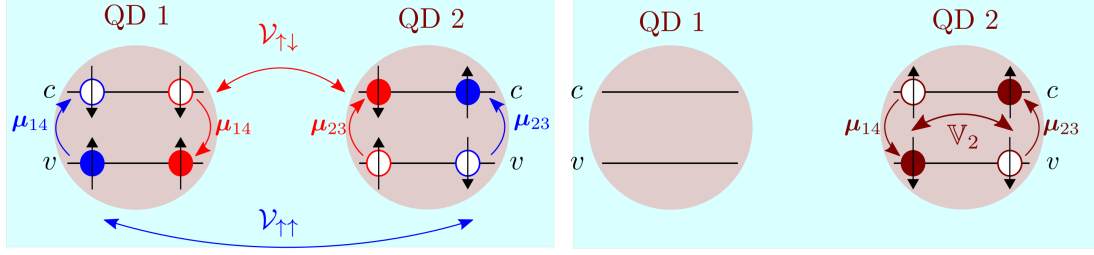


Figure 2.7 The spin-sensitive Förster coupling as excitation energy transfer between the colloidal QDs (on the left) and the intradot dipole-dipole Coulomb coupling (on the right). The dipole-dipole coupling is determined by the microscopic dipole moments μ_{14} and μ_{23} .

the diagonal of the Hamiltonian. Collecting all terms, the following abbreviations are introduced:

$$\mathcal{E}_0 := 2\varepsilon_{v1} + 2\varepsilon_{v2} + 2V_{11}^{\text{mm}} + 2V_{22}^{\text{mm}} + 8V_{12}^{\text{mm}}, \quad (2.29)$$

$$\mathcal{E}_1 := \varepsilon_{c1} - \varepsilon_{v1} - 2V_{11}^{\text{mm}} + 2V_{11}^{\text{mm}} - 4V_{12}^{\text{mm}} + 4V_{12}^{\text{mm}}, \quad (2.30)$$

$$\mathcal{E}_2 := \varepsilon_{c2} - \varepsilon_{v2} - 2V_{22}^{\text{mm}} + 2V_{22}^{\text{mm}} - 4V_{12}^{\text{mm}} + 4V_{12}^{\text{mm}}. \quad (2.31)$$

Since the spin configurations do not directly influence the monopole-monopole coupling elements and therefore, they are not included in this notation. Due to the symmetry regarding the pairwise change of the indices, all Coulomb terms appear twice.

While the free particle Hamiltonian and the monopole-monopole Coulomb coupling determine the diagonal elements of the pure electronic Hamiltonian, all dipole-dipole excitation transfers, given in App. A.2.1, appear as off-diagonal elements. Including the symmetry of the pairwise permutation of the indices in the Coulomb coupling, the Förster coupling between two QDs is determined by two spin configurations: the spin-preserving processes given by $\sigma = \sigma'$ and the spin-flipping processes with $\sigma \neq \sigma'$. Therefore, the spin-selective Förster coupling elements are characterized by $\mathcal{V}_{\uparrow\uparrow} = \mathcal{V}_{\downarrow\downarrow}^*$ and $\mathcal{V}_{\uparrow\downarrow} = \mathcal{V}_{\downarrow\uparrow}^*$. Due to the Pauli principle in a two-level system, the intradot dipole-dipole coupling elements \mathbb{V}_i only includes spin-flipping processes ($\sigma \neq \sigma'$) and therefore, they are determined by the quantum dot number.

Collecting all interdot and intradot Coulomb coupling elements, the pure electronic Hamiltonian matrix (without the electron-light interaction) [35, 62] can be transformed into the basis of the localized single exciton states:

$$H_{\text{el},X} = \begin{pmatrix} \mathcal{E}_0 + \mathcal{E}_1 & 2\mathbb{V}_1 & 2\mathcal{V}_{\uparrow\uparrow} & 2\mathcal{V}_{\uparrow\downarrow} \\ 2\mathbb{V}_1^* & \mathcal{E}_0 + \mathcal{E}_1 & 2\mathcal{V}_{\downarrow\uparrow} & 2\mathcal{V}_{\downarrow\downarrow} \\ 2\mathcal{V}_{\uparrow\uparrow}^* & 2\mathcal{V}_{\downarrow\uparrow}^* & \mathcal{E}_0 + \mathcal{E}_2 & 2\mathbb{V}_2 \\ 2\mathcal{V}_{\uparrow\downarrow}^* & 2\mathcal{V}_{\downarrow\downarrow}^* & 2\mathbb{V}_2^* & \mathcal{E}_0 + \mathcal{E}_2 \end{pmatrix}. \quad (2.32)$$

The Hamiltonian matrix in Eq. (2.32) shows, that the monopole-monopole coupling induces an energy renormalization in comparison to the uncoupled system [35]. In case of the Förster coupling, the off-diagonal dipole-dipole coupling elements induce a non-radiative energy transfer between the QDs [34]. Since the off-diagonal matrix elements couple different exciton states, they induce a delocalization of the exciton states. Thus, induced by the Coulomb interaction, the exciton states are delocalized over the whole system and therefore cannot be allocated to the single localized QDs. A calculation of these delocalized states is given in Sec. 2.3.2.

If multiple excitations are included, as in the case of the multidimensional spectroscopy, double exciton states also called biexciton states occur. In analogy to the single exciton states

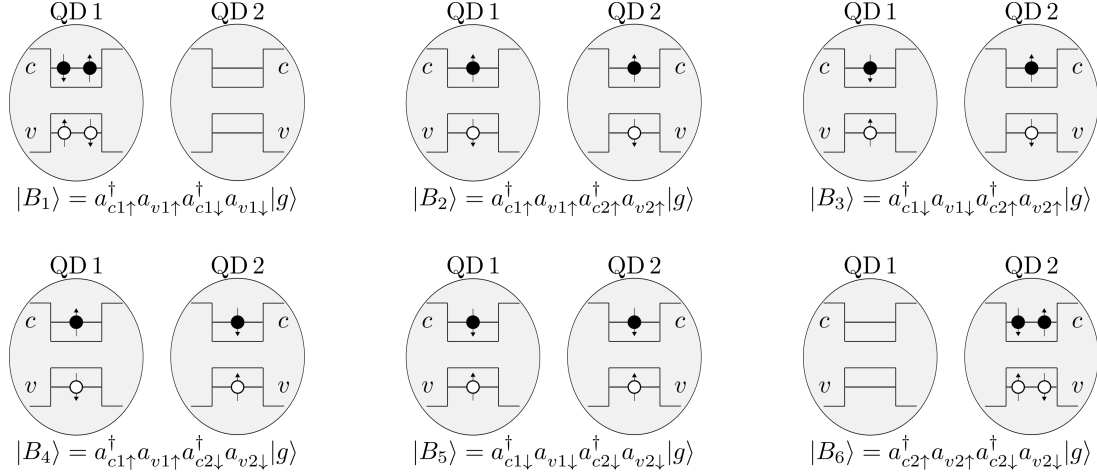


Figure 2.8 A system of two colloidal QDs provides six local bright double exciton states as eigenstates of the free particle Hamiltonian. In analogy to the singly excited states, the doubly excited states $|B_i\rangle$ are written in the electron-electron picture and depicted in the electron-hole picture. Either both excitons are located in one QD or they are separated in each QD respectively.

in Eq. (2.27), the local double exciton states $|B_{ij}\rangle$ of the uncoupled system are generated from the ground state as follows:

$$|B_{ij}\rangle = a_{cn_i\sigma_i}^\dagger a_{vn_i\sigma_i} a_{cn_j\sigma_j}^\dagger a_{vn_j\sigma_j} |g\rangle. \quad (2.33)$$

Thus, for the example of two Coulomb coupled colloidal QDs, six local bright doubly excited states occur, as illustrated in Fig. 2.8:

$$|B_1\rangle = a_{c1\uparrow}^\dagger a_{v1\uparrow} a_{c1\downarrow}^\dagger a_{v1\downarrow} |g\rangle, \quad (2.34a)$$

$$|B_2\rangle = a_{c1\uparrow}^\dagger a_{v1\uparrow} a_{c2\uparrow}^\dagger a_{v2\uparrow} |g\rangle, \quad (2.34b)$$

$$|B_3\rangle = a_{c1\downarrow}^\dagger a_{v1\downarrow} a_{c2\uparrow}^\dagger a_{v2\uparrow} |g\rangle, \quad (2.34c)$$

$$|B_4\rangle = a_{c1\uparrow}^\dagger a_{v1\uparrow} a_{c2\downarrow}^\dagger a_{v2\downarrow} |g\rangle, \quad (2.34d)$$

$$|B_5\rangle = a_{c1\downarrow}^\dagger a_{v1\downarrow} a_{c2\downarrow}^\dagger a_{v2\downarrow} |g\rangle \text{ and} \quad (2.34e)$$

$$|B_6\rangle = a_{c2\uparrow}^\dagger a_{v2\uparrow} a_{c2\downarrow}^\dagger a_{v2\downarrow} |g\rangle. \quad (2.34f)$$

If both excitons are located in one QD, the Coulomb interaction occurs as intradot coupling. In the case of separated excitons, each QD include one exciton and therefore, the Coulomb coupling induces an interdot interaction between both colloidal QDs.

Since multiple excitation processes induce double exciton states, a formulation of the pure electronic Hamiltonian H_{el} in the basis of these biexciton states should be introduced. In analogy to the transformation in the single exciton basis, all terms of the Hamiltonian, given in App. A.1 are collected and the matrix elements can be calculated, cf. App. A.2.2. As in the case of the single exciton basis, the diagonal elements of the pure Hamiltonian matrix includes the free particle Hamiltonian H_0 (cf. Eq. (2.1)) and the monopole-monopole Coulomb elements. For convenience, the following abbreviations for the diagonal elements of the Hamiltonian matrix are introduced:

$$E_{011} := \mathcal{E}_0 + 2\mathcal{E}_1 + \mathcal{E}_{11}, \quad (2.35)$$

$$E_{012} := \mathcal{E}_0 + \mathcal{E}_1 + \mathcal{E}_2 + \mathcal{E}_{12}, \quad (2.36)$$

$$E_{022} := \mathcal{E}_0 + 2\mathcal{E}_2 + \mathcal{E}_{22}, \quad (2.37)$$

including additional shifts caused by the doubly excited states:

$$\mathcal{E}_{11} := 2V_{11}^{mm} + 2V_{11}^{mm} - 4V_{11}^{mm} , \quad (2.38)$$

$$\mathcal{E}_{12} := 2V_{12}^{mm} + 2V_{12}^{mm} - 2V_{12}^{mm} - 2V_{12}^{mm} , \quad (2.39)$$

$$\mathcal{E}_{22} := 2V_{22}^{mm} + 2V_{22}^{mm} - 4V_{22}^{mm} . \quad (2.40)$$

The off-diagonal elements are determined by the dipole-dipole Coulomb elements which couple different biexciton states. Thus, the resulting matrix of the pure electron Hamiltonian matrix $H_{\text{el}} = H_0 + H_C$ represented in the basis of the local bright double exciton states (cf. Eqs. (2.34) and Fig. 2.8) reads:

$$H_{\text{el}BB} = \begin{pmatrix} E_{011} & 2\mathcal{V}_{\downarrow\uparrow} & 2\mathcal{V}_{\uparrow\uparrow} & 2\mathcal{V}_{\downarrow\downarrow} & 2\mathcal{V}_{\uparrow\downarrow} & 0 \\ 2\mathcal{V}_{\downarrow\uparrow}^* & E_{012} & 2\mathbb{V}_1 & 2\mathbb{V}_2 & 0 & 2\mathcal{V}_{\uparrow\downarrow} \\ 2\mathcal{V}_{\uparrow\uparrow}^* & 2\mathbb{V}_1^* & E_{012} & 0 & 2\mathbb{V}_2 & 2\mathcal{V}_{\downarrow\downarrow} \\ 2\mathcal{V}_{\downarrow\downarrow}^* & 2\mathbb{V}_2^* & 0 & E_{012} & 2\mathbb{V}_1 & 2\mathcal{V}_{\uparrow\uparrow} \\ 2\mathcal{V}_{\uparrow\downarrow}^* & 0 & 2\mathbb{V}_2^* & 2\mathbb{V}_1^* & E_{012} & 2\mathcal{V}_{\downarrow\uparrow} \\ 0 & 2\mathcal{V}_{\uparrow\downarrow}^* & 2\mathcal{V}_{\downarrow\downarrow}^* & 2\mathcal{V}_{\uparrow\uparrow}^* & 2\mathcal{V}_{\downarrow\uparrow}^* & E_{022} \end{pmatrix} . \quad (2.41)$$

The monopole-monopole Coulomb coupling induces energy renormalization regarding the uncoupled system, while the dipole-dipole coupling induces a delocalization of the states. For retrieving a formulation based on the eigenenergies of the Hamiltonian, the matrices of the pure electron Hamiltonian in the single exciton basis in Eq. (2.32) as well as in the biexciton basis given in Eq. (2.41) need to be diagonalized. The resulting description is based on delocalized exciton states and will be introduced in the following section.

2.3.2 Delocalized exciton states

Since the dipole-dipole Coulomb interactions occur off-diagonal, they couple different electronic states. Thus, the Coulomb coupling hybridizes the local QD states into new delocalized exciton states [4]. These states represent the eigenstates of the pure electronic Hamiltonian H_{el} . Therefore, a new three band model consisting of the ground state as well as the delocalized single and double exciton states is introduced. Since these states are delocalized over the whole structure, they cannot be identified with the isolated QD states.

The new delocalized basis set of exciton states $|e\rangle$ is given by a linear combination of the local single exciton states in Eq. (2.27) [81]:

$$|e\rangle = \sum_i \eta_i^e |X_i\rangle \quad (2.42)$$

$$|e\rangle = \sum_i \eta_i^e a_{cn_i\sigma_i}^\dagger a_{vn_i\sigma_i} |g\rangle . \quad (2.43)$$

The coefficients η_i^e of the transformation into the new delocalized basis are numerically obtained by diagonalizing the Hamiltonian given in the single exciton states in Eq. (2.32). These new delocalized exciton states represent the eigenstates of the pure electronic Hamiltonian, including the Coulomb interaction: $(H_0 + H_C)|e\rangle = E_e|e\rangle$.

In an analog way, the delocalized double exciton states $|f\rangle$ generated by local biexciton states

in Eq. (2.33) are:

$$|f\rangle = \sum_{i,j \neq i} \eta_{ij}^f |B_{ij}\rangle \quad (2.44)$$

$$|f\rangle = \sum_{i,j \neq i} \eta_{ij}^f a_{cn_i \sigma_i}^\dagger a_{vn_i \sigma_i'} a_{cn_j \sigma_j}^\dagger a_{vn_j \sigma_j'} |g\rangle. \quad (2.45)$$

Again, the coefficients η_{ij}^f of the linear combination of the double exciton states have to be numerically calculated as coefficients of the diagonalization of the Hamiltonian matrix in the basis of the local biexciton states in Eq. (2.41). Accordingly, the new delocalized biexciton states are the eigenstates of the pure electronic Hamilton operator: $(H_0 + H_C)|f\rangle = E_f|f\rangle$, analog to the delocalized single exciton states.

As a result of the new three band system consisting of the ground state and the delocalized exciton states, the pure electronic Hamiltonian reads:

$$H_{\text{el}} = H_0 + H_C = E_g |g\rangle\langle g| + \sum_e E_e |e\rangle\langle e| + \sum_f E_f |f\rangle\langle f|. \quad (2.46)$$

The delocalized exciton states enable descriptions to be done in the eigensystem of a Hamiltonian directly including the influence of the Coulomb coupling. Therefore processes and observables can be formulated in this simple three band system. In the following section the dipole operator in Eq. (2.20) is transformed to the new basis of the delocalized states to express the coupling between the electrons of the system and the photons of the exciting pulses.

2.3.3 Transforming the dipole operator into the delocalized basis

Since the dipole-dipole Coulomb interaction induces off-diagonal matrix elements in the Hamiltonian, new delocalized exciton states as eigenstates of the pure electronic Hamiltonian occur as introduced in Sec. 2.3.2. Therefore, other observables are transformed into the new basis of delocalized exciton states, since this directly includes the influence of the Coulomb coupling. For describing excitation processes, as typically involved in the optical spectroscopy, the electron-light interaction introduced in Sec. 2.2.2 needs to be formulated in the eigensystem of the pure electron Hamiltonian. Since the dipole operator determines the electron-light interaction, in this section the formulation of the dipole operator in the delocalized basis is introduced.

In the approach of the electron-light interaction, the dipole operator, which was introduced in Eq. (2.20), determines the transitions in the electronic system. The delocalized exciton base is based on the identity:

$$1 = |g\rangle\langle g| + \sum_e |e\rangle\langle e| + \sum_f |f\rangle\langle f| + \dots. \quad (2.47)$$

In the following, only single exciton states $|e\rangle$ and double exciton states $|f\rangle$ are included and therefore, further terms of the identity Eq. (2.47) are neglected. Using the selection rules for a zinc-blende nanocrystal [3] and assuming that only dipole transitions between the ground and single exciton states as well as between single and double exciton states occur [2], the dipole operator in the delocalized exciton base reads:

$$\mathbf{d}_{\text{el}} = \sum_e \left(\mathbf{d}_{ge} |g\rangle\langle e| + \mathbf{d}_{eg} |e\rangle\langle g| \right) + \sum_{e,f} \left(\mathbf{d}_{ef} |e\rangle\langle f| + \mathbf{d}_{fe} |f\rangle\langle e| \right). \quad (2.48)$$

As visible in Eq. (2.48), the dipole operator in the delocalized base \mathbf{d}_{el} is determined by the dipole transitions between the exciton states. Thus, these dipole transitions need to be calculated. We

start with the dipole transition from the ground state $|g\rangle$, which keeps its format, to a single exciton state $|e\rangle$ defined in Eq. (2.43). Therefore, the dipole operator \mathbf{d} in the local QD states given in Eq. (2.20) needs to be transformed into the delocalized states as follows:

$$\begin{aligned} \mathbf{d}_{ge} &= \langle g|\mathbf{d}|e\rangle \\ \mathbf{d}_{ge} &= \sum_{i,j} \eta_j^e \left(\chi_{vc}^{n_i} \boldsymbol{\mu}_{vc}^{n_i \sigma_i} \underbrace{\langle g|a_{vn_i \sigma_i}^\dagger a_{cn_i \sigma_i} a_{cn_j \sigma_j}^\dagger a_{vn_j \sigma_j}|g\rangle}_{\delta_{ij}} + \chi_{cv}^{n_i} \boldsymbol{\mu}_{cv}^{n_i \sigma} \underbrace{\langle g|a_{cn_i \sigma_i}^\dagger a_{vn_i \sigma_i} a_{cn_j \sigma_j}^\dagger a_{vn_j \sigma_j}|g\rangle}_0 \right) \\ \mathbf{d}_{ge} &= \sum_i \eta_i^e \chi_{vc}^{n_i} \boldsymbol{\mu}_{vc}^{n_i \sigma_i}. \end{aligned} \quad (2.49)$$

Since the dipole element denotes a transition from the ground g state to an exciton state with the index e , it describes one component of the dipole transition in the delocalized exciton base. But since the dipole operator keeps its cartesian components, defined by the microscopic dipole transition $\boldsymbol{\mu}_{vc}^{n_i \sigma_i}$ (given in Eq. (2.21)), the dipole transition \mathbf{d}_{ge} is written as a cartesian vector. Analogously, the dipole transition from a delocalized exciton state to the ground state is:

$$\mathbf{d}_{eg} = \langle e|\mathbf{d}|g\rangle = \sum_i \eta_i^{e*} \chi_{cv}^{n_i} \boldsymbol{\mu}_{cv}^{n_i \sigma_i}. \quad (2.50)$$

For calculating the formal introduced coefficients η_i^e , the transformation matrix used to diagonalize the single exciton Hamiltonian in Eq. (2.32) is needed: $H_{\text{el}XX}^D = \mathbf{T}^{e\dagger} H_{\text{el}XX} \mathbf{T}^e$. Thus, the transformation matrix \mathbf{T}^e is numerically calculated by diagonalizing the Hamiltonian written in the basis of delocalized single exciton states $H_{\text{el}XX}$. Therefore, the basis transformation for the dipole operator of the localized exciton states into the delocalized exciton states can be written using the hermitian transformation matrix \mathbf{T}^e :

$$\mathbf{d}_{eg} = \mathbf{T}^{e\dagger} \mathbf{d}_{Xg}. \quad (2.51)$$

Since the system of two colloidal QDs includes four bright local single exciton states, as introduced in Sec. 2.3.1, the dipole transition from the ground state g to a local exciton state X occurs as:

$$\mathbf{d}_{Xg} = \begin{pmatrix} \chi_{cv}^1 \boldsymbol{\mu}_{cv}^{1\uparrow} \\ \chi_{cv}^1 \boldsymbol{\mu}_{cv}^{1\downarrow} \\ \chi_{cv}^2 \boldsymbol{\mu}_{cv}^{2\uparrow} \\ \chi_{cv}^2 \boldsymbol{\mu}_{cv}^{2\downarrow} \end{pmatrix}. \quad (2.52)$$

Accordingly, the components of the dipole transition from the ground state g to an exciton state e are calculated as follows:

$$\mathbf{d}_{eg} = \mathbf{T}_{1e}^{e*} \chi_{cv}^1 \boldsymbol{\mu}_{cv}^{1\uparrow} + \mathbf{T}_{2e}^{e*} \chi_{cv}^1 \boldsymbol{\mu}_{cv}^{1\downarrow} + \mathbf{T}_{3e}^{e*} \chi_{cv}^2 \boldsymbol{\mu}_{cv}^{2\uparrow} + \mathbf{T}_{4e}^{e*} \chi_{cv}^2 \boldsymbol{\mu}_{cv}^{2\downarrow}. \quad (2.53)$$

Similar to Eq. (2.49) for the dipole moment between the ground and single exciton state, the dipole transitions from a delocalized single exciton state $|e\rangle$ to a double exciton state $|f\rangle$ and vice versa are calculated:

$$\mathbf{d}_{ef} = \langle e|\mathbf{d}|f\rangle = \sum_{i,j}^{i \neq j} \eta_i^{e*} \eta_{ij}^f \chi_{vc}^{n_j} \boldsymbol{\mu}_{vc}^{n_j \sigma_j} \quad \text{and} \quad \mathbf{d}_{fe} = \langle f|\mathbf{d}|e\rangle = \sum_{i,j}^{i \neq j} \eta_i^e \eta_{ij}^{f*} \chi_{cv}^{n_j} \boldsymbol{\mu}_{cv}^{n_j \sigma_j}. \quad (2.54)$$

Again, the dipole transition \mathbf{d}_{ef} denotes a component of the dipole operator in the basis of the delocalized exciton states as well as a three dimensional cartesian vector. For calculating the development coefficients η_{ij}^f , the Hamiltonian matrix represented in the double exciton states,

which are given in Eq. (2.41), is diagonalized: $H_{\text{el}BB}^D = \mathbf{T}^{\dagger} H_{\text{el}BB} \mathbf{T}^f$. Accordingly, the dipole operator describing the transitions from the local single exciton states X to the doubly excited states B is transformed into the new delocalized basis as follows:

$$\mathbf{d}_{fe} = \mathbf{T}^{\dagger} \mathbf{d}_{BX} \mathbf{T}^e. \quad (2.55)$$

Using the basis of the single exciton states in Eq. (2.28) and the bright double exciton states in Eq. (2.34), the dipole operator in the matrix form reads

$$\mathbf{d}_{BX} = \begin{pmatrix} \chi_{cv}^1 \boldsymbol{\mu}_{cv}^{1\downarrow} & \chi_{cv}^1 \boldsymbol{\mu}_{cv}^{1\uparrow} & 0 & 0 \\ \chi_{cv}^2 \boldsymbol{\mu}_{cv}^{2\uparrow} & 0 & \chi_{cv}^1 \boldsymbol{\mu}_{cv}^{1\uparrow} & 0 \\ 0 & \chi_{cv}^2 \boldsymbol{\mu}_{cv}^{2\uparrow} & \chi_{cv}^1 \boldsymbol{\mu}_{cv}^{1\downarrow} & 0 \\ \chi_{cv}^2 \boldsymbol{\mu}_{cv}^{2\downarrow} & 0 & 0 & \chi_{cv}^1 \boldsymbol{\mu}_{cv}^{1\uparrow} \\ 0 & \chi_{cv}^2 \boldsymbol{\mu}_{cv}^{2\downarrow} & 0 & \chi_{cv}^1 \boldsymbol{\mu}_{cv}^{1\downarrow} \\ 0 & 0 & \chi_{cv}^2 \boldsymbol{\mu}_{cv}^{2\downarrow} & \chi_{cv}^2 \boldsymbol{\mu}_{cv}^{2\uparrow} \end{pmatrix}. \quad (2.56)$$

Therefore, the components of the transformed dipole operator in the basis of the delocalized exciton states giving the transition from an exciton state $|e\rangle$ to a double exciton state $|f\rangle$ reads:

$$\begin{aligned} \mathbf{d}_{fe} = & \chi_{cv}^1 \boldsymbol{\mu}_{cv}^{1\uparrow} (\mathbf{T}_{2e}^e \mathbf{T}_{1f}^{f*} + \mathbf{T}_{3e}^e \mathbf{T}_{2f}^{f*} + \mathbf{T}_{4e}^e \mathbf{T}_{4f}^{f*}) + \chi_{cv}^1 \boldsymbol{\mu}_{cv}^{1\downarrow} (\mathbf{T}_{1e}^e \mathbf{T}_{1f}^{f*} + \mathbf{T}_{3e}^e \mathbf{T}_{3f}^{f*} + \mathbf{T}_{4e}^e \mathbf{T}_{5f}^{f*}) \\ & + \chi_{cv}^2 \boldsymbol{\mu}_{cv}^{2\uparrow} (\mathbf{T}_{1e}^e \mathbf{T}_{2f}^{f*} + \mathbf{T}_{2e}^e \mathbf{T}_{3f}^{f*} + \mathbf{T}_{4e}^e \mathbf{T}_{6f}^{f*}) + \chi_{cv}^2 \boldsymbol{\mu}_{cv}^{2\downarrow} (\mathbf{T}_{1e}^e \mathbf{T}_{4f}^{f*} + \mathbf{T}_{2e}^e \mathbf{T}_{5f}^{f*} + \mathbf{T}_{3e}^e \mathbf{T}_{6f}^{f*}) \end{aligned} \quad (2.57)$$

Since the dipole transitions between the delocalized exciton states are formulated, the dipole operator in the basis of the eigenstates of the pure electronic Hamiltonian \mathbf{d}_{el} in Eq. (2.48) can be calculated. This allows the electron-light interaction to be included into the description based on the effects of the Coulomb coupling. This formalism plays an important role for the calculation of the spectroscopic signatures of colloidal QDs.

2.4 Rotation of three dimensional objects

In this section, the fundamentals for the rotations of the colloidal QDs in the solvent are briefly introduced. Firstly, the typically used and intuitively understandable Euler angle description is introduced. Since an uniform distribution of all angles is quite difficult in this frame, the formalism of the quaternions is introduced. In this description no singularities occur and all angle are naturally equally distributed. This will be important for describing the stochastic motion of colloidal QDs in the solvent. Finally, the displacement of rotations on a discrete grid is discussed and an occurring loss of information is demonstrated.

2.4.1 Euler angles

An intuitive approach, which is quite often used for describing an arbitrary rotation of an object in three dimensions, is represented by the Euler angles. For three rotations around the Cartesian coordinate axes, there exists 24 different definitions of the Euler angle representation [82]. The rotation matrices for the rotation around the three Cartesian axes reads

$$\mathbf{R}_x = \begin{pmatrix} 1 & 0 & 0 \\ 0 & \cos \alpha & -\sin \alpha \\ 0 & \sin \alpha & \cos \alpha \end{pmatrix}, \quad \mathbf{R}_y = \begin{pmatrix} \cos \beta & 0 & \sin \beta \\ 0 & 1 & 0 \\ -\sin \beta & 0 & \cos \beta \end{pmatrix}, \quad \mathbf{R}_z = \begin{pmatrix} \cos \gamma & -\sin \gamma & 0 \\ \sin \gamma & \cos \gamma & 0 \\ 0 & 0 & 1 \end{pmatrix}. \quad (2.58)$$

The combinations of these matrices give different Euler angle representations, and the rotation angles are defined as follows [83]:

$$\lambda \in (-\pi, \pi] \quad \vartheta \in \left[-\frac{\pi}{2}, \frac{\pi}{2}\right] \quad \varphi \in (-\pi, \pi]. \quad (2.59)$$

Since many conventions of the sequence of rotation axis are valid, a fixed combination is consequently chosen to get the rotation matrix $\mathbf{R} = \mathbf{R}_x(\lambda)\mathbf{R}_y(\vartheta)\mathbf{R}_z(\varphi)$. Accordingly, the rotation matrix including the three Euler angles occurs

$$\mathbf{R} = \begin{pmatrix} \cos \vartheta \cos \varphi & -\cos \vartheta \sin \varphi & \sin \vartheta \\ \cos \lambda \sin \varphi + \sin \lambda \sin \vartheta \cos \varphi & \cos \lambda \cos \varphi - \sin \lambda \sin \vartheta \sin \varphi & -\sin \lambda \cos \vartheta \\ \sin \lambda \sin \varphi - \cos \lambda \sin \vartheta \cos \varphi & \sin \lambda \cos \varphi + \cos \lambda \sin \vartheta \sin \varphi & \cos \lambda \cos \vartheta \end{pmatrix}. \quad (2.60)$$

The result of the orientation using the Euler angle representation is influenced by the definitions of the rotation axes and the sequence of the angles chosen to determine the rotation. The combined rotations are ambiguous, since different combinations in the Euler angle representation result in the same orientation of the object. Furthermore, a degeneracy of the rotations are possible, if two of the rotation axes are equal. In this case, called the gimbal lock, a degree of freedom is lost for angle values near 0.5π [83].

The dipole orientations of colloidal QDs changes due to their movement in the solvent. For including the mean rotational orientation, a statistical average over all orientations can be calculated [84]. For random orientations, the influence of the sequence of Euler rotations is neglected, since the angle average is calculated [82]. If the time scales of the movement and the physically measurements are separable, the angle averaging is simply given by an integral expression including the Euler angles, as given in Ref. [84]:

$$\langle f \rangle = \frac{1}{8\pi^2} \int_0^\pi d\vartheta \int_0^{2\pi} d\lambda \int_0^{2\pi} d\varphi f(\vartheta, \lambda, \varphi) \sin \vartheta. \quad (2.61)$$

The weighing factor $\sin \vartheta$ should ensure, that the orientations are uniformly distributed over the unit sphere, but it does not avoid the high density of orientations at the poles [82].

For describing the rotations of colloidal QDs freely diffusing in the solvent, the angular orientations need to be uniformly distributed. For the monopole-monopole Coulomb coupling an analytical angle average can be calculated, since the orientations do not directly influence the strength of the coupling. In the case of the dipole-dipole interactions, which is directly determined by the relative orientation of the dipole vectors, all angular orientations need to be explicitly calculated. Thus, the angular orientations are randomly chosen. If Euler angles are picked randomly, the pole coordinates will occur more often due to the sinus and cosine representation. Thus, a new formalism for picking Euler angles which are equally distributed over all angles needs to be introduced which is not quite simple. Furthermore, the areas where a gimbal lock occur need to be avoided [83]. Alternatively, as introduced in the following section, quaternions can be used, since they are naturally equally distributed for all angles.

2.4.2 Quaternions

Since the colloidal QDs freely rotate in the solvent, the diffusion is described by picking randomly chosen angular positions. Therefore, the possible orientations need to be equally distributed over all angular positions. Thus, a description of the rotation based on quaternions is chosen, since they naturally include an equal distribution. Furthermore, in comparison to Euler angles, quaternions do not have singularities and rotations can be composed very efficiently using quaternions [85].

Quaternions were formulated and introduced by Olinde Rodrigues and William Rowan Hamilton as a system of complex numbers with three complex axes: $i^2 = j^2 = k^2 = ijk = -1$. Therefore, a quaternion q has a real part q_0 and three imaginary parts q_1 , q_2 and q_3 [83, 85]:

$$q = q_0 + iq_1 + jq_2 + kq_3. \quad (2.62)$$

The complex conjugated quaternion is given by:

$$q^* = q_0 - iq_1 - jq_2 - kq_3. \quad (2.63)$$

The norm of a quaternion is

$$|q| = \sqrt{qq^*} = \sqrt{q_0^2 + q_1^2 + q_2^2 + q_3^2}, \quad (2.64)$$

and the inverse of a quaternion, which gives $qq^{-1} = 1$ reads

$$q^{-1} = \frac{q^*}{qq^*}. \quad (2.65)$$

Unit quaternions are characterized by $|q| = 1$ and thus, they show the following relation: $q^{-1} = q^*$. Particularly, quaternions are used for describing the rotation of a three dimensional object. A unit quaternion represents a rotation with the angle $\alpha = 2 \arccos(q_0)$ around the rotation axis given by the vector $\mathbf{v} = (v_1, v_2, v_3)$ [83]. Since this representation directly include the rotation axis, there are no alternatively description as in the case of the Euler angle representation.

A composition of rotations is given by the product of the quaternions. Thus, the multiplication of two quaternions is introduced:

$$pq = p_0q_0 - p_1q_1 - p_2q_2 - p_3q_3 + i(p_0q_1 + p_1q_0 + p_2q_3 - p_3q_2) \quad (2.66)$$

$$+ j(p_0q_2 - p_1q_3 + p_2q_0 + p_3q_1) + k(p_0q_3 + p_1q_2 - p_2q_1 + p_3q_0). \quad (2.67)$$

The product of two quaternions does not commute. Alternatively, a vector part \mathbf{q} , which includes the imaginary parts and a scalar part q_0 can be introduced [86]

$$q = q_0 + \mathbf{q} = q_0 + iq_1 + jq_2 + kq_3. \quad (2.68)$$

In this notation, a quaternion describing a scalar has a zero vector part: $q = [q_0, \mathbf{0}]$, while a pure quaternion has a zero scalar part: $q = [0, \mathbf{q}]$ [85]. Furthermore, using the definition in (2.68), the multiplication of two quaternions can be simplified as:

$$pq = p_0q_0 - \mathbf{p} \cdot \mathbf{q} + p_0\mathbf{q} + q_0\mathbf{p} + \mathbf{p} \times \mathbf{q}. \quad (2.69)$$

Since, the product of two quaternions q and p gives the combination of the connected rotation, the relative orientation of two quaternions, which means the relative orientation of the two rotation axis, reads

$$q_{\text{relative}} = q^{-1}p. \quad (2.70)$$

The relative angle between those quaternions is given as:

$$\alpha_{\text{relative}} = 2 \arctan 2 \left(\sqrt{q_1^2 + q_2^2 + q_3^2}, q_0 \right). \quad (2.71)$$

For calculating a quaternion from an initial Euler representation, the three quaternions giving the rotations around the cartesian axes are introduced:

$$q_x = \left(\cos \frac{\lambda}{2}, \sin \frac{\lambda}{2}, 0, 0 \right), \quad (2.72)$$

$$q_y = \left(\cos \frac{\lambda}{2}, 0, \sin \frac{\lambda}{2}, 0 \right), \quad (2.73)$$

$$q_z = \left(\cos \frac{\lambda}{2}, 0, 0, \sin \frac{\lambda}{2} \right). \quad (2.74)$$

Then, the combination of these quaternions, in relation to the chosen Euler representation concerning the rotations around the different axes, give the quaternion determining the Euler description:

$$q_{\text{euler}} = q_x q_y q_z. \quad (2.75)$$

Analogously to the Euler description, rotations determined by quaternions can be described using a matrix as follows:

$$R = \begin{pmatrix} 1 - 2(q_2^2 + q_3^2) & 2(q_1 q_2 - q_0 q_3) & 2(q_0 q_2 + q_1 q_3) \\ 2(q_1 q_2 + q_0 q_3) & 1 - 2(q_1^2 + q_3^2) & 2(q_2 q_3 - q_0 q_1) \\ 2(q_1 q_3 - q_0 q_2) & 2(q_0 q_1 + q_2 q_3) & 1 - 2(q_1^2 + q_2^2) \end{pmatrix}. \quad (2.76)$$

Comparing the coefficients of (2.60) with (2.76), equations for calculation the Euler angles from the quaternion of the rotation are formulated:

$$\lambda = \arctan \left(\frac{2(q_0 q_1 - q_2 q_3)}{1 - 2(q_1^2 + q_2^2)} \right), \quad (2.77)$$

$$\vartheta = \arcsin(2(q_0 q_2 + q_1 q_3)), \quad (2.78)$$

$$\varphi = \arctan \left(\frac{2(q_0 q_3 - q_1 q_2)}{1 - 2(q_2^2 + q_3^2)} \right). \quad (2.79)$$

Note, for a correct implementation in computer languages according the full range of the Euler angles, given in Eq. (2.59), the arctan 2 function is used instead of the arctan, which is defined as

$$\arctan 2(x, y) = \begin{cases} \arctan\left(\frac{x}{y}\right) & x > 0 \\ \arctan\left(\frac{x}{y}\right) + \pi & x < 0, y \geq 0 \\ \arctan\left(\frac{x}{y}\right) - \pi & x < 0, y < 0 \\ \frac{\pi}{2} & x = 0, y > 0 \\ -\frac{\pi}{2} & x = 0, y < 0 \\ \text{undefined} & x = 0, y = 0 \end{cases}. \quad (2.80)$$

Reproducing the Euler angles over the whole angular domain back from the quaternions is not quite simple. The arc tangent has a restricted co-domain between $(-0.5\pi, 0.5\pi)$. Furthermore, q and $-q$ determine the same rotations and thus, some care needs to be taken comparing two orientations given by quaternions [85].

In order to randomly chose quaternions which are equally distributed over all angles, all elements of the quaternions are randomly picked form the interval between -1 and 1. Then, all tuples showing a magnitude greater than the unit magnitude:

$$q_0^2 + q_1^2 + q_2^2 + q_3^2 \geq 1 \quad (2.81)$$

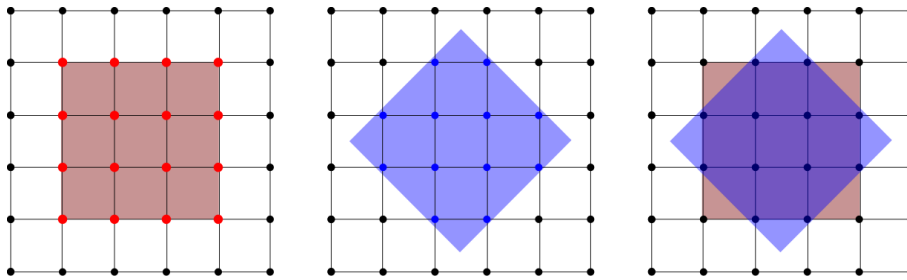


Figure 2.9 Rotation of a body with $\alpha = 0.25\pi$ on a discrete grid. If the square is rotated, the number of grid points covered by the body changes. At the left hand side, the square includes 16 red grid points, while in the rotated square in the middle only covers 12 blue grid points.

are rejected [83]. Finally, the resulting quaternion is normalized. In the following, this method is used to calculate the random orientations of the colloidal QDs diffusing in the solvent.

Euler angles may be more natural to understand and use than quaternions. Furthermore, a calculation based on Euler angles is as quick as a calculation based on quaternions and both can be formulated being equally compact to storage [83]. Nevertheless, quaternions can be easily manipulated as matrices and additionally, they are homogeneously distributed over all angular positions. Additionally, a random choice of the quaternions is simply reached by randomly picking the components of the quaternions under the normalization conditions. Thus, quaternions can be easily used to determine millions of angular orientations as needed for investigation of the Brownian motion of the colloidal QDs in Chap. 5.

2.4.3 Rotation on a grid

If the translation or the rotation of a body is restricted on a discrete grid, as usually in numerical simulations, information on the movement will be lost. The smaller the distances between the grid points, the less important is the loss of information. Since the loss of information during the rotation of a body results in the variation of the shape of the body, rotations are more difficult to operate on a discrete grid. Thus, in this section effects caused by rotations displaced on a discrete grid are investigated.

In numerical simulations, it is necessary to introduce discrete grids, which determine the position used for further calculations. Positions beyond the grid are described using approximations and known properties such as curve progressions. Often in complex calculations, it is not possible to implement very small distances between the grid points. The choice of the grid spacing is determined by the relation between the computation time as well as the memory requirements to the replicability of known properties such as physical correlations.

In this thesis, the spatial-dependent Coulomb coupling needs to be numerically calculated. Since the coupling is determined by the QD arrangements, all spatial positions and angular orientations require the calculation of the Coulomb coupling elements. Accordingly, the numerical requirements are high. Therefore, the grid used for the reconstruction of the spatial positions and the angular orientations required for the calculation of the Coulomb coupling cannot be too small otherwise the numerical requirements strongly rise.

For demonstrating the effect of losses by a rotation, a square displaced on a discrete 2d grid is plotted in Fig. 2.9. On the grid the information of the square are stored in 16 grid points (marked red). After a rotation of the square around $\alpha = 0.25\pi$, the body covers less grid points (depicted on the middle). Now only 12 blue marked dots store the information of the same sized square. The decrease of the number of grid point displaying the body indicates the loss of information in the case of a rotated body. If a coordinate of the body does not reach a grid point after the

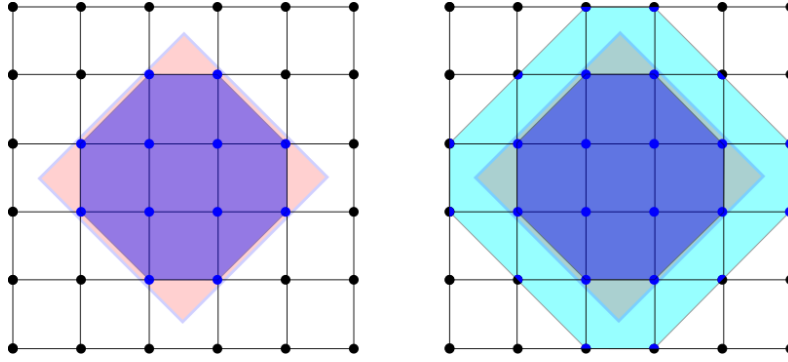


Figure 2.10 Approximations for the rotation of a body on a discrete grid. The red square marks the transformed body resulting from a continuous motion, the blue bodies are determined by the grid point positions. On the left hand side, information not appearing on the grid are cut off. The blue body occurs smaller and its shape is changed concerning the red body. On the right hand side, the values between the grid point are weighted to their direct neighbor grid points, depicted with proportionate blue and black plotted grid points. This includes a change in the size and the shape of the body, but all information of the positions beyond the grid points are stored together in the bordering grid points.

rotation, it can not be disposed directly. Therefore, approximations are needed to work with the transformed coordinates.

In Fig. 2.10 two different approaches of the handling of the transformed positions beyond the grid points are schematically depicted. On the left hand side of the figure, the positions outside the grid points are simply cut off (blue body). This induces a change of the shape of the body. Thus, information and symmetry properties are lost, both influencing the numerical results. If the grid points can be arranged very densely, the loss of information does not strongly influence the results. In this case, the approach presents a simple and good approximation of the rotation on the discrete grid. If the distances between the grid points cannot be small enough, the changes in the shape and varying symmetry conditions will strongly influence the results.

Another approach for handling the transformed positions beyond the grid points is given by a weighting of the information to the bordering grid points, depicted on the right hand side of Fig. 2.10. The position of the coordinate concerning its distance to each of the neighbor grid points gives a weighting factor. The products of the value from the transformed coordinate and the weighting factor are stored in the neighbor grid points, as schematically depicted in Fig. 2.10. This induces an extension of the body to all neighbor grid points. If a transformed coordinate is identical with a position of a grid point, the weighting factor to the other grid points is zero. In all other cases, the neighbor grid points are used for storing the information of the coordinates beyond the grid positions. In particular, for bigger distances between the grid points the method avoids the loss of an important part of information. Therefore, this method is used for the numerical calculations used in this thesis. Nevertheless, since the body is extended to neighboring grid points, the shape as well as the size of the body is changed and other symmetry conditions can occur influencing the results.

For demonstrating the influence of the errors resulting from the rotations on a discrete grid, in Fig. 2.11 exciton energies of colloidal QDs are calculated as functions of the rotation angle around the different cartesian axes. The changes in the shape of the QDs, induced by transformations beyond the grid points, result in aberrations from a smooth curve progression. In particular, for angular transformations with $n\pi/4$ with n as odd number the most inaccuracies occurs, visible as peaks at these positions.

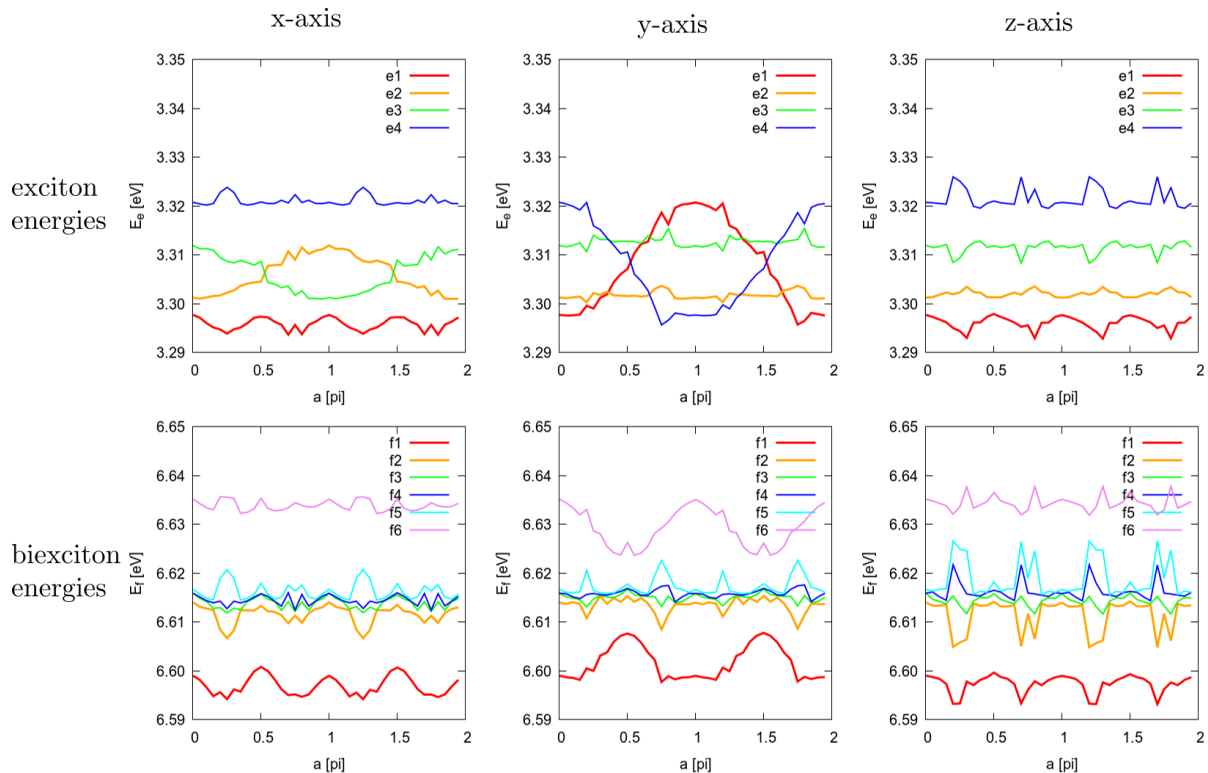


Figure 2.11 Exciton energies of two Coulomb coupled colloidal QDs rotated on a discrete grid. Since the rotation is displaced on a discrete grid, the diagrams show aberrations from a smooth curve progression. In particular, the angular position of $\alpha = 0.25\pi$ and $\alpha = 0.75\pi$ are the most defective rotations on discrete grid points, since the diagrams show strongly peaked curves in these regions. Note, that not only the loss of information during the rotations displaced on the discrete grid induces aberrations from a smooth curve progression, since other effects are also included in these calculations. Nevertheless, the sharp small peaks result from errors caused by the rotation and can be reduced by increasing the number of grid points covering the QDs.

Chapter 3

Calculation of Coulomb coupling elements

The Coulomb interaction inside and between nanostructures plays an important role, even in the case of non-overlapping electron wave functions, since the coupling influences the optical and electrical properties [4,28]. Due to the Coulomb interaction, the individual characteristics of the QDs are modified and new delocalized exciton energy states are formed [4,16,29]. Therefore, the Coulomb coupling induces exciton energy shifts [5,6] as well as excitation transfer [34,35].

Often, the calculation of Coulomb coupling elements requires the evaluation of a six dimensional spatial integral, cf. Sec.2.2.1. Therefore, it represents a significant limiting factor in quantum mechanical calculations. If the size or the complexity of the investigated system increases, many coupling elements need to be determined. The resulting computational constraints require an efficient method for a fast numerical calculation of the Coulomb coupling. Especially, if the calculation of a high number of coupling elements is required, as in the case of Coulomb coupled colloidal QDs moving in a solvent, the Poisson Green's function method (PGF method), introduced in this chapter, represents a promising approach for increasing the efficiency in the numerical calculation.

In the following, we present the PGF method as a computational method which reduces the numerical effort in the calculation of Coulomb coupling elements in real space. The method as well as parts of the chapter are published in [49], ©2016 American Physical Society. In contrast to methods simplifying the calculation of the Coulomb coupling, which are typically based on symmetry conditions, the PGF method is very general since it is not restricted to specific symmetries of the model system or geometry properties in the Green's function. Since the method decreases the number of spatial integrals, a fast calculation of the Coulomb coupling elements is achieved. Additionally, the method enables an arbitrarily spatially dependent dielectric permittivity to be included.

Following the approach of the PGF method, we analyze the Coulomb coupling between two colloidal QDs in varying spatial arrangements. That includes the electrostatic monopole-monopole Coulomb coupling between electrons and holes respectively [30], as well as the Förster dipole-dipole coupling [31,32] as nonradiative resonant energy transfer between the QDs [33]. For demonstrating the feasibility of the approach, we calculate inter nanostructure couplings without explicitly specifying the Green's function of the problem. Since the PGF method naturally includes a spatially dependent dielectric function, the influence of the dielectric permittivity on the Coulomb coupling elements is investigated. Additionally, for self-organized QDs embedded in a host material, we calculate the Coulomb coupling for bound electron and hole QD states coupled to many continuum states [30]. Here we show, that a drastic reduction of computational costs is also possible with the presented method, if typical symmetries, such as radial symmetry

of the QD confinement potential, are included.

3.1 Poisson Green's function method

The calculation of Coulomb coupling elements for quantum dynamical treatments, e.g., in cluster or correlation expansion schemes, represents a significant limiting factor in numerical quantum mechanical calculations, if the evaluation of the typically used six dimensional spatial integral is included, cf. Sec. 2.2.1. Since the size or the complexity of the investigated system increases, many coupling elements occur. The resulting computational constraints for the calculation of the Coulomb coupling require an efficient method for a fast numerical calculation.

In this section, we present the PGF method, published in [49], as a computational method to reduce the numerical complexity by decreasing the number of spatial integrals for arbitrary geometries. We use a Green's function formulation of the Coulomb coupling and introduce a generalized scalar potential as a solution of a generalized Poisson equation with a generalized charge density as inhomogeneity. This enables a fast calculation of Coulomb coupling elements and additionally, a straightforward inclusion of boundary conditions and arbitrarily spatially dependent dielectrics through the Coulomb Green's function.

3.1.1 Concepts in the literature

Since the Coulomb coupling plays an important role in many systems and calculations, in the literature there exists many different concepts for the calculation of the coupling elements. This section gives an overview of the typically used concepts and methods used for the calculation of the Coulomb interaction. Then, the PGF method is classified into these concepts. The method as well as parts of this section are published in [49], ©2016 American Physical Society.

Systems involving only a few electronic levels have been investigated in detail in quantum dynamical calculations, this includes e.g., QD interband transitions [40] and their modifications due to a dielectric medium [87]. For larger or asymmetric complex systems, the numerical computation of the Coulomb coupling constitutes a significant limiting factor and therefore, approaches to efficiently calculate the Coulomb interaction are needed. Often, a radial symmetry is exploited and spherical coordinates are used to simplify the spatial integrals. Thus, the Coulomb potential can be expressed by Legendre polynomials [31, 55]. In Ref. [6], spherical coordinates were used to calculate the Coulomb interaction of a molecular complex, which is influenced by the presence of an adjunct metal nanoparticle. Typically, in quantum dynamical calculations of QD systems, several analytic approaches are based on the symmetries of the QD confinement [39, 40, 88] and the shape of the electron wave functions [37] for facilitating the evaluation of the Coulomb interaction.

If the system includes the calculation of a high number of coupling elements, the resulting computational constraints [46, 55] require an efficient model to calculate the Coulomb coupling elements numerically. In Ref. [46], a generalization of a multipole expansion [89] was presented for electronic structure calculations (e.g., for large molecules) to reduce the numerical effort for an increasing system size. For the Coulomb coupling involving continuum states, which influence dephasing [90] and scattering processes [91, 92] as well as the formation of excitons between carriers of the QD and the continuum [30], a high number of coupling elements occurs. In addition, many Coulomb elements need to be calculated for varying arrangements of the nanostructures, since the Coulomb coupling between the carriers of spatially separated systems depends on the distance and the angular orientation [4].

A method for an efficient numerical calculation of Coulomb coupling elements is given by a transformation of the electron wave functions into the Fourier space. The Fourier transformation

can be used to separate the integrals of the two-particle Coulomb interaction, if the Coulomb potential for a homogeneous medium in free space is considered [41, 55, 93]. In real space, the connection of the electron wave functions with the Coulomb potential results in a six dimensional integral. In contrast, in the Fourier domain, the Coulomb coupling for a spatially homogeneous medium is simply given as a product of the electron wave functions and the Coulomb potential. Accordingly, the calculation of a three-fold integral is required, and additionally, three dimensional Fourier transformations needs to be done. Compared to a six dimensional integral in real space, the numerical complexity is reduced in the Fourier domain. However, a singularity of the Coulomb potential is also present in Fourier space and the Fourier transformation can not be applied with the same numerical reduction for spatially inhomogeneous dielectrics.

For nanostructures such as QDs, a calculation of the Coulomb coupling in the Fourier domain often includes form factors, which are defined by a Fourier transformation of the product of two electron wave functions. For example in Ref. [55], form factors were introduced to calculate the Coulomb matrix elements between exciton and biexciton states for the impact ionization in semiconductor nanocrystals with surface polarization. In Ref. [37], form factors of an in-plane Fourier transformation and the construction of orthogonal plane waves [47] were used to simplify the calculation of the Coulomb coupling between a QD and a wetting layer. In the spherical symmetric case, the form factors can be formulated using spherical coordinates in the Fourier domain [40] to further reduce the computational costs.

In contrast, in this chapter we present a numerical method for an efficient calculation of Coulomb coupling elements in real space, which is not restricted to specific symmetry properties of the permittivity or the whole system. The PGF method, which is published in Ref. [49], naturally includes the screening introduced through a spatially dependent permittivity. We reduce the computational complexity by decreasing the dimension of the spatial integrals, required for the calculation of Coulomb coupling elements, as illustrated in the scheme in Fig. 3.1. This is achieved by using a Green's function formulation of the Coulomb potential [59, 73, 94]. We identify a generalized scalar potential as a solution of the generalized Poisson equation with a generalized charge density as inhomogeneity, determined by the complex electron wave functions.

Since solvers and libraries such as PETSc [95], used for an efficient numerical computation of partial differential equations [96, 97], are available, a calculation of the Coulomb potential based on the solution of a differential equation is feasible with a straightforward implementation. Furthermore, solving a modified Poisson equation offers the possibility of including screening effects as well as the influence of a spatially dependent dielectric function $\varepsilon(\mathbf{r})$ [48, 59]. In this way, induced surface charge effects, which can result in energetic shifts [73] (e.g., for the band gap and exciton resonances), can be included by solving the Poisson differential equation with appropriate boundary conditions [48].

The PGF method [49] (©2016 American Physical Society), presented in detail in the following section, is very general and allows an efficient calculation of Coulomb coupling elements without being restricted to a specific analytic expression of the Green's function or to particular system symmetries. We achieve a similar reduction in the numerical complexity as in a calculation of the Coulomb potential in Fourier domain using form factors, but without the restriction to the Coulomb potential in free space with a spatially homogeneous dielectric constant ε_r .

Similar methods as used in Ref. [59] are already known and used by different authors in other contexts such as ab initio treatments and electronic structure calculations. In Ref. [94], a Green's function representation of the solution of a Poisson equation was introduced to calculate the screening of the classical interaction of electrons of a quantum dot with gate electrodes. Therefore, the Green's function is explicitly determined and the screened electrostatic energy in a dielectric material is calculated. In Refs. [54, 98, 99], the Coulomb potential is obtained from solving a Poisson equation to calculate the Coulomb energy in the context of electronic structure

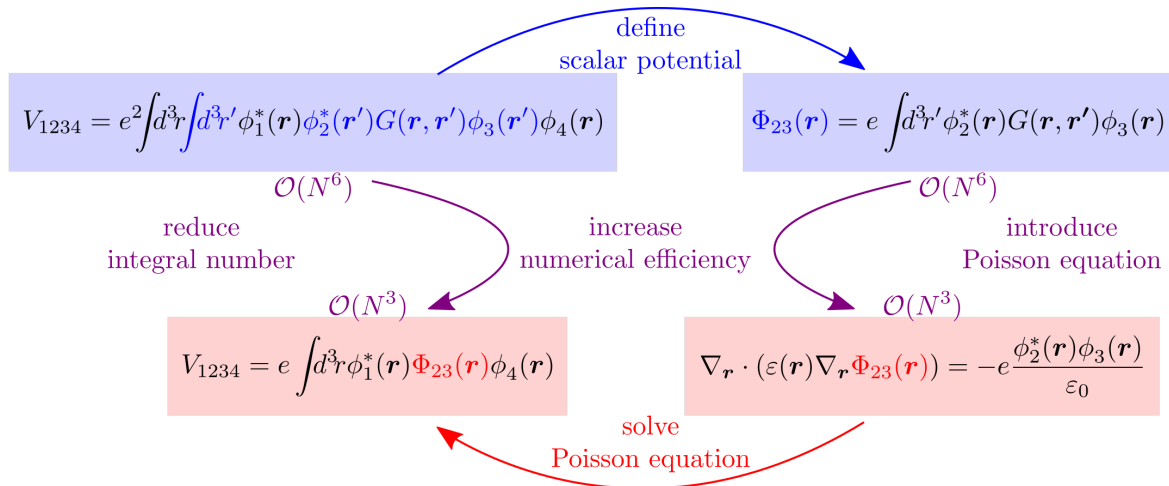


Figure 3.1 PGF method for increasing the efficiency in numerical calculations of Coulomb coupling elements. Typically, the calculation of the Coulomb interaction requires the evaluation of a six dimensional integral. In the Green’s function formalism, a scalar potential, which includes a three dimensional integral, is defined for decreasing the numerical complexity. This scalar potential is calculated by solving a generalized Poisson equation. Using the solution of the Poisson equation the number of integrals in the calculation of Coulomb elements is reduced.

calculations. Especially for including the influence of a spatially inhomogeneous medium, a generalized Poisson equation can be introduced, as is done in Refs. [59, 73, 100]. Additionally, a Poisson equation can be used to reach a linear scaling of the Coulomb problem with the system size [101]. Furthermore, other methods exist, which include a Poisson equation to calculate many Coulomb coupling elements. For example in Ref. [102], a method was introduced, based on the expansion of the charge density in a specific set of functions, to reduce the number of integrals required for the calculation of Coulomb interactions in the context of a density functional theory.

Nevertheless, as far as we are aware, a method based on the Green’s function formulation of a solution of a Poisson equation without the restriction to certain symmetries or an explicit Green’s function and the resulting wide range of applications is not yet discussed in the literature devoted to the QD community. Therefore, in the next section, we present the PGF method for increasing the numerical efficiency in real space without being restricted to specific symmetries, e.g., of the QD confinement potential or the electron wave functions, and without explicitly determining an analytic Green’s function.

3.1.2 Approach of the PGF method

Similar to the derivation of the Hamiltonian in Sec. 2.2.1, the numerical efficient PGF method [49] (©2016 American Physical Society) for a fast calculation of Coulomb coupling elements is based on a Green’s function representation of the solution of a generalized Poisson equation [94] (analog to Eq. (2.6)). The method, schematically illustrated in Fig. 3.1, reduces the high computational complexity of Eq. (2.11) by introducing a generalized scalar potential $\Phi_{23}(\mathbf{r})$, which includes the Green’s function. This approach separates the number of integrals from a six dimensional integral in Eq. (2.11) to two separate three dimensional integrals:

$$V_{1234} = e \int d^3r \phi_1^*(\mathbf{r}) \Phi_{23}(\mathbf{r}) \phi_4(\mathbf{r}). \quad (3.1)$$

Thus, to reproduce the Coulomb coupling element formula of Eq. (2.11), the scalar potential $\Phi_{23}(\mathbf{r})$ is given by:

$$\Phi_{23}(\mathbf{r}) = e \int d^3r' \phi_2^*(\mathbf{r}') G(\mathbf{r}, \mathbf{r}') \phi_3(\mathbf{r}'). \quad (3.2)$$

The Green's function in Eq. (3.2), which includes properties of the geometry [94], is determined by Eq. (2.7) in a dielectric medium with a spatially dependent dielectric function $\varepsilon(\mathbf{r})$ [48]. Following the derivation of the Hamiltonian in Sec. 2.2.1, the generalized scalar potential, given by Eq. (3.2), can be identified as a Green's function representation of the solution of a generalized Poisson equation [94], analog to Eq. (2.8):

$$\Phi_{23}(\mathbf{r}) = \int d^3r' G(\mathbf{r}, \mathbf{r}') \varrho_{23}(\mathbf{r}'). \quad (3.3)$$

Therefore, the generalized charge density $\varrho_{23}(\mathbf{r})$, described by the corresponding electron wave functions [54], is introduced as: $\varrho_{23}(\mathbf{r}) = e\phi_2^*(\mathbf{r})\phi_3(\mathbf{r})$. Note, that the electron wave functions may be complex. Thus, the charge density $\varrho_{23}(\mathbf{r})$ and the scalar potential $\Phi_{23}(\mathbf{r})$ may be complex as well and therefore, they are not directly measurable but mathematical quantities, solely intended for the calculation of Coulomb coupling elements.

Accordingly, for applications in materials with spatially varying permittivities, a generalized Poisson equation determines the generalized scalar potential $\Phi_{23}(\mathbf{r})$ of the Coulomb interaction [39, 100], analog to Eq. (2.6), with a potentially complex charge density as the inhomogeneity:

$$\nabla_{\mathbf{r}} \cdot (\varepsilon(\mathbf{r}) \nabla_{\mathbf{r}} \Phi_{23}(\mathbf{r})) = -\frac{\varrho_{23}(\mathbf{r})}{\varepsilon_0}. \quad (3.4)$$

For example, if the dielectric constant of the system differs from that of the surrounding medium, such as in the case of colloidal QDs moving in a solvent, surface charge effects may be considered [87, 103]. The PGF method offers the possibility of including such effects as appropriate geometries in $\varepsilon(\mathbf{r})$ or as boundary conditions for $\Phi_{23}(\mathbf{r})$ [104] by solving the generalized Poisson Eq. (3.4). To solve such differential equation e.g., finite-difference methods [100] or finite elements methods [105, 106] can be used. Nowadays, solvers are very fast and highly optimized [96, 97], so that together with an integration of Eq. (3.1), a fast calculation and implementation of the Coulomb coupling is accomplished.

In Refs. [73, 94], the Green's function representation of a generalized Poisson equation is used, to calculate the Coulomb interaction for applications in material by determining the Green's function explicitly. The numerical calculation of $\Phi_{23}(\mathbf{r})$ is applicable to a larger variety of systems than the derivation of a specialized analytic expressions. Therefore, we propose to solve the Poisson equation directly, without specifying the Green's function explicitly. Nevertheless, this reduces the numerical complexity of the six dimensional integral in Eq. (2.11).

The numerical effort for evaluating the integrals of the two-particle Coulomb interaction in Eq. (2.11) scales with $\mathcal{O}(N^6)$, where N is the number of grid points in one dimension assuming a cubic grid used to discretize the problem. The formalism of using a discrete grid as well as some resulting problems in the description of continuous movements are introduced in Sec. 2.4.3. In the PGF method [49] (©2016 American Physical Society), the three dimensional integral in Eq. (3.1), which scales with the system size $\mathcal{O}(N^3)$, needs to be evaluated during the calculation of Coulomb coupling elements. Additionally, the generalized scalar potential $\Phi_{23}(\mathbf{r})$, used to separate the integral expression in Eq. (2.11), is determined by the numerical solution of the Poisson Eq. (3.4). Due to the development of efficient solvers for differential equations, a linear scaling with the system size in three dimensions $\mathcal{O}(N^3)$ can be obtained [97, 101, 107] e.g., by

using multigrid methods [108], as is done in this thesis, which are also included in libraries such as PETSc [95].

A transformation into the Fourier space can be used to efficiently calculate the Coulomb coupling by separating the integrals of the two-particle Coulomb interaction in the Fourier domain. For a spatially homogeneous medium, the Coulomb coupling elements in Fourier domain are given as a product of the electron wave functions and the Coulomb potential. Therefore, the formalism of the Fourier transformation includes the evaluation of a three dimensional integral in Fourier space scaling with $\mathcal{O}(N^3)$ for the reciprocal grid. In addition, three dimensional Fourier transformations of the electron wave functions are needed to determine form factors [40, 41]. Therefore, a fast Fourier transform [109] is used, which scales with $\mathcal{O}(N^3 \log N)$ [97, 108, 110]. In contrast to the transformation into the Fourier space, the presented PGF method is not restricted to the case of a homogeneous dielectric medium ϵ_r in free space [70] and therefore, effects caused by a spatially dependent dielectric medium can be included, as needed for Coulomb coupled colloidal QDs moving in a solvent. Furthermore, using the PGF method, singularities in the Green's function are avoided, which often increase the numerical costs.

The PGF method represents a very general and efficient method to numerically calculate a high number of Coulomb coupling elements. Without the restrictions to specific material systems, symmetry properties or explicit Coulomb Green's function, the method enables Coulomb coupling elements to be calculated in a wide range of application. While the model system of two Coulomb coupled colloidal QDs diffusing in a solvent will be analyzed very detailed in the approach of this thesis, in the following section some other applications of the method are shortly presented.

3.1.3 Applications of the method

In the following, we demonstrate, that the PGF method can also be applied with great benefit, if specific symmetries are considered, which simplify the Coulomb coupling elements. If certain symmetries are available, such as the spherical symmetry of the model system [54, 55], the scalar potential $\Phi_{23}(\mathbf{r})$ can be calculated adapted to the specific conditions. Especially, if a homogeneous material system is assumed, the dielectric environment ϵ_r stays constant for all spatial positions and an explicit form of the Coulomb Green's function can be assumed simplifying the calculations of the Coulomb coupling elements. Calculations concerning the spatial depending Coulomb coupling of colloidal QDs in a homogeneous environment are given in detail in Sec. 3.4.3.

Often, modifications of the Coulomb potential due to screening are necessary [76, 93, 111]. In the case of a homogeneous medium, the dielectric function ϵ_r is constant and therefore, the left hand side of the Poisson Eq. (3.4) is given by the Laplace operator $\Delta_{\mathbf{r}}$ operating on the scalar potential $\Phi_{23}(\mathbf{r})$. Screening in the Yukawa form for homogeneous media may be included into the formula of the PGF method [49] (©2016 American Physical Society) by introducing a constant screening factor α in the Poisson Eq. (3.4) with a constant dielectric function ϵ_r :

$$(\Delta_{\mathbf{r}} - \alpha^2) \Phi_{23}(\mathbf{r}) = -\frac{\rho_{23}(\mathbf{r})}{\epsilon_r \epsilon_0}. \quad (3.5)$$

Therefore, the definition of the Green's function in Eq. (2.7) for an isotropic medium is adapted for screening by including the screening constant α :

$$(\Delta_{\mathbf{r}} - \alpha^2) G_{\alpha}(\mathbf{r}, \mathbf{r}') = -\frac{1}{\epsilon_r \epsilon_0} \delta(\mathbf{r} - \mathbf{r}'). \quad (3.6)$$

Then, the PGF method can be applied straightforwardly using Eq. (3.1) and Eq. (3.3) to calculate screened Coulomb coupling elements in real space. The Yukawa potential $G_{\alpha}(\mathbf{r}, \mathbf{r}') = e^{-\alpha|\mathbf{r}-\mathbf{r}'|}/(4\pi\epsilon_0\epsilon_r|\mathbf{r}-\mathbf{r}'|)$ with its Fourier transform $G_{\alpha}(\mathbf{q}) = 1/(\epsilon_0\epsilon_r(q^2 + \alpha^2))$, which is typically used to account for screening in semiconductors with a homogeneous medium [112] (cf. Eq. (3.6)), represents the Green's function.

Additionally, the method greatly reduce the numerical effort if a specific symmetry such as radial symmetry occurs. In a variety of many-body systems, a finite number of localized discrete energy states is coupled via Coulomb interaction to a continuum of states from an embedding system. Therefore, in the following, we present the example of a QD embedded in a host material determined with a spatially homogeneous dielectric constant ϵ_r . Since the Coulomb coupling between bound QD states and electrons located in free continuum states occurs [113], a high number of Coulomb coupling elements needs to be calculated. Other examples, which can be calculated in a similar way, are impurities in a bulk medium or other nanostructures such as quantum wells [114] and wires [115] as well as molecular systems [88, 116].

The unbound continuum states in a bulk semiconductor are characterized by a three dimensional wave vector \mathbf{k} and therefore, the calculation of the Coulomb interaction between a bound state in a QD and many continuum states in the embedding material [30] requires the calculation of a high number of coupling elements. Typically, in pure bulk materials, electron wave functions are expanded in plane waves. Since the presence of the QD confinement potential modifies the continuum wave functions, a description beyond the plane wave approximation may be necessary [91, 93]. Therefore, the PGF method, presented in Sec. 3.1.2, can be used to efficiently calculate the Coulomb coupling elements for modified continuum wave functions.

If the confinement potential is rotational symmetric, spherical coordinates can be used to simplify the calculation of the Coulomb coupling. Therefore, the envelope of the electron wave functions are decomposed into a product of a radial part $R^l(r)$ and spherical harmonics $Y_m^l(\vartheta, \varphi)$, with l denoting the angular momentum number and m the magnetic quantum number: $\xi(\mathbf{r}) = R^l(r)Y_m^l(\vartheta, \varphi)$. For a formulation of the PGF method [49] ((©2016 American Physical Society) in spherical coordinates, the Green's function is separated into a radial part $g^l(r, r')$ and spherical harmonics [31, 55]:

$$G(\mathbf{r}, \mathbf{r}') = \sum_{lm} \frac{1}{\epsilon_0 \epsilon_r} Y_m^{l*}(\vartheta, \varphi) Y_m^l(\vartheta', \varphi') g^l(r, r'). \quad (3.7)$$

For an analytical evaluation of the angular part given by the spherical harmonics, the Coulomb coupling of the QD ground state to the continuum states is investigated. To follow the approach of the PGF method, in case of a radial symmetric confinement potential, the Green's function and the charge density are used to express the scalar potential $\Phi_{23}(\mathbf{r})$ for the radial symmetric case using the Poisson equation Eq. (3.4) in spherical coordinates with momentum $l = 0$:

$$\left(\frac{\partial^2}{\partial r^2} + \frac{2}{r} \frac{\partial}{\partial r} \right) \Phi_{23}^0(r) = -e \frac{R_2^{0*}(r) R_3^0(r)}{4\pi \epsilon_0 \epsilon_r}. \quad (3.8)$$

Now, the radial part of the scalar potential $\Phi_{23}^0(r)$, obtained by a numerical solution of Eq. (3.8), is used to calculate the Coulomb coupling elements for a radial symmetric problem:

$$V_{1234} = e \int dr r^2 R_1^{l*}(r) \Phi_{23}^0(r) R_4^l(r) \delta_{14}^\lambda \delta_{14}^\sigma \delta_{23}^\lambda \delta_{23}^\sigma \delta_{14}^l \delta_{14}^m. \quad (3.9)$$

In the case of a radial symmetric confinement potential, the computational requirements for calculating Coulomb coupling elements are significantly reduced, since Eq. (3.9) only requires the evaluation of a one dimensional spatial integral. Since the continuum states are only occupied near the energetic minimum of continuum levels and the coupling to the QD's resonances decreases, the number of continuum states in numerical calculations is finite [91]. However, to reach numerical convergence, a high number of coupling elements needs to be calculated [30].

We used the PGF method for an efficient numerical calculation of bound-to-continuum Coulomb coupling elements. Moreover, we have shown, that the PGF method can also exploit

symmetries to further reduce the computational cost for calculating Coulomb coupling elements. In the following sections, we introduce the model system of two Coulomb coupled colloidal QDs in real space and demonstrate the efficient calculation of the Coulomb coupling elements following the approach of the PGF method. Since in the case of colloidal QDs diffusing in the solvent, the distances and dipole orientations are changed frequently, a high number of Coulomb coupling elements needs to be calculated. First, we calculate the interdot as well as the intradot coupling elements for the monopole and dipole order without specifying the Green's function to an explicit analytic form. Then, we analyze the influence of the spatial arrangement of the colloidal QDs to each other on the strength of the Coulomb coupling. Finally, we investigate how a spatially dependent dielectric environment, which is naturally included in the formalism of the PGF method, determines the Coulomb coupling elements.

3.2 Calculation of different orders in the Coulomb coupling

The Coulomb interaction between two semiconductors contains the monopole-monopole coupling as well as the Förster induced excitation transfer. Although, in the PGF method [49] the Green's function is not specified to an explicit analytic form, terms connected with the monopole-monopole interaction and the Förster coupling are identified. That enables the specific effects, caused by the different order in the Coulomb interaction, to be analyzed.

The PGF method for an efficient numerical calculation of the Coulomb coupling elements does not rely on specific symmetries of the system. To demonstrate the wide range of applications, we calculate the Coulomb coupling between two colloidal QDs with varying spatial arrangements. We identify terms describing the monopole-monopole interaction as well as the dipole-dipole coupling between the two QDs, a very common approach [40, 62], but without using an explicit analytic form of the Green's function.

3.2.1 Taylor series of the Green's function

For identifying the coupling terms connected with the monopole-monopole, the monopole-dipole, and the dipole-dipole coupling, the Taylor series of the Green's function used for the calculation of the Coulomb coupling elements is carried out. Since the calculation of the Coulomb elements in the PGF method is not restricted to a specific geometry, the Taylor series of an arbitrary Green's function is introduced. Starting from the general form of the Coulomb coupling elements in Eq. (2.11), the multi-indices are evaluated concerning the quantum numbers, which determines the Coulomb coupling: the bandindex λ , the QD number n , and the spin configuration σ . Thus, the Coulomb coupling elements are calculated as follows:

$$V_{1234} = e^2 \int d^3r \int d^3r' \phi_{\lambda_1 n_1 \sigma_1}^*(\mathbf{r}) \phi_{\lambda_2 n_2 \sigma_2}^*(\mathbf{r}') G(\mathbf{r}, \mathbf{r}') \phi_{\lambda_3 n_3 \sigma_3}(\mathbf{r}') \phi_{\lambda_4 n_4 \sigma_4}(\mathbf{r}). \quad (3.10)$$

In the approach of the envelope function description, the electron wave functions $\phi(\mathbf{r})$ in Eq. (3.10) are written as a product of an envelope function $\xi(\mathbf{r})$ and a lattice periodic Bloch part $u(\mathbf{r})$ [41, 55]:

$$\phi_{\lambda n \sigma}(\mathbf{r}) = \xi_{\lambda n}(\mathbf{r}) u_{\lambda n \sigma}(\mathbf{r}). \quad (3.11)$$

Thus, the Coulomb coupling elements including the electron envelopes and Bloch functions read

$$V_{1234} = e^2 \int d^3r \int d^3r' \xi_{\lambda_1 n_1}^*(\mathbf{r}) u_{\lambda_1 n_1 \sigma_1}^*(\mathbf{r}) \xi_{\lambda_2 n_2}^*(\mathbf{r}') u_{\lambda_2 n_2 \sigma_2}^*(\mathbf{r}') G(\mathbf{r}, \mathbf{r}') \\ \cdot \xi_{\lambda_3 n_3}(\mathbf{r}') u_{\lambda_3 n_3 \sigma_3}(\mathbf{r}') \xi_{\lambda_4 n_4}(\mathbf{r}) u_{\lambda_4 n_4 \sigma_4}(\mathbf{r}). \quad (3.12)$$

Using the usual scale separation [34], the spatial operator \mathbf{r} is separated into the center position

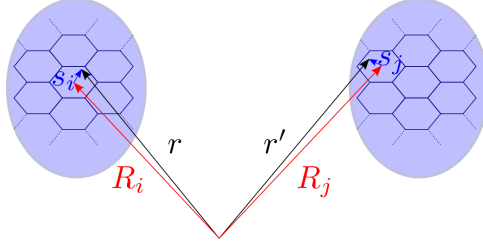


Figure 3.2 A scale separation of the spatial vector \mathbf{r} into the center position of the i th unit cell \mathbf{R}_i and the positioning inside the unit cell \mathbf{s}_i . The same is done with the second spacial operator \mathbf{r}' for the j th unit cell. The spatial vectors \mathbf{r} and \mathbf{r}' can be located in one QD or in both QDs respectively.

\mathbf{R}_i of the i th unit cell and a spatial operator \mathbf{s}_i located in the unit cell [55] $\mathbf{r} = \mathbf{R}_i + \mathbf{s}_i$, which is schematically depicted in Fig. 3.2. Therefore, the integration of the spatial positions is changed into a summation of all unit cells and an integration over one cell [41]. Using the periodicity of the Bloch functions $u(\mathbf{R}_i + \mathbf{s}_i) = u(\mathbf{s}_i)$ and the assumption that the envelope function, which is slowly varying and therefore nearly constant on the size of the unit cell, is determined by the center position of the unit cell: $\xi(\mathbf{R}_i + \mathbf{s}_i) \approx \xi(\mathbf{R}_i)$, the Coulomb coupling elements are

$$V_{1234} = e^2 \sum_{i,j} \xi_{\lambda_1 n_1}^*(\mathbf{R}_i) \xi_{\lambda_2 n_2}^*(\mathbf{R}_j) \xi_{\lambda_3 n_3}(\mathbf{R}_j) \xi_{\lambda_4 n_4}(\mathbf{R}_i) \cdot \int d^3 s_i \int d^3 s_j u_{\lambda_1 n_1 \sigma_1}^*(\mathbf{s}_i) u_{\lambda_2 n_2 \sigma_2}^*(\mathbf{s}_j) G(\mathbf{R}_i + \mathbf{s}_i, \mathbf{R}_j + \mathbf{s}_j) u_{\lambda_3 n_3 \sigma_3}(\mathbf{s}_j) u_{\lambda_4 n_4 \sigma_4}(\mathbf{s}_i). \quad (3.13)$$

For identifying the terms which are connected to the monopole and dipole coupling, the Green's function is expanded in both arguments in a Taylor series. Therefore, a multidimensional Taylor series is used

$$\text{T}f(x_1, \dots, x_N)|_{\mathbf{x}=\mathbf{a}} = \sum_{n_1}^{\infty} \cdots \sum_{n_N}^{\infty} \frac{1}{n_1! \cdots n_N!} (x_1 - a_1)^{n_1} \cdots (x_N - a_N)^{n_N} \cdot \frac{\partial^{n_1}}{\partial x_1^{n_1}} \cdots \frac{\partial^{n_N}}{\partial x_N^{n_N}} f(a_1, \dots, a_N). \quad (3.14)$$

For an arbitrary Green's function with two three dimensional arguments \mathbf{s}_n and $\mathbf{s}_{n'}$, the Taylor series for the two expansion points around zero is

$$G(\mathbf{R}_i + \mathbf{s}_i, \mathbf{R}_j + \mathbf{s}_j)|_{\substack{\tilde{\mathbf{s}}_i=0 \\ \tilde{\mathbf{s}}_j=0}} = G(\mathbf{R}_i, \mathbf{R}_j) + \left[\mathbf{s}_i \cdot \nabla_{\tilde{\mathbf{s}}_i} G(\mathbf{R}_i + \tilde{\mathbf{s}}_i, \mathbf{R}_j + \tilde{\mathbf{s}}_j) \right]_{\substack{\tilde{\mathbf{s}}_i=0 \\ \tilde{\mathbf{s}}_j=0}} + \left[G(\mathbf{R}_i + \tilde{\mathbf{s}}_i, \mathbf{R}_j + \tilde{\mathbf{s}}_j) \widehat{\nabla_{\tilde{\mathbf{s}}_j} \cdot \mathbf{s}_j} \right]_{\substack{\tilde{\mathbf{s}}_i=0 \\ \tilde{\mathbf{s}}_j=0}} + \left[\mathbf{s}_i \cdot \nabla_{\tilde{\mathbf{s}}_i} G(\mathbf{R}_i + \tilde{\mathbf{s}}_i, \mathbf{R}_j + \tilde{\mathbf{s}}_j) \widehat{\nabla_{\tilde{\mathbf{s}}_j} \cdot \mathbf{s}_j} \right]_{\substack{\tilde{\mathbf{s}}_i=0 \\ \tilde{\mathbf{s}}_j=0}} + \dots \quad (3.15)$$

While the zeroth order of the Taylor expanded Green's function (first term in Eq. (3.15)) represents the monopole-monopole interaction, the first order in both arguments, \mathbf{s}_i and \mathbf{s}_j , constitutes the dipole-dipole coupling (last term in Eq. (3.15)) such as the dipole induced Förster coupling transfer. For quantum dynamical calculations, the mixed terms of the monopole-dipole interaction, represented by the second and third term, will often be neglected in a rotating wave approximation [4], but can be included if necessary (e.g., for carrier multiplication). Terms of higher order in the Taylor expansion [34] are discarded here, but they can be included in principle in a similar way (as is done in Sec. 3.5.3 for quadrupole-quadrupole terms in the Coulomb

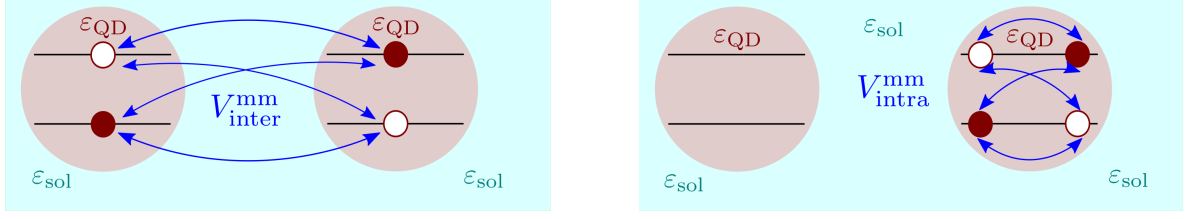


Figure 3.3 Schema of the electrostatic monopole-monopole Coulomb coupling between two colloidal QDs in a solvent, which occurs between electrons and holes. The Coulomb elements can be distinguished between the interdot coupling as an interaction between both QDs (left hand side) and the intradot coupling, where both charge carriers are located in one QD (right hand side).

potential). We see, using the Green's function formalism, the monopole-monopole as well as the dipole-dipole contributions can be identified without specifying a closed analytic expression for the Green's function. In the following sections, we will explicitly specify the monopole-monopole as well as the dipole-dipole Coulomb coupling elements in the formalism of the PGF method [49].

3.2.2 Monopole-monopole coupling elements

Using the PGF method, the electrostatic monopole-monopole coupling between the electrons and the holes of the QDs, which is schematically depicted in Fig. 3.3, should be calculated. The monopole-monopole Coulomb coupling is given by the direct coupling between the charge densities of the nanostructures. It can be divided into the intradot coupling, where both charge densities are located in the same QD, and the interdot coupling as interaction between the nanostructures. For calculating the monopole-monopole Coulomb coupling elements, the first term of the Green's function Taylor series in Eq. (3.15) (which represents the zeroth order) is included into the equation of the Coulomb coupling in Eq. (3.13):

$$V_{1234}^{\text{mm}} = e^2 \sum_{i,j} \xi_{\lambda_1 n_1}^*(\mathbf{R}_i) \xi_{\lambda_2 n_2}^*(\mathbf{R}_j) \xi_{\lambda_3 n_3}(\mathbf{R}_j) \xi_{\lambda_4 n_4}(\mathbf{R}_i) \cdot \int d^3 s_i \int d^3 s_j u_{\lambda_1 n_1 \sigma_1}^*(\mathbf{s}_i) u_{\lambda_2 n_2 \sigma_2}^*(\mathbf{s}_j) G(\mathbf{R}_i, \mathbf{R}_j) u_{\lambda_3 n_3 \sigma_3}(\mathbf{s}_j) u_{\lambda_4 n_4 \sigma_4}(\mathbf{s}_i). \quad (3.16)$$

Using the normalization condition of the Bloch functions over the volume of a unit cell V_{uc} , as is done in Ref. [4],

$$\frac{1}{V_{\text{uc}}} \int d^3 s_i u_{\lambda n \sigma}^*(\mathbf{s}_i) u_{\lambda' n' \sigma'}(\mathbf{s}_i) = \delta_{\lambda \lambda'} \delta_{n n'} \delta_{\sigma \sigma'}, \quad (3.17)$$

the monopole-monopole coupling elements read

$$V_{1234}^{\text{mm}} = e^2 V_{\text{uc}}^2 \sum_{i,j} \xi_{\lambda_1 n_1}^*(\mathbf{R}_i) \xi_{\lambda_2 n_2}^*(\mathbf{R}_j) G(\mathbf{R}_i, \mathbf{R}_j) \xi_{\lambda_3 n_3}(\mathbf{R}_j) \xi_{\lambda_4 n_4}(\mathbf{R}_i) \delta_{14}^{\lambda n \sigma} \delta_{23}^{\lambda n \sigma}. \quad (3.18)$$

For convenience, the Kronecker delta relations for the different quantum numbers, which ensure the selection rules, are merged together as follows: $\delta_{ij}^{\lambda n \sigma} = \delta_{\lambda_i \lambda_j} \delta_{n_i n_j} \delta_{\sigma_i \sigma_j}$. Under the assumption, that the unit cells densely cover the QD, the summation over all cells can be transformed into an integral:

$$\sum_i = \frac{(\Delta \mathbf{R}_i)^3}{(\Delta \mathbf{R}_i)^3} \sum_i \rightarrow \frac{1}{V_{\text{uc}}} \int d^3 r. \quad (3.19)$$

Therefore, for an arbitrary Green's function $G(\mathbf{r}, \mathbf{r}')$ the monopole-monopole Coulomb coupling elements, which can be divided into interdot coupling elements with $n \neq n'$ and intradot coupling with $n = n'$, as illustrated in Fig. 3.3, are calculated:

$$V_{1234}^{\text{mm}} = e^2 \int d^3r \int d^3r' \xi_{\lambda_1 n_1}^*(\mathbf{r}) \xi_{\lambda_2 n_2}^*(\mathbf{r}') G(\mathbf{r}, \mathbf{r}') \xi_{\lambda_3 n_3}(\mathbf{r}') \xi_{\lambda_4 n_4}(\mathbf{r}) \delta_{14}^{\lambda n \sigma} \delta_{23}^{\lambda n \sigma}. \quad (3.20)$$

The Coulomb interaction depends on the spatial arrangement of the nanostructures, which includes the distance between the QDs as well as the relative angular positioning of QDs to each other. Therefore, a high number of coupling elements needs to be calculated, if the positioning of the QDs changes during the measurements. Particularly without assuming specific symmetries of the QD confinement potential or the Green's function, the six dimensional integral in Eq. (3.20) is numerically demanding. For a numerical efficient calculation of the Coulomb coupling elements, the PGF method is used, according to the workflow illustrated in Fig. 3.1. Hence, the number of integrals, required to determine the monopole-monopole interaction, is reduced by introducing a generalized scalar potential $\Phi_{23}^{\text{m}}(\mathbf{r})$, as presented in Sec. 3.1 in Eq. (3.2):

$$\Phi_{23}^{\text{m}}(\mathbf{r}) = e \int d^3r' \xi_{\lambda_2 n_2}^*(\mathbf{r}') G(\mathbf{r}, \mathbf{r}') \xi_{\lambda_3 n_3}(\mathbf{r}') \delta_{23}^{\lambda n \sigma}. \quad (3.21)$$

Including the monopole scalar potential in Eq. (3.21) into the equation of the monopole-monopole Coulomb coupling elements reduces the numerical effort from the six dimensional spatial integral in Eq. (3.20) to a three dimensional integral:

$$V_{1234}^{\text{mm}} = e \int d^3r \left(\xi_{\lambda_1 n_1}^*(\mathbf{r}) \Phi_{23}^{\text{m}}(\mathbf{r}) \xi_{\lambda_4 n_4}(\mathbf{r}) \delta_{14}^{\lambda n \sigma} \right). \quad (3.22)$$

Following the approach of the PGF method [49], the monopole scalar potential in Eq. (3.22) is determined by solving the generalized Poisson equation in the monopole case:

$$\nabla_{\mathbf{r}} \cdot (\varepsilon(\mathbf{r}) \nabla_{\mathbf{r}} \Phi_{23}^{\text{m}}(\mathbf{r})) = -e \frac{\xi_{\lambda_2 n_2}^*(\mathbf{r}) \xi_{\lambda_3 n_3}(\mathbf{r})}{\varepsilon_0}. \quad (3.23)$$

Eq. (3.23) shows, that the inhomogeneity of the generalized Poisson equation for the monopole-monopole Coulomb interaction is determined by a product of the electron envelope functions for the corresponding QD band indices $\lambda_{2/3}$ and the QD numbers $n_{2/3}$. The numerical solution of Eq. (3.23) enables a calculation of the monopole-monopole Coulomb coupling elements without inserting an explicit Green's function. Accordingly, using the PGF method, as published in Ref. [49], numerically demanding singularities can be avoided. Without implying a restriction to a certain symmetry of the QD confinement potential or the Coulomb Green's function, the efficiency of the calculation of Coulomb coupling elements is increased in the PGF method. Furthermore, the influence of an inhomogeneous medium, which is required for the calculation of the Coulomb coupling between colloidal QDs in a solvent, is naturally included by the permittivity $\varepsilon(\mathbf{r})$ in Eq. (3.23).

3.2.3 Dipole-dipole coupling elements

The dipole-dipole Coulomb coupling elements, given by the last term of the Green's function's Taylor series in Eq. (3.15), include the Förster excitation transfer between the colloidal QDs as well as an intradot coupling, schematically depicted in Fig. 3.4. Whereas the influence of the intradot dipole interaction is very small and negligible, the effects caused by the so-called Förster interaction play an important role in Coulomb coupled systems. If one QD is excited, the excitation energy can be transferred to the other QD by the Förster mechanism [3]. Thus,

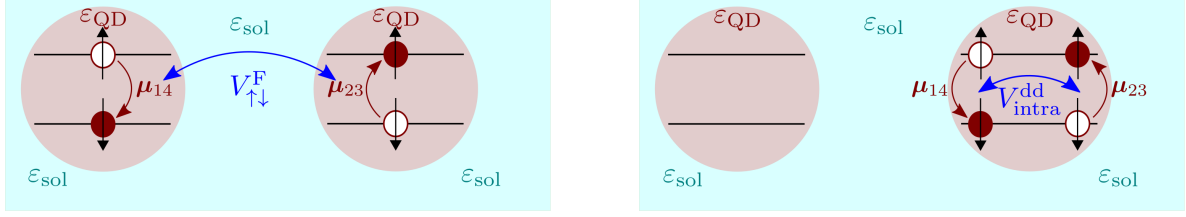


Figure 3.4 The dipole-dipole Coulomb coupling can be distinguished between the interdot Förster induced excitation transition between the two QDs (left hand side) and the dipole-dipole intradot coupling located in one QD (right hand side).

even in the case of non-overlapping electron wave functions of the two colloidal QDs, there is an excitation transfer for small distances between the nanostructures, induced by the dipole-dipole Förster coupling as resonant excitation energy transfer. Inserting the last term of the Coulomb Green's function Taylor series in Eq. (3.15) into the equation of the Coulomb coupling elements Eq. (3.13) leads to:

$$V_{1234}^{\text{dd}} = e^2 \sum_{i,j} \xi_{\lambda_1 n_1}^*(\mathbf{R}_i) \xi_{\lambda_2 n_2}^*(\mathbf{R}_j) \xi_{\lambda_3 n_3}(\mathbf{R}_j) \xi_{\lambda_4 n_4}(\mathbf{R}_i) \int d^3 s_i \int d^3 s_j u_{\lambda_1 n_1 \sigma_1}^*(\mathbf{s}_i) u_{\lambda_2 n_2 \sigma_2}^*(\mathbf{s}_j) \cdot \left[\mathbf{s}_i \cdot \nabla_{\tilde{\mathbf{s}}_i} G(\mathbf{R}_i + \tilde{\mathbf{s}}_i, \mathbf{R}_j + \tilde{\mathbf{s}}_j) \nabla_{\tilde{\mathbf{s}}_j} \cdot \mathbf{s}_j \right]_{\substack{\tilde{\mathbf{s}}_i = 0 \\ \tilde{\mathbf{s}}_j = 0}} u_{\lambda_3 n_3 \sigma_3}(\mathbf{s}_j) u_{\lambda_4 n_4 \sigma_4}(\mathbf{s}_i). \quad (3.24)$$

For identifying the dipole-dipole interactions, the microscopic interband transition dipole moments $\boldsymbol{\mu}_{ll'}$, which are given by the Bloch functions of the unit cells [34, 76], are defined as follows, analog to the definition given in Sec. 2.2.2:

$$\boldsymbol{\mu}_{ll'} = \frac{e}{V_{\text{uc}}} \int d^3 s_i u_{\lambda_l n_l \sigma_l}^*(\mathbf{s}_i) \mathbf{s}_i u_{\lambda_{l'} n_{l'} \sigma_{l'}}(\mathbf{s}_i) \delta_{n_l n_{l'}} \delta_{\sigma_l \sigma_{l'}}. \quad (3.25)$$

Note, that the interband transition moments $\boldsymbol{\mu}_{ll'}$, which appear during the usual scale separation, depend on the spin configurations [3] σ_l and $\sigma_{l'}$. The differentiation of the Green's function in Eq. (3.24) can be transformed from the variable $\tilde{\mathbf{s}}_i$ to \mathbf{R}_i since they belong to the same entry:

$$\left[\nabla_{\tilde{\mathbf{s}}_i} G(\mathbf{R}_i + \tilde{\mathbf{s}}_i, \mathbf{R}_j + \tilde{\mathbf{s}}_j) \right]_{\substack{\tilde{\mathbf{s}}_i = 0 \\ \tilde{\mathbf{s}}_j = 0}} = \left[\nabla_{\mathbf{R}_i} G(\mathbf{R}_i + \tilde{\mathbf{s}}_i, \mathbf{R}_j + \tilde{\mathbf{s}}_j) \right]_{\substack{\mathbf{R}_i = \mathbf{R}_i - \tilde{\mathbf{s}}_i \\ \mathbf{R}_j = \mathbf{R}_j - \tilde{\mathbf{s}}_j}}. \quad (3.26)$$

Based on the assumption, that the Green's function does not significantly change on the scale of the unit cells, the summation over the unit cells can be transformed into an integration. Using the transformation of the differentiation and identifying the microscopic dipole moments results in the following equation for the Coulomb coupling elements in the dipole-dipole case:

$$V_{1234}^{\text{dd}} = \int d^3 r \int d^3 r' \xi_{\lambda_1 n_1}^*(\mathbf{r}) \xi_{\lambda_2 n_2}^*(\mathbf{r}') \xi_{\lambda_3 n_3}(\mathbf{r}') \xi_{\lambda_4 n_4}(\mathbf{r}) \boldsymbol{\mu}_{14} \cdot \nabla_{\mathbf{r}} G(\mathbf{r}, \mathbf{r}') \nabla_{\mathbf{r}'} \cdot \boldsymbol{\mu}_{23} \delta_{14}^{n\sigma} \delta_{23}^{n\sigma}. \quad (3.27)$$

The Kronecker delta relations, ensuring the selection rules, are merged together as follows: $\delta_{ij}^{n\sigma} = \delta_{n_i n_j} \delta_{\sigma_i \sigma_j}$. For evaluating the nabla operators effecting the arbitrary Green's function, a multidimensional integration by parts is used

$$\int_{\Omega} d^3 r \mathbf{r} \cdot \nabla \chi = \int_{\partial\Omega} d\mathbf{f} \cdot \mathbf{r} \chi - \int_{\Omega} d^3 r \chi \nabla \cdot \mathbf{r}, \quad (3.28)$$

under the assumption of vanishing boundary integrals. Finally, applying the multidimensional integration by parts twice, the equation for the calculation of the dipole-dipole Coulomb coupling

elements reads

$$V_{1234}^d = \int d^3r \int d^3r' \nabla_{\mathbf{r}} \cdot \left(\xi_{\lambda_1 n_1}^*(\mathbf{r}) \boldsymbol{\mu}_{14} \xi_{\lambda_4 n_4}(\mathbf{r}) \right) G(\mathbf{r}, \mathbf{r}') \nabla_{\mathbf{r}'} \cdot \left(\xi_{\lambda_2 n_2}^*(\mathbf{r}') \boldsymbol{\mu}_{23} \xi_{\lambda_3 n_3}(\mathbf{r}') \right) \delta_{14}^{n\sigma} \delta_{23}^{n'\sigma}. \quad (3.29)$$

Since the microscopic transition moments $\boldsymbol{\mu}_{ll'}$ vanishes for equal bandindices $l = l'$, only the dipole transitions with $\lambda_1 \neq \lambda_4$ and $\lambda_2 \neq \lambda_3$ determine the dipole-dipole Coulomb coupling. As in the case of the monopole-monopole coupling terms, the dipole-dipole Coulomb coupling can be divided into the interdot coupling with $n \neq n'$ and the intradot coupling with $n = n'$, as schematically depicted in Fig. 3.4. Furthermore, the interdot coupling is separated into spin-preserving processes with $\sigma = \sigma'$ and spin-flipping processes with $\sigma \neq \sigma'$.

For applying the PGF method, as introduced in Sec. 3.1 and published in Ref. [49], a Poisson equation for the first order in the Taylor expansion Eq. (3.15) needs to be formulated. Thus, a generalized scalar potential $\Phi_{23}^d(\mathbf{r})$ of the Coulomb dipole interaction of a QD is introduced

$$\Phi_{23}^d(\mathbf{r}) = \int d^3r' G(\mathbf{r}, \mathbf{r}') \nabla_{\mathbf{r}'} \cdot \left(\xi_{\lambda_2 n_2}^*(\mathbf{r}') \boldsymbol{\mu}_{23} \xi_{\lambda_3 n_3}(\mathbf{r}') \right). \quad (3.30)$$

With the Green's function fulfilling the condition in Eq. (2.7), Eq. (3.30) represents the solution of the following generalized Poisson equation:

$$\nabla_{\mathbf{r}} \cdot (\varepsilon(\mathbf{r}) \nabla_{\mathbf{r}} \Phi_{23}^d(\mathbf{r})) = \frac{\nabla_{\mathbf{r}} \cdot \left(\xi_{\lambda_2 n_2}^*(\mathbf{r}) \boldsymbol{\mu}_{23} \xi_{\lambda_3 n_3}(\mathbf{r}) \right)}{\varepsilon_0}. \quad (3.31)$$

In the dipole case, the Poisson equation is induced by the dipole distribution, which includes the QD's envelope functions $\xi_{\lambda_i n_i}$ and the microscopic interband transition dipole moment $\boldsymbol{\mu}_{23}$. Therefore, the scalar potential $\Phi_{23}^d(\mathbf{r})$ has a different unit than the scalar potential of the monopole-monopole coupling $\Phi_{23}^m(\mathbf{r})$ in Eq. (3.23). In the approach of the PGF method, the generalized scalar potential Φ_{23}^d is obtained numerically from the Poisson Eq. (3.31), using efficient solvers and libraries such as PETSc [95]. Including this solution in the equation of the dipole-dipole Coulomb coupling elements in Eq. (3.29), the numeric effort for the calculation is significantly reduced:

$$V_{1234}^d = \int d^3r \nabla_{\mathbf{r}} \cdot \left(\xi_{\lambda_1 n_1}^*(\mathbf{r}) \boldsymbol{\mu}_{14} \xi_{\lambda_4 n_4}(\mathbf{r}) \right) \Phi_{23}^d(\mathbf{r}) \delta_{\sigma_1 \sigma_4} \delta_{\sigma_2 \sigma_3}. \quad (3.32)$$

The strength of the dipole-dipole coupling between colloidal QDs in a solvent is influenced by the distance between the nanostructures as well as by the relative orientation of the QD's dipole moments to each other [4].

We have shown, that the PGF method allowed us to calculate the monopole-monopole and the dipole-dipole Coulomb coupling respectively, without the necessity of assuming an explicit form of the Green's function. For both contributions, the generalized scalar potential is calculated for a specific generalized Poisson equation. We showed that, based on the Taylor expansion of the Green's function, the Coulomb coupling elements of the monopole-monopole as well as the dipole-dipole contribution of the Coulomb interaction can be calculated numerically efficiently without being restricted to a specific symmetry or permittivity by using an adapted Poisson equation. In the next sections, we explicitly calculate the monopole-monopole and Förster coupling elements for two colloidal QDs in varying spatial positions. Thus we can investigate the influence of the distance between the QDs and their relative dipole orientation to each other on the Coulomb coupling elements. Furthermore, the influence of the spatial dielectric function on the coupling elements is analyzed.

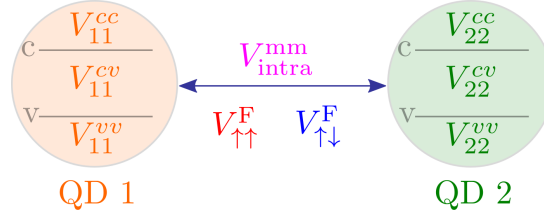


Figure 3.5 A schematic sketch of the Coulomb coupling elements of two colloidal QDs. The intradot coupling is given by the monopole-monopole elements of the n 'th QD ($n \in 1, 2$) V_{nn}^{cc} , V_{nn}^{vv} and V_{nn}^{cv} . The interdot coupling is classified as monopole-monopole V_{intra}^{mm} and spin-selective Förster coupling elements $V_{\uparrow\uparrow}^F$ and $V_{\uparrow\downarrow}^F$.

3.3 Position dependent Coulomb coupling of colloidal QDs

In this section, we calculate and analyze the influence of the spatial arrangement of two colloidal QDs on the strength of the Coulomb coupling between them. Colloidal QDs, as presented in Sec. 2.1, diffuse in the surrounding solvent and thus, they change their positioning frequently. The motion of the colloidal QDs induces changes in the center-to-center distance between the QDs as well as in their relative angular orientation, both determining the strength of the Coulomb coupling, respectively. Thus, for the calculation of the arrangement specific Coulomb interaction, a high number of coupling elements needs to be calculated. Therefore, the PGF method, introduced in Sec. 3.1 and published in Ref. [49], is used for the calculations.

3.3.1 Distance dependence

As we will see in this section, the distance between the colloidal QDs strongly influences the Coulomb coupling elements. The standard simplified form of the dipole-dipole coupling between two point-like emitters in a homogeneous medium reads [34, 117]:

$$V_{12} = \frac{1}{4\pi\epsilon_0\epsilon_r} \left(\frac{\boldsymbol{\mu}_1 \cdot \boldsymbol{\mu}_2}{|\mathbf{R}_{12}|^3} - 3 \frac{(\boldsymbol{\mu}_1 \cdot \mathbf{R}_{12})(\boldsymbol{\mu}_2 \cdot \mathbf{R}_{12})}{|\mathbf{R}_{12}|^5} \right), \quad (3.33)$$

with $\mathbf{R}_{12} = \mathbf{r}_1 - \mathbf{r}_2$ denoting the emitter's distance and $\boldsymbol{\mu}_i$ the dipole moment of the emitter i . This approximative equation shows, that the distance strongly determines the strength of the Coulomb coupling. However, since the distance between the QDs can be very small or if a spatial dependent dielectric function needs to be included, we have to go beyond the point-dipole form of Eq. (3.33), as is done in Refs. [4, 41, 62]. An explicit calculation and analysis of the so-called point-dipole approximation will be given in Sec. 3.5.

In the following, we will fully calculate the Coulomb coupling elements for CdSe/ZnTe core/shell QDs in water (material parameters are presented in Sec. 2.1.1) for varying distances with fixed angular orientations. While one QD stays in the initial position, the other QD systematically changes its position. The calculations are done for different fixed angular dipole orientations. The Coulomb coupling elements for two semiconductor QDs modeled by a two-level system are characterized by the bandindex $b \in \{v, c\}$, the QD number $n \in \{1, 2\}$, and the spin configuration $\sigma \in \{\uparrow, \downarrow\}$. For introducing the notations, all counting Coulomb elements calculated in this section are schematically depicted in Fig. 3.5.

We start with the calculation of the monopole-monopole Coulomb coupling, as introduced in Sec. 3.2.2, which includes interdot as well as intradot coupling elements. While QD 1 stays in the initial position, the second QD moves along the x-axis and the distance between the both QDs increases. The calculations for Fig. 3.6 are done for two different initial angular orientations of the two QDs to each other. In both cases, the monopole-monopole interdot coupling elements

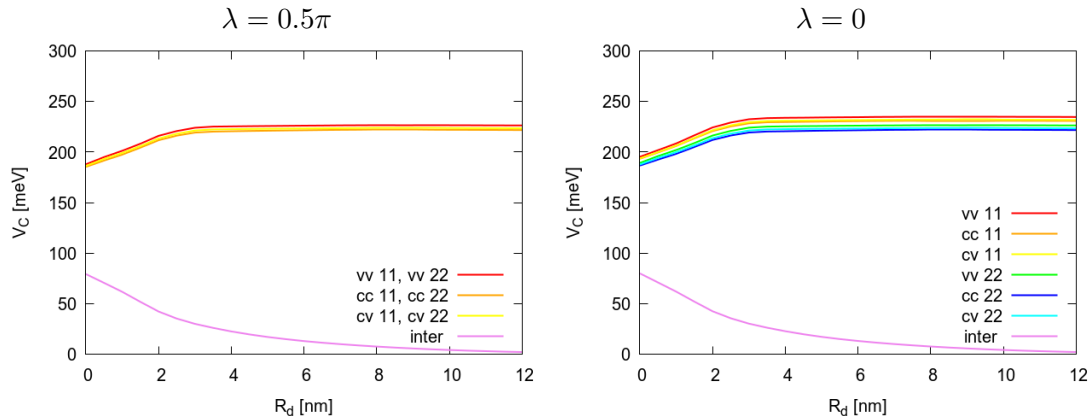


Figure 3.6 The monopole-monopole Coulomb coupling elements are determined by the distances between the QDs in different fixed initial angular orientations. The Coulomb interaction is divided into the intradot and the interdot coupling. While the interdot coupling decreases with increasing distance, the intradot coupling shows a distance dependence for small distances only. Then, all intradot coupling elements reach a saturation value. According to the angular orientation, the intradot coupling elements from the different QDs insignificantly differ ($\lambda = 0.5\pi$) or coincide ($\lambda = 0$).

are equal and decreases with increasing distance. In the case of a spatially homogeneous medium with $\varepsilon_r = \text{const}$, the typically used form of the Coulomb coupling in the monopole case reads:

$$G(\mathbf{r}, \mathbf{r}') = \frac{1}{4\pi\varepsilon_0\varepsilon_r} \frac{1}{R_d}. \quad (3.34)$$

The equation gives the $1/R_d$ -dependence of the interdot monopole Coulomb elements, which determines the curves of the interdot elements even if a spatially dependent dielectric function is included, as visible in Fig. 3.6. In contrast to the monopole-monopole interdot coupling elements, the intradot elements show a distance-dependent behavior for small distances only.

Since the permittivity of the QDs differs from the permittivity of the surrounding medium (e.g., colloidal QDs moving in a solvent), the interdot as well as the intradot Coulomb coupling elements in Eq. (3.20) are influenced by the distance between the QDs, as illustrated in Fig. 3.6. The generalized Poisson equation in Eq. (3.23) for calculating the monopole-monopole Coulomb coupling elements includes the influence of the inhomogeneous medium through the dielectric function $\varepsilon(\mathbf{r})$, which is determined by the distance between the QDs. If the QDs are close to each other, in a distance smaller than four nanometers, even the monopole-monopole intradot coupling elements are influenced by the distance to the other QD. This effect is evoked by the dielectric mismatch caused by the other QDs, which will be discussed in more detail in Sec. 3.4. If the distance between the colloidal QDs increases, the intradot coupling elements reach a saturation value. Since the intradot monopole coupling stays constant even in the case of big QD distances, it determines the monopole shifts and peak positions concerning the excitation energy.

The diagrams in Fig. 3.7 show the Förster coupling elements for an increasing distance R_d between the QDs for three different angular positions λ of the moving QD. Since the Förster coupling between the two QDs decreases with increasing distance, it plays an important role if the QDs are close to each other. But, as the diagrams illustrate, in distances of $R_d = 12$ nm its influence is already negligible. In most angular positions the Förster elements are spin selective. Thus, they can be divided into spin preserving coupling elements $V_{\uparrow\uparrow}^F$ with the complex analog $V_{\downarrow\downarrow}^F$ with $\sigma_i = \sigma_j$ and the spin flipping elements $V_{\uparrow\downarrow}^F$ and $V_{\downarrow\uparrow}^F$ with $\sigma_i \neq \sigma_j$ [4], schematically depicted in Fig. 3.4. If the dipole axis are orthogonal to each other (as in the case $\lambda = 0.5\pi$), the spin splitted elements are degenerated. For investigating the influence of the relative dipole-

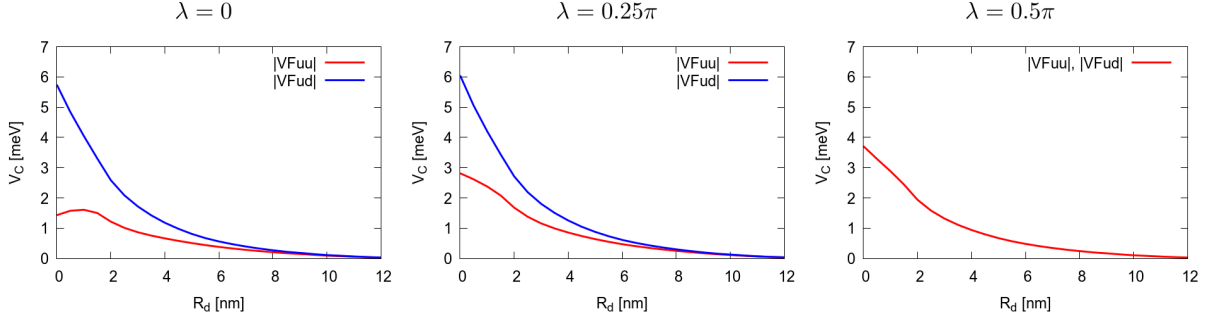


Figure 3.7 The diagrams show the Förster coupling elements as a function of the distance R_d between the QDs in three different fixed angular orientations of the moving QD. With increasing distance between the colloidal QDs the strength of the Förster coupling decreases in all three cases. In the first two dipole orientations, the Förster elements show a spin splitting, which is degenerated in the case of an relative angle of $\lambda = 0.5\pi$.

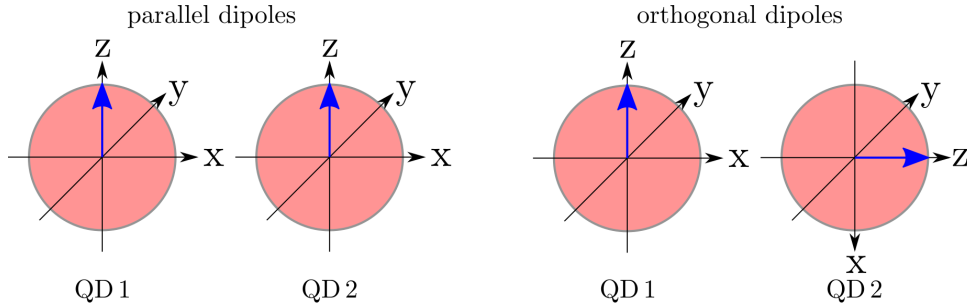


Figure 3.8 Two different initial orientations of the dipole vectors in relation to each other. In the first case (on the left), the dipole moments of the two colloidal QDs are parallelly orientated. The second case (on the right) shows an orthogonal orientation of the dipole vectors to each other.

dipole orientation on the Förster coupling elements, in the next section the coupling elements are calculated in a fixed distance but with systematically changing angular orientations. The dipole-dipole intradot coupling elements (cf. Fig. 3.4) are very small compared to the Förster elements (two orders of magnitude) and therefore, their influence is generally negligible. Furthermore, the inaccuracy caused by the calculation on a discrete grid, for a more detailed discussion see Sec. 2.4.3, is percentaged much higher for small values and thus, the error in the calculations superimposes the physical interpretation.

We have seen in the calculations done in this section, that the distance between the two colloidal QDs plays an important role for the monopole-monopole coupling elements as well as for the Förster excitation transfer. While the interdot coupling decreases with increasing distance, the intradot coupling reaches a saturation value and therefore, they determine the Coulomb shifts for bigger distances as a constant value.

3.3.2 Influence of the angular orientation

Colloidal QDs, diffusing in the solvent, change their spatial positions as well as their angular orientations. Not only the distance between the QDs determines the strength of the Coulomb coupling but also their relative dipole-dipole orientation [3, 4]. The influence of the angular orientation on the monopole-monopole and Förster Coulomb coupling elements is calculated in this section. Therefore, the Coulomb coupling elements for the rotation around the three Cartesian axis are calculated, while the distance between the QDs stays constant. As initial

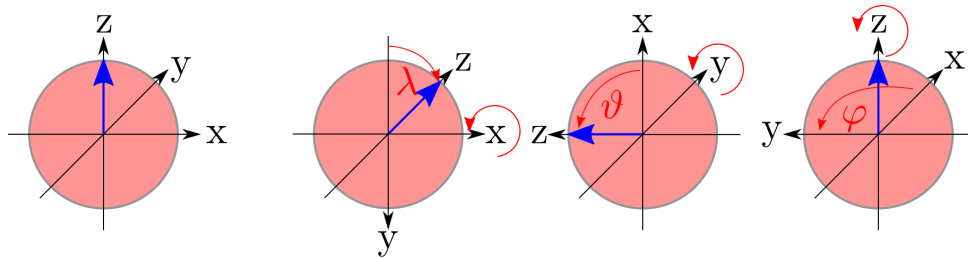


Figure 3.9 Scheme of the three different Euler angles. One QD is fixed while the other QD rotates in a fixed distance, starting from a position of two parallel orientated dipole operator (blue arrows). The rotation around the x-axis is given by the angle λ , the y-axis induces the angle ϑ and the rotation around the z-axis gives φ .

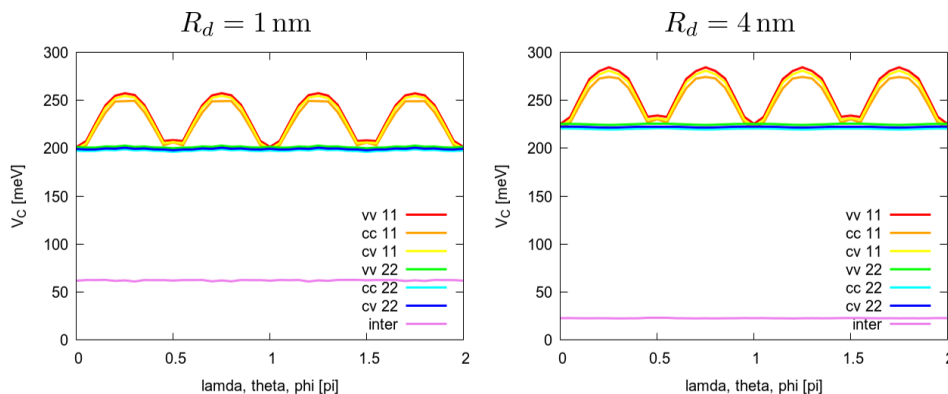


Figure 3.10 The monopole-monopole Coulomb coupling elements as a function of the Euler angles in two different fixed distances. Since the rotations around the three cartesian axis results in the same coupling strengths, the x-axis represents all Euler angles. The distance influences the Coulomb coupling elements, as discussed in Sec.3.3.1, while the monopole-monopole interdot elements are not influenced by the rotation angles. Only the intradot coupling elements of the rotating QD are periodically influenced by the rotation. A discussion of the induced inaccuracy of the projection of a continuous rotation on a discrete grid is given in Sec.2.4.3.

orientation of the two dipole vectors in relation to each other, we do calculations for a parallel orientation as well as for an initially orthogonal orientation, cf. Fig. 3.8. Generally, the rotation is given by three Euler angles for each QD respectively, as introduced in Sec. 2.4. The schematic sketches in Fig. 3.9 illustrate the different rotations of the two colloidal QDs around the three Cartesian axis starting from a parallel orientation of the QD's dipole vectors.

First, we calculate the influence of the different rotations around the Cartesian axis on the monopole-monopole coupling elements. Fig. 3.10 shows the dependence of the monopole-monopole Coulomb coupling elements on the relative angular orientation of the two colloidal QDs. Since all rotations around the different Cartesian axis result in the same angular dependence, the x-axis in Fig. 3.10 represents all Euler angles respectively. While the monopole-monopole interdot coupling elements as well as the intradot coupling elements of the fixed QD (QD 2) stay constant for all angular positions, the intradot coupling elements of the rotating QD are influenced by the rotation angle. Thus, only the moving QD (QD 1) is affected by the rotation angle. Since both QDs are generally equal, the guess that the inaccuracy effects in the monopole intradot coupling elements are caused by the rotation seems likely. A discussion of the effect of the projection of the rotation on a discrete grid is given in Sec. 2.4.3. The most inaccuracy occurs for angles with $n\pi/4$, while it vanishes for $n\pi$ rotations. In the next section, we will see, that in the case of an homogeneous dielectric environment all monopole-monopole coupling elements

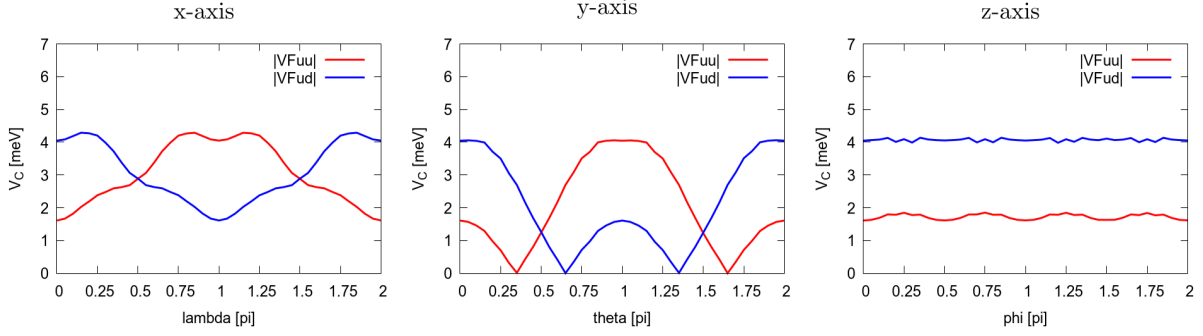


Figure 3.11 The Förster elements as a function of the rotation of one QD around the three Cartesian axis in a distance of $R_d = 1$ nm. In contrast to the monopole-monopole elements, the Förster elements are strongly influenced by the dipole-dipole orientation of the QDs to each other, which is determined by the three independent rotation angles λ , θ , and ϕ . Furthermore, the coupling elements are spin-selective and can be classified as spin-preserving (VFuu) and spin-splitting (VFud) elements. The rotation around the x-axis and the y-axis are given by a cosine function, while the rotation around the z-axis does not influence the Förster elements.

stay equal while the QD rotates. Thus, the spatial dependent dielectric function induces the changes in the intradot monopole-monopole Coulomb elements.

For investigating the influence of the relative dipole-dipole orientation to each other, the Förster coupling elements are calculated as a function of the rotation around the Cartesian axis in Fig. 3.11. The Förster coupling elements are strongly influenced by the angular orientation of the colloidal QDs which is determined by the orientation of the crystal axis inducing the microscopic dipole moments μ_{ij} . Since they are perpendicular to the crystal c-axis, which is orientated along the Cartesian z-axis, as given in the Eqs. (2.21a) and (2.21b), a rotation around the z-axis does not influence the Förster elements. The rotation around the x-axis and the y-axis show a 2π -periodic symmetry in a cosine function profile. The Förster elements are spin-selective for the spin-preserving $V_{\uparrow\uparrow}^F$ and the spin-flipping elements $V_{\uparrow\downarrow}^F$ for all angles except 0.5π and 1.5π , where they are degenerated. The amplitude of the function is determined by the distance between the QDs. The diagrams in Fig. 3.11 are calculated for a distance of $R_d = 1$ nm. The smaller the distances between the QDs the bigger the amplitude, which determines shifts caused by the angular orientation. Additionally, the amplitude is influenced by the rotation axis. As Fig. 3.11 shows, the rotation around the y-axis shows a bigger amplitude than the rotation around the x-axis. Nevertheless, both amplitudes decreases with increasing distance between the colloidal QDs, as discussed in Sec. 3.3.1.

The calculations for the rotations in Fig. 3.11 are done for QDs arranged along the x-axis starting with the same dipole orientation for both QDs. But this starting orientation of the dipole vectors does not include all relative orientations of the two dipole moments to each other for the rotations around the Cartesian axis. Therefore, the Förster elements are calculated starting from an initial perpendicular orientation of the dipole vectors to each other. The results are given in Fig. 3.12. The amplitudes of the diagrams strongly differs from that in the case of an initial parallel orientation of the dipole vectors, depicted in Fig. 3.11. Thus, the rotation around the x-axis as well as the rotation around the z-axis do not influence the Förster elements, if the QDs show perpendicular orientated dipole moments. In the initial perpendicular orientation of the dipole vectors, the projection of the relative orientation of the two dipole moments does not change while one QD rotate around the x-axis or the z-axis. In contrast, for a parallel starting position of the two dipole vectors, the projection of the relative orientation is influenced by the rotation around the x-axis and the y-axis. Only the rotation around the z-axis does not change the projection in both cases.

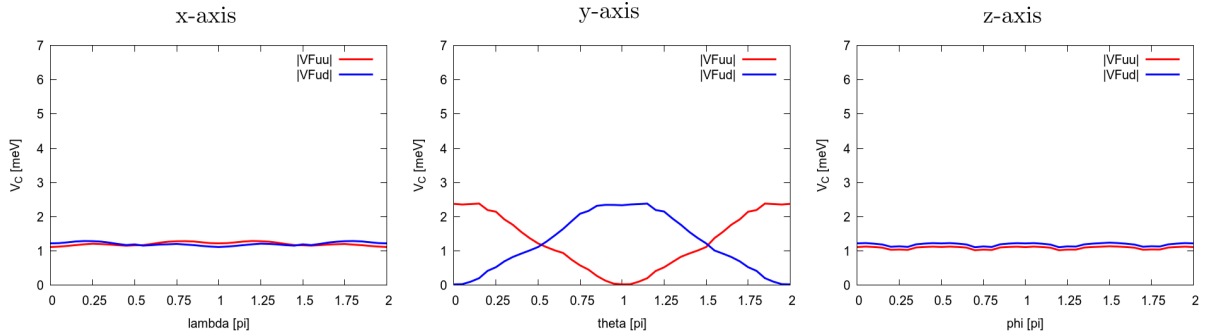


Figure 3.12 The Förster elements for the rotation of one QD around the three Cartesian axis in a distance of $R_d = 1$ nm for QDs with an initially orthogonal dipole orientation to each other. Only the rotation around the y-axis strongly influences the strength of the Förster coupling elements. In the cases of the x-axis and z-axis rotations, the projection of the dipole moments to each other results in one point, and accordingly it does not influence the coupling. While the rotation around the y-axis changes the length of the dipole-dipole projection.

The interplay between the spatial distance and the angular orientation and its influence on the Coulomb coupling elements for an arbitrary motion in three dimensions is complex. It includes many different aspects, since for the spatial arrangement of the QDs in three dimensions many degrees of freedom influence the results. In this section, we have only shown a few spatial QD arrangements and calculated the resulting coupling elements. The spatial arrangement is also determined by the size and the shape of the QDs and the resulting spatially dependent permittivity, as we will discuss in the next section. Since the diffusion of the colloidal QDs in the solvent presents a complex mechanisms, many parameters including the QD arrangements and the material compositions influence the strength of the Coulomb coupling. In App. D a scheme of the program mode is given including the input and output parameters. This gives an overview of the high number of parameters influencing the strength of the coupling and the diffusive motion of the colloidal QDs.

3.4 Spatially dependent dielectric permittivity

Each material is characterized by a specific dielectric constant ϵ . Since the material of the colloidal QDs differs from the material of the surrounding solvent, the whole dielectric environment is given by a spatially dependent dielectric function $\epsilon(\mathbf{r})$. This arbitrarily complex dielectric environment includes information on the size and shape of the colloidal QDs, which diffuse in the solvent, as well as on their spatial arrangement [59]. Furthermore, the properties of the surrounding material, given by the properties of the solvent in the case of colloidal QDs, determines the dielectric function and therefore, they influences the Coulomb coupling between the QDs.

In this section, we analyze the influence of the whole dielectric environment on the strength of the Coulomb coupling of two colloidal QDs. Therefore, we use the PGF method, presented in Sec. 3.1, which allows us to calculate all Coulomb coupling elements for a general dielectric function. Thus, we first investigate the influence of the solvent's dielectric permittivity on the Coulomb interaction between the QDs. Then, we vary the material composition and size of the colloidal QDs and analyze the effects on the monopole and dipole elements. Finally, we compare the fully calculated Coulomb coupling elements, where the spatially dependent dielectric function includes all material information, with the Coulomb coupling in different homogeneous dielectric media.

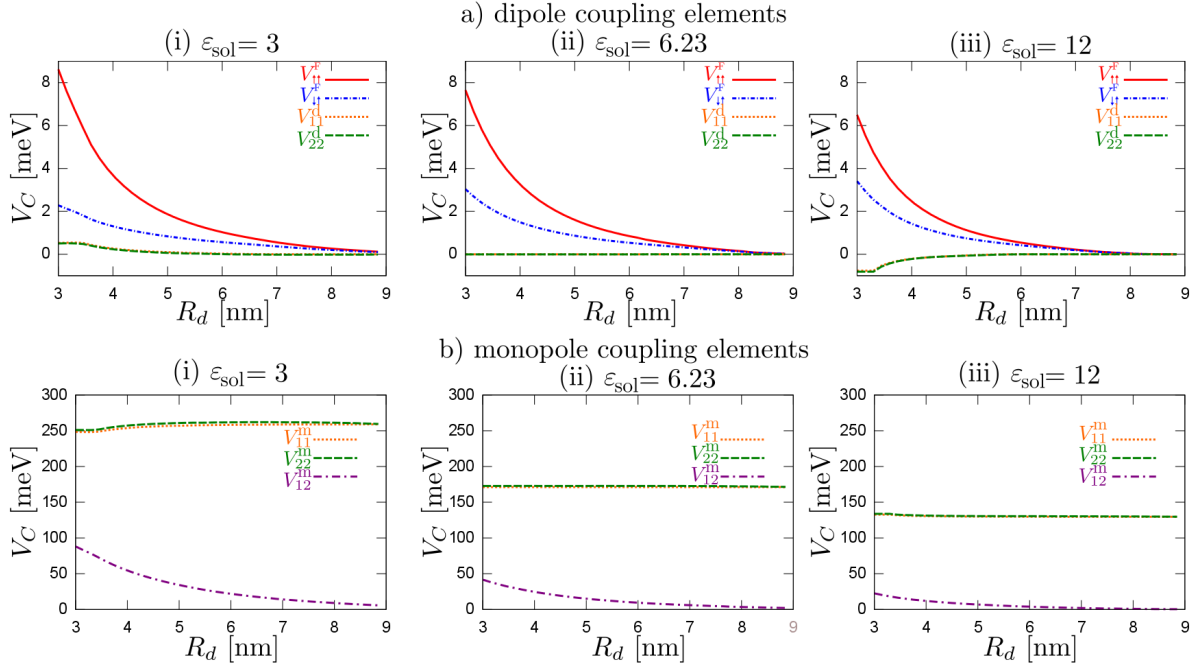


Figure 3.13 Coupling elements of the a) dipole-dipole and b) monopole-monopole Coulomb interaction as a function of the QD's center-to-center-distances for different solvent's permittivities. The value of the dielectric constant of the solvent ϵ_{sol} is (i) smaller, (ii) equal or (iii) greater than the permittivity of the QDs $\epsilon_{\text{QD}} = 6.23$. The coupling strength as well as the curve progression are influenced by the value of the dielectric constant of the medium. Only in the case (ii) where QDs and solvent have the same permittivity, the dipole and monopole intradot coupling elements ($V_{11}^{\text{d/m}}$ and $V_{22}^{\text{d/m}}$) stay constant for all distances between the QDs.

3.4.1 Solvent induced dielectric mismatch

In the following, we analyze the influence of the relation of the dielectric constants from the QDs and the surrounding solvent on the monopole-monopole and dipole-dipole Coulomb coupling elements. Since the calculation of the Coulomb coupling elements is based on the generalized Poisson equation (3.4), as in the approach of the PGF method introduced in Sec. 3.1, the influence of the spatially dependent permittivity of the medium on the coupling elements is naturally included. Thus, the Coulomb coupling elements are calculated for different dielectric constants of the surrounding solvent's permittivity ϵ_{sol} . The colloidal QDs are assumed to be small colloidal CdSe QDs with a radius of $r_{\text{QD}} = 1.5$ nm and a constant permittivity of $\epsilon_{\text{QD}} = 6.23$.

Fig. 3.13 illustrates the influence of the solvent's dielectric constant on the center-to-center distance's behavior of the Coulomb coupling elements. If the permittivity of the embedding material is equal to the QD's permittivity, as in Fig. 3.13(ii), and thus, the dielectric environment is homogeneous over the whole structure, the intradot coupling elements stay constant. They do not depend on the center-to-center distance R_d of the QDs and present a material specific parameter. In contrast, in the range of small center-to-center distances, the intradot coupling elements in Fig. 3.13(i) and Fig. 3.13(iii) are not constant but reach a material specific saturation value for an increasing distance. Thus, the intradot monopole-monopole coupling elements in Fig. 3.13(b) as well as the intradot dipole-dipole coupling elements in Fig. 3.13(a) are influenced by the dielectric mismatch caused by the other QDs.

Since the dielectric constant of the QDs differs from the surrounding medium, the whole dielectric environment is represented by a spatially dependent function $\epsilon(\mathbf{r})$. The dielectric

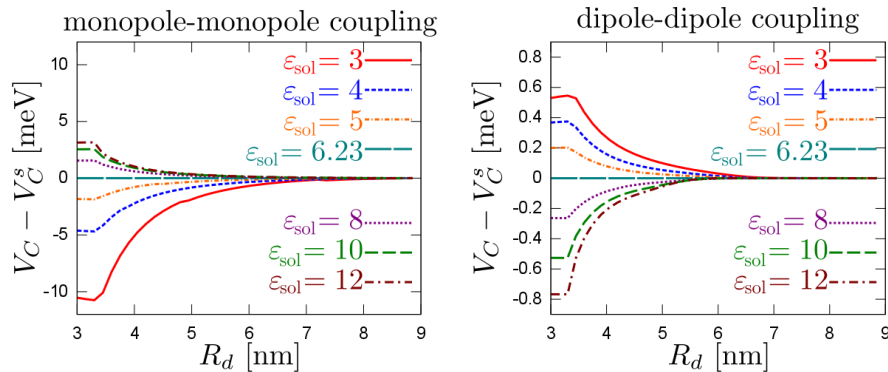


Figure 3.14 The intradot coupling elements of the a) dipole and b) monopole interaction for different permittivities of the solvent, centered at their saturation values. If the dielectric constant of the medium is smaller than that of the QDs ($\epsilon_{\text{QD}} = 6.23$), the dipole elements decrease with growing distance between the QDs, while the monopole elements increase. For a solvent's permittivity greater than that of the QDs, the curve progression shows an opposite behavior.

mismatch, induced by the contrast between the internal and external dielectric constants, results in surface charges [69]. Accordingly, if the dielectric environment is not approximated as a homogeneously distributed dielectric permittivity, as in Fig. 3.13(ii), an image charge distribution on the interface surfaces occurs [69]. Therefore, even the intradot coupling elements, where both charge carriers are only located in one QD, are influenced by the dielectric properties of the other QD, if the QDs are arranged close to each other. For an increasing distance between the QDs, the effect vanishes and the intradot coupling elements reach a constant material specific value. Especially, in the case of the intradot dipole-dipole coupling, the effect is very small and will be difficult to quantify in experimental set-ups. Nevertheless, the effect caused by the dielectric mismatch induces Coulomb shifts and thus, it influences for example the positions in optical spectra.

To illustrate the deviation of the intradot coupling elements from their material specific saturation value, in Fig. 3.14 the monopole-monopole as well as the dipole-dipole intradot coupling elements are plotted embedded in different solvent materials and respectively shifted by their saturation values. In a region of small center-to-center distances, the intradot coupling elements differ from the material specific constant. If the value of the solvent's permittivity is smaller than that of the QDs, the amplitude of the dipole-dipole elements decreases while the monopole-monopole amplitude increases. If the permittivity of the medium is bigger than that of the QDs, the coupling elements show an opposite behavior. The higher the difference between the permittivities of the QDs and the solvent, the bigger the deviation from the saturation value. For an increasing distance between the QDs, the influence of the dielectric mismatch vanishes and the intradot coupling elements reach their material specific saturation value.

The relation of the QDs permittivities to the surrounding material influences the strength of the Coulomb coupling. If the QDs are arranged close to each other, the properties of the whole dielectric environment induce distance dependent shifts and deviations from the material specific values. In the case of a homogeneous dielectric permittivity, the effects of the dielectric mismatch vanish and the intradot coupling elements are constant for all distances. Since in this section we have analyzed the influence of the solvent's permittivity, in the following we investigate the influence of the QD properties on the strength of the Coulomb coupling.

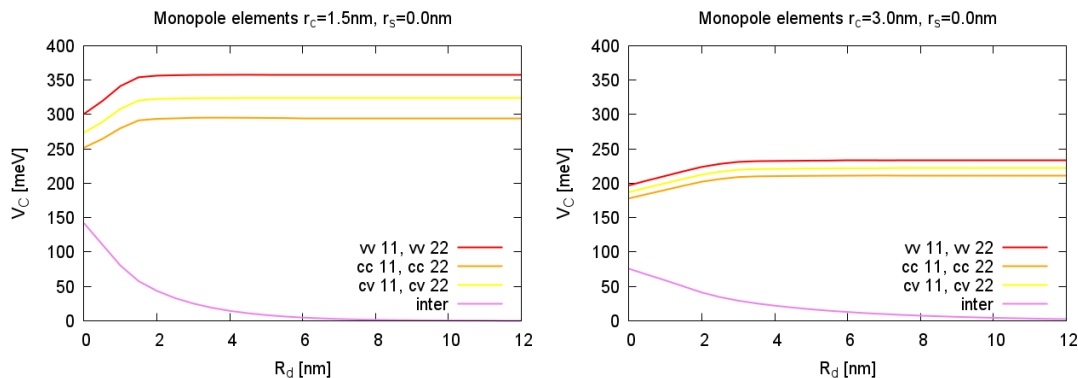


Figure 3.15 Influence of the QD's size (on the left $r = 1.5$ nm and on the right $r = 3.0$ nm) on the distance dependence of monopole-monopole Coulomb coupling elements. For the bigger QD (right) the amplitude of the intradot coupling elements is decreased and shifted together. The influence of the dielectric mismatch for small distances ($R_d < 2$ nm) is decreased. For the smaller QDs (left) the interdot couplings are bigger but they decrease faster for an increasing distance between the QDs.

3.4.2 Size effects and core/shell structure of colloidal QDs

Depending on the synthesis process, colloidal QDs can be fabricated with a variety of compositions [13, 18] and diameters [11, 17]. Since the size and shape of the colloidal QDs strongly influences the optical and electronic properties [9, 10], we calculate the Coulomb coupling elements of different sized and structured colloidal QDs.

The most important parameter for tuning the optical and electronic properties of colloidal QDs is given by the diameter of the QDs. A variety of studies investigates the size-dependent band gap of the colloidal QDs [14, 15]. Here, we calculate the influence of the size of the colloidal QDs on the Coulomb coupling elements. Therefore, we follow the approach of the PGF method [49] introduced in Sec. 3.1, for colloidal QDs with two different diameters $r = 1.5$ nm and $r = 3.0$ nm. Generally, both parameter set-ups represent small colloidal QDs, since we do not change the general parameter set-up.

Fig. 3.15 shows, that the QD size determines the amplitude of the monopole-monopole coupling elements. The bigger the QDs, the smaller the strength of the intradot Coulomb elements and the smaller the differences between the different bandindex induced intradot elements V_{ii}^{cc} , V_{ii}^{vv} and V_{ii}^{cv} . For the smaller QD the dielectric permittivity stronger influences the amplitude in the range on small distances between the QDs (a detailed discussion of the influence of the permittivity is given in Sec. 3.4.1). Since the dielectric permittivity is assumed to change its value monotonously as a softened step-function, in very small QDs the permittivity is mostly not constant. Therefore, the changes in the permittivity strongly influences the Coulomb coupling elements. For bigger QDs, the changes in the amplitude of the monopole-monopole intradot coupling elements caused by the dielectric function decreases but its influence on the second QD, which does not carry the charge density, is present over a longer distance between the QDs. The bigger the QDs, the bigger the influence of the QD's properties on the whole dielectric environment.

The monopole-monopole interdot coupling elements in Fig. 3.15 as well as the Förster elements in Fig. 3.16 show strongly size dependent amplitudes for small distances between the QDs ($R_d < 2$ nm). For smaller QDs the amplitude of the interdot Coulomb coupling is higher but it decreases faster with increasing distance between the QDs. Thus, for bigger colloidal QDs the strength of the Coulomb coupling becomes more long-ranged. The composition of the whole structure and geometry influences the strength of the Coulomb coupling elements.

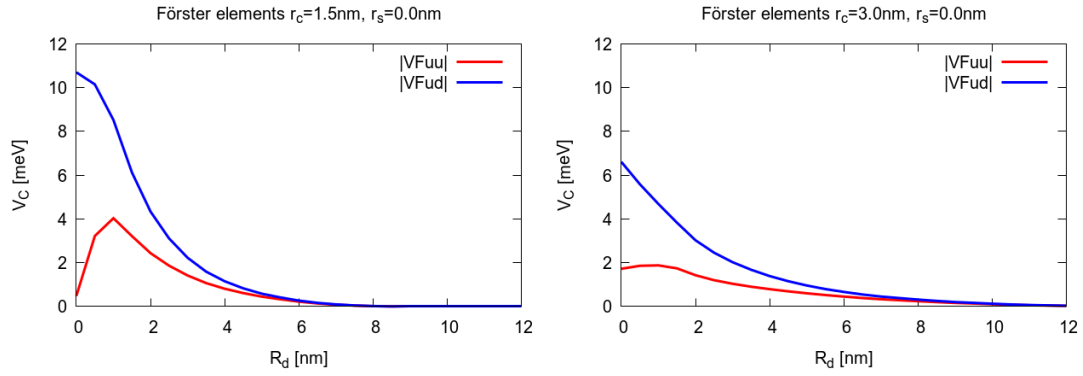


Figure 3.16 Förster coupling elements for two different sized QDs with $r = 1.5$ nm on the left and $r = 3.0$ nm on the right. Especially for small distances between the QDs ($R_d < 2$ nm) the influence of the dielectric mismatch is increased for smaller QDs. For bigger QDs, the strength of the dipole-dipole coupling is smaller but it decreases not so fast as in the case of the smaller QDs with increasing distance.

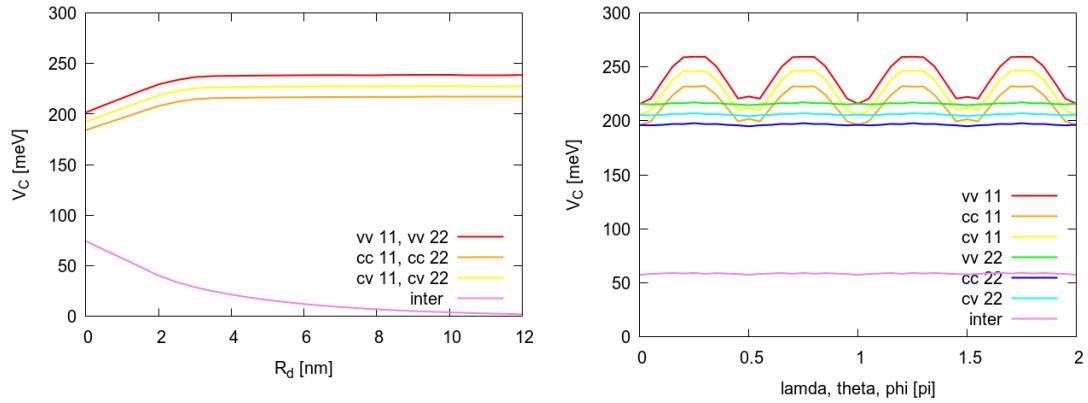


Figure 3.17 Monopole-monopole Coulomb elements of colloidal CdS/ZnSe core/shell QDs with $r_c = 1.5$ nm and $r_s = 1.5$ nm. The interdot coupling does not differ from the couplings of CdSe/ZnTe QDs as presented before. The strength of the coupling is also comparable to the case of the CdSe/ZnTe QDs. In contrast, the shifts in the intradot coupling elements caused by the splitting in the band indices is increased.

Not only the size of the QDs but also the material parameters influences the dielectric environment, as presented for the solvent's properties in Sec. 3.4.1. Therefore, we calculate the Coulomb coupling elements for another material system without changing the other conditions such as the size of the QDs or the permittivity of the solvent. For a comparison with the results for the CdSe/ZnTe QDs given in Sec. 3.3.1 and Sec. 3.3.2, we chose same sized CdS/ZnSe QDs with $r_c = 1.5$ nm and $r_s = 1.5$ nm. The material parameters of such colloidal QDs are given in Sec. 2.1.1.

Compared with the results of the dependence on the distance in Fig. 3.6 and the orientation angles in Fig. 3.9, the interdot monopole-monopole coupling elements are approximately equal while the bandindex induced splitting of the intradot coupling elements is increased. All in all, the physically behavior as well as the general strength of the Coulomb coupling stay constant for both material systems. While the interdot coupling is mostly determined by the dielectric constant of the solvent, the intradot couplings are influenced by the properties of the QDs. Since the material systems differ from each other, the confinement potential is changed and therefore

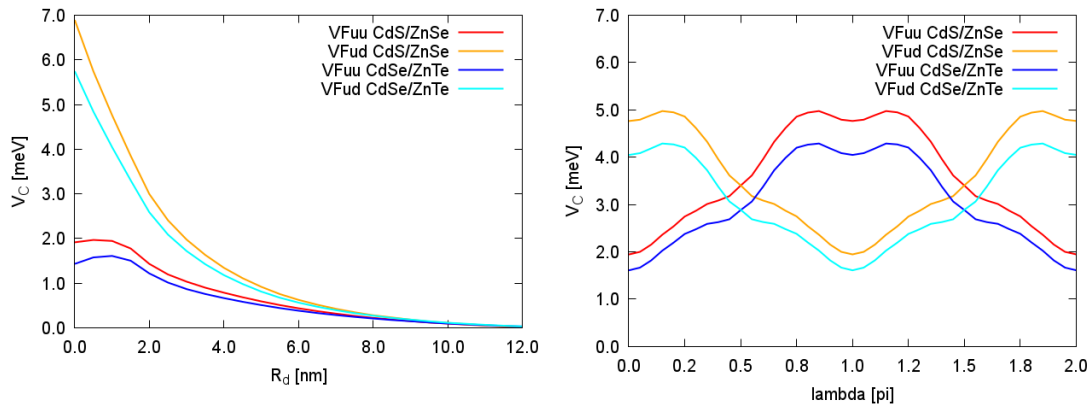


Figure 3.18 Förster elements of colloidal CdS/ZnSe core/shell QDs in comparison to CdSe/ZnTe QDs. The amplitude of the Coulomb coupling is lightly shifted, while the general physical behavior stay equal. Only in the range of small distances between the QDs with $R_d < 2$ nm the influence of the dielectric mismatch plays an important role and thus, the material system changes the curve progression.

the eigenproblem gives other results in the eigenenergies, as introduced in Sec. 2.1.2.

The Förster coupling as an interdot dipole-dipole Coulomb interaction is mostly influenced by the properties of the solvent and the geometry (such as the size of the QDs and the core/shell structure) of the whole system as well as the properties of the microscopic dipole moments. Since all these parameters were put constantly, the material lightly changes the amplitude of the Förster elements. In the range of small distances between the QDs the influence of the QD's dielectric constant, which is determined by the material of the QDs, plays a more important role. Since the material systems show similar properties, the effect in the strength of the Coulomb coupling is very distinct. Other materials showing very different dielectric and confinement properties will stronger influence the Coulomb coupling. Especially, if the relation between the dielectric constant of the solvent and the QDs is changed, as presented in Sec. 3.4.1 or if the size effects in the core/shell structure are varied. This should be analyzed in the following.

For investigating the influence of the QD type, as introduced in Sec. 2.1.2, we calculate the Coulomb coupling elements for two QD systems each with a radius of $r_{\text{QD}} = 3$ nm once as CdSe cores without any shell structure as well as QDs with a CdSe core with $r_c = 1.5$ nm and a ZnTe shell with $r_s = 1.5$ nm. Since the QDs have the same radius, the resulting effects are not introduced by size properties of the QDs but by the dielectric permittivity, cf. Sec. 3.4.1, and the QD types induced by the composition of the core/shell structure. As introduced in Sec. 2.1.2, core/shell QDs can be divided into type-I and type-II QDs [18]. While for type-I QDs, consisting of one material only, the electron and holes are confined in the same volume [68] and form an direct exciton, in type-II core/shell QDs the electrons and holes are separated in the different materials. Since we investigate very small colloidal QDs with well-separated energy levels, the core/shell QDs are defined as quasi type-II QDs showing a partial spatial separation of the electrons and holes. The electron is located at the core material, while the hole is delocalized over the entire volume of the QDs [18]. By varying the thickness of the shell material, a change between the QD types occurs. Thus, the optical and electrical properties of colloidal QDs can be selectively manipulated by changing the relation of the core to shell width influencing the overlap of electron and hole wave functions.

The monopole-monopole intradot coupling elements change their amplitude as well their shifts caused by the bandindex-splitting, as visible in Fig. 3.19. In analogy to the material induced changes in the strength of the Coulomb coupling given in Fig. 3.17, these effects are not

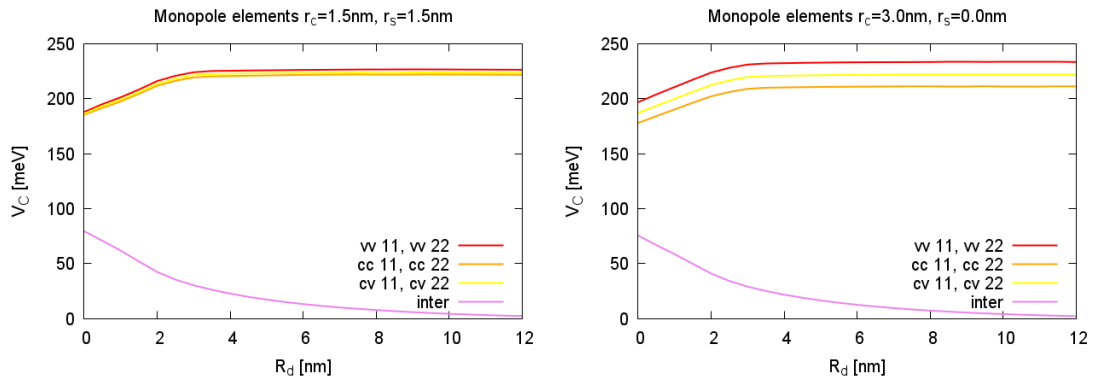


Figure 3.19 The monopole-monopole Coulomb coupling elements of QDs with a radius of $r=3.0$ nm. The first plot shows a core/shell QD structure with $r_c = 1.5$ nm and $r_s = 1.5$ nm. The second plot shows a type-I QD consisting of the core material only.

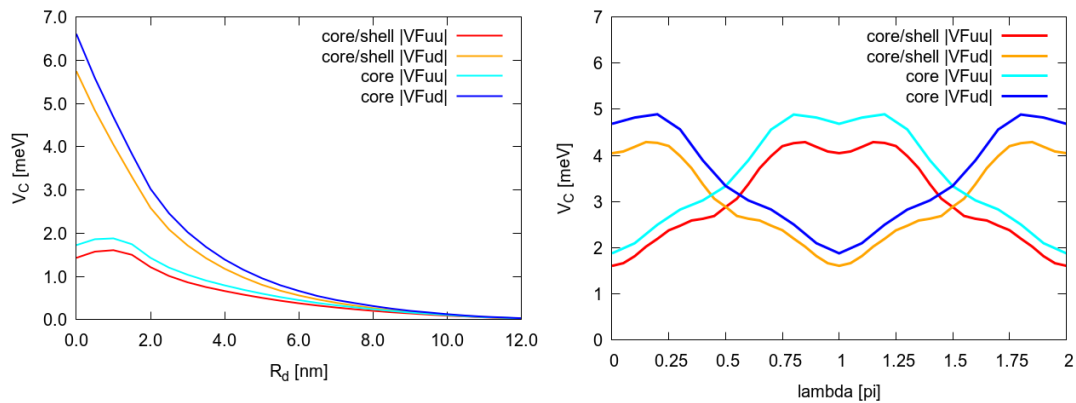


Figure 3.20 The size of the colloidal QD influences the Förster coupling elements. The diagram on the right hand side shows the dipole-dipole Coulomb coupling elements of QD with a radius of $r=3.0$ nm and in contrast of a core/shell QD structure with $r_c = 1.5$ nm and $r_s = 1.5$ nm.

influenced by the size of the QDs but by the dielectric mismatch. Since the core/shell structure changes the material properties and therefore the curve progression in the spatially dependent dielectric function $\varepsilon(\mathbf{r})$, the amplitude of the intradot coupling elements is varied too. The interdot coupling are determined by the properties of the solvent and therefore, they are not appreciable influenced by the QD types.

Fig. 3.20 shows the distance as well as the angular dependence of the Förster elements for a type-I QD (blue) and for a core/shell quasi type-II QD (red) with the same total QD radius. Since the Förster elements as interdot Coulomb interaction are more influenced by the dielectric properties of the solvent then of the QDs, the QD-type lightly changes the strength of the Coulomb coupling. The Förster induced excitation transfer between the QDs plays an important role for small distances between the QDs. Therefore, a variation of the shell thickness simultaneously changing the size of the QDs, determines the strength of the Förster coupling elements. The shell thickness for increasing sized QDs separated the electrons and holes and therefore it reduces the overlap of the electron wave functions. Accordingly, as visible in Fig. 3.21, the Förster elements are strongly influenced by the size and the shell thickness. An increasing shell reduces the influence of the dielectric core/shell mismatched and thus, the curve progression for small distances is changed by the variation of the shell thickness.

In conclusion, we see that the strength of the Coulomb coupling elements is influenced by

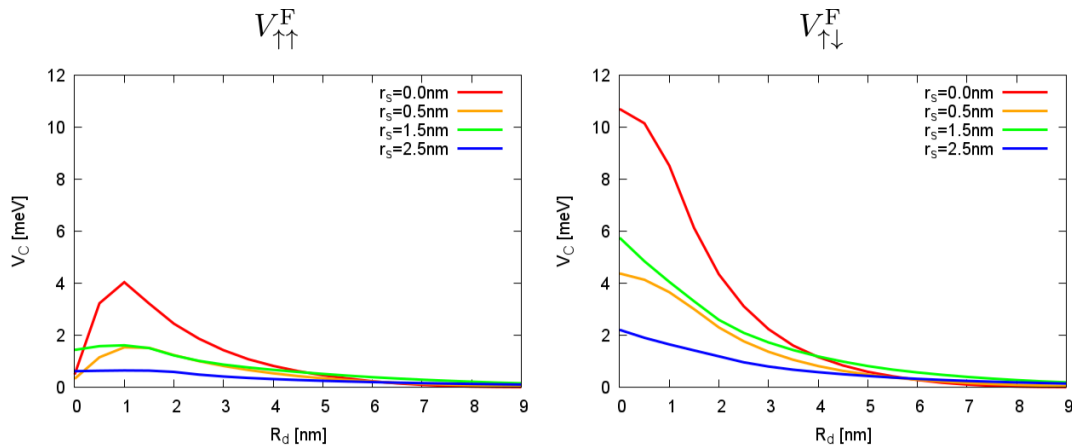


Figure 3.21 Förster coupling elements as a function of the distance between the QDs, calculated for colloidal QDs with the same core ($r_{\text{CdSe}} = 1.5 \text{ nm}$) but a varying shell thickness. The shell thickness as well as the size of the QDs influence the amplitude and the curve progression of the Förster coupling elements. The bigger the shell, the less the influence of the dielectric mismatch on the Förster elements.

many parameters. Especially, the properties of the dielectric environment, induced by the size and the compositions of the colloidal QDs, influences the curve progression as well as the amplitude of the Coulomb elements in the monopole and the dipole case. The Förster coupling as a short range interaction is strongly influenced by the size of the QDs. While the intradot coupling elements are determined by the QD dielectrics, the interdot coupling is mostly influenced by the solvent's dielectric constant, as presented in Sec. 3.4.1. For further investigating the influence of the dielectric environment on the Coulomb coupling elements, we compare the fully calculated spatially dependent dielectric function with a homogeneous environment in the next section.

3.4.3 Homogeneous dielectric environment

Using the PGF method, we have analyzed in the last sections how different material compositions and size effects influence the Coulomb coupling elements due to the resulting complex dielectric function. Since the PGF method naturally includes an arbitrarily complex spatially dependent permittivity, effects caused by a dielectric mismatch can be investigated. Now, we assume the whole dielectric environment to be homogeneous and compare the influence on the Coulomb coupling with the results of the fully calculated spatially dependent dielectric function. The homogeneous dielectric environment combines the properties of the QDs and the surrounding solvent as a kind of a weighted averaged value.

The composition of different materials and a diverse weighting of the dielectric permittivities of the QDs and the surrounding medium results in varying homogeneous environments. Therefore, the Coulomb coupling elements are calculated for different values of the homogeneous dielectric permittivity. Hence, the influence of the dielectric environment on the strength of the Coulomb coupling can be investigated and the results can be compared with the fully calculated coupling elements.

Fig. 3.22 shows the distance dependence of the monopole-monopole intradot and interdot coupling elements for varying homogeneous environments. In a homogeneous environment, there is no dielectric mismatch since the permittivities of the QDs do not differ from the surrounding solvent. Thus, there is no distance dependence in the intradot coupling elements since the environment stays constant for all distances and orientations (see also right hand diagram in Fig. 3.23).

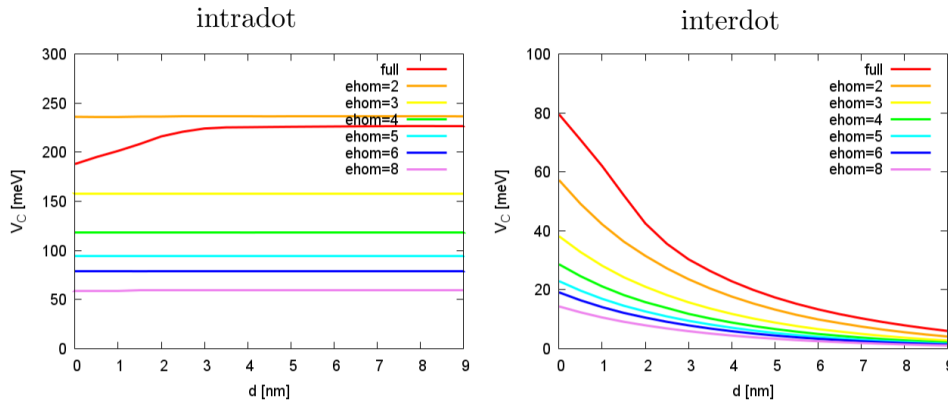


Figure 3.22 Comparison of the fully calculated intradot and interdot monopole-monopole Coulomb coupling elements (red curve) with the coupling resulting from different homogeneous environments. While the fully calculated intradot elements show a distance-dependent shift for a small distance between the QDs, in a homogeneous environment the intradot coupling stays constant. The material properties determine the strength of the monopole-monopole coupling.

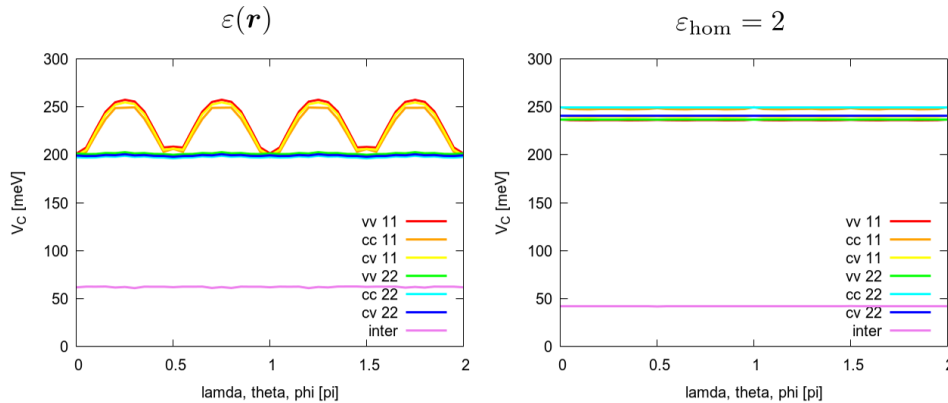


Figure 3.23 Comparison of the rotation of the monopole-monopole Coulomb coupling elements on the left hand with the spatially dependent dielectric function $\varepsilon(\mathbf{r})$ and the right hand with a homogeneous dielectric constant for the whole system with $\varepsilon_{\text{hom}} = 2$. In a homogeneous environment the intradot elements are constant for all angular orientations.

In the case of a homogeneous dielectric environment, the effect of the distance-dependent shifts in the intradot coupling elements for closely arranged QDs vanishes. Nevertheless, the value of the dielectric environment determines the strength of the intradot coupling elements and thus, it induces a constant material specific Coulomb shift. Furthermore, the material influences how fast the interdot monopole-monopole coupling decreases with an increasing distance between the QDs.

A comparison with the Coulomb elements which results from the spatially dependent dielectric function $\varepsilon(\mathbf{r})$ (red curves in Fig. 3.22), indicates that an environment with $\varepsilon_{\text{hom}} = 2$ shows the smallest deviations. For the full calculation the solvent is given by water with $\varepsilon_{\text{sol}} = 1.78$, while the CdSe/ZnTe QDs induces $\varepsilon_{\text{CdSe}} = 6.23$ for the core and $\varepsilon_{\text{CdSe}} = 7.28$ for the shell, cf. Sec. 2.1.1. Thus, the monopole-monopole Coulomb coupling elements seem to be mostly determined by the solvent's permittivity, in the case of a homogeneous permittivity.

In Fig. 3.23 the dependence of the monopole-monopole Coulomb elements on the angular orientation is given for a spatially dependent dielectric function $\varepsilon(\mathbf{r})$ on the left hand side and for a homogeneous dielectric medium characterized by $\varepsilon_{\text{hom}} = 2$ on the right hand side. Since the material system determines the amplitude of the coupling elements, the diagrams show a different

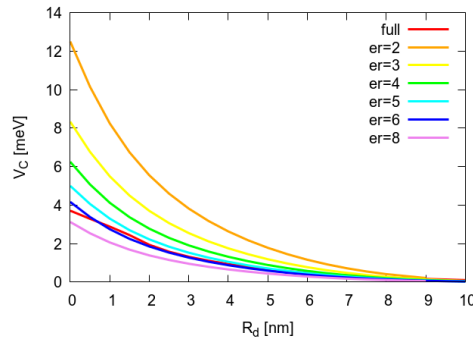


Figure 3.24 Comparison of the fully calculated Förster elements (red curve) with coupling elements resulting from different homogeneous environments. Only for small distances the curve progression of the full calculation differs from the homogeneous case with $\varepsilon_r = 6$. The value of the dielectric environment determines the amplitude of the Förster elements.

Coulomb strength, even in this parameter adapted case. Furthermore, the bandindex induced splitting of the monopole-monopole intradot elements is influenced by the material system. In the case of a homogeneous environment, the shifts caused by the different monopole-monopole elements V_{ii}^{cc} , V_{ii}^{cv} and V_{ii}^{vv} decrease compared to the case of the spatially dependent dielectric function. The main difference is given by the oscillations in the fully calculated case, which are induced by the dielectric mismatch and increased by the inaccuracy of the projection of the continuous rotation on a discrete grid, as discussed in Sec. 2.4.3. Since in a homogeneous medium the permittivity is constant independent from the QD's positioning, effects caused by differences in the dielectric environment vanish.

The Förster dipole-dipole coupling, as interdot excitation transfer between the colloidal QDs, decreases with increasing distance, as visible in Fig. 3.24. Again, all effects caused by a dielectric mismatch, which is induced by the usage of different permittivities and the resulting spatially dependent dielectric function, vanish in the case of a homogeneous environment. Nevertheless, the properties of the homogeneous environment influences the strength of the Coulomb coupling and the distance depending decreasing of the Förster elements. In contrast to the monopole-monopole Coulomb elements in Fig. 3.23, the fully calculated Förster elements can be approached with an homogeneous environment $\varepsilon_{\text{hom}} = 6$. Therefore, the Förster excitation transfer between the QDs is mostly influenced by the properties of the QDs.

In Fig. 3.25, Förster elements calculated with the spatially dependent dielectric function and with the elements in a homogeneous environment with $\varepsilon_{\text{hom}} = 6$ are plotted together. Especially, in the region of small center-to-center distances with $R_d < 2$ nm, the results differ from each other since in this region the dielectric mismatch plays an important role. For bigger distances, the distance dependence of Förster elements in both cases coincides. The curve progression for the angular dipole-dipole orientation is plain for the homogeneous environment and the material induced amplitude is smaller. But, the cosine-like behavior for the spin-splitting and the spin-preserving Förster elements and therefore, the general physical properties are preserved.

In the case a homogeneous dielectric environment, effects caused by the dielectric mismatch, occurring in a spatially dependent permittivity, vanish. Therefore, the fully calculated Coulomb coupling elements show different curve progression if the QDs are arranged close to each other. For an increasing distance, the differences between the fully calculated Coulomb elements and the elements resulting from a homogeneous medium show the same physical properties and very similar dependence on the distance and the angular orientations. Since the monopole-monopole and Förster elements occur on different spatial scales, the dielectric permittivity influencing these

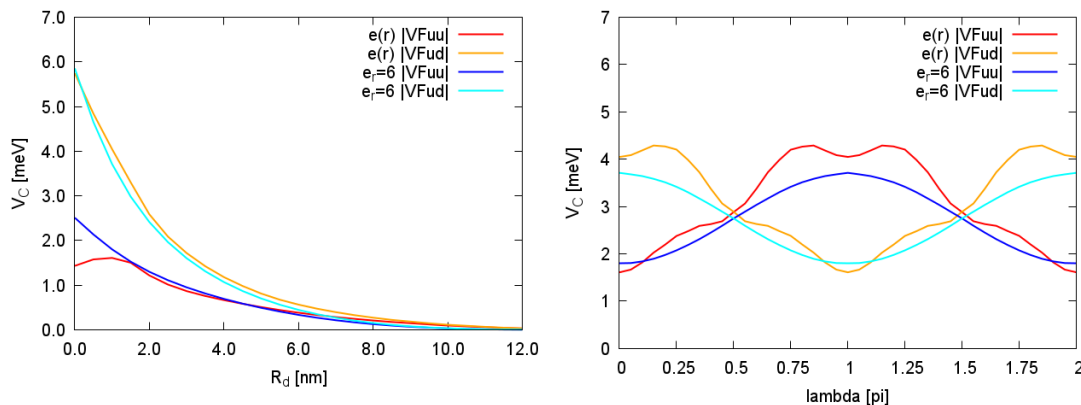
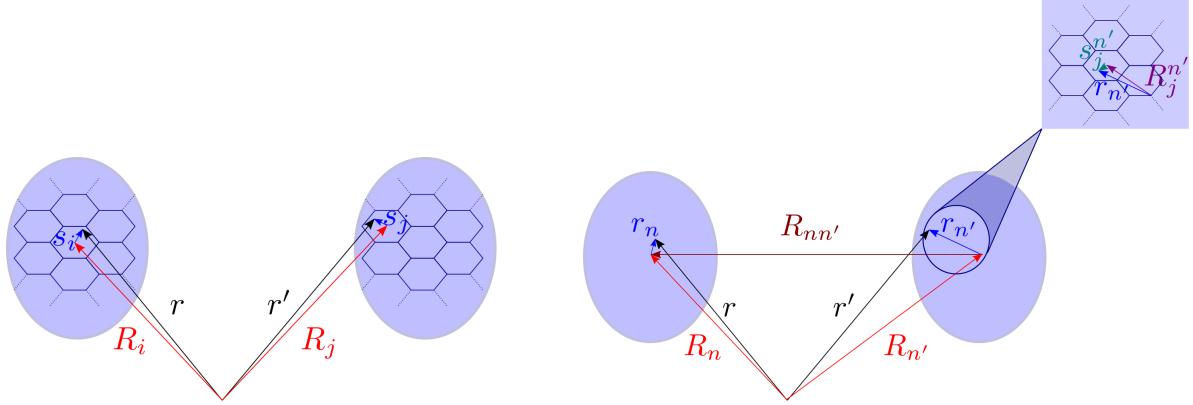


Figure 3.25 Comparison of the distance (left hand side) and orientation (right hand side) dependence of the fully calculated Förster elements with elements in an homogeneous environment with $\epsilon_{\text{hom}} = 6$. The curves resulting from the homogeneous environment are plain and differ in the region of small distances from the results of the full calculation including a spatial-dependent dielectric function $\epsilon(\mathbf{r})$.

coupling elements can be distinguished. While the monopole-monopole Coulomb elements are mostly influenced by the solvent's permittivity, the Förster excitation transfer is influenced by the dielectric properties of the colloidal QDs. For describing the Coulomb coupling elements in a homogeneous environment as adapted as possible to the results from the full calculation, the intradot monopole-monopole shifts are based on a different homogeneous environment than the interdot Förster elements. These coupling mechanisms occur on different energy scales as well as on dividing spatial locations. Thus, a parameter adapted description of the Coulomb coupling with a homogeneous environment greatly determines the physical processes and the strength of the Coulomb coupling if the QDs are not very close to each other (order of the QD radius). In the next section, we will introduce a model for a very fast calculation of the interdot dipole-dipole Coulomb coupling which is based on the parameter adapted description of the Coulomb coupling in a homogeneous medium.

3.5 Point-dipole approximation

The results of the microscopically calculated Coulomb coupling elements in Sec. 3.2 should be compared with an analytical approximation of the Coulomb potential. While the full calculation based on the PGF method [49] naturally includes the influence of an arbitrarily spatially dependent dielectric function $\epsilon(\mathbf{r})$, in an analytic solution the dielectric environment is assumed to be homogeneous over the whole system. Thus, the Green's function for the Coulomb coupling between the two QDs is given by the free space Coulomb potential. To identify the influence of the monopole and dipole terms, analogously to the calculations done in the approach of the PGF method, the Taylor series of the free space Coulomb potential is formulated. Accordingly, the leading terms are calculated influencing the diagonal as well as the off-diagonal elements of the pure electronic Hamiltonian, as introduced in Sec. 2.3. This leads to the often used point-dipole approximation [34, 117] of the interdot dipole-dipole Coulomb coupling. Finally, we compare the results of the point-dipole approximation with the fully calculated Förster elements in the case of an homogeneous environment adapted to the material parameters, as given in Sec. 3.4.3.



(a) A scale separation of the spatial vector \mathbf{r} into the center position of the i th unit cell \mathbf{R}_i and the positioning inside the cell \mathbf{s}_i . The same is done with the second spatial operator \mathbf{r}' for the j th unit cell. The spatial vectors can be located in one QD or separated into both QDs.

(b) Scale separation into the position of the QD's centers \mathbf{R}_n and $\mathbf{R}_{n'}$ and a variation inside the QD \mathbf{r}_n and $\mathbf{r}_{n'}$ respectively. A second scale separation transforms the vector from the QD's center position $\mathbf{r}_{n'}$ into the center position of the j th unit cell \mathbf{R}_j' and a variation inside the unit cell \mathbf{s}_j' .

Figure 3.26 Different separation of the spatial operators \mathbf{r} and \mathbf{r}' , depicted in the case of the inter-QD coupling.

3.5.1 Taylor series of the free space Coulomb potential

For identifying the influence of the monopole-monopole and the dipole-dipole Coulomb coupling separately, the Taylor series of Coulomb Green's function needs to be formulated, as done in Sec. 3.2.1. In a spatially homogeneous medium, the Coulomb interaction is typically represented by the free space Green's function [31, 54]:

$$G(\mathbf{r}, \mathbf{r}') = \frac{qq'}{4\pi\epsilon_0\epsilon_r} \frac{1}{|\mathbf{r} - \mathbf{r}'|}. \quad (3.35)$$

Thus, in a homogeneous medium with ϵ_r determined by the free space Coulomb potential the strength of the Coulomb coupling is given by:

$$V_{1234}^{\text{pd}} = \frac{q_1 q_2 q_3 q_4}{4\pi\epsilon_0\epsilon_r} \int d^3r \int d^3r' \phi_1^*(\mathbf{r}) \phi_2^*(\mathbf{r}') \frac{1}{|\mathbf{r} - \mathbf{r}'|} \phi_3(\mathbf{r}') \phi_4(\mathbf{r}). \quad (3.36)$$

In Sec. 3.4.3, we have calculated, that in the case of a homogeneous medium, the arrangement specific Coulomb coupling is determined by the interdot couplings, since the intradot couplings are constant. Accordingly, the spatial vector can be separated into the center position of the QD \mathbf{R}_n and the innerdot positioning of the charges \mathbf{r}_n resulting in $\mathbf{r} = \mathbf{R}_n + \mathbf{r}_n$, which is schematically illustrated in Fig. 3.26(b). The center-to-center distance vector between the QDs is given by $\mathbf{R}_{nn'} = \mathbf{R}_n - \mathbf{R}_{n'}$. Using this scale separation, the Coulomb coupling elements are:

$$V_{1234}^{\text{pd}} = \frac{q_1 q_2 q_3 q_4}{4\pi\epsilon_0\epsilon_r} \int d^3r_n \int d^3r_{n'} \phi_1^*(\mathbf{r}_n) \phi_2^*(\mathbf{r}_{n'}) \frac{1}{|\mathbf{R}_{nn'} + \mathbf{r}_n - \mathbf{r}_{n'}|} \phi_3(\mathbf{r}_{n'}) \phi_4(\mathbf{r}_n). \quad (3.37)$$

For identifying the terms of the Coulomb potential which are connected with the monopole and dipole coupling, the spatial dependent term of the Green's function is expanded in a multidimensional Taylor series (cf. Eq. (3.14)) for two expansion points given by the interdot positions \mathbf{r}_n and $\mathbf{r}_{n'}$. The related calculations are given in App. B.3. Following the assumption that the interdot charge transitions \mathbf{r}_n and $\mathbf{r}_{n'}$ are small compared to the center-to-center distance between

the QDs $\mathbf{R}_{nn'}$, the Taylor expansion of the free particle Coulomb potential reads

$$\begin{aligned} \mathbb{T} \left(\frac{1}{|\mathbf{R}_{nn'} + \mathbf{r}_n - \mathbf{r}_{n'}|} \right)_{\substack{\mathbf{r}_n = \mathbf{0} \\ \mathbf{r}_{n'} = \mathbf{0}}} &= \frac{1}{|\mathbf{R}_{nn'}|} - \frac{\mathbf{R}_{nn'} \cdot (\mathbf{r}_n - \mathbf{r}_{n'})}{|\mathbf{R}_{nn'}|^3} \\ &+ \frac{\mathbf{r}_n \cdot \mathbf{r}_{n'}}{|\mathbf{R}_{nn'}|^3} - 3 \frac{(\mathbf{r}_{n'} \cdot \mathbf{R}_{nn'}) (\mathbf{R}_{nn'} \cdot \mathbf{r}_n)}{|\mathbf{R}_{nn'}|^5} + \dots \end{aligned} \quad (3.38)$$

The first term gives the monopole-monopole Coulomb coupling, the second term is connected to mixed monopole-dipole couplings and the last two terms determine the dipole-dipole coupling. Terms of higher order are not explicitly included here, but can be added if needed. This will be done in Sec. 3.5.3 for quadrupole-quadrupole corrections terms. Now, the Taylor series can be used to calculate the strength of the interdot Coulomb coupling in Eq. (3.37).

3.5.2 Coulomb coupling approximation

For evaluating the integrals in Eq. (3.37) to calculate the Coulomb coupling between two colloidal QDs in a homogeneous medium, the wave functions are written as a product of an envelope function $\xi(\mathbf{r}_n)$ and a lattice periodic Bloch part $u(\mathbf{r}_n)$, as introduced in Eq. (2.15). Thus, the spatial operator \mathbf{r}_n , located inside the n th QD, is separated into \mathbf{R}_i^n as a vector from the QD's center position \mathbf{R}_n to the center position of the i th unit cell and \mathbf{s}_i^n as a variation inside the unit cell: $\mathbf{r}_n = \mathbf{R}_i^n + \mathbf{s}_i^n$, cf. small picture in Fig. 3.26(b). Using the periodicity of the Bloch functions $u(\mathbf{R}_i^n + \mathbf{s}_i^n) = u(\mathbf{s}_i^n)$ and the assumption that the envelope function is nearly constant on the size of the unit cell $\xi(\mathbf{R}_i^n + \mathbf{s}_i^n) \approx \xi(\mathbf{R}_i^n)$, the terms are analogously evaluated as done in Eq. (3.13). For convenience, an overlap integral including the envelope functions is introduced as a scaling factor [59]:

$$O_{ll'}^n = \int d^3 \tilde{\mathbf{r}}_n \xi_l^*(\tilde{\mathbf{r}}_n) \xi_{l'}(\tilde{\mathbf{r}}_n). \quad (3.39)$$

The first term of the Taylor expansion in Eq. (3.38) gives the point-like monopole-monopole coupling at the QD's center positions using the normalized condition of the Bloch functions in Eq. (3.17):

$$V_{1234}^{\text{pd-mm}}(\mathbf{R}_n, \mathbf{R}_{n'}) = \frac{q_{14} q_{23} O_{14}^n O_{23}^{n'}}{4\pi \epsilon_0 \epsilon_r |\mathbf{R}_{nn'}|} \delta_{14} \delta_{23}. \quad (3.40)$$

An evaluation of the Kronecker-deltas, together with the connected charges of the electrons $q = e$ and of the holes $q = -e$, results in a vanishing monopole-monopole coupling term, since there are equally numbered positive and negative terms. Furthermore, mixed terms connected to a monopole-dipole coupling (second term in Eq. (3.38)) are neglected, since they equal zero in an usually used rotating wave approximation. Therefore, this interdot approximation of the Coulomb coupling in a homogeneous medium is determined in the first order by the dipole-dipole interaction, given by the last two terms in the Taylor series in Eq. (3.38). To get the Coulomb interaction in the point-dipole approximation, the two dipole-dipole terms need to be evaluated. Thus, the scale separation into the QD's center position, the variation over the unit cells, and the product ansatz of the wave functions are applied on the first dipole-dipole term in Eq. (3.38), which results in:

$$\begin{aligned} V_{1234}^{\text{pd-1}} &= \sum_{i,j} \frac{q_{14} q_{23} \xi_1^*(\mathbf{R}_i^n) \xi_2^*(\mathbf{R}_j^{n'}) \xi_3(\mathbf{R}_j^{n'}) \xi_4(\mathbf{R}_i^n)}{4\pi \epsilon_0 \epsilon_r} \int d^3 r_i^n \int d^3 r_j^{n'} \\ &\cdot u_1^*(\mathbf{s}_i^n) u_2^*(\mathbf{s}_j^{n'}) \left(\frac{\mathbf{R}_i^n \cdot \mathbf{R}_j^{n'}}{|\mathbf{R}_{nn'}|^3} + \frac{(\mathbf{R}_i^n \cdot \mathbf{s}_j^{n'}) + (\mathbf{s}_i^n \cdot \mathbf{R}_j^{n'})}{|\mathbf{R}_{nn'}|^3} + \frac{\mathbf{s}_i^n \cdot \mathbf{s}_j^{n'}}{|\mathbf{R}_{nn'}|^3} \right) u_3(\mathbf{s}_j^{n'}) u_4(\mathbf{s}_i^n). \end{aligned} \quad (3.41)$$

Analogously, the second dipole-dipole term gives

$$V_{1234}^{\text{pd-2}} = \sum_{i,j} \frac{qq'\xi_1^*(\mathbf{R}_i^n)\xi_2^*(\mathbf{R}_j^{n'})\xi_3(\mathbf{R}_j^{n'})\xi_4(\mathbf{R}_i^n)}{4\pi\epsilon_0\epsilon_r} \cdot \int d^3r_i^n \int d^3r_j^{n'} u_1^*(\mathbf{s}_i^n)u_2^*(\mathbf{s}_j^{n'}) \left(\frac{(\mathbf{R}_{nn'} \cdot (\mathbf{R}_i^n + \mathbf{s}_i^n))(\mathbf{R}_{nn'} \cdot (\mathbf{R}_j^{n'} + \mathbf{s}_j^{n'}))}{|\mathbf{R}_{nn'}|^5} \right) u_3(\mathbf{s}_j^{n'})u_4(\mathbf{s}_i^n). \quad (3.42)$$

Now, the summation of the unit cells is transformed into an integration, as is done in Eq. (3.19). The concerning calculations are given in App.B.3.1. In analogy to the definition of the microscopic transition dipole moment in Eq. (3.41), a macroscopic dipole moment, dependent on the envelope functions, is introduced:

$$\mathbf{D}_{ll'}^n = \int d^3\tilde{r}_n \xi_l^*(\tilde{r}_n)\tilde{r}_n \xi_{l'}(\tilde{r}_n). \quad (3.43)$$

An evaluation of the Kronecker deltas resulting from the normalization condition of the Bloch function introduced in Eq. (3.17), conducts equal envelope functions in the macroscopic dipole moments in Eq. (3.43) with $\mathbf{D}_{ll'}^n$. Such macroscopic dipole moment is introduced as a statical dipole moment, since the bandindex does not change and is no dynamical transitions occurs. The squared absolute values of the envelope functions ξ_l , which give the electron probability densities, represents a symmetric function in each Cartesian direction, whereas the spatial vector \tilde{r} is anti-symmetric. Thus, the product of both factors represents an anti-symmetric function. Accordingly, the integral of the statical macroscopic dipole moments, including the spatial vector with the QD's center position \mathbf{R}_n as the origin, should vanish:

$$\mathbf{D}_{ll}^n = \int_{-r_{\text{QD}}}^{r_{\text{QD}}} d^3\tilde{r} |\xi_l(\tilde{r})|^2 \tilde{r} = 0. \quad (3.44)$$

Hence, all dipole terms including the statical macroscopic dipole-dipole moments \mathbf{D}_{ll}^n with equal envelope functions vanish due to the Bloch normalize condition. An explicit calculation of the resulting terms is given in the appendix in App.B.3.1. Accordingly, terms only consisting dynamical dipole transitions $\boldsymbol{\mu}_{ij}^n$ preserve and thus, they determine the strength in the point-dipole Coulomb coupling as follows:

$$V_{1234}^{\text{pd}} = \frac{q_{14}q_{23}O_{14}^n O_{23}^{n'}}{4\pi\epsilon_0\epsilon_r} \left(\frac{\boldsymbol{\mu}_{14}^n \cdot \boldsymbol{\mu}_{23}^{n'}}{|\mathbf{R}_{nn'}|^3} - 3 \frac{(\mathbf{R}_{nn'} \cdot \boldsymbol{\mu}_{14}^n)(\mathbf{R}_{nn'} \cdot \boldsymbol{\mu}_{23}^{n'})}{|\mathbf{R}_{nn'}|^5} \right). \quad (3.45)$$

This interdot Coulomb coupling resulting from the point-like dipole approximation includes the center-to-center distance vector between the two QDs $\mathbf{R}_{nn'}$ as well as the microscopic transition dipole moments of the QDs $\boldsymbol{\mu}_{14}^n$ and $\boldsymbol{\mu}_{23}^{n'}$. The resulting approximated Coulomb coupling of the free space Coulomb potential in the dipole-dipole order does not include monopole moments. Accordingly, in the point-like dipole approximation the strength of the Coulomb coupling is determined in the first leading order by the dipole-dipole interaction.

Even in this approximation, the Coulomb coupling is determined by the distance between the QDs as well as their relative dipole-dipole orientation given by the microscopic dipole moments. A calculation of the Coulomb coupling of two colloidal QDs in the point-dipole approximation, assuming a homogeneous environment, is given in Sec. 3.5.4. Furthermore, the projection of the dipole moments regarding the distance vector influences the strength of the Coulomb coupling in the point-dipole approximation. The scaling factor defined in Eq. (3.39) does not depend on

the distance and orientations of the colloidal QDs to each other. Therefore, the approximative calculation of the Coulomb coupling in Eq. (3.45) is very fast since no step-wise evaluations of position dependent integrals are required. Hence, if the dielectric environment can be assumed to be homogeneous, the approximation represents a very efficient way to calculate a high number of orientation dependent interdot dipole-dipole Coulomb coupling elements. Since the distances between the QDs are very small or the influence of a spatially dependent dielectric function or surface charge effects play an important role, we have to go beyond the point-dipole form of Eq. (3.45), as is done in Refs. [4, 41, 62]. Especially, if an arbitrary spatially dependent dielectric function $\epsilon(\mathbf{r})$ needs to be included, the PGF method introduced in Sec. 3.1 represents a promising approach for reducing the numerical effort in the fully calculation of the Coulomb coupling elements.

3.5.3 Statical macroscopic quadrupole-quadrupole correction terms

Since for the statical macroscopic dipole moment D_{ll}^n all terms equals zero, the quadrupole terms are calculated finding the first leading non-vanishing terms for the statical case. As calculated in Sec. 2.3, the dipole-dipole coupling induces off-diagonal elements in the pure electronic Hamiltonian $H_{el} = H_0 + H_C$ in the exciton base, while the monopole-monopole terms give the diagonal elements. Since in the point-dipole approximation all monopole terms, as well as all statical dipole terms equal zero, we have to go to the second order in both spatial arguments in the Taylor series of the free particle Coulomb potential in Eq. (3.35). Accordingly, in the Taylor expansion Eq. (3.38) the quadrupole-quadrupole terms are added to get the first non-vanishing order in the diagonal elements. But only the statical terms are taken into account, since they determine the diagonal elements of the Hamiltonian, while the dynamical terms induce off-diagonal elements. Mixed terms in the Taylor series, like monopole-quadrupole and dipole-quadrupole terms are generally neglected, since they usually vanish in a rotating wave approximation. The terms of the Taylor expansion which are connected with the quadrupole-quadrupole coupling include the second order in both expansion points. In App. B.3.2 the Taylor series respecting only the statical terms of the quadrupole-quadrupole interaction is calculated.

Following the calculations done for the point-like dipole terms in Sec. 3.5.2, a scale separation concerning the QD center-to-center position illustrated in Fig. 3.26(b) and the envelope function approximation are used. Then, only the statical terms without any dynamical transition moments are considered. Since the lower ordered mixed terms of statical D_{ll}^n and dynamical transitions vanish and the dynamical transitions are described by the point-like dipole-dipole approximation, only the statistical term of the Coulomb coupling elements is transformed to the quadrupole-quadrupole order. The terms and the results of the calculation are given in App. B.3.2.

Now, analog to the definition of the macroscopic dipole moment in Eq. (3.43), a macroscopic quadrupole moment is introduced:

$$Q_{ij}^{ll'} = \int d^3\tilde{r} \tilde{\xi}_l^*(\tilde{\mathbf{r}}) (3\tilde{r}_i \tilde{r}_j - \tilde{\mathbf{r}}^2 \delta_{ij}) \xi_{l'}(\tilde{\mathbf{r}}). \quad (3.46)$$

Using the definition of the macroscopic dipole moment and collecting all terms resulting from the statical quadrupole-quadrupole terms of the Taylor series, the statical quadrupole-quadrupole Coulomb interaction in a point-like approximation results in:

$$V_{1234}^{qqstatic} = \frac{q_{14}q_{23}}{16\pi\epsilon_0\epsilon_r} \sum_{ijk} \left(\frac{Q_{ij}^{14}Q_{ij}^{23}}{|\mathbf{R}|^5} + 4 \frac{R_i Q_{ij}^{14} Q_{jk}^{23} R_k}{|\mathbf{R}|^7} - 2 \frac{m^{14}m^{23}}{|\mathbf{R}|^5} - 3 \frac{M_{ij}^{14}M_{ij}^{23}}{|\mathbf{R}|^5} - 24 \frac{R_i M_{ij}^{14} M_{jk}^{23} R_k}{|\mathbf{R}|^7} + 105 \sum_l \frac{R_i R_j M_{ij}^{23} M_{kl}^{14} R_k R_l}{|\mathbf{R}|^9} \right) \delta_{14}^{\lambda n \sigma} \delta_{23}^{\lambda n \sigma}. \quad (3.47)$$

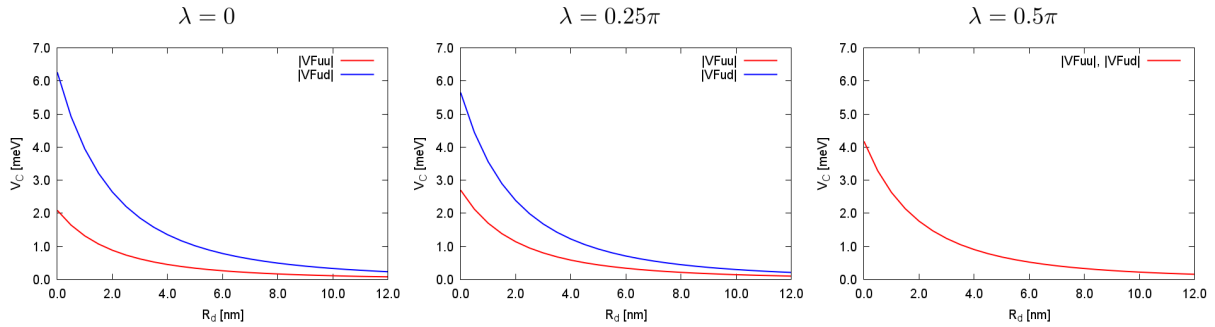


Figure 3.27 The Förster coupling elements calculated in the point-dipole approximation as a function of the distance R_d between the QDs in three different fixed angular orientations of the moving QD. With increasing distance between the colloidal QDs the strength of the Förster coupling decreases in all three cases. In the first two dipole orientations, the Förster elements show a spin splitting, which is degenerated in the case of an relative angle of $\lambda = 0.5\pi$.

Note, that the equation includes correction terms to the quadrupole-quadrupole coupling, introduced as a scalar term for the diagonal elements:

$$m^{ll'} = \int d^3\tilde{r} \tilde{\xi}_l^*(\tilde{\mathbf{r}}) \tilde{\mathbf{r}}^2 \xi_{l'}(\tilde{\mathbf{r}}_n), \quad (3.48)$$

and a tensor term

$$M_{ij}^{ll'} = \int d^3\tilde{r} \tilde{\xi}_l^*(\tilde{\mathbf{r}}) \tilde{r}_i \tilde{r}_j \xi_{l'}(\tilde{\mathbf{r}}_n). \quad (3.49)$$

Thus, the first non-vanishing order of the interdot diagonal elements of the Coulomb coupling in the point-like approximation is given by the statical quadrupole-quadrupole coupling, together with correction terms to the quadrupole-quadrupole coupling.

3.5.4 Förster elements in the point-dipole approximation

In this section, the results of the point-like Coulomb coupling should be compared with the fully calculated Förster elements calculated in Sec. 3.3. Therefore, the distance dependence of the Coulomb elements on the distance as well as on the dipole-dipole orientation are calculated using the model of the point-dipole approximation. To get a similar parameter set-up, same sized colloidal QDs are arranged in the same initial positions as used in Sec. 3.3. Since the point-dipole approximation gives in the leading order the dipole-dipole Coulomb coupling, the results are compared with the Förster elements. In Sec. 3.4.3 was shown how the dipole-dipole elements in a homogeneous environment can be adapted to the Coulomb elements resulting from the calculation including a complex spatially dependent permittivity. Thus, for adapting the values of the dipole-dipole coupling, the homogeneous environment is characterized by $\varepsilon_{\text{hom}} = 6$.

Comparing the results of Fig. 3.27 and Fig. 3.28 for the point-dipole model with the fully calculated Förster elements in Fig. 3.7 and Fig. 3.11, we see that the parameter adapted model describes the arrangement specific properties of the Coulomb dipole-dipole elements very well. The strength of the Coulomb coupling as well as the physical characteristics are generally identical. As interdot coupling, the Coulomb elements calculated in the dipole approximation decrease with increasing distance between the colloidal QDs. Furthermore, the spin-splitting in spin-preserving $V_{\uparrow\uparrow}$ and spin-flipping $V_{\uparrow\downarrow}$ Förster elements occurs even in the formalism of the point-dipole approximation. Since the relative orientations of the dipole moments to each other determine the Coulomb coupling in the point-dipole approximation, cf. Eq. (3.45), the strength

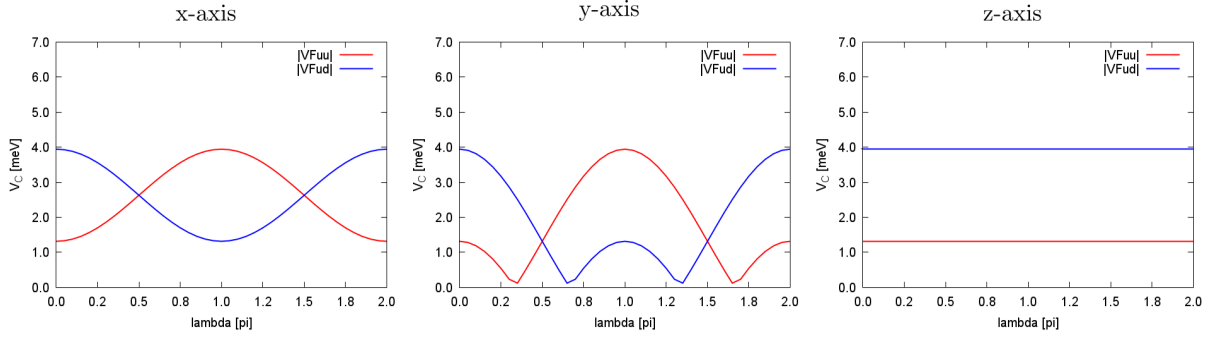


Figure 3.28 The Förster elements in the point-dipole approximation as a function of the rotation of one QD around the three Cartesian axis in a distance of $R_d = 1$ nm. The coupling elements are spin-selective and can be divided into spin-preserving (VFuu) and spin-splitting (VFud) elements. The rotation around the x-axis and the y-axis are given by a cosine function, while the rotation around the z-axis does not influence the Förster elements.

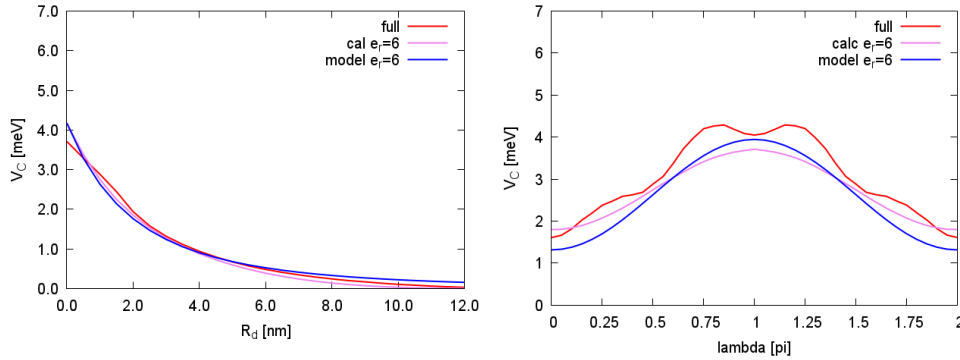


Figure 3.29 Comparison of the fully calculated Förster elements, the calculated elements in an homogeneous environment of $\epsilon_{\text{hom}} = 6$ and the elements resulting from the point-dipole approximation.

of the coupling is strongly influenced by the relative angular orientation of the QDs to each other. For the rotation of one QD around the x-axis and the y-axis, the Förster elements show a cosine-like curve progression. Rotations around the z-axis do not influence the Coulomb strength, since the microscopic QDs are orientated along the crystal c-axis coinciding with the cartesian z-axis.

For a direct comparison, of the Förster coupling elements, in Fig. 3.29 the results of the full calculation in a spatially dependent dielectric permittivity as well as the results from a homogeneous dielectric environment and the dipole-approximation are plotted together. Differences in the three models for the calculation of the Coulomb coupling are small. Due to the adaption of the parameters to the full calculated Coulomb coupling, the amplitude as well as the physical properties are determined very well with the point-dipole approximation. Only in the case of very small distances between the QDs differences in the three models occur. Due to effects caused by the dielectric mismatch can not be described following the approach of the point-dipole approximation. Since the derivation of the approximation includes, that the distance between the QDs needs to be bigger than the intradot charge transitions (cf. Sec. 3.5.1), the results of the model are only valid for not too small distances between the QDs (the distance should be bigger than the range of the QD's radius).

In conclusion, it was shown, that the point-dipole approximation reproduces very well the results of the Förster coupling elements, particularly if the parameters are adapted to the results of full calculation. But if the QDs are arranged in a very short distance to each other or if surface charges or other effects caused by dielectric mismatches should be investigated, we have to go

beyond the point-dipole approximation. Especially, if effects caused by a spatially dependent dielectric function are included or if a high number of coupling elements occur, the PGF method presents a good approach for the full calculation of the Coulomb coupling. Furthermore, since the monopole-monopole terms equal zero in the point-dipole approximation, material specific shifts caused by the intradot coupling elements are not included in the model of the dipole approximation and need to be added by other calculations. Since in a homogeneous medium the intradot monopole-monopole elements are constant, they can be simply included as constant shifts in the calculation of the Coulomb coupling.

3.6 Conclusion

A numerical method, based on a Green's function representation of the solution of a generalized Poisson equation, was presented to calculate Coulomb coupling elements efficiently by decreasing the number of integrals in the two-particle Coulomb interaction. The PGF method [49] (©2016 American Physical Society) can be applied to a broad range of applications, since the method is not restricted to specific symmetries of the potential or the wave functions. Furthermore, a spatially inhomogeneous dielectric function can be included by using the solution of a generalized Poisson equation. Thus, the influence of a medium and e.g., surface charge effects can be included.

Though, the presented method does not prevent the application of commonly used simplifications. In case of radial symmetry, the reduction of the computational time can be huge, since only an one dimensional differential equation and one spatial integral need to be calculated. Accordingly, the Poisson Green's function method presents a general approach to increase the computational efficiency in numerical calculations of Coulomb coupling elements.

The strength of the formalism was demonstrated, particularly with regard to the calculation of a high number of Coulomb coupling elements, by using the method for the calculation of the spatially dependent Coulomb coupling between colloidal QDs moving in the solvent. By expanding the Green's function of two Coulomb coupled QDs in a Taylor series, an identification of terms connected to the monopole-monopole and the dipole-dipole interaction is possible without using an explicit analytic form of the Green's function. Since the PGF method enables a fast numerical calculation of Coulomb coupling elements to be done, the influence of the spatial arrangement of the colloidal QDs was analyzed systematically. This includes variations in the distance between the two colloidal QDs as well as changes in their relative dipole-dipole orientation to each other. Both influences the strength of the Coulomb coupling. Furthermore, since the PGF method naturally includes an arbitrarily complex spatially dependent dielectric function, the influence of the dielectric environment on the Coulomb coupling elements was investigated. Thus, it was shown, that the solvent's permittivity as well as the material compositions and the size of the QDs determine the strength of the Coulomb coupling. The results were compared with calculations done for a homogeneous environment.

Finally, the fully calculated Förster elements following the approach of the PGF method were compared with a point-dipole approximation for the interdot dipole-dipole Coulomb coupling. It was demonstrated, that the dipole approximation reproduces the results concerning the strength of the Coulomb coupling and the physical characteristics very well. Particularly, if the free parameters are adapted to the values of the calculations following the approach of the PGF method, the results match together. But, if the QDs are arranged very close to each other or if effects caused by a dielectric mismatch need to be respected, we have to go beyond the point-dipole approximation. Nevertheless, the point-dipole approximation represents a very fast method for the calculation of the Coulomb coupling, since no integrals need to be evaluated. Therefore, if the motion of the colloidal QDs induces a huge number of spatially dependent coupling elements, as in the case of the Brownian motion of colloidal QDs, the point-dipole approximation enables the

calculations to be done fast and efficiently.

Chapter 4

Arrangement dependent signatures in two dimensional spectra

The multidimensional optical coherent spectroscopy represents a powerful tool for the visualization of couplings between nanostructures [1]. While linear spectroscopy indirectly provides information on the electronic populations [118], the signatures in the two dimensional (2d) spectroscopy are directly correlated to coupling processes and induced excitation energies. Therefore, multidimensional spectroscopy represents a possibility to get structural information on complex systems, since coupling processes can be observed directly [79]. Thus, coherent multidimensional spectroscopy provides information on complex many-body interactions [118] and it enables deeper insights into the mechanism of excited state processes [119].

Recent developments concerning the formalism of optical coherent spectroscopy, such as the ultrashort laser technologies, enables the extension of spectroscopic methods and measurements to be done continuously [119, 120]. Since changes in the couplings between multiple emitters become visible with a femtosecond time resolution [119] the method of the two dimensional spectroscopy can be applied to a wide range of applications [118]. This includes the example of biological systems [20, 21] as well as researches on semiconductor nanostructures [1, 4, 118].

In this chapter, the characteristic optical signatures of diffusing QDs in different spatial arrangements and with varying orientations are calculated. Since the signatures in the 2d spectra are directly related to the coupling processes, an analysis of the spectroscopic signatures represents a possibility of visualizing and analyzing the interplay between the spatial positions of the colloidal QDs and the resulting strength of the Coulomb coupling. Thus, the formalism of the multidimensional coherent spectroscopic can be used as an method of analyzing the interplay between the motion and the related Coulomb coupling of the colloidal QDs. A further investigation of the Brownian motion of colloidal QDs and the resulting averaged signatures will be given in Chap. 5.

Here, first the double quantum coherence spectroscopy (DQCS) is introduced. Therefore, the sequence of exciting pulses in the heterodyne detections is visualized by Feynman diagrams [2] and the signal giving the 2d spectra is determined. Then, the DQCS resulting from a full calculation of the Coulomb coupling elements based on the PGF method, which was introduced in Sec. 3.1, are calculated including the influence of a spatially dependent dielectric function. The results are compared with the spectroscopic signatures based on the point-dipole approximation given in Sec. 3.5. The influence of the spatial positions as well as the angular orientations of the colloidal QDs on the signatures in the DQCS is investigated. Furthermore, the dependence of the signatures on the polarization of the exciting pulses and on the dephasing rate is introduced.

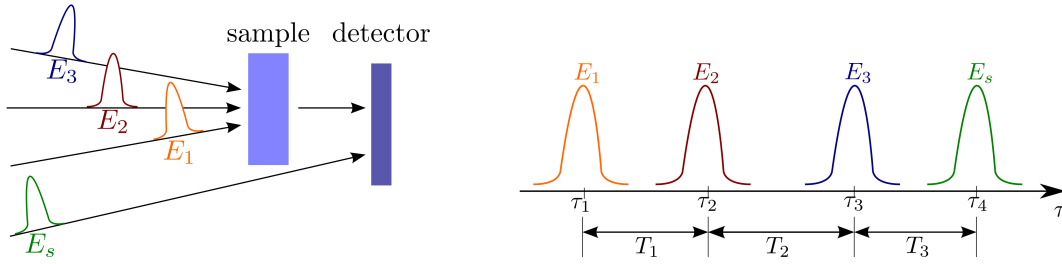


Figure 4.1 Sequence of four well separated pulses in the approach of the heterodyne detection. Three pulses interact with the sample, while the fourth pulse is used for detecting the emitted field via interference. The time intervals between the pulses determine the spectroscopic signal. Thus, the signal can be tuned by varying the time intervals T_i .

4.1 Double quantum coherence spectroscopy

In contrast to linear spectroscopy, shortly introduced in App. C, couplings of the individual transitions directly determine the signatures in the multidimensional coherent spectroscopy [1]. Correlations between excitons can be directly observed, which is impossible in the linear spectroscopy [80]. Therefore, multidimensional spectroscopy represents a powerful tool for the visualization and investigation of the interdot and the intradot couplings as well as the excitation energy transfer between the nanostructures. Thus, in this section, we introduce the DQCS for identifying effects of the Coulomb coupling between colloidal QDs on optical excited excitons and biexcitons [16]. Firstly, the heterodyne detection for getting the spectroscopic signatures is introduced. Then, Feynman diagrams are used to graphically illustrate the interaction processes resulting from the exciting laser pulses. Finally, the related signal determining the DQCS is defined.

4.1.1 Heterodyne detection

Due to developments in the ultrashort laser technologies, measurements based on multidimensional coherent spectroscopy [79] become possible. The detection, which occurs either phase sensitive (heterodyne) or phase insensitive (homodyne) [118], is based on a sequence of four temporally well separated laser pulses, as schematically depicted in Fig. 4.1. Thus, the multidimensional spectroscopy, as a kind of a nonlinear four-wave mixing technique [121], is given by the mixing of multiple electromagnetic excitation fields in the sample [1]. Since in the heterodyne detection the amplitude and the phase of the electric field are measured, the sequence of the excitation pulses must have well-defined wave vectors or phases [2]. Thus, it requires a precise tuning of multiple laser pulses. While the first three pulses interact with the sample, the fourth pulse, as a reference pulse, interferes with the transmitted intensity and the resulting field is detected [1]. The fixed relation of the wave vectors of the pulse sequence defines the 2d spectra technique. The resulting quantum pathways, which can be illustrated using specific Feynman diagrams [2], cf. Sec. 4.1.2, are distinguished by the combination of the wave vector and the time-ordering selection of the pulses [79].

The optical electric field is composed of the three excitation pulses [2]:

$$\mathbf{E}(\mathbf{r}, t) = \sum_{j=1}^3 \sum_{u_j=\pm 1} \mathbf{E}_j^{u_j}(\mathbf{r}, t - \tau_j) e^{iu_j(\tilde{\mathbf{k}}_j - \omega_j(t - \tau_j))}. \quad (4.1)$$

Here, $\mathbf{E}_j^{u_j}$ denotes the envelope of the j th pulse, while the factor $u_j = \pm 1$ gives the positive or rather negative frequency components of the optical field with $\mathbf{E}_j^{-1} = (\mathbf{E}_j^{+1})^*$. The variable $\tilde{\mathbf{k}}_j$

gives either the wave vector product $\tilde{k}_j = \mathbf{k}_j \cdot \mathbf{r}$ or the phase $\tilde{k}_j = \varphi_j$ of the j th pulse depending on the detection mechanism and the experimental set-up. The total signal is determined by the combination of the wave vectors or phases: $k_s = u_1 k_1 + u_2 k_2 + u_3 k_3$.

In the heterodyne detection, a reference pulse interferes with the transmitted intensity and the resulting field is detected. For the signatures in the DQCS, which provide information on the singly and the doubly excited states, the reference pulse for detecting the emitted field is given by the following relation between the exciting pulses: $k_s = k_1 + k_2 - k_3$ [121]. Note, that the variable k_i denotes either the phase φ_i or the wave vector \mathbf{k}_i of the i th pulse. The pulse sequence, which perturbs the equilibrium of the QD electrons, enables an observation of the electronic correlations to be done during the time intervals between the pulses [2]. Thus, in experimental set-ups, the signature is varied by time delays [118].

The resulting spectroscopic signal, as a scalar product of the induced third order polarization $\mathbf{P}_{k_s}^{(3)}(t)$ with the electric detection field, is determined by the time intervals between the well separated pulses of the sequence, cf. Fig. 4.1:

$$S(T_3, T_2, T_1) = \int_{-\infty}^{\infty} dt \mathbf{P}_{k_s}^{(3)}(t) \cdot \mathbf{E}_s^*(t - \tau_s) e^{i\omega_s(t - \tau_s)}. \quad (4.2)$$

The third-order polarization $\mathbf{P}_{k_s}^{(3)}(t)$ in the direction k_s is related to a combined third-order response function of the colloidal QDs [121]. This response function is given by a sum of combinations of the four time correlation functions of the dipole operator [4] according to the two contributing Liouville pathways [2], which will be introduced in the following section. Transforming the time intervals between the pulses into the Fourier domain gives the signatures in the 2d spectra. In this thesis, the first and second time intervals T_1 and T_2 are transformed into the Fourier domain. Thus, caused by the specific phase matching of the DQCS, the spectroscopic signatures are directly determined by the single exciton states $|e\rangle$ and biexciton states $|f\rangle$ [122]. A calculation of the signal according to the phase matching is given in the following section.

4.1.2 Feynman diagrams and spectroscopic signatures

The Coulomb coupling creates excitons as delocalized collective electronic excitations of coupled QDs [79]. Caused by the off-diagonal dipole-dipole Coulomb coupling, different QD states are coupled to each other. Therefore, the resulting exciton states are delocalized over the whole system and can not be identified with local QD states. Accordingly, due to the Coulomb coupling between two colloidal QDs new delocalized exciton states $|e\rangle$ and double exciton states $|f\rangle$ occur. The resulting three band model, which consists of the ground state and the delocalized exciton states, was introduced in Sec. 2.3. The delocalized exciton states represent the eigenstates of the pure electronic Hamiltonian $H_{el} = H_0 + H_C$ [4], and thus, they directly include effects caused by the Coulomb coupling.

In the DQCS, multiple time-ordered ultrashort laser pulses induce coherences between the ground state, the singly excited states and the doubly excited exciton states [119]. Thus, the exciton and the biexciton energies are directly accessible [80]. Therefore, by determining the resulting combined third order response function, the optical signatures of colloidal QDs in varying spatial arrangements are calculated. These characteristic signatures in the 2d spectra enable the visualization of the interplay between the spatial-dependent Coulomb coupling and the QD arrangements. The contributions of the signal, given in Eq. (4.2), can be represented by two double-sided Feynman diagrams [2], as schematically depicted in Fig. 4.2

An analysis of the Feynman paths given in Fig. 4.2 provides information on the correlated induced excitation energies [118]. The vertical lines in the Feynman diagrams represent the ket

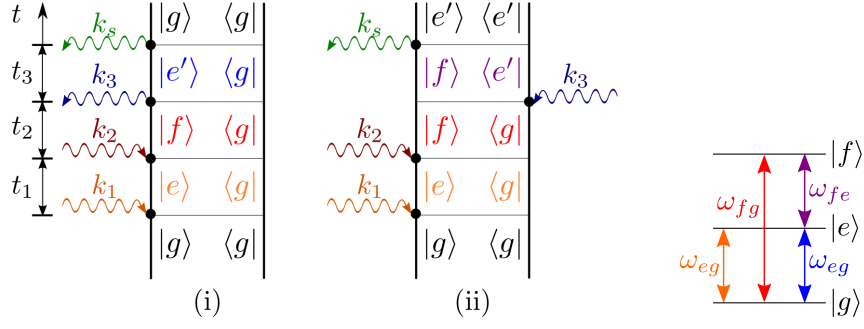


Figure 4.2 Feynman diagrams and level schema of the exciton states of DQCS due to the phase matching $k_s = k_1 + k_2 - k_3$: In both paths, the first pulse k_1 induces a coherence between the ground state $|g\rangle$ and a single exciton state $|e\rangle$, evolving for a time t_1 . k_2 creates a coherence between a double exciton state $|f\rangle$ and the ground state $|g\rangle$. After a time t_2 , the third pulse k_3 creates in (i) a coherence between the ground state $|g\rangle$ and a single exciton state $|e'\rangle$ and in (ii) a coherence between single $|e'\rangle$ and double exciton state $|f\rangle$ [123]. The fourth pulse, used for the detection, gives the signal.

and the bra of the density matrix [118]. The time evolution goes from the bottom to the top and at the beginning of each time interval a pulse induces a new state (illustrated by the curly arrows). In both Feynman contributions, the first pulse with k_1 creates a single exciton $|e\rangle$ to ground state $|g\rangle$ coherence during the first time interval t_1 . The second pulse k_2 , showing the same phase direction, induces a coherence between the doubly excited state $|f\rangle$ and the ground state $|g\rangle$. Thus, in both Feynman contributions, the system shows coherent superpositions between the single exciton or rather the biexciton state and the ground state [122]. Therefore, this spectroscopy is called double quantum coherence. The third pulse with k_3 creates the system state either to the ground state to exciton coherence (Fig. 4.2 (i)) or to a coherence between the single- and biexciton states (Fig. 4.2 (ii)). The fourth pulse k_s is used for receiving the signal in the heterodyne detection. The final states of the density matrix are given by the ground state in the first Feynman contribution (Fig. 4.2 (i)) and an exciton state in the second Feynman path (Fig. 4.2 (ii)).

Under the assumption of well separated pulses [2], the signal in Eq. (4.2) is transformed into the Fourier domain for the first and the second time arguments T_1 and T_2 , while the third time interval T_3 is fixed [4]. During these time intervals, coherences between the ground state to the exciton state and between the biexciton to ground state are induced, giving the spectroscopy its name. Thus, the signal of the DQCS can be expressed as a function of the frequencies of the excitations Ω_1 and Ω_2 , which are related to the exciton and biexciton energies. The total signal of the two contributing Feynman pathways, illustrated in Fig. 4.2, is given by a summation of the signatures of the two quantum paths: $S(T_3, \Omega_2, \Omega_1) = S_{(i)}(T_3, \Omega_2, \Omega_1) + S_{(ii)}(T_3, \Omega_2, \Omega_1)$. The two contributing signatures which results from the two Feynman pathways reads

$$S_{(i)}(T_3, \Omega_2, \Omega_1) = -\frac{i}{\hbar^3} \sum_{ee'f} (\mathbf{d}_{fe'}^* \cdot \mathbf{E}_s^*(\omega_{fe'} - \omega_s)) (\mathbf{d}_{e'g}^* \cdot \mathbf{E}_3^*(\omega_{e'g} - \omega_3) e^{-i\xi_{fe'} T_3}) \cdot \frac{\mathbf{d}_{fe} \cdot \mathbf{E}_2(\omega_{fe} - \omega_2)}{\Omega_2 - \xi_{fg}} \frac{\mathbf{d}_{eg} \cdot \mathbf{E}_1(\omega_{eg} - \omega_1)}{\Omega_1 - \xi_{eg}} \quad \text{and} \quad (4.3)$$

$$S_{(ii)}(T_3, \Omega_2, \Omega_1) = \frac{i}{\hbar^3} \sum_{ee'f} (\mathbf{d}_{e'g}^* \cdot \mathbf{E}_s^*(\omega_{e'g} - \omega_s)) (\mathbf{d}_{fe'}^* \cdot \mathbf{E}_3^*(\omega_{fe'} - \omega_3) e^{-i\xi_{e'g} T_3}) \cdot \frac{\mathbf{d}_{fe} \cdot \mathbf{E}_2(\omega_{fe} - \omega_2)}{\Omega_2 - \xi_{fg}} \frac{\mathbf{d}_{eg} \cdot \mathbf{E}_1(\omega_{eg} - \omega_1)}{\Omega_1 - \xi_{eg}}. \quad (4.4)$$

Here, the complex transition frequencies $\xi_{ij} = \omega_{ij} - i\gamma_{ij}$ are introduced including the resonance frequencies $\omega_{ij} = \omega_i - \omega_j$ and a dephasing rate γ_{ij} as homogeneous broadening of the transition from j to i . In the low temperature limit, the dephasing rate for colloidal CdSe QDs is around 1 meV [124]. For higher temperatures around $T = 300$ K, which are needed for describing the Brownian motion of colloidal QDs in water, as will be done in Chap. 5, the dephasing rate is higher and will be assumed as 10 meV [125]. Assuming that the laser pulses with a circular polarization p are very short and thus, show a narrow band width in the frequency domain, the amplitude function of the optical field is set to one $E_i(\omega) = 1$ resulting in $\mathbf{E}_i(\omega) = \mathbf{e}_p$ with $p \in \{l, r\}$. Thus, regarding the circular polarization the excitation pulses are divided into the left polarization with $\mathbf{e}_l = \frac{1}{\sqrt{2}}(\mathbf{e}_x - \mathbf{e}_y)$ and the right polarization with $\mathbf{e}_r = \frac{1}{\sqrt{2}}(\mathbf{e}_x + \mathbf{e}_y)$.

The dipole transitions in Eq. (4.3) and Eq. (4.4) with $\mathbf{d}_{ij}^* = \mathbf{d}_{ji}$ are written in the basis of the delocalized exciton states, representing the eigenstates of the pure electronic part of the Hamiltonian $H_{el} = H_0 + H_C$. The transformation of the dipole operator into the delocalized exciton basis is given in Sec. 2.3.3. In the exciton basis, the macroscopic dipole operator, which is determined by the microscopic interband transition dipole moments $\boldsymbol{\mu}_{cv}^{n\sigma}$ and $\boldsymbol{\mu}_{vc}^{n\sigma}$ defined in Eq. (2.18), includes transitions from the ground state to an exciton state $\mathbf{d}_{ge} = \langle g|\mathbf{d}|e\rangle$ as well as transitions between exciton and double exciton states $\mathbf{d}_{ef} = \langle e|\mathbf{d}|f\rangle$, which are derived in Sec. 2.3.3.

The calculation of the signal functions for the contributing Feynman pathways in Eq. 4.3 and Eq. 4.4 allowed the signatures in DQCS, which depend on the Fourier transformed pulse delays, to be retrieved. The resulting signal is determined by the laser pulses with the frequency Ω_1 for the exciton resonances and with Ω_2 for the double exciton resonances. The technique of the DQCS can be used for visualizing coupling processes. Since the signals resulting from the two Feynman pathways given in Eq. (4.3) and Eq. (4.4) are equal in the case of an uncorrelated system [122], the coupling dependent signatures vanish [79]. Thus, in the next sections, the influence of the spatial-dependent Coulomb coupling on the signatures in the 2d spectra should be investigated.

4.2 Fully calculated 2d spectra with a spatially dependent the dielectric permittivity

For investigating the fingerprints of the distance and orientation dependent Coulomb coupling, the spectroscopic signatures in the DQCS are calculated. The diffusion of the colloidal QDs in the solvent results in frequently changing QD's arrangements. Since the strength of the Coulomb coupling is influenced by the arrangement of the QDs relative to each other, different spatial positions and angular orientations result in specific signatures in the 2d spectra. Therefore, the signatures in the DQCS, directly influenced by the coupling processes, represent a possibility of visualizing the interplay between the Coulomb coupling and the motion of the colloidal QDs.

In this section, the characteristic spectroscopic signatures in the 2d spectra are analyzed in dependence to their specific QD arrangement. To include the influence of the spatially dependent dielectric permittivity, the Coulomb coupling elements are fully calculated using PGF method, which was introduced in Sec. 3.1. Accordingly, the spectroscopic signatures in the DQCS are calculated for different spatial arrangements of the colloidal QD. Finally, the influence of the QD size as well as the material composition concerning the core/shell structure on the spectra is investigated.

4.2.1 Signatures depending on the QD arrangements

Each spatial QD arrangement, including the transversal positions as well as the angular dipole-dipole orientation, influences the strength of the Coulomb coupling, as calculated in detail in Sec. 3.3. For the calculations of the spatial dependent Coulomb coupling of two colloidal QDs with varying spatial positions, the PGF method is used, cf. Sec. 3.1. This enables the influence of the distances between the CdSe/ZnTe QDs in water and their angular orientation to be visualized by the connected signatures in the 2d spectra. Furthermore, the influence of the spatial dependent dielectric environment $\varepsilon(\mathbf{r})$ is directly included in the approach of the PGF method [49].

The signals in the DQCS, given in Eq. (4.3) and Eq. (4.4), are determined by the laser pulses with the frequency Ω_1 and Ω_2 . Thus, the signatures show single exciton resonances along the Ω_1 axis and biexciton resonances along the Ω_2 axis. Accordingly, the position of the signal in the DQCS indicates the energy of the involved transitions between the ground and the exciton states on the $E_e = \hbar\Omega_1$ -axis and between the ground and the biexciton states on the $E_f = \hbar\Omega_2$ -axis. Therefore, the 2d spectra provide information on the involved delocalized single exciton states and biexcitons states. The color coding used in the 2d spectra indicates the signal strength. In the 2d spectra, transitions of the unperturbed states appear as diagonal peaks, while the coupling induces off-diagonal features [1]. To balance the weak and the strong features in the DQCS, a nonlinear scale is chosen: $S_{nl} = \text{arsinh}(|S(T_3, \Omega_2, \Omega_1)|/N)$ including a normalization constant N [1].

For investigating the influence of the spatial dependent Coulomb coupling of the colloidal QDs in the DQCS, the spectroscopic signatures of different QD arrangements are calculated. Since the Coulomb coupling depends on the distance between the QDs as well as on their relative dipole-dipole orientation, calculated in Sec. 3.3, the DQCS show characteristic signature depending on the relative positions of the two colloidal QDs in water.

Fig. 4.3 shows the DQCS of the two Coulomb coupled QDs in three different distances R_d and two relative angular orientations, resulting from the rotation around the x-axis, respectively. In order to get the spectroscopic signatures, the QDs are excited with the circular polarized pulse sequence of $\mathbf{e}_l \mathbf{e}_r \mathbf{e}_l \mathbf{e}_r$. An analysis of the influence of the excitation direction on the 2d spectra is given in Sec. 4.3.3. The blue dots in the spectra mark all possible exciton energies resulting from the specific position of the two QDs. As introduced in Sec. 2.3, these exciton eigenenergies result from the diagonalization of the Coulomb Hamiltonian, and hence, account for the influence of the dipole-dipole Coulomb coupling. As visible in the spectra in Fig. 4.3 not all possible resonances occur in the signal, since not all transitions are optically allowed [122]. The polarization sequence together with the relative dipole-dipole orientation of the QDs regarding the excitation direction determines which exciton energies are excited and which Förster induced signatures occur.

The spectra in Fig. 4.3 show signatures along the cross diagonal through the exciton and the corresponding double exciton energy (dotted line), which is connected with the energies of the unperturbed QDs. For small distances between the QDs, the connected peaks are slightly shifted by the Coulomb interaction. Additionally, off-diagonal peaks occur induced by the dipole-dipole Coulomb coupling between the two colloidal QDs. The independent transitions only occur as diagonal elements, whereas the coupled transitions are represented as off-diagonal elements and therefore, they evoke cross peaks [1]. Hence, for the small distance of $d = 1$ nm between the QDs, where the influence of the Coulomb coupling is very high, the signatures are clearly separated into different exciton and double exciton peaks. With increasing distance, the strength of the Coulomb coupling decreases until the peaks shift together and the spectroscopic signatures coincide along the cross diagonal for big QD distances. Since the QDs are identical, only one exciton peak remains for big distances. The double excitons can be separated into both QDs as well as located in one QD as a biexciton [79]. Therefore, for big distances two double exciton energies occur.

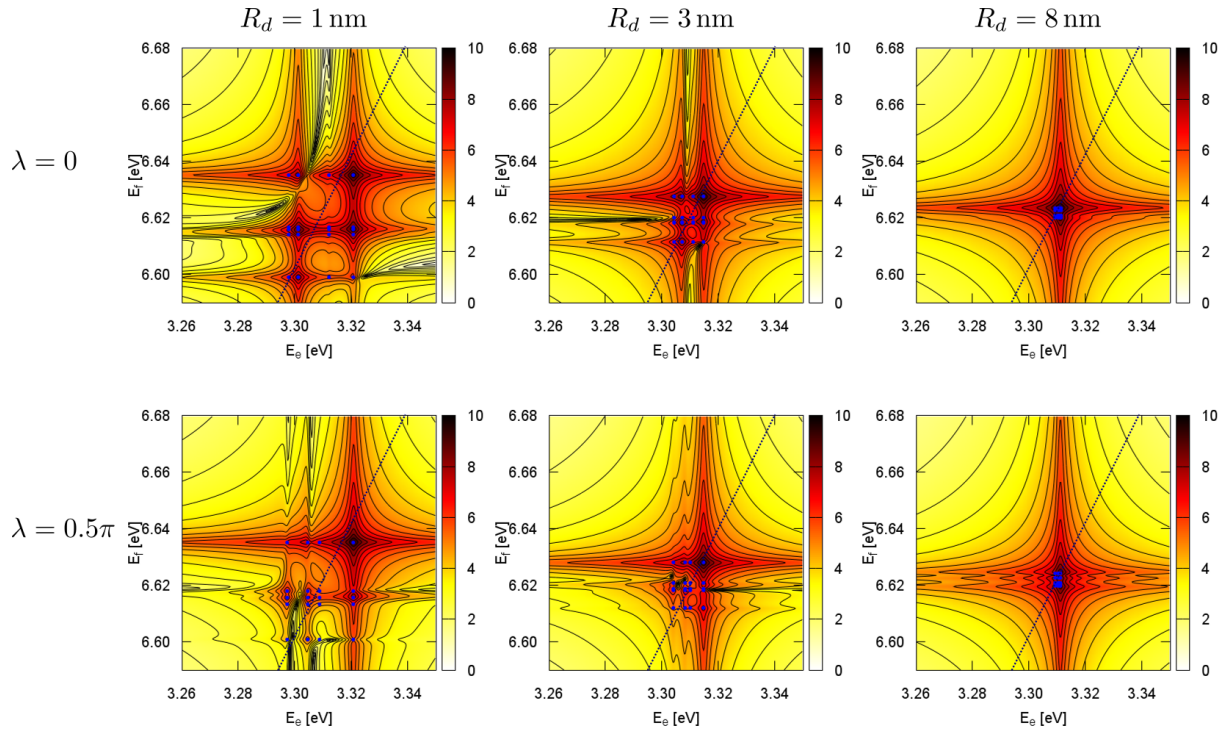


Figure 4.3 The DQCS for three different distances R_d between the QDs and two relative orientations respectively: $\lambda = 0$ as parallel orientation and $\lambda = 0.5\pi$ as orthogonal orientation resulting from a rotation around the x-axis. The blue dots mark the possible exciton eigenenergies and the dotted line gives the cross diagonal along the unperturbed exciton energies. The signatures in the 2d spectra are strongly influenced by the relative QD positions. The varying angular orientation together with the excitation direction determine which of the eigenenergies are excited and thus induce spectroscopic signatures. For the small distance of $d = 1$ nm between the QDs, the signatures are clearly separated due to the high influence of the Coulomb coupling. With increasing distance, the strength of the Coulomb coupling decreases and therefore, the peaks shift together and coincide for big distances between the QDs.

In contrast, for small distances R_d between the two colloidal QDs, the DQCS in Fig. 4.3 show specific energy shifts and signatures concerning the angular orientation given by the rotation angle λ around the spatial x-axis. This is induced by the dipole-dipole Förster coupling between the nanostructures, calculated in Sec. 3.3, which depends on the relative dipole orientation of the QDs to each other. Due to the spin selective Förster induced excitation transfer, the hybridization of the local exciton states changes with the angular orientation of the colloidal QDs. Therefore, the 2d optical spectra show characteristic peaks for the different QD arrangements. These peaks will show up corresponding to splittings between various levels. Therefore, the DQCS provides information on the electron correlations sensitive even for weak couplings [122].

Due to the spin selective coupling, the fully calculated DQCS in Fig. 4.3 show separated peaks for small distances between the colloidal QDs. In the case of parallel orientated dipole operators with $\lambda = 0$, the spin preserving as well as the spin flipping occurs strongly shifted from each other. In contrast, in the case of perpendicularly orientated QDs with $\lambda = 0.5\pi$, the spin flipping and spin preserving Förster elements are shifted relative to each other and thus they are nearly degenerated. For increasing distance R_d between the QDs, the Förster induced splitting of the signatures in the DQCS vanishes, since the Förster interaction decreases. Since terms of the monopole-monopole intradot coupling are also included, the shifts and peak positions are not only influenced by the interdot coupling. Accordingly, in the DQCS for big distances between the nanostructures one exciton and two double exciton peaks remain determined by the intradot coupling elements.

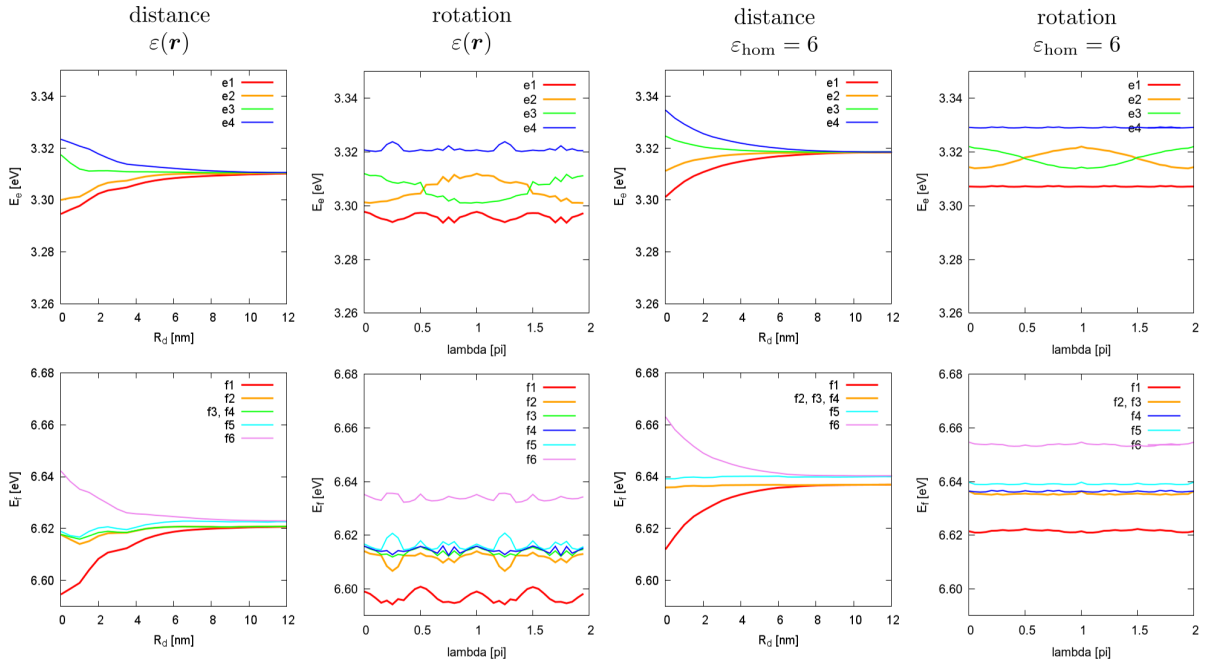


Figure 4.4 Exciton energies as functions of the distance between the QDs and their relative dipole-dipole orientation as a result of the rotation around the x-axis. At the top the exciton energies are given, while at the bottom the double exciton energies are depicted. The two left hand side columns are calculated in a spatial dependent dielectric environment $\varepsilon(\mathbf{r})$ and the two diagrams on the right hand side give the results in a homogeneous dielectric environment with $\varepsilon_{\text{hom}} = 6$. The general physical behavior concerning the variations caused by the QD arrangements is equal in both cases. The exciton energies decrease for increasing distance, but the saturation value resulting from the constant monopole-monopole intradot shifts differs in both cases. For small distances the influence of the dielectric mismatches for $\varepsilon(\mathbf{r})$ induces aberrations from a smooth curve progression that can be observed in the case of $\varepsilon_{\text{hom}} = 6$. Additionally, effects caused by errors resulting from the rotation on a discrete grid occur.

To determine the shift in the DQCS qualitatively, in Fig. 4.4 the exciton energies are calculated as a function of the distance between the QDs as well as a function of the angular orientation concerning the rotation around the x-axis. On the left hand side the diagrams show the exciton energies for a full evaluation of the Coulomb coupling in a scheme of a spatial dependent dielectric permittivity, characterized with $\varepsilon(\mathbf{r})$. In contrast, the diagrams on the right hand side are calculated assuming a homogeneous dielectric environment with $\varepsilon_{\text{hom}} = 6$.

The diagrams in Fig. 4.4 show, that all exciton shifts (at the top) and two of the double exciton shifts (at the bottom) decrease with increasing distance between the QDs analogously to the interdot Coulomb coupling as calculated in Sec. 3.3. The constant double exciton shifts are determined by the material specific intradot coupling. Since the two colloidal QDs consist of the same materials and have the same size, only one exciton peak remains for big distances, determined by the intradot monopole-monopole Coulomb coupling. Due to the fact that the composed double exciton can be located in one QD or separated into both QDs, for the double exciton two peaks occur for big distances, energetically shifted by the biexciton energy.

In the region of small distances the influence of the dielectric permittivity, discussed in Sec. 3.4, causes a dielectric mismatch, mirror charges and a screening of the Coulomb energy. Thus, the exciton energies from the fully calculated Coulomb coupling show aberrations from a smooth curve progression, in contrast to the curves resulting from calculations done in a homogeneous environment. Furthermore, particularly in the curves giving the dependence on the angular orientations, effects and errors resulting from the description on a discrete grid occur, as mentioned in Sec. 2.4.3. Since the calculations for the varying angular orientation are done in the fixed small distance of $R_d = 1$ nm, the aberrations are distinct. Generally, the physical behavior of the exciton energies concerning the variation of the spatial and angular orientations is equal in particular for big distances between the QDs. For comparing the corresponding spectroscopic signatures, the DQCS in an homogeneous dielectric environment with $\varepsilon_{\text{hom}} = 6$ are calculated for the same spatial arrangements as used in Fig. 4.3.

The 2d spectra given in Fig. 4.5 for the different QD arrangements in the homogeneous dielectric environment show, analogously to the DQCS in Fig. 4.3, that the shifts decrease and thus, the peaks coincide for an increasing distance. The angular orientation determines which peaks are excited in the spectra. Since the influence of the spatial dependent dielectric permittivity only plays an important role for small distances between the QDs, in these cases the resulting signatures in the DQCS differ from each other. The effect is more distinct in the case of parallel orientated QDs with $\lambda = 0$ due to the Förster coupling being spin separated.

The value of the homogeneous dielectric environment ε_{hom} determines the strength of the Coulomb coupling because of the screening effects. Furthermore, the permittivity determines the constant monopole-monopole intradot coupling, as presented in Sec. 3.4.3. Since the constant value of the dielectric environment changes, all signatures are shifted in the 2d spectra. Accordingly, the homogeneous dielectric environment with $\varepsilon_{\text{hom}} = 6$ is chosen as an adaption to the results of the full calculation, cf. Sec. 3.4.3. Since the values are adapted to the interdot coupling and not to the intradot coupling, for big distances a shift of the saturation values occurs. In the model of the point-dipole approximation, which will be analyzed in the following in Sec. 4.3, the interdot and intradot couplings are independently adjusted to the results of the full calculation of the Coulomb coupling, since they occur on different energetic scales and spatial positions.

In summary, it can be confirmed, that the signatures of this two dimensional spectroscopy are determined by the Coulomb interaction between the nanostructures, which is characteristically influenced by the QD spatial positioning. Accordingly, in the DQCS of two Coulomb coupled colloidal QDs, the QD arrangements show characteristic optical signatures for varying QD distances and relative spatial orientations. Since the strength of the Coulomb coupling,

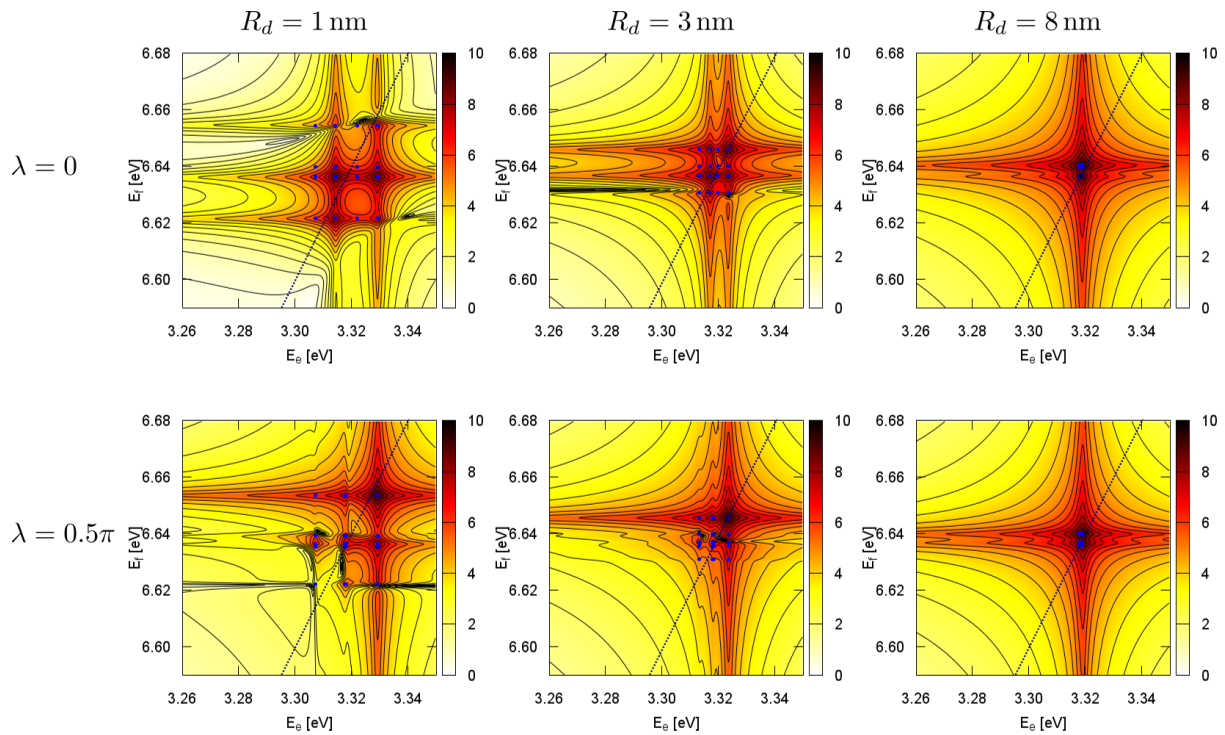


Figure 4.5 DQCS for three different QD's distances and two angular orientations calculated for a homogeneous dielectric environment with $\epsilon_{\text{hom}} = 6$. For small distances in dependence on the angular orientation, diagonal and off-diagonal peaks occur shifted by the Coulomb coupling. For an increasing distance the shifts decrease and the peaks coincide to one exciton and two biexciton peaks.

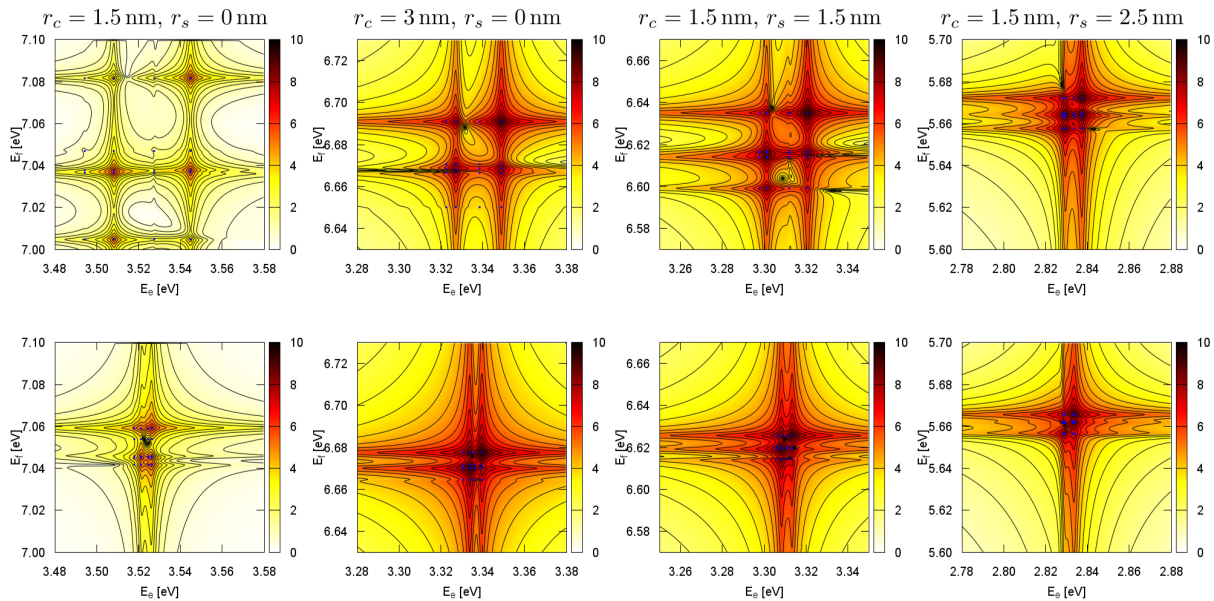


Figure 4.6 DQCS depending on QD sizes and core/shell structures for two different distances between the QDs: $R_d = 1$ nm at the top and $R_d = 4$ nm at the bottom. The two spectra on the left hand side are calculated for QDs without a shell ($r_s = 0$) for differently sized QDs with $r_c = 1.5$ nm and $r_c = 3$ nm. The Coulomb shifts and induced peaks are strongly influenced by the size of the QDs. The two spectra in the middle result from equally sized QDs with and without a core/shell structure. The exciton energies and the Coulomb induced shifts are smaller if a core/shell structure is used. The two spectra on the right hand side demonstrate the influence of a growing shell which comes along with a growing QD size. In this case, even for the small distance between the QDs (top) the Coulomb induced shifts are small and the signatures are only lightly separated compared to the other QD structures.

which determines the signatures in the DQCS, is not only influenced by the QD arrangements and the dielectric environment, as discussed in Sec. 3.4, in the following the effects of a variation of the size of the colloidal QDs and the core/shell structure is investigated.

4.2.2 Variation of size and shape of the colloidal QDs

The strength of the Coulomb coupling between two colloidal QDs diffusing in water is not only influenced by the spatial QD arrangement but also by the material properties and the size of the QDs, as calculated in Sec. 3.4.2. Therefore, in this section the influence of the QD size and the composition of their core/shell structure on the spectroscopic signatures in the DQCS is investigated.

Thus, the 2d spectra of different sized but still small colloidal QDs, since the other parameters are assumed to be fixed, are calculated. Furthermore, the signatures of same sized QDs with and without a core/shell structure are investigated. For combining the influence of the distance between the QDs and effects caused by the size and the material composition, the spectra are evaluated for the small distance of $R_d = 1$ nm and the bigger distance of $R_d = 4$ nm.

As the DQCS in Fig. 4.6 show, Coulomb induced shifts as well as the peak positions are influenced by the size of the QDs and the core/shell structure. As observed in the previous section, the Coulomb coupling is strongly influenced by the center-to-center distance between the QDs and a growing size implies that the center-to-center distances increases even for a constant distance R_d between the QDs. The bigger the QD the smaller the influence of the interdot Coulomb coupling. Particularly for small QDs as (depicted on the left hand side of Fig. 4.6),

caused by the strong distance depending strength of the Coulomb coupling, the signatures in the 2d spectra show Coulomb induced signatures and strongly shifted peaks. For small QDs the exciton energies are higher. Furthermore, the influence of the dielectric mismatches is increased caused by the changes in the value of the dielectric permittivity. For an increasing QD size, the Coulomb induced shifts as well as the exciton energies decrease.

The spatial dielectric permittivity $\varepsilon(\mathbf{r})$ is determined by the QD's position, the size, the material composition, and the core/shell structure. Thus, in particular for small distances, the effects caused by the changes in the dielectric environment influence the signatures in the 2d spectra, as visible in Fig. 4.6. This includes the strength of the Coulomb coupling, resulting in specific shifts of the peaks in the spectra, as well as the intradot coupling, which determines the general position of the signatures in the spectra concerning the exciton and biexciton energies. Especially the positions of the peaks for big distances between the QDs are given by the constant monopole-monopole intradot coupling, which is determined by the dielectric environment (cf. Sec. 3.4).

The relation of the core to shell thickness determines where the charge carriers in the QDs are located and whether a separation of the charge carriers occurs resulting in a strong decreasing of the overlap of the electron and hole wave functions, as it was introduced in Sec. 2.1.2. Thus, comparing the two signatures resulting from same sized QDs in the middle of Fig. 4.6, the exciton energies as well as the shifts in same sized QDs are decreased if a core/shell structure occurs.

The two DQCS spectra on the right hand side of Fig. 4.6 are calculated for colloidal QDs with the same core radius but with a varying shell thickness. For an increasing shell thickness, which equally increases the size of the colloidal QD, the Coulomb induced shifts as well as the exciton energies further decrease. Thus, even for the small distance between the colloidal QDs at the top of the figure, the Coulomb induced shifts are small and with increasing distance the signatures resulting from the interdot coupling coincide fast.

The optical signatures in the DQCS are strongly influenced by the spatial arrangement of the colloidal QDs relative to each other. Since the material composition as well as the size of the QDs determine the eigenenergies and the dielectric environment, the peak positions and the occurring shifts are also influenced by these parameters. Accordingly, the 2d spectra provide information on the size and the materials of the colloidal QDs. Generally, the influence of the QD arrangement is visible for all material systems but if the QDs are big the influence of the interdot Coulomb coupling on the spectroscopic signatures vanishes.

4.3 2d spectra based on the point-dipole approximation

The point-dipole approximation represents a good approximation for the interdot Coulomb coupling if the distances between the QDs are not smaller than their radius, as introduced in Sec. 3.5. In particular, if a huge number of coupling elements needs to be calculated resulting from the motion of the colloidal QDs, the point-dipole approximation enables the calculations to be done very fast. In the following, the spectroscopic signatures in DQCS, determined by the QD arrangements, are calculated based on the Coulomb coupling in the formalism of the point-dipole approximation.

In Sec. 4.2.1 arrangement dependent signatures generated by a full calculation of the Coulomb coupling, are analyzed in the DQCS. This includes the interdot as well as the intradot coupling elements and the influence of a spatial dependent dielectric permittivity. In this section, the results are compared with the optical signatures in DQCS which are based on the interdot Coulomb coupling in the point-dipole approximation adapted to the results of the full calculation, as introduced in Sec. 3.5. Furthermore, the influence of the different rotations around the cartesian axis and the direction of the circular polarized laser pulses are investigated. Finally, the influ-

ence of the temperature depending dephasing rate on the spectroscopic signatures is calculated. Particularly for the Brownian motion which will be analyzed in the following chapter Chap. 5, a description based on the diffusion of the colloidal QDs in water at room temperature is required.

4.3.1 Comparison with the fully calculated signatures

The calculations of the interdot Förster coupling elements in the formalism of the point-dipole approximation, done in Sec. 3.5, demonstrated that the model describes very well the physical behavior as well as the strength of the Coulomb coupling. The dependence on the distances between the QDs and the relative dipole-dipole orientations can be represented by the results of the point-dipole approximation. Since the model requires a homogeneous dielectric environment, effects caused by the dielectric mismatch do not occur. Additionally, based on the derivation of the method in Sec. 3.5.1, only interdot couplings are included. Since the interdot monopole-monopole order vanish in the model, the dipole-dipole interaction determines the Coulomb coupling as the leading order.

In the point-dipole approximation the homogeneous dielectric environment, appearing as a weighted averaged permittivity, is adapted to the values of the fully calculated Förster coupling elements, as it was introduced in Sec. 3.5.4. Furthermore, the monopole-monopole intradot shifts, resulting from the full calculation of the Coulomb coupling, are added as constant diagonal elements of the pure electronic Hamiltonian (cf. Sec. 2.3.1). While the interdot coupling is determined by the dielectric environment, the strength of the intradot coupling elements is influenced by the QDs properties. Thus, both parameters can be separately adapted to the results of the full calculation. Hence, the physical behavior of the interdot dipole-dipole coupling as well as the monopole induced intradot shifts of the signatures in the 2d spectra are adapted very well to the results of the full calculation.

In the diagrams in Fig. 4.7 the exciton energies (at the top) as well as the double exciton energies (at the bottom) resulting from the point-dipole approximation (continuous curves) and the full calculation (dots) are plotted together. The distance dependence on the left hand side shows a good agreement of the two methods apart from the region of small distances. In this region, the fully calculated exciton energies are affected by the dielectric mismatch caused by the spatially dependent permittivity $\varepsilon(\mathbf{r})$, cf. Sec. 3.4.1. Thus the dots resulting from the fully calculated exciton energies deviate from the curve progression given by the point-dipole approximation. For distances bigger than $R_d = 4$ nm the arrangement specific characteristics of the exciton energies resulting from the both approaches are equal. In the derivation of the point-dipole approximation for the Taylor series, it was assumed that the variations inside the QDs are much smaller than the center-to-center distance between the QDs, as schematically illustrated in Fig. 3.26. Thus, the results are only valid for not too small distances (approximately not smaller than the radius of the QDs).

The calculations for the dependence on the angular orientation in Fig. 4.7 are done with a fixed small distance of $R_d = 1$ nm, and thus, the aberrations are particularly increased. Therefore, the exciton energies resulting from the different approaches are slightly shifted. Furthermore, the fully calculated exciton energies (given by the dots) show aberrations from a smooth curve progression as it occurs in the case of the point-dipole approximation (continuous curves) which is caused by the dielectric mismatch and noise terms resulting from the rotations on the discrete grid. Nevertheless, both methods for the calculation of the Coulomb coupling elements show an agreement in principle concerning the physical behavior for the distances and the rotations.

In order to compare the resulting spectroscopic signatures, DQCS are calculated for the same distances and orientations as in Fig. 4.3 but instead of the full calculation of the Coulomb coupling the point-dipole approximation is used, as presented in Sec. 3.5. Here, a homogeneous dielectric constant, averaged by the material constants of the system, is assumed. The resulting

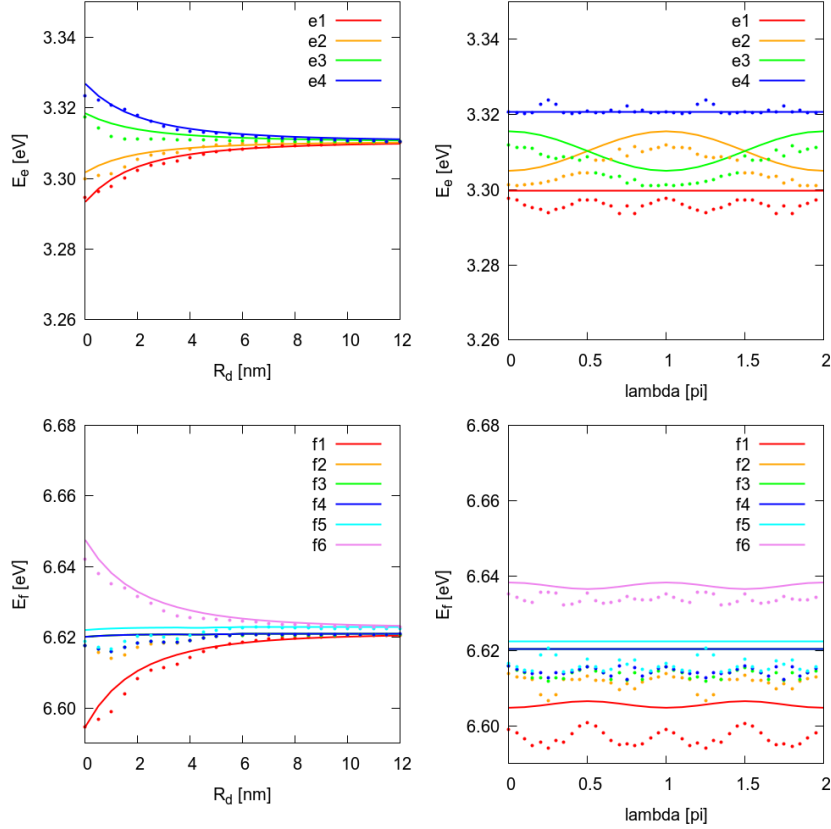


Figure 4.7 Comparison of the exciton (top) and biexciton (bottom) energies of the point-dipole approximation (continuous curves) with the results from the full calculation (dots). In both cases the exciton energies depend on the QD distance and their relative dipole-dipole orientation. Due to the influence of the dielectric mismatch for small distances, the results differ from each other in this region. Since the calculations concerning the dependence on the rotational orientations are done with the fixed distance of $R_d = 1$ nm, the energies resulting from the model are shifted concerning the fully calculated dots. Furthermore, the influence of the aberrations caused by the varying dielectric environment are distinct, since they results from a small distance. Nevertheless, the general angular dependences are similar.

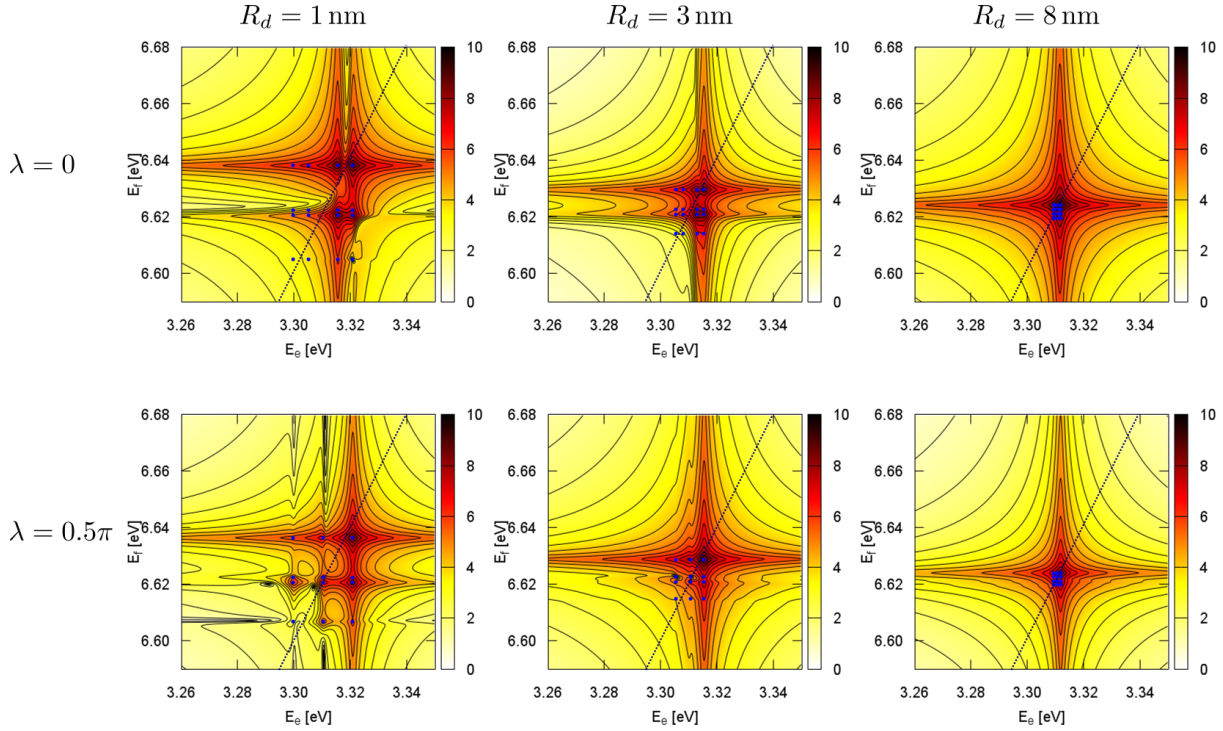


Figure 4.8 The DQCS show the signatures for three different distances R_d between the QDs in two different dipole orientations: $\lambda = 0$ for the same orientation and $\lambda = 0.5\pi$ as rotation around the spatial x-axis. The blue dots mark the electronic eigenenergies. The signatures are strongly influenced by the relative QD positions. The varying angular orientation determines which eigenenergies are excited. The distance shifts the energies: For small distances the Coulomb coupling shifts the signatures. For an increasing distance the signatures are shifted towards the cross diagonal of the unperturbed energies such that the peaks coincide.

exciton and biexciton energies are marked with blue dots. The signatures in Fig. 4.8 are given for the three different distances for parallel orientated QDs ($\lambda = 0$) and respectively for QDs that possess rectangularly oriented dipole moments ($\lambda = 0.5\pi$). In analogy to the fully calculated spectra in Sec. 4.2, along the Ω_1 axis the singly excited states with ω_{eg} occur, while on the Ω_2 axis the doubly excited states ω_{fg} are visible. The color of the bar indicates the signal strength.

In further analogy to the fully calculated signatures in Fig. 4.3, the DQCS in Fig. 4.8 show for small distances big Coulomb induced shifts which decrease with increasing distance between the QDs. Furthermore, the angular orientation, regarding the relative dipole-dipole orientation of the QDs but also regarding the direction of the excitation field, determines which energies are excited and thus occur in the spectra. For parallel orientated dipole moments (at the top), two biexciton energies occur in the spectra while in the case of the fully calculated Coulomb coupling elements three biexciton energies are visible for small distances. In response to an increased QD distance, the signatures coincide into one exciton peak and two biexciton peaks. In this case both methods gives the same results. In the case of the fully calculated Coulomb coupling, the peaks shift toward energies along the cross diagonal, as they do in the case of the point-dipole approximation. For distances between the QDs bigger than $R_d = 10$ nm (cf. Fig. 4.7), the influence of the interdot coupling is negligible and the induced shifts vanish. Here, only the constant intradot monopole-monopole elements determine as material properties the peak positions in the 2d spectra. The influence of the angular orientations around the different cartesian axes is analyzed in detail in the following section.

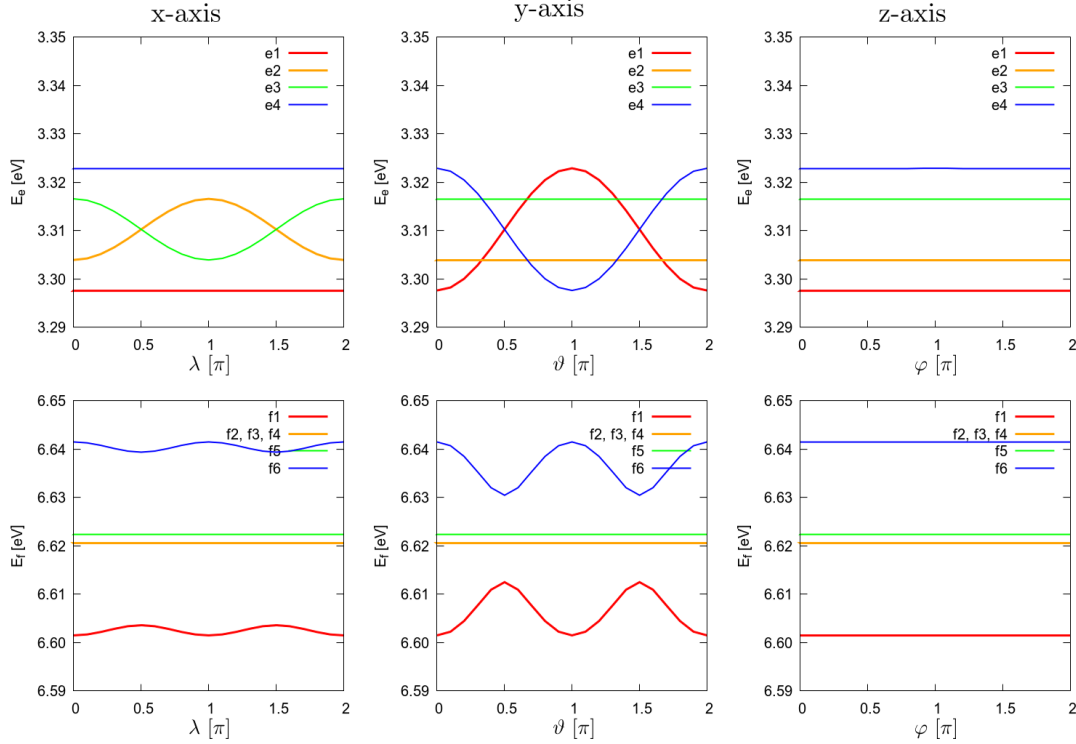


Figure 4.9 Exciton (top) and biexciton (bottom) energies as functions of the three Euler angles λ , ϑ and φ respectively. All rotations are calculated in the fixed distance of $R_d = 1$ nm. Each diagram includes four exciton and double exciton curves respectively. For all rotations the resulting exciton energies are 2π -periodic and symmetric concerning a line parallel to the exciton axis. The rotations around the x-axis and the y-axis include two exciton and biexciton energies which change with the angular orientation following a cosine curve progression. The other two biexciton curves are independent form the Euler angles. The rotation around the z-axis does not influence the exciton energies.

4.3.2 Rotation around the cartesian axis

Since the colloidal QDs diffuse in all three dimensions and freely change their dipole orientation, the resulting movement and relative QD arrangements are complex. The distance is composed of three cartesian coordinates and the angular orientation, given in the Euler description (cf. Sec. 2.4.1), which includes three angles for each QD respectively. As it was calculated in Sec. 3.3.2 and Sec. 3.5.4, the strength of the Coulomb coupling is not only determined by the distances but also by each of the rotation around the different cartesian axes. Thus, in the following section, the influence of the different rotation angles on the signatures in the DQCS is investigated. Therefore, the exciton and double exciton energies are calculated as functions of the three Euler angles.

The diagrams in Fig. 4.9 show the angular dependence of the exciton (at the top) and the double exciton energies (at the bottom) for a fixed QD distance of $R_d = 1$ nm. The variations of the angular orientation start from a parallel orientation of the dipole moments, cf. Sec. 3.3.2. Each diagram includes four different curve progressions for the exciton energies. Furthermore, all diagrams are symmetric concerning a parallel to the exciton axis and they are 2π -periodic or generally constant. According to the diagrams on the right hand, the exciton and biexciton energies are not influenced by rotations around the z-axis. The dipole moments are orientated along the z-axis and therefore, the relative orientation does not change for rotations around this. For rotations around the x-axis and the y-axis, a cosine profile of the exciton energies occurs.

This behavior results from the angular dependence of the Förster coupling elements, as it was calculated in Sec. 3.5.4.

In particular the exciton energies (at the top of Fig. 4.9) are determined by the spin-selective splitting of the Förster elements. Depending on the direction of excitation in relation to the orientation of the dipole moments, the energies show the characteristic cosine profile or they stay constant. As the results in Sec. 4.3.1 show, for an increasing distance between the QDs the exciton energies are shifted together and one exciton peak corresponding to the unperturbed systems remains. In the case of the biexciton energies (at the bottom of Fig. 4.9), two Förster induced signatures occur showing an angular depending curve progression. The amplitude of these double exciton energies is influenced by the rotation axis. The two doubly excited energies in the middle of the diagram stay constant for all angular orientations. Furthermore, as the results in Sec. 4.3.1 show, these energies are independent from the distance between the QDs and thus, they determine the energies in the case of big distances. These energies result from the doubly excited QDs. One of these doubly excited exciton energies corresponds to the double energy of two isolated QDs excited with one exciton respectively. The other doubly excited energy gives the biexciton energy where two excitons are excited in one QD. Since the two colloidal QDs are equal, the energies from the two different QDs coincide and two constant double exciton energies remain for big distances between the QDs. Thus, these biexciton energies, determined by the material properties, are constant for all distances and angular orientations.

The DQCS in Fig. 4.10 gives the spectroscopic signatures for three different angles (given by the columns) rotated around the three cartesian axis (represented by the lines). For comparison, the spectrum resulting from the starting position of two parallel orientated QDs is given on the left hand side. The blue dots mark the connected exciton energies given in Fig. 4.9. The positions of the exciton energies is determined by the strength of the Coulomb coupling and the induced Coulomb shifts. In the 2d spectra it is visible, how the positions of the exciton energies change depending on the angular orientations. These exciton energies indicate the possible positions of peaks in the spectra. Furthermore, they determine the shifts of the signatures and thus, they show whether the peaks coincide. Nevertheless, not only the position of the exciton energies in the spectra determines which signatures occur.

Destructive and constructive interferences of the parts of the total double quantum coherence signature, cf. Sec. 4.1.2, determine which signatures occur in the 2d spectra. Though, the exciton energies are not influence by rotations around the z-axis, the 2d spectra in the bottom line in Fig. 4.10 show angular dependent signatures. Even if the strength of the Coulomb coupling is not influenced by rotations around the z-axis, the QDs rotate in the solvent and thus, they change their positioning regarding the direction of excitations. Therefore, different QD orientations lead to the excitation of varying signatures even if the exciton energies remain identical (compare the most right column of Fig. 4.9 with the spectra at the bottom in Fig. 4.10). The relative orientation of the QDs concerning the direction of excitation determines which signatures are excited, while the strength of the Coulomb coupling determines which energies occur. Thus, a complex interplay between the excitation field and the position dependent Coulomb coupling gives the signatures in the DQCS.

Since not only the relative dipole-dipole orientation of the colloidal QDs but also their angular orientation regarding the field of excitation influence the signatures in the DQCS, in the next section such influence of external parameters should be investigated. Therefore, the polarization of the exciting pulses is varied. Furthermore, the influence of the temperature dependent dephasing rate will be the matter of investigation.

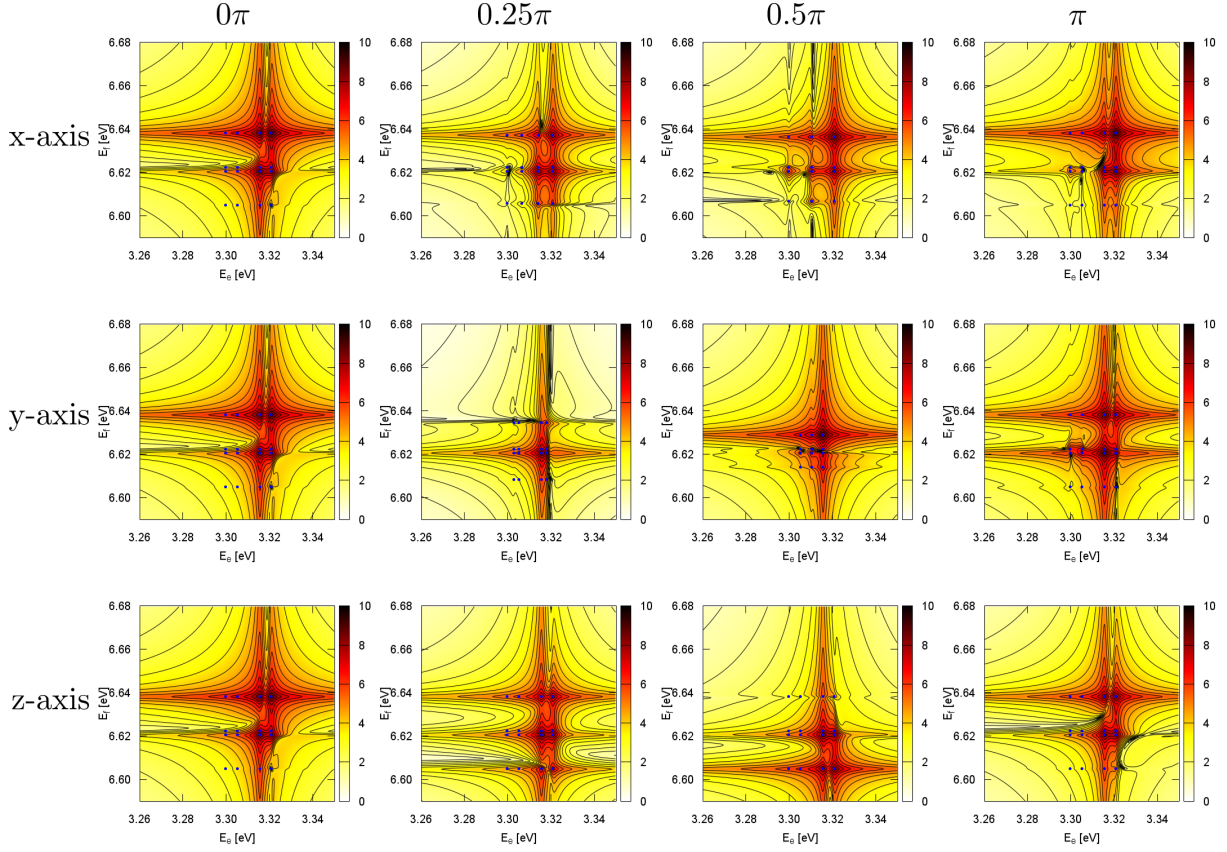


Figure 4.10 DQCS for rotations around the different cartesian axis. In a fixed distance of $R_d = 1$ nm, the spectra for three different QD rotations around the three cartesian axis are calculated. The polarization of the excitation is $e_l e_r e_l e_r$. The blue dots mark the connected exciton and biexciton energies giving peaks and shifts induced by the Coulomb couplings. For comparison, the starting position for two parallel orientated QDs is given on the left hand side. The signatures resulting from rotations with an angle of π give nearly the same signatures since the exciton energies are identical or, because of the spin-degeneration, swapped. For the angular orientations of 0.5π the biexciton energies show strong shifts while the exciton energies coincide to three possible peaks for the rotations around the x-axis and the y-axis, in contrast to the four exciton energies for the z-axis. For the rotation of 0.25π around the y-axis the exciton energies shift nearly together to two possible positions and thus, only one exciton peak remains in contrast to the rotations around the other axis. Though the exciton energies do not change for the rotations around the z-axis, the spectra show different signatures for the QD orientations. Since the QDs are excited with a sequence of laser pulse to generate the spectra, a rotation of the QDs change their angle regarding the direction of this excitation, which determines the occurrence of signatures.

4.3.3 Polarization and dephasing

The signatures in the DQCS are determined by the relative spatial position of the QDs and by the material properties of the colloidal QDs, due to the influence of these parameters on the strength of the Coulomb coupling. Additionally, the orientation of the QDs concerning the field which excites the QDs induces varying signatures in the 2d spectra. In order to further investigate the influence of the excitation on the DQCS, the polarization of the four pulses used in the heterodyne detection (cf. Sec. 4.1.1) is varied. Furthermore, the influence of the temperature, which determines the dephasing rate of the electronic transitions in the QDs, on the spectroscopic signatures is introduced in the following.

The process of retrieving the DQCS involves the excitation of the colloidal QDS by a sequence of four temporally well separated pulses which must have a fixed phase relation. Due to the spin selection rules for the electronic transition, using circularly polarized light enables the exciton states to be distinguished [3]. Thus, for exciting the Förster coupling elements spin-selective, cf. Eq. (2.21), the laser pulses are characterized by two directions: the left polarized pulses with $\mathbf{e}_l = \frac{1}{\sqrt{2}}(\mathbf{e}_x - \mathbf{e}_y)$ and the right polarization with $\mathbf{e}_r = \frac{1}{\sqrt{2}}(\mathbf{e}_x + \mathbf{e}_y)$. For investigating the influence of the polarization of the pulse sequence, DQCS are calculated for equal QDs arrangements which are excited with different polarized pulse sequences.

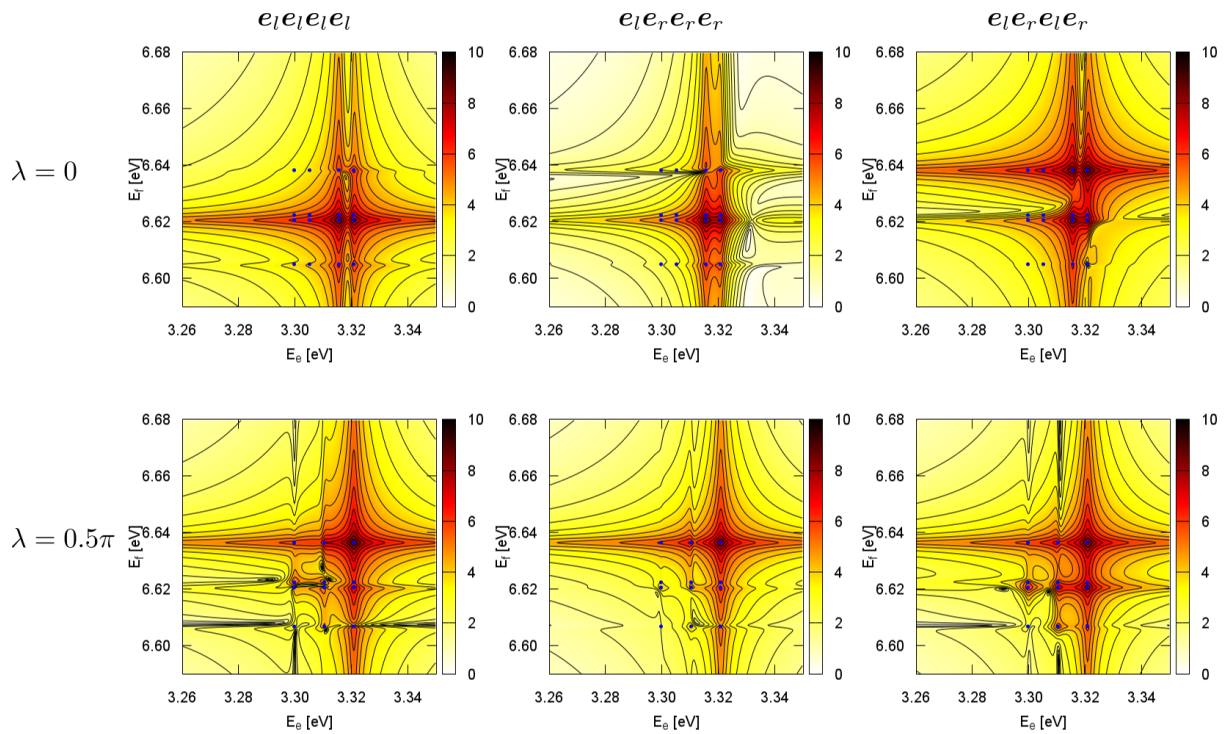


Figure 4.11 DQCS for QDs in a fixed distance of $R_d = 1$ nm and with two different angular orientations: $\lambda = 0$ at the top and $\lambda = 0.5\pi$ at the bottom. The spectra are excited with varying compositions of the polarization direction of the exciting four pulses. In particular in the case of parallel orientated QDs (at the top), the composition of the polarization directions determines which signatures in the 2d spectra are excited. If two QDs are orientated in different directions (at the bottom), the direction of the exciting pulses influences the strength of the signatures in the spectra.

The DQCS in Fig. 4.11 gives the signatures resulting from alternated compositions of the polarization directions of the exciting laser pulses. The spectra at the top of the figure are calculated for two QDs with parallel orientated dipole moments, while for the spectra at the

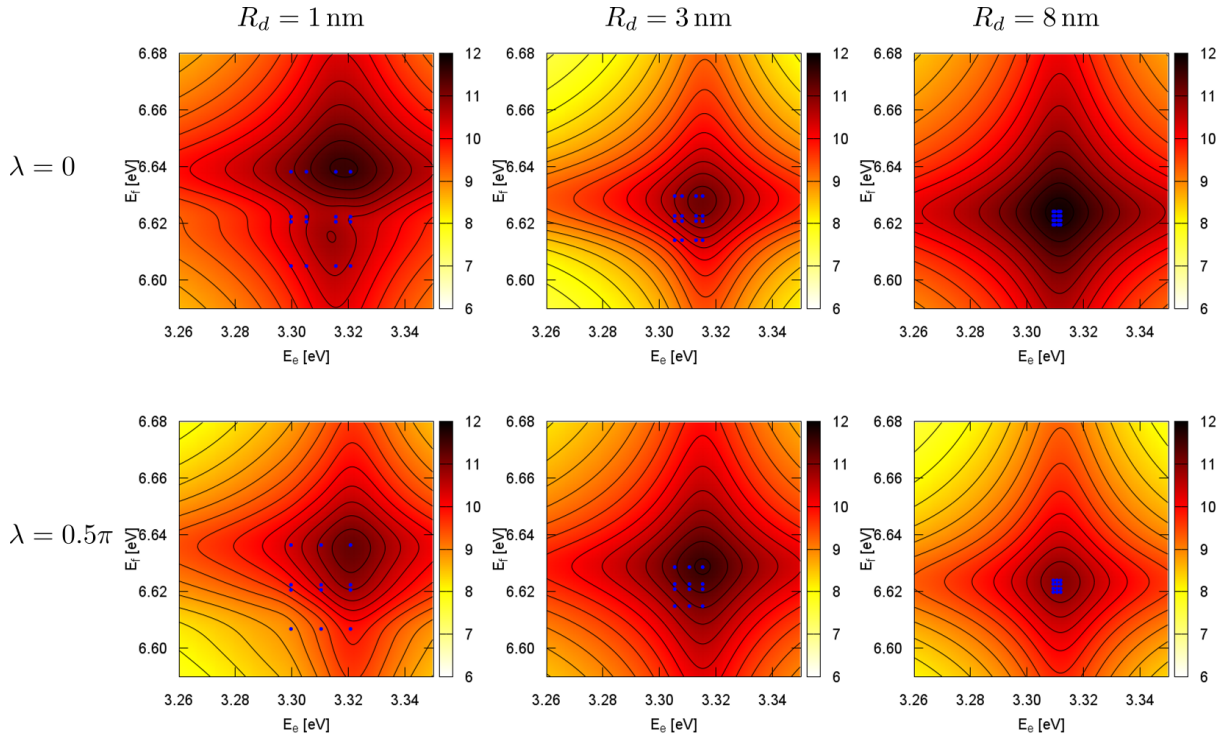


Figure 4.12 DQCS for QDs in different spatial arrangements plotted with a larger dephasing rate of 10 meV. Compared to the spectra with a dephasing rate of 1 meV, the signatures in these spectra are broadened and thus a hybridization in separated peaks cannot be resolved even for small QD distances. Nevertheless, the signatures show shifts and shape transformations caused by the spatially dependent Coulomb coupling between the colloidal QDs.

bottom one QD is rotated by $\lambda = 0.5\pi$ around the x-axis. Thus, the QDs show a rectangular orientation to each other. A comparison of the spectra resulting from the same QD arrangement but excited with a varying polarized pulse sequence show, that the direction of the excitation determines which signatures occur in the spectra. In particular for parallel orientated QDs, peaks corresponding to different exciton energies (given by the blue dots in the spectra) are excited in dependence on the polarization direction. If the QD orientations are mixed, the direction of the excitation determines the signal strength given by the color coding of the 2d spectra. Thus, the occurrence of signatures in the 2d spectra is not only influenced by the spatial position of the QDs but also by the polarization of the exciting laser pulse sequence.

An other external parameter that impacts the computation of the DQCS is given by the temperature. Since colloidal QDs diffuse in the solvent, the temperature plays an important role for the motion of the QDs. If colloidal QDs should be investigated, the room temperature represents a good value to observe QD movements in the solvent. The temperature does not only influence the motion of the colloidal QDs but also their dephasing rate concerning the optically excited transitions. Since the spectra in this chapter were calculated for a dephasing rate of 1 meV for the low temperature limit [124], in the following signatures resulting from a higher dephasing rate of 10 meV are presented [125].

In Fig. 4.12 the spectra are calculated for the same positions as in the approach of the point-dipole approximation in Sec. 4.3.1, but the dephasing is increased for calculations at room temperature. The process of dephasing is a damping process that describes the ongoing loss of phase equality of two quantum objects (here the QDs) which goes along with decay of mutual states, like the excitons. Thus, it induces a broadening of the spectroscopic signatures. Accordingly, the

hybridization of the signatures is merged together and therefore, only one peak in the spectra remains for all QD positions. Nevertheless, this peak shows shifts and shape transformations at very small QD distances because of the increased Coulomb coupling between close QDs. Due to the relation of the QD's dipole orientation to the external field, the intensity of the signatures varies depending on the angular positioning of the colloidal QDs.

It was shown, that also external parameters, such as the direction of excitation and the dephasing, influence the occurrence of signatures in the DQCS. Even of QDs in the same QD arrangements, different exciton energies are excited if the polarization of the pulse sequence is changed. Otherwise, if the dephasing rate is increased together with the temperature, a hybridization of the different exciton energies cannot be observed in the spectra since all signatures coincide. Nevertheless, the spectra provide information on the QD arrangement, as it will be presented in the next chapter. In Chap. 5 the higher dephasing rate is used for describing the Brownian motion of the colloidal QDs in water at room temperature.

4.4 Conclusion

The DQCS was introduced providing information on the exciton and double exciton energies. Therefore, the position dependent Coulomb coupling between colloidal QDs diffusing in water was visualized by an analysis of the signatures in the 2d spectra. Being directly determined by the coupling processes, signatures in the DQCS represent a possibility of investigating the interplay between the motion of the colloidal QDs and the resulting Coulomb coupling between them.

Firstly, the Coulomb coupling elements of colloidal QDs in different spatial arrangements were calculated using the formalism of the PGF method, which was introduced in Sec. 3.1. Here, for each QD position the spectroscopic signatures were calculated including the dependence on a spatially varying dielectric permittivity. It was shown, that the distances between the QDs as well as their relative angular orientations influence the signatures in the DQCS. The exciton and biexciton energies together with the angular orientations of the QDs determined the peaks and Coulomb induced shifts in the 2d spectra. In particular, for small distances well separated signatures occurred in the 2d spectra. With an increasing distance between the QDs the shifts decreased and for big distances they coincided to one exciton and two double exciton peaks. The position of the peaks was determined by the intradot coupling. The intradot shifts, which represent a material property, as well as the interdot Coulomb induced shifts were influenced by the size and the material composition of the QDs.

The results of the full calculation were compared with signatures which were based on the point-dipole approximation for the interdot dipole-dipole Coulomb coupling. Generally, the exciton energies and the spectroscopic signatures resulting from the different methods were similar. In particular, for bigger distances between the colloidal QDs the signatures in the DQCS become equal. Aberrations occurred in the region of small distance, since there the influence of the dielectric permittivity played an important role. Furthermore, the point-dipole approximation is only valid for distances bigger than the radius of the QDs.

Additionally, it was shown that not only the distance between the QDs but also their angular orientations together with the rotation axis determined the occurrence of specific signatures in the DQCS. Furthermore, the polarization of the exciting sequence of laser pulses could be used to excite specific exciton peaks. The spatial dependent Coulomb coupling determined the possible exciton energies in the spectra. Thus, the signatures in the 2d spectra result from a complex interplay between the position dependent Coulomb coupling and the relative orientation of the colloidal QDs concerning the field of the excitation pulses.

Finally, it was shown, that the hybridization of the peaks in the DQCS spectra, which was

particularly visible for small distances between the QDs, was only observable for a low dephasing rate. If this damping constant was adapted to a system at room temperature, as it will be needed for describing the motion of colloidal QDs diffusing in water in the following chapter, the signatures were broadened. In this case, the different signatures were merged together in one main peak. Since the Coulomb induced shifts were still visible, even for a bigger dephasing rate the signatures in the DQCS provided information on the spatial QD arrangements and the corresponding Coulomb coupling. This will be analyzed more detailed in Chap. 5.

Chapter 5

Brownian motion of colloidal QDs analyzed by averaged 2d spectra

In this chapter, the interplay between the Brownian motion of colloidal QDs and the position-dependent Coulomb coupling is investigated by analyzing the signatures in averaged 2d spectra. In multidimensional coherent spectroscopy, introduced in Sec. C, the signatures are directly induced by the interaction processes between the QDs [1] and thus, they can be used for detecting and analyzing the spatial-dependent couplings and excitation transfers [2]. Since in the DQCS an analysis of the averaged QD positions does not influence the motion of the QDs, the signatures provide information on the characteristics of the Brownian motion.

The manipulable brightness and photostability of the colloidal QDs make them excellent markers for visualizing biological processes [20,21]. Therefore, analyzing the Brownian motion is of particular interest since the motion is directly related to the transport of molecules and cells in biological systems [23,24]. The QD labeling provides an insight into the cellular processes [25], if the motion of the QDs can be tracked on their characteristic time scales [21,24]. For getting the correct trajectory, the measurement time must be adapted to the velocity of the particle [23].

In assemblies of colloidal QDs [26,27], the optical and electrical properties are changed due to the Coulomb interaction between the QDs [4,28]. The most important role plays the nonradiative resonant Förster energy transfer between the QDs [31–33], which modifies the individual characteristics of the QDs and forms new delocalized exciton energy states [4,16,29]. The Coulomb coupling between colloidal QDs is determined by the distance between the dots and their relative dipole orientation [3,4] to each other, as calculated in Sec. 3.3. Hence, the Brownian motion of the colloidal QDs influences the strength of the Coulomb coupling between the QDs. Since the Coulomb coupling induces exciton energy shifts [5,6] as well as excitation transfer [34,35], the signatures in the multidimensional coherent spectra show characteristic shifts for different averaged distances between the QDs, as introduced in Chap. 4. Therefore, by analyzing the signatures in averaged 2d spectra characteristic of the Brownian motion of the colloidal QDs can be investigated.

To identify characteristic stochastic quantities, long time trajectories need to be calculated including a high number of spatial and angular positions. For a fast calculation of the resulting huge number of Coulomb coupling elements, the model of the point-dipole approximation introduced in Sec. 3.5 is used for determining the strength of the coupling between the diffusing colloidal QDs. The results and parameters of the model system are adjusted and added by results of the full calculation of the Coulomb coupling.

In the following, the characteristics of the Brownian motion of the two colloidal QDs in water are investigated by analyzing the specific signatures in averaged 2d spectra. Therefore, in the first section the formalism of the Brownian motion used to calculate the trajectories of the QDs

diffusing in the solvent is introduced. Due to the coupling between the colloidal QDs depending on the spatial positions and the dipole orientations, the translational as well as the rotational diffusion are introduced for spherical QDs. To obtain an averaged spectrum, the Coulomb coupling and the spectroscopic signatures are calculated for each step in the trajectory. It is presented how such system can be realized to fast reach a convergence in the signatures. Since the periodic simulation boxes indicates the concentration of the QDs in the solvent, the relation between the averaged distances and the averaged DQCS is analyzed. Finally, the influence of the solvent's viscosity on the signatures is investigated.

5.1 Brownian Motion

In an aqueous solution, colloidal QDs frequently change their positions and orientations caused by the diffusion. This influences the Coulomb interaction between the QDs [126]. The theory of the Brownian motion represents a simple way to describe nonequilibrium dynamics determining the random positions and the averaged velocity of microscopic particles immersed in a fluid. In the thermal equilibrium, the molecules of the fluid move with the thermal energy $k_B T$ [127]. Since the fluid molecules are much smaller than the colloid, a diffusive motion occurs resulting from the collisions with the molecules of the surrounding fluid and random encounters with other particles [128, 129]. As a result, the colloidal QDs change their spatial position as well as their dipole orientations.

In the following, the characteristics of the Brownian motion of the two spherical colloidal QDs in water are investigated. The motion of the QDs is determined by trajectories including the spatial positions and the angular orientations of the QDs. Thus, the formalism of the translational diffusion and the rotational diffusion, which independently occur from each other, are introduced.

5.1.1 Translational motion

The diffusion of the colloidal QDs in the solvent results in a stochastic motion. Following the fluctuation-dissipation theorem [22], the Brownian motion determines the nonequilibrium dynamics given by the random positions and the averaged velocity of the colloids.

The stochastic motion of particles immersed in the fluid, induced by collisions with molecules of the solvent, is determined by the time evolution of the mean-square displacement. The displacement, which includes the random positions and an averaged velocity, linearly expands with the time in the long time limit [130]. While the particles show a ballistic motion at very short time scales, the motion of the Brownian particles becomes diffusive at long time scales [131]. The resulting Brownian motion is determined by the frictional force given by the friction coefficient γ and by the stochastic force \mathbf{F}_s as follows: [22]

$$m \frac{d\mathbf{v}(t)}{dt} = -\gamma \mathbf{v}(t) + \mathbf{F}_s(t). \quad (5.1)$$

The Langevin equation in Eq. (5.1), which gives the fundamental dynamics of stochastic motions, is composed by the frictional forces and the random forces, which are related to each other by the fluctuation-dissipation theorem [22]. Here, the stochastic force is characterized by a Gaussian white noise, which means, that the time average over the stochastic force equals zero $\langle \mathbf{F}_s(t) \rangle = 0$ and distinct time intervals are not correlated $\langle \mathbf{F}_s(t) \mathbf{F}_s(t') \rangle = B \mathbf{1} \delta(t - t')$. The strength B of the fluctuating force \mathbf{F}_s is related to the magnitude of the frictional force via the fluctuation-dissipation theorem [22]:

$$B = 2\gamma k_B T. \quad (5.2)$$

At long time scales, the motion of the colloidal QDs is diffusive and the influence of the inertia can be neglected [23, 128]. By neglecting the inertia $m \frac{d\mathbf{v}(t)}{dt} = 0$, and without any external force the overdamped Langevin equation for the Brownian motion is formulated as follows:

$$\mathbf{v}(t) = \frac{1}{\gamma} \mathbf{F}_s(t). \quad (5.3)$$

With $\mathbf{v}(t) = \frac{d\mathbf{r}(t)}{dt}$, the random motion of a colloid is determined by the stochastic force modified by the friction coefficient

$$\mathbf{r}(t) = \frac{1}{\gamma} \int_0^t dt' \mathbf{F}_s(t'). \quad (5.4)$$

Without an external force, the stochastic motion of a colloid is isotropic and therefore, the mean displacement equals zero for any time $\langle \mathbf{r}(t) \rangle = 0$ [127]. Nevertheless, a particle diffuses, which can be described by the Einstein formula for the mean-squared displacement in d dimensions at long time scales:

$$\langle \mathbf{r}(t) \mathbf{r}(t) \rangle = 2dDt. \quad (5.5)$$

During the time interval Δt , the diffusion length L gives the averaged travel distance of the particle [126], which is given by the root of the mean-squared displacement $L = \sqrt{2dDt}$. The diffusion coefficient D determines the characteristics of the Brownian motion, since it relates the thermal energy and the friction. If the friction is determined by the Stokes' law, the Stokes-Einstein equation [22] gives the diffusion coefficient:

$$D = \frac{k_B T}{\gamma}. \quad (5.6)$$

Using the diffusion coefficient and a rescaled stochastic force $\boldsymbol{\eta}(t)$, which is characterized by the following gaussian relations: $\langle \boldsymbol{\eta}(t) \rangle = 0$ and $\langle \boldsymbol{\eta}(t) \boldsymbol{\eta}(t') \rangle = \mathbf{1} \delta(t - t')$, the Brownian motion of a particle reads [127]

$$\frac{d\mathbf{r}(t)}{dt} = \sqrt{2D} \boldsymbol{\eta}(t). \quad (5.7)$$

In the following, the formalism of the translational Brownian motion is applied to the model system of two Coulomb coupled colloidal QDs, cf. Fig. 5.1. Thus, the equations are evaluated for spherical particles, since the colloidal QDs are viewed as hard-spheres diffusing in the fluid. In the region of low Reynolds-number, the inertial forces are negligible in comparison to the viscous forces. Accordingly, for small spherical objects with the radius r_p in a fluid with the viscosity ν , the translational friction is determined by the Stoke's law [20]:

$$\gamma_{\text{trans}} = 6\pi\nu r_p. \quad (5.8)$$

Since the diffusion of a Brownian particle is related to the friction [22], the Stokes-Einstein-Sutherland relation between the thermal energy and the friction gives the translational diffusion coefficient [23, 126, 129]:

$$D_{\text{trans}} = \frac{k_B T}{6\pi\nu r_p}. \quad (5.9)$$

Accordingly, the translational diffusion of a spherical colloid is directly determined by the temperature and the inverse of the fluid's viscosity and the particle size.

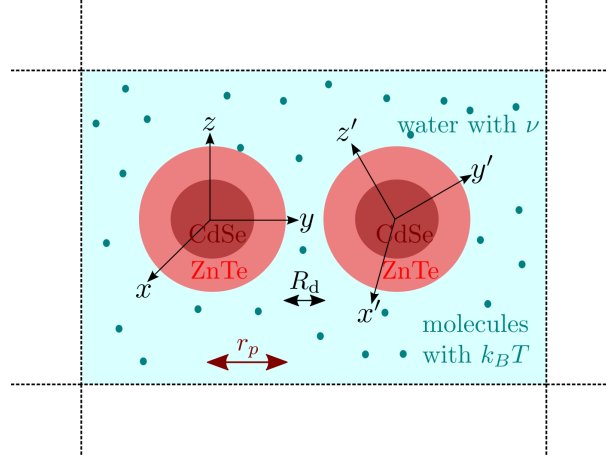


Figure 5.1 Model of two spherical colloidal QDs diffusing in water. Collisions with water molecules induce a stochastic motion of the QDs. Thus, they frequently change their spatial positions and angular orientations resulting in a Brownian motion.

5.1.2 Rotational motion

The stochastic motion of a colloid does not only include a translational diffusion but also a stochastic change of the particle's orientation. In the model of spherical colloidal QDs, the angular position is given by the orientation of the permanent transition dipole moment which is induced by the crystal *c*-axis of the QDs [59]. Thus, the rotational diffusion constant D_{rot} for such a spherical particle with radius r_p and rotational friction constant $\gamma_{\text{rot}} = 8\pi\eta r_p^3$ determines the stochastic change of the particle's orientation as follows:

$$D_{\text{rot}} = \frac{k_B T}{8\pi\eta r_p^3}.$$

Eq. (5.10) shows, that the size of the particle strongly influences the rotational diffusion. Furthermore, in analogy to the translational diffusion, the temperature and the inverse of the viscosity determine the rotational diffusion coefficient. The characteristic time describing the stochastic reorientation of a particle diffusing in d dimensions is given by the persistence time τ_{rot} , which is related to the inverse of the rotational diffusion constant D_{rot} [127]:

$$\tau_{\text{rot}} = \frac{1}{(d-1)D_{\text{rot}}}. \quad (5.10)$$

Following the assumption that there is no coupling between the translational and the rotational motion of a particle in the fluid, they occur independently. To demonstrate the influence of the temperature, the solvent's viscosity and the size of the particles, characteristic quantities of the Brownian motion are calculated for different parameter setups. In the following, the Brownian motion of small colloidal QDs should be investigated, and thus, the particle's size is chosen in the typical region of such QDs. For getting an overview of the solvent's influence, the values of the temperatures and the viscosities cover a wide range of values.

The results in Table 5.1 show that the characteristic time- and length-scales of the Brownian motion of spherical particles in a flow are influenced by the particle size as well as by the temperature and the viscosity of the fluid. All particles in the different fluids show a diffusion length L smaller than 1 nm, while the characteristic change of their orientations is given in the nanosecond to microsecond time-scale. For instance a colloidal QD with a radius of $r_p = 3$ nm approximately needs 60 ps to reorientate in water at room temperature.

Table 5.1 Diffusion constants of the translational D_{trans} and rotational D_{rot} Brownian motion of spherical colloidal QDs in varying solvents. The diffusion length L , here for a time interval of $\Delta t = 1$ ns, as well as the persistence time τ_{rot} are influenced by the temperature T , the solvent's viscosity ν and the radius r_p of the spherical QD.

T [K]	ν [mPa·s]	r_p [nm]	D_{trans} [(nm) ² /ns]	D_{rot} [1/ns]	$L(1\text{ns})$ [nm]	τ_{rot} [ns]
200	15 (ethanol)	3.0	0.0033	0.0004	0.14	1250.0
200	15 (ethanol)	1.5	0.0065	0.0029	0.20	172.4
300	1 (water)	3.0	0.0732	0.0081	0.66	61.7
300	1 (water)	1.5	0.1465	0.0651	0.94	7.7
425	3 (motor oil)	3.0	0.0346	0.0038	0.45	131.6
425	3 (motor oil)	1.5	0.0692	0.0307	0.64	16.3

Inserting the persistence time into the diffusion length gives a product of a constant scaling factor ($\alpha = 1.733$) and the size of the QD: $L(\tau_{\text{rot}}) = \alpha r_p$. Accordingly, smaller QDs with $r_p = 1.5$ nm, which need less time to reorientate, pass an averaged distance of $L(\tau_{\text{rot}}) = 2.6$ nm, while bigger sized QDs with $r_p = 3.0$ nm move $L(\tau_{\text{rot}}) = 5.2$ nm during the persistence time.

The mean luminescence decay time for colloidal QDs in water at room temperature is in the nanosecond time-scale (e.g., 40 ns for CdTe QDs) [77]. During this time interval, the QDs show a characteristic stochastic drift in water of some nanometers. Therefore, in the photoluminescence spectroscopy, the Brownian motion of the colloidal QDs influences the resonant energy transfer between the QDs, as it was concluded in Ref. [126]. In the heterodyne detection, introduced in Sec. 4.1, the four wave mixing signal of the multidimensional coherent spectroscopy is determined by induced polarizations [121]. The dephasing time of polarizations in the QDs, which is influenced by the temperature [132], occurs on a picosecond time-scale. Hence, the Brownian motion of spherical QDs diffusing in water shows a different time-scale than the microscopic polarizations. Therefore, the multidimensional nonlinear spectroscopy, such as the DQCS, may be used to calculate characteristic optical signatures of colloidal QDs. The spectroscopy used in this thesis allows the observation of electronic correlations to be done during the time intervals between the pulses [2]. Accordingly, the interplay between the Brownian motion and the spatial dependent Coulomb coupling of colloidal QDs diffusing in water can be investigated.

The mean velocity of a Brownian particle increases with the temperature of the fluid and decreases with increasing particle size [23]. The short time scales of the motion represents a challenge for the measurement of the motion of the colloidal QDs, since it requires a good spatial and temporal resolution for the small particles [23]. The optical investigation by analyzing the spectroscopic signature in the DQCS represents a method for a fast investigation of the main characteristics of the Brownian motion without influencing the current trajectory. In the following sections, the trajectories resulting from the diffusion of colloidal QDs are calculated using the formalism of the Brownian motion. To get statistical convergent signatures in averaged DQCS, long trajectories need to be implemented.

5.2 Implementation of the Brownian motion of colloidal QDs

In this section, it is presented how the long trajectories resulting from the Brownian motion of two colloidal QDs are implemented. Since the optical signals occur on an ultrafast time scale, the motion of colloidal QDs with their characteristic trajectories can be treated via snapshots, each represented by a specific QD arrangement. Thus, each snapshot requires the calculation of the Coulomb coupling elements and the corresponding spectroscopic signal for the specific point in time. All snapshots together give the trajectory of the colloidal QDs [23]. To obtain stochastic

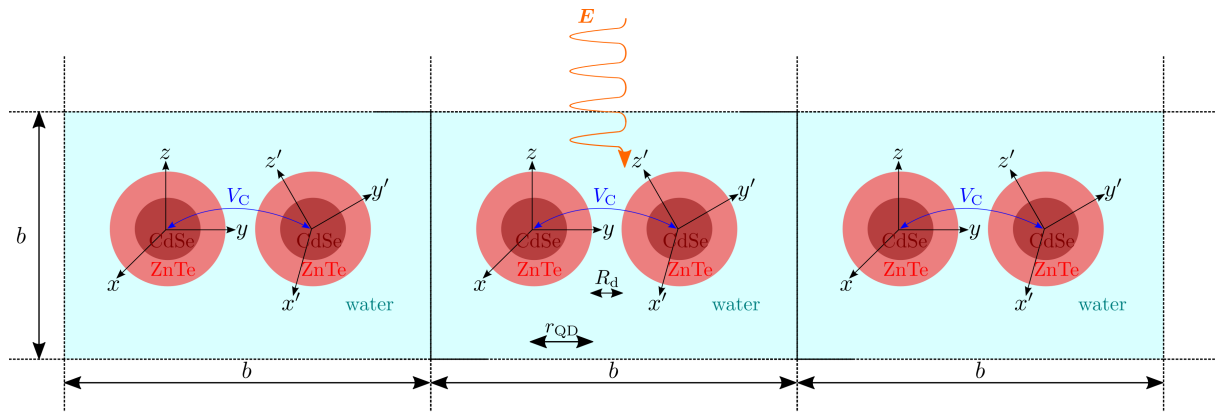


Figure 5.2 Scheme of the simulation boxes which are determined by the width b with periodic boundary conditions in three dimensions (plotted are only two). Each simulation box exactly includes two colloidal CdSe/ZnTe QDs in water. Due to the Brownian motion the QDs changing their spatial positions and angular orientations. This induces a specific Coulomb coupling V_C determined by the smallest distance between the periodic QDs. Since the motion is investigated by multidimensional coherent spectra, the QDs are excited by a sequence of laser pulses E .

relevant conclusions, a huge number of QD positions needs to be implemented. Each position determines its own Coulomb coupling elements inducing characteristic shifts in the 2d spectra. Adding all spectroscopic signatures divided by their total number gives the averaged spectrum.

In the following, the simulation box for describing the pairwise Coulomb coupling between two colloidal QDs with its periodic boundary conditions is introduced. The size of the boxes indicates the particle concentration in the solvent. Then, a handling of the trajectories is presented, which enables a stochastic convergence in the positions and orientations to be reached approximatively. Thus, signatures in the averaged spectra can be used to identify stochastic relevant quantities.

5.2.1 Simulation box with periodic boundary conditions

For simulating the pairwise Coulomb coupling between colloidal QDs diffusing in the solvent, a simulation box, characterized by the box width b , with periodic boundary conditions in three dimensions is introduced. Each box exactly includes two colloidal QDs, schematically depicted in Fig. 5.2. A schematic sketch illustrating the mode of the program used to get the 2d spectra is given in App. D. The trajectories of the Brownian motion of these two colloidal QDs, introduced in Sec. 5.1, are calculated inside the box complying the periodic boundary conditions. Since the motion of the QDs in the solvent is determined by a translational and a rotational diffusion, the trajectories include the positions of the QDs and their angular orientations. To get the spectroscopic signatures the QDs are excited with a well defined sequence of laser pulses, cf. Sec. 4.1.

Independently from the simulation box, the smallest distance between the QDs determines the Coulomb coupling. Since the strength of the Coulomb coupling is strongly influenced by the distance between the QDs, as analyzed in detail in Sec. 3.3, it is assumed, that only the smallest distance determines the coupling. Thus, couplings to other QDs are neglected, since the smallest distance gives the leading order in Coulomb coupling.

The size b of the simulation box indicates the concentration of the QDs in the solvent. If the width of the simulation boxes is large compared to the size of the QDs, the colloidal QDs freely diffuse in the solvent and big distances occur, cf. Fig. 5.3. For small simulation boxes, the QDs are close to each other and the concentration of QDs in the solvent is high. Therefore, the free moving space of the colloidal QDs is restricted. If the distances between the QDs are small,

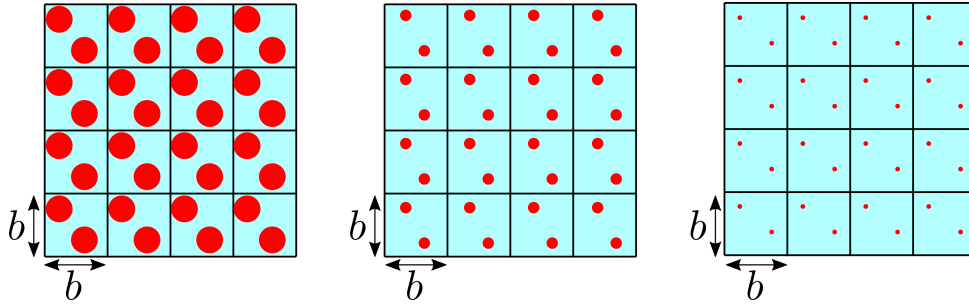


Figure 5.3 Size of the periodic simulation boxes b determining the concentration of the QDs in the solvent. The box size is varied in relation to the size of the QDs (which stays constant in the model, while in the picture it is plotted the other way round). Small simulation boxes indicates a high concentration of QDs in the solvent (left hand side), while a wide box size represents a low concentration of QDs and thus big distances between the colloidal QDs (right hand side).

the Coulomb coupling plays an important role, due to the coupling strength strongly increasing with a decreasing distance between the QDs, as calculated in Sec. 3.3. Such interplay between the concentration of the QDs and the strength of the Coulomb coupling should be investigated in the following Sec. 5.3.1 by analyzing the averaged signatures in 2d spectra.

Since in the simulations only the smallest distance induces the coupling between the QDs, the size of the simulation box should not be too small to get reliable information from the model. If the distances between all QDs are too small and thus the concentration is very high, couplings to other QDs occur and the model needs to be adapted. Since the calculation of the Coulomb coupling requires the knowledge of all positions each inducing a specific strength in the Coulomb coupling, such model causes high computational requirements. In this thesis, the focus lies on the stochastic convergent Brownian motion of the QDs. Therefore, millions of QD positions are evaluated concerning the Coulomb coupling between two QDs. If the box size is very small compared to the size of the QDs, a non-physical trembling of the QDs would be investigated since the Brownian motion is restricted by the size of the simulation box. If the concentration of the QDs is very high, the Brownian motion occurs at short time scales and the influence of the inertia cannot be neglected [23]. Thus, for the calculation of a very high concentration of QDs other dynamics occur. Accordingly, for using the formalism introduced in Sec. 5.1, the simulation boxes need to be small enough to restrict the colloidal QDs in their free movement for describing high concentrations but not so small that one QD couples to more than one other QD to get valid assumptions resulting from the model system. Since the mean distance between colloidal particles is often greater than their radius [133] and they are usually surrounded by a ligand [20,23], the model used in this thesis taking its restrictions into account represents a good approximation for describing the Brownian motion of colloidal QDs at long time scales.

5.2.2 Trajectory including positions and angular orientations

The colloidal QDs frequently change their spatial position and their angular orientations due to the diffusion in the solvent. The different kinds of diffusion, introduced in Sec. 5.1, occur independently from each other. Thus, for each QD the trajectories include the three cartesian components of the spatial vector \mathbf{r}_{QD_n} and four components of the quaternions q_{QD_n} giving the angular orientation, cf. Sec. 2.4.2. These parameters are used in the program mode to calculate the 2d spectra, as schematically depicted in App. D. Altogether, the trajectory of the Brownian motion consists of N steps of the translational diffusion, resulting in N distances between the QDs and M dices in the rotational diffusion determined by M quaternions.

Since in this thesis stochastic characteristics of the Brownian motion of colloidal QDs should

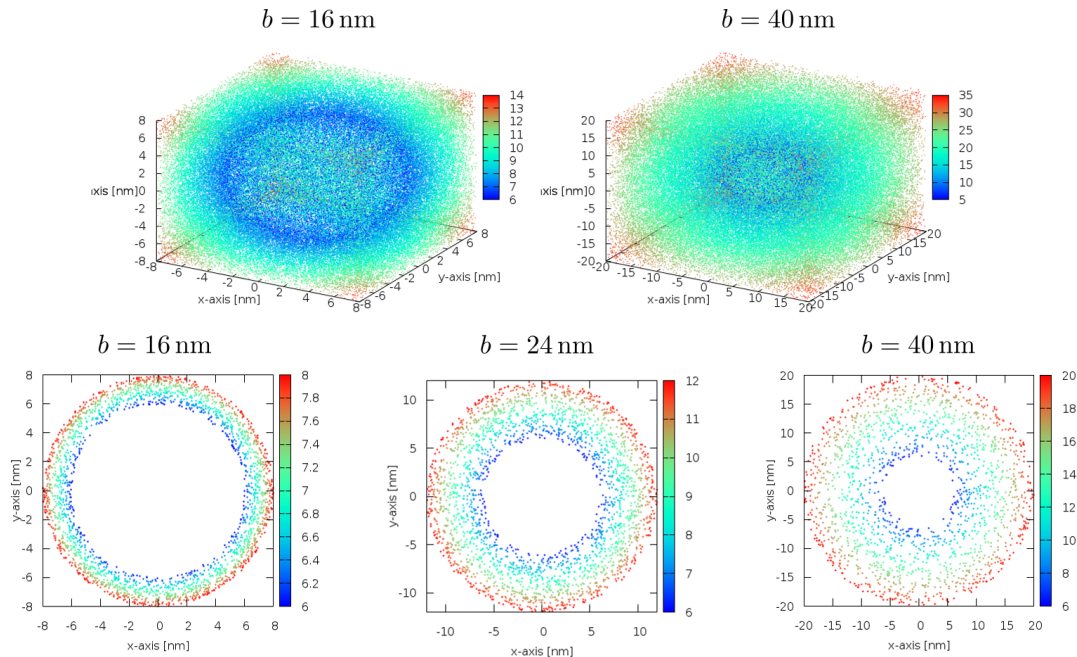


Figure 5.4 3d positions and 2d maps illustrating the distribution of the distance vector. Each dot represents a spatial position of the distance vector resulting from a random walk of two colloidal QDs including 100000 steps in the trajectory. The coloring gives the norm of the distance vector between the QDs. The calculations are done in different sized simulation boxes. Since the QDs have a radius of $r_{\text{QD}} = 3$ nm, the center-to-center distances are not smaller than $R_d = 6$ nm, while the box size determines the biggest distance. Since no clustering or gaps in the positions of the distance vector are visible, the distance vector is equally distributed.

be investigated using DQCS, cf. Sec. 4.1, the distances as well as the angular orientations need to be equally distributed. The calculation of the angular orientation is based on quaternions, introduced in Sec. 2.4.2, which naturally ensure all angles to be equally distributed. A clustering of angular orientations regarding the pole coordinates, as in the case of rotations based on the Euler angle description, does not appear if quaternions are used. Thus, the angular orientations of the colloidal QDs are randomly chosen and equally distributed over the whole domain.

In the following, the distribution of the spatial vector giving the translational positions of the QDs is analyzed. Since the Coulomb coupling is determined by the smallest distance between the QDs, the distribution of the distance vector $\mathbf{R}_d = \mathbf{r}_{\text{QD}1} - \mathbf{r}_{\text{QD}2}$ is used. Regarding the periodicity of the simulation boxes, the interacting QDs must not occur in the same simulation box. Depending on the box size b , the distance vector should reach every position inside the box while the norm of the vector includes all possible distances between the QDs. Thus, the distribution of the distance vector is calculated for different box sizes. The 3d diagrams and the 2d cuts in Fig. 5.4 illustrate the spatial arrangement of the distance vector colored by the norm of the vector. Since each colloidal QD has a radius of $r_{\text{QD}} = 3$ nm, in all cases the smallest distance is given by $R_{d,\text{min}} = 6$ nm. The size of the simulation box determines the biggest distance between the QDs. The diagrams concerning the spatial distribution indicate, that in principle all spatial positions are reached by the distribution vector. No gaps or clusterings of specific positions are recognizable. Therefore, the distance vector and the related QD positions are equally distributed over the whole simulation box.

For further investigating the distribution of the distance vector, in the histograms in Fig. 5.5 all distances occurring in regions of $\Delta R_d = 0.1$ nm are counted. To get significant information independently from the stochastic walk, 10 million steps are included in the calculations. The

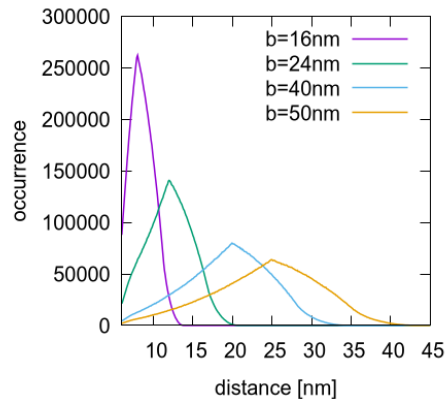


Figure 5.5 Histograms of the distribution of the distance in different sized simulation boxes resulting from a random walk including 10 million different positions each with an own angular orientation. Depending on the box size, the bell curve show a distribution over the area with a maximum. The periodic boundaries indicate that the distances are smaller than the box size and the increasing branch is not Gaussian.

resulting histograms, calculated for different box sizes b , show a non-Gaussian bell curved distribution depending on the box size. The smallest distance is given by the double radius of the QDs while the size of the box determines the range of the distances. Nevertheless, the distances occurring in the simulation are much smaller than the box size indicates. The boundary conditions of the simulation boxes are periodical and only the smallest distance between the QDs respecting all neighbor simulation boxes gives the leading order. Thus, the resulting distances between the Coulomb coupled QDs are smaller than the box size. Furthermore, the curve progression is not simply given by a Gaussian distribution. Nevertheless, the occurrence of the distances is given by a bell curve with a maximum at the middle of the range and there are no distances which show dissenting properties. In conclusion, there are no stochastic clusters or omissions in the distribution of the translational QD positions.

Respecting the Brownian motion of the colloidal QDs, each step in the trajectories represents a time interval in which the diffusion induces changes in the QD arrangements characterized by the diffusion coefficients [23] (cf. Sec. 5.1). Using equidistant time steps in the measurement, here spectroscopic methods are used, the trajectory of the QDs can be visualized. Tracking the Brownian motion and determining the trajectories of individual QDs [20, 21, 134] or small QD clusters [135] is quite challenging. For getting the correct trajectory, the measurement time must be adapted to the velocity of the particle [23]. In contrast in this thesis to get statistic stable solutions, the steps of the translational movement are not equidistantly picked in time to received a fast as possible convergence of all spatial positions. Thus, the number of translational steps, which determines the positions used to calculate the strength of the Coulomb coupling and the resulting spectroscopic signatures, are chosen randomly. Accordingly, the trajectories cannot be reconstructed anymore. Instead, an equal distribution of all positions inside the simulation box is reached faster and thus, a convergence of all trajectories occurs faster.

Fig. 5.6 shows a color map which is composed of cuts through 2d spectra parallel to the single exciton axis. Each of these single spectra are calculated for a fixed distance between the QDs. All together gives distance depending 2d maps of the absolute values and the real and imaginary part of the 2d spectra. The color coding gives the spectroscopic signatures. The resulting color maps illustrate, that the signatures strongly change in the region of small distances between the QDs, while for big distances the signatures slowly vary. To fast reach a convergence, in the calculation of a high number of QD arrangements, the frequency of picking a not equidistant

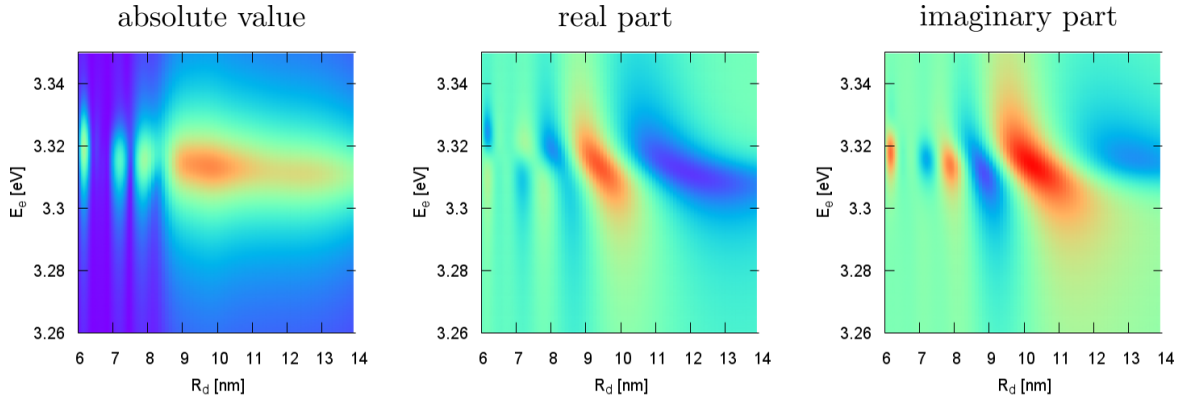


Figure 5.6 2d maps composed of distance-dependent cuts through spectra of single signatures for QDs with a fixed angular orientation ($\lambda = 0$). In the region of distances smaller than $R_d = 9$ nm the signatures show a strong distance depending curve progression. For an increasing distance the signatures slowly vary. Thus, for bigger distances less distance cuts are needed to get the full curve progression, while for small distances very close steps in the distances are required.

step is adapted depending on the distance. Therefore, the number of the total steps from which a specific step is chosen is weighted by a distance depending function. Accordingly, steps in the translational trajectory are statistically picked more often, if they result in small distances between the colloidal QDs. Steps connected with bigger distances between the QDs are not picked that often.

5.2.3 Convergence of the QD positions

To get stochastically converged signatures in the 2d spectra, the trajectories resulting from the Brownian motion of the colloidal QDs need to be very long including a huge number of QD arrangements. Information on the characteristics of the motion concerning the QD arrangements cannot be obtained before the signatures in the 2d spectra are independent from the particular trajectory. In this section, the convergence of the angular orientations and the spatial positions of the colloidal QDs should be analyzed. Therefore, deviations in the cuts through the signatures in the averaged spectra are investigated.

To reach an averaged signature in the DQCS, all single signatures resulting from each QD arrangement are added respectively, weighted by their statistical occurrence, and then they are divided by the total number of steps N in the related trajectory. For comparing the signatures resulting from different trajectories of the Brownian motion of the colloidal QDs, cuts through the main peak parallel to the exciton axis in the DQCS are used.

Starting with the investigation of the convergence of the rotational diffusion, the QDs are fixed in their distance to each other and only the angular orientation is modified. The cuts through the resulting averaged signatures for different numbers M of total rotation angles, which are given by quaternions, are plotted in the diagrams in Fig. 5.7 for five different trajectories (called runs) respectively.

The diagrams in Fig. 5.7 show, that for the small number $M = 100$ the cuts through the five runs strongly differ from each other. For an increasing number of angles, the deviations caused by the different angular trajectories decreases. In the case of $M = 10000$ the differences in the signatures of the five runs are very small and they completely vanish in the case $M = 100000$ and all runs coincide. Thus, the angular orientations have reached their convergence if 100000 angular orientations are included in the trajectory. The Euler angles as well as the quaternions

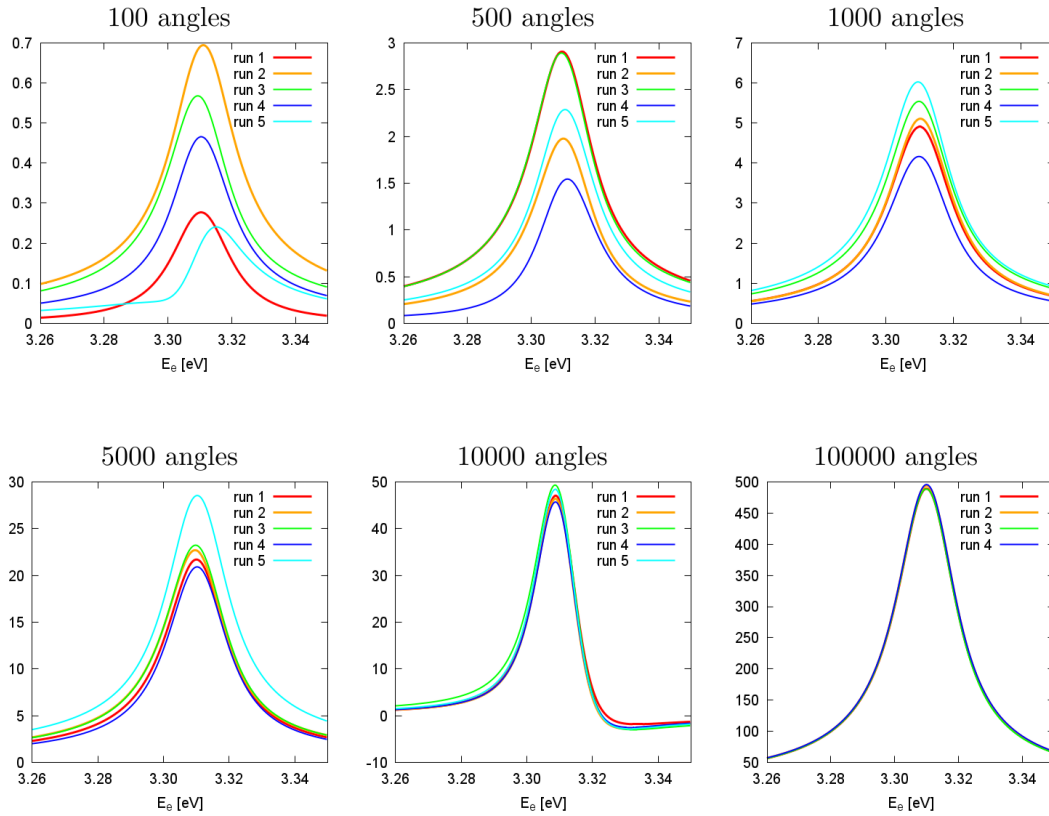


Figure 5.7 Random variation of the angular orientations of both colloidal QDs in a fixed distance to each other. In different diagrams the total number of angles is varied. Since the deviations between the different runs vanish, the angular orientations reach their convergence if 100000 angles are included in the trajectories.

show a small restricted domain. Therefore, the convergence of the angular orientation is reached for a realizable number of angles.

To analyze the convergence behavior of the translational diffusion of the colloidal QDs, the angular orientation is fixed and analogously to the convergence of the angular orientations, the total number of the spatial arrangements is varied. To faster reach the convergence, as was introduced in Sec. 5.2.1, the steps in the translational part of the trajectory are picked randomly and weighted by the distance. The deviations of the cuts through the signatures in the 2d spectra resulting from different trajectories are investigated. Since the signatures in the DQCS are also influenced by the real part and the imaginary part, they are also included in the following convergence analysis.

The diagrams in Fig. 5.8 show, that for an increasing number of steps the deviations between the different runs in the cuts through the spectroscopic signatures decreases. A total convergence where all curves resulting from different trajectories coincide cannot be reached not even in the case of 20 million steps. Especially for the cuts through the absolute value, comparing the runs for 10 million and 20 million steps, the differences are not significantly reduced. Thus, to reach the convergence, the total number of steps needs to be strongly increased. Since in the case of 20 million steps the differences caused by the trajectories are small, these results should be compared to a walk with 100 million steps.

Thus, in Fig. 5.9 five runs with 20 million steps respectively (red and blue curves) are plotted together with the averaged run including the 100 million steps (orange and light blue curves). The calculations are done for two different sized simulation boxes (red curves with $b = 20$ nm

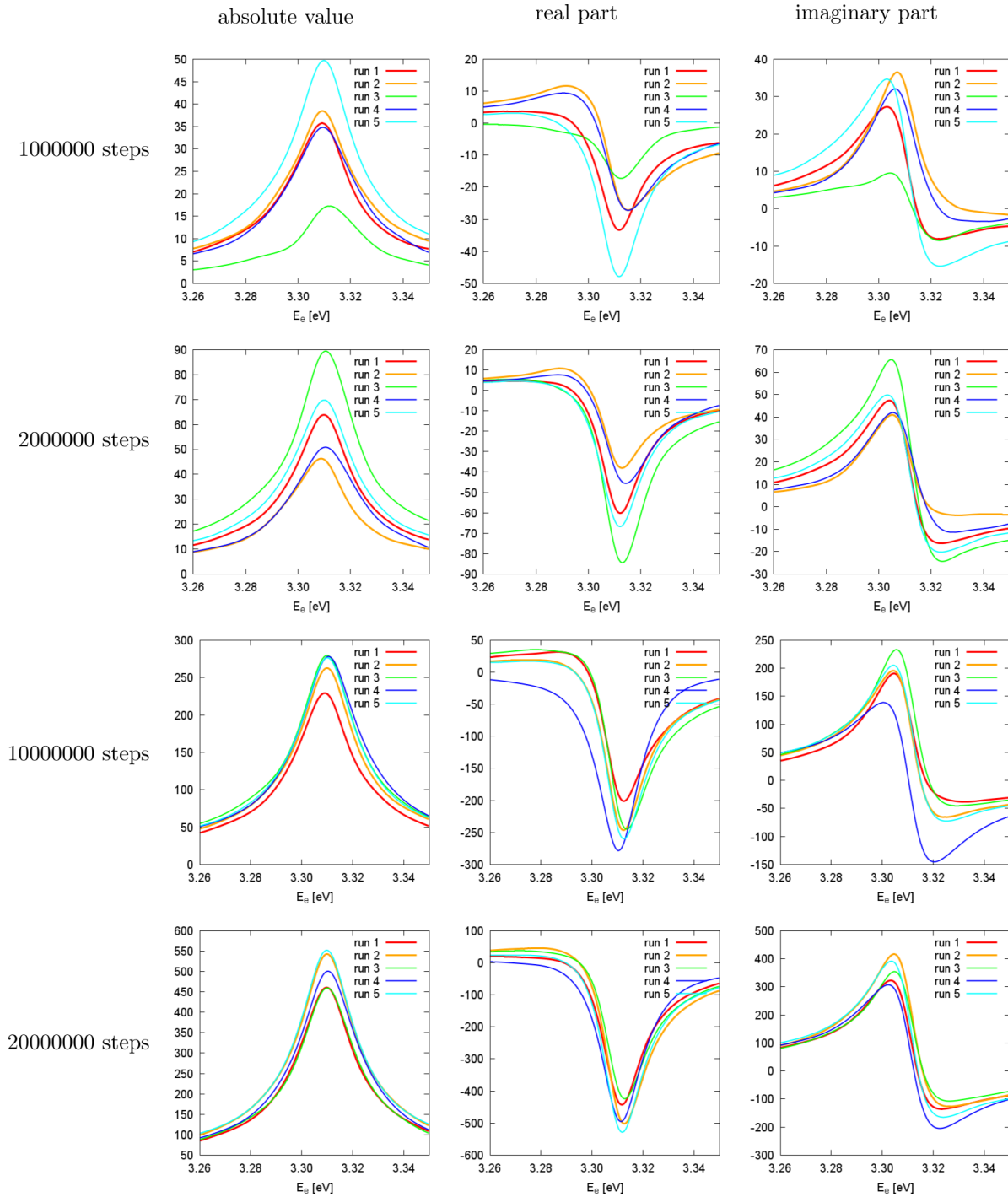


Figure 5.8 Random variation of the translational positions of the two QDs respectively. To identify the convergence, cuts through the absolute value, the real part and the imaginary part of averaged 2d spectra are used. Each position gets its own angular orientation, and therefore, the angular orientations reached the convergence. A total convergence of the spatial positions where all cuts resulting from different trajectories coincide is not reached. If the trajectories of the Brownian motion consist of 20 million steps, the differences in the signatures caused by the specific trajectory are small.

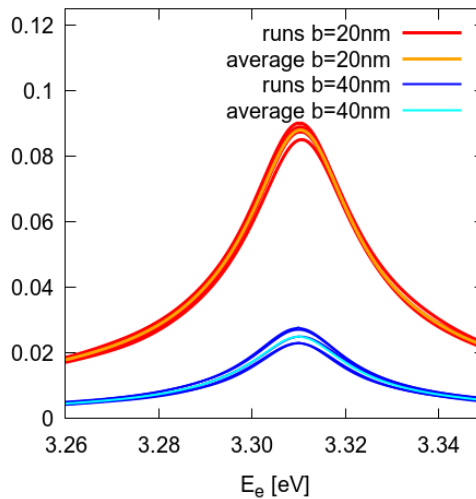


Figure 5.9 Cuts through 2d spectra calculated for two different sized boxes showing the deviations of 5 different runs each with 20 million steps from their average run. The trajectory of the averaged run includes 100 million steps. The mean squared deviation of the runs with 20 million steps from the averaged is given by 3% for the small box with $b = 20$ nm and 10% for the box with $b = 40$ nm.

and blue curves with $b = 40$ nm). Determining the root mean square deviation from the value of 100 million steps gives a difference in the smaller box of 3% and 10% in the case of the bigger simulation box. Thus, the deviations in the case of 20 million steps are smaller than 10% in comparison to a run consisting of 100 million steps. The numerical cost are highly increased in the case that all trajectories consist of 100 million steps. Since for each QD arrangement, consisting of the angular orientation and the spatial position, the Coulomb coupling as well as the spectroscopic signatures need to be calculated, the numerical requirements are very high for this huge numbers of steps. Therefore, the averaged signatures in the following section are composed of 20 million steps each with an own angular orientation. The error caused by the not fully convergent signatures account for approximately 10%. While the rotational diffusive part of the trajectory is equally distributed and convergent since quaternions are used, the convergence of the translational part is reached more faster by randomly choosing the time steps and weight their occurrence depending on the distance between the QDs, as it was introduced in Sec. 5.2.1.

5.3 Averaged spectra of QDs showing Brownian motion

Colloidal QDs diffuse in the solvent and thus, they frequently change their spatial positions as well as their angular orientation. This Brownian motion of the colloidal QDs should be investigated in the following section by analyzing the spectroscopic signatures in averaged 2d spectra. Since the Coulomb coupling is determined by the spatial arrangement of the QDs to each other, as calculated in Sec. 3.3, the single signatures in the DQCS show specific shifts for each arrangement, as introduced in Sec. 4.2. The statistical motion of the colloidal QDs reaches a convergence, if the trajectory of the motion includes millions of steps, cf. Sec. 5.2.3. Thus, an averaged spectrum provides information on the characteristics of the stochastic parameters influencing the movement and the coupling between the QDs.

5.3.1 Influence of the particle concentration

Since the strength of the Coulomb coupling is strongly influenced by the distances, the concentration of colloidal QDs in the solvent induces characteristic signatures in the averaged 2d spectra. The size of the simulation boxes with periodic boundary conditions in three dimensions determines the concentration of the particles, cf. Sec. 5.2.1. To get the stochastically convergent 2d spectra, each trajectory describing the Brownian motion includes 20 million spatial positions with an angular orientation respectively. Thus, the signatures in the averaged spectra reached a convergence as discussed in Sec. 5.2.3.

In an averaged spectrum, the signal is given by the average of all single signatures resulting from each QD position determined in the trajectory of the Brownian motion. Hence, all spectroscopic signatures resulting from the position dependent Coulomb coupling between the QDs are calculated and added together, divided by the number of positions. Thus, the magnitude of the Coulomb induced shifts concerning the QD arrangement (cf. Sec. 4.2) as well as their occurrence determine the signal in the averaged spectrum. For a fast and efficient calculation of the Coulomb coupling the point-dipole approximation is used as introduced in Sec. 3.5.

For analyzing the interplay between the averaged QD's distances and the resulting signatures in the 2d spectra, the Coulomb coupling and the DQCS are calculated in dependence on the size of the simulation box b . This gives the concentration of the QDs in a volume element. With increasing size of the simulation boxes the averaged distance between the QDs increases too. For small distances the strong Coulomb coupling induces features which determine the spectroscopic signatures. In contrast, for big distances between the QDs only the constant intradot shifts determine the signatures, as discussed in detail in Sec. 4.2. To investigate how the different concentrations influences the spectroscopic signatures, the averaged DQCS as well as the 2d maps of their real and imaginary part are calculated. The interference of both phase contributions defines the signal in the DQCS [80].

Since the averaged spectra result from Brownian motions with long trajectories, the spectra always include signatures resulting from a strong Coulomb coupling between the QDs as well as the constant shifts induced by the intradot coupling. The occurrence of the single signatures in the spectra determines the amplitude and the extension of the peaks in the DQCS. If the concentration of QDs in the solvent is high, and the movement occurs in a small periodic simulation box, a high number of Coulomb induced signatures showing big shifts are added to get the averaged spectrum. Thus, as visible in the DQCS in the top of Fig. 5.10, the averaged signature shows a big extension and a high amplitude. In contrast, in a solvent with a low concentration of QDs, only a few signatures resulting from small distances contribute to the averaged spectrum. Therefore, amplitude and extension of the averaged peak in the 2d spectra are decreased.

The 2d maps in the middle and at the bottom of Fig. 5.10 show the real part and the imaginary part of the averaged DQCS respectively. Generally, the real and imaginary parts are (anti-) symmetric along and perpendicular to the diagonal axis. Thus, the absolute signal is symmetric along the diagonal and the antidiagonal axis [118]. A variation of the box size causes the symmetry of the real and the imaginary part concerning the diagonal to be broken. A phase shift relating the real and the imaginary part occurs for an increasing averaged distance between the QDs. After a critical phase transformation occurring for simulation boxes between $b = 40$ nm and $b = 50$ nm, the real and the imaginary parts of the averaged 2d spectra change their curve progression. Since the box size is related to the concentration of QDs in the solvent, around this critical region, the QDs change their physical behavior depending to the averaged distances between each other. For a high QD concentration, the QDs are coupled to each other since the averaged distance are small enough that the Coulomb coupling plays an important role. As a consequence, a QD clustering induced by couplings occurs [136]. If the concentration decreases, the distances decreases as well, cf. Fig. 5.3. Thus, the QDs freely move inside the solvent and

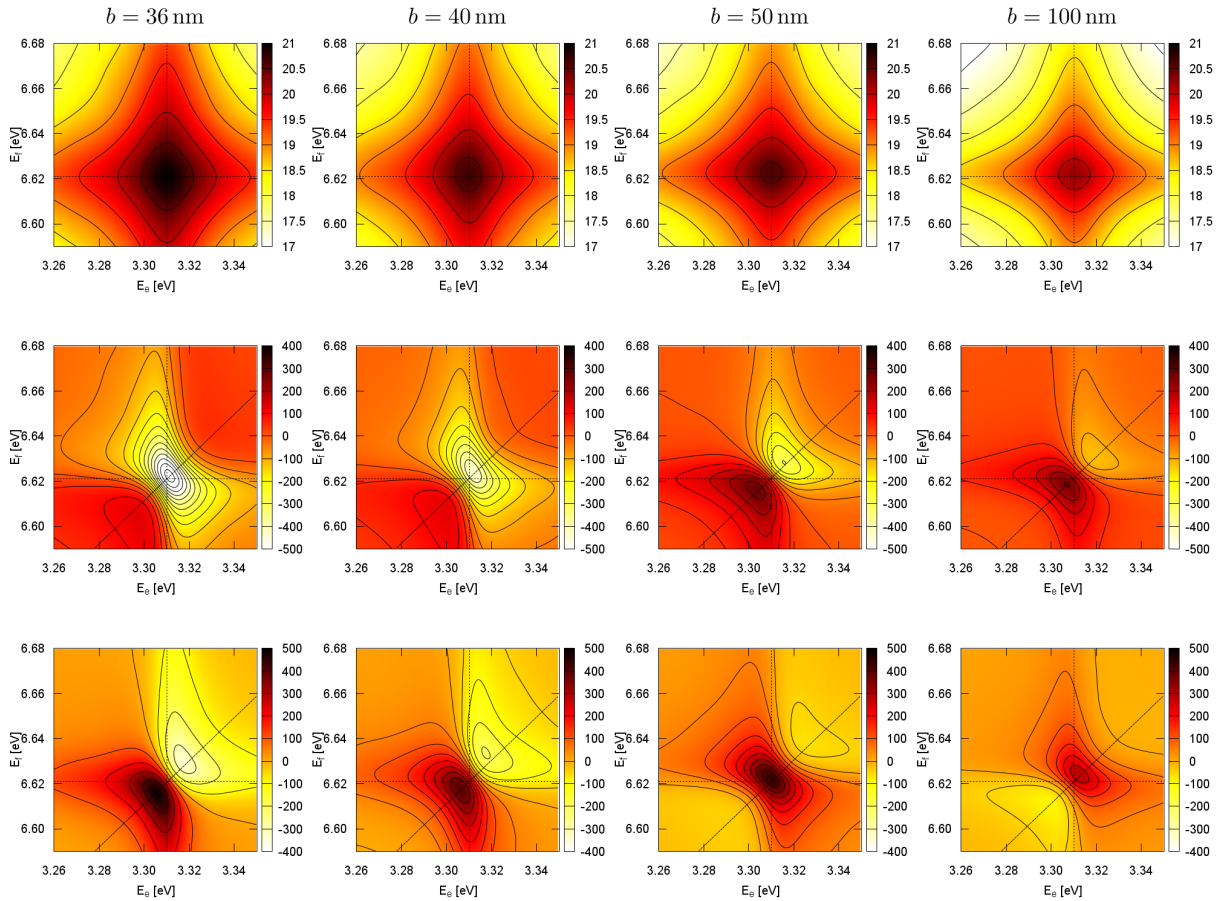


Figure 5.10 Averaged DQCS and their real and the imaginary parts calculated for different sized boxes b . The calculations are done for a solvent's viscosity of $\nu = 1$ mPas and a temperature of $T = 300$ K. For an increasing box size the amplitude in the DQCS decreases. For box sizes between $b = 36$ nm and $b = 50$ nm a phase shift occurs and the signatures in the real and the imaginary part broke the symmetry along the dotted antidiagonal and switch their curve progression.

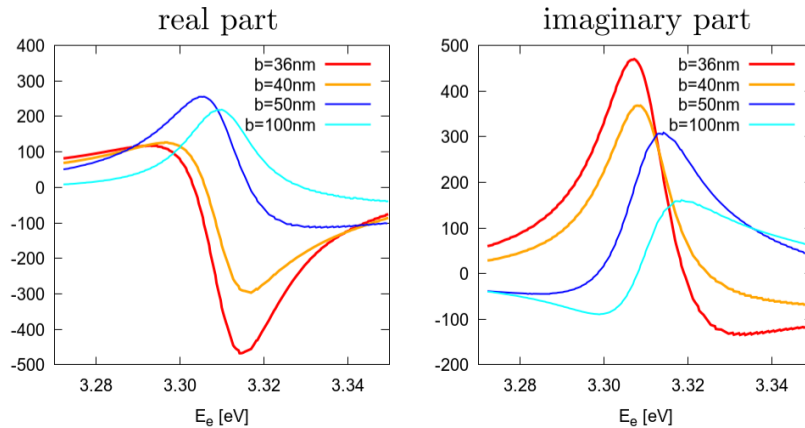


Figure 5.11 Cuts along the diagonal through the real and the imaginary parts of 2d spectra depicted in Fig. 5.10 for different box sizes b . Since the curve progression changes for box width bigger than $b = 40$ nm, the cuts show the phase transformation in the real and the imaginary part. For the real parts the minima vanish and maxima occur. For both phase contributions, the extrema are switched and shifted along the exciton axis.

the occurrence of QD accumulations becomes more and more improbably.

To demonstrate the phase shift in the real and the imaginary parts of the DQCS, 1d cuts through the 2d maps along the antidiagonal giving in Fig. 5.10 are plotted in Fig. 5.11. The cuts clearly illustrate that the curve progression changes with an increasing box size b . Especially for the real part, it is visible that the minima of simulation boxes vanish and maxima occur for boxes with a size of $b = 50$ nm or higher. Accordingly, an analysis of the phase of the real or the imaginary part of an averaged 2d spectra provides information on the concentration of the QDs in the solvent concerning the occurrence of QD accumulations. Especially if the colloidal QDs are surrounded by ligand molecules [137], van der Waals forces occur and increase the formation of clusters [135]. Since the characterizing of small clusters is challenging [135, 137], an analysis of the signatures in the 2d spectra may be a helpful tool to get information on the occurrence of accumulations of colloidal QDs.

Fig. 5.12 shows cuts through the averaged signatures in the DQCS for different sizes of the simulation box. On the left hand side, the diagrams gives the amplitude of the signatures in the spectra, while on the right hand side the cuts are normalized. For an increasing box size the amplitudes decrease except of the case $b = 20$ nm. In this case the concentration of the QDs is very high and the distances between the dots are very small. As discussed in Sec. 3.3, for small distances the influence of the Coulomb coupling is high. But if the QDs are very close to each other, they couple to more than one other QDs. The model used for these calculations needs to be adapted, as discussed in Sec. 5.2.1. Furthermore, if the averaged distances between the QDs are very small, the Brownian motion of the QDs is very constricted by the simulation boxes and an unphysical trembling of the QDs occurs. Thus, to get valid information, the averaged distances between the QDs and therefore the simulation boxes should not be smaller than the magnitude of the radius of the QDs.

Generally, the curve progression of the cuts through the averaged signatures in the DQCS for different sized boxes are similar to each other. On the right hand side of Fig. 5.12, the normalized cuts show lightly differing curve progressions. For small simulation boxes the Coulomb shifts are increased due to small distances occurring more often. Thus, the signatures in the averaged spectra are broadened. This broadening decreases for an increasing box size. The effect ends in the region of the phase shifts in the real and imaginary part ($b = 40$ nm and $b = 50$ nm). In this

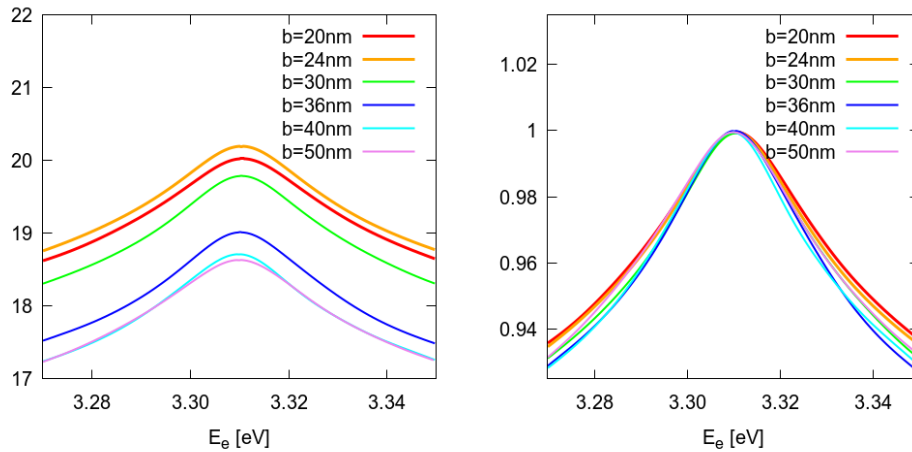


Figure 5.12 Cuts through the averaged signatures in the DQCS along the exciton axis for varying box sizes b . On the left hand side the cuts show an decreasing amplitude for an increasing box size. On the right hand side the curves are normalized and thus, changes in the curve progression are visible. For an increasing box size the broadening of the peak in the DQCS decreases. The effect is reserved in the region of the phase shift starting by $b = 40$ nm.

region the curve progression changes and the signatures are again broadened.

For further investigate the influence of the simulation box size on the averaged spectroscopic signatures, 1d cuts through the main peak in the DQCS parallel to the exciton axis are calculated. The cuts are done through the 2d maps of the absolute value, the real part and the imaginary parts, given in the diagrams in Fig. 5.13. To get a better description concerning the QD concentration, the curves are scaled by the inverse of the box volume. In the top of Fig. 5.13 the diagrams show that the amplitudes strongly decreases with increasing size of the simulation boxes b . The quantity of QD arrangements in the Brownian motion with small distances between the QDs determines the amplitude of the signal in the averaged spectra. If the concentration of QDs in the solvent is high, many Coulomb induced single signatures are added in the averaged spectrum which provokes an increasing amplitude of the signal. The curves at the bottom of Fig. 5.13 result from the extrema of the cuts. The maximum of the absolute value of the spectroscopic signatures show a box size induced decreasing. This is related to the decreasing of the strength of the Coulomb coupling with increasing distance, cf. Sec. 3.3.1.

Fig. 5.13 shows that the amplitude of the real part (middle diagrams) and the imaginary part (right hand side) decrease with increasing size of the boxes in the same magnitude as the absolute value. Caused by the strong decreasing of the amplitude and the scaling concerning a volume unit, the phase shift illustrated in Fig. 5.11 is almost vanishing. The diagrams in the bottom show the dependence on the box size of the real part's minima and the imaginary part's maxima. Thus, a curve progression, where the maxima and minima are switched, is not representable in this description.

In conclusion, it is visible that the size of the simulation boxes, which is related to the concentration of QDs in the solvent, influences the signatures in the averaged 2d spectra. Accordingly, an analysis of the averaged DQCS provides information on the concentration of the QDs and their averaged arrangement. Especially the real or the imaginary part enable conclusions on the average distances between the QDs and concerning effects of accumulations of the colloidal QDs. In the following, it will be investigated how the parameters determining the Brownian motion of the QDs influences the signatures in the averaged 2d spectra.

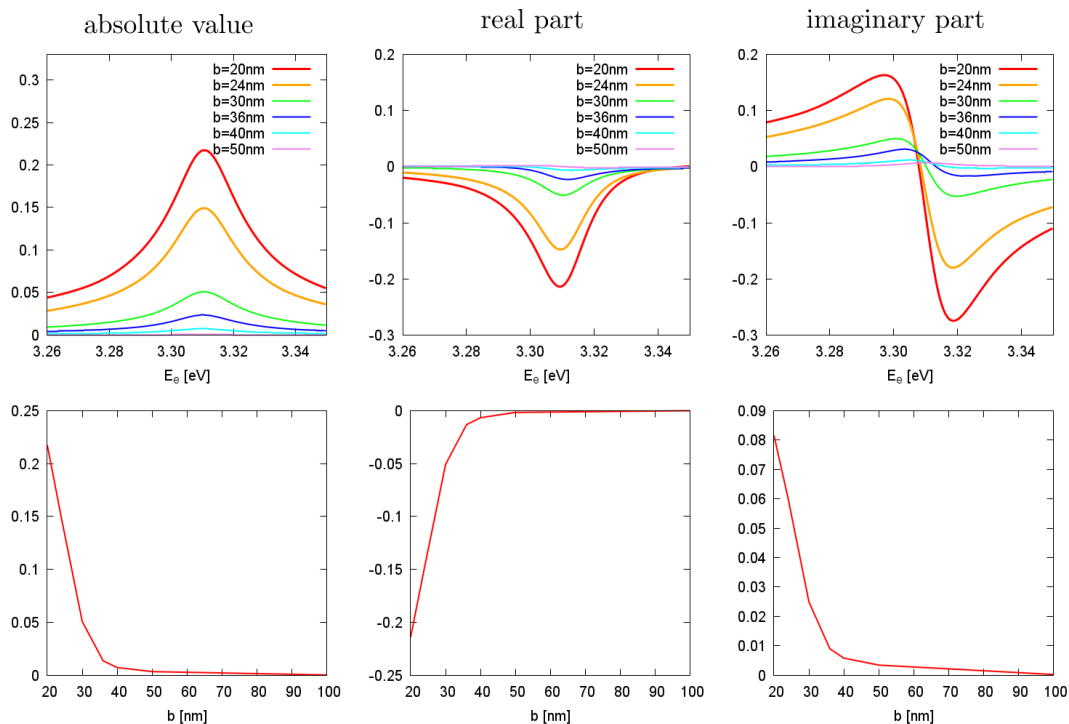


Figure 5.13 Minima and maxima of cuts through the absolute value and the real and imaginary parts of the DQCS for different sized boxes. On the top, the cuts show an decreasing amplitude for a increasing size of the simulation box b . The curves are scaled by the inverse of the volume unit of the simulation box. On the bottom the dependence of the extrema is given as a function of the box size. The distance depending decreasing is determined by the strength of the Coulomb coupling.

5.3.2 Influence of the solvent's viscosity

In the last section, we have shown that the QD concentration, given by the size of the periodic simulation boxes, determines the signatures in the averaged 2d spectra. In this section, we investigate how the solvent's viscosity influences the averaged spectroscopic signatures. The Brownian motion of the colloidal QDs is induced by the translational and rotational diffusion in the solvent, cf. Sec. 5.1. The diffusion coefficients are determined by the size of the particles as well as the viscosity of the solvent and the temperature. Thus, these parameters describe the motion of the colloidal QDs and gives the trajectories inside the simulation boxes.

Fig. 5.14 shows that, in contrast to the variation of the box size b in Sec. 5.3.1, changes in the solvent's viscosity ν do not induce a phase transformation in the real or imaginary part. Except for a light variation in the amplitude all averaged signatures from Brownian motions in solvent with different viscosities are similar. The symmetries (and antisymmetries in the case of the real part) along the diagonal and the antidiagonal are preserved. A variation of the periodic box size indicates a change in the concentration of QDs in the solvent. Thus, the movement as well as the averaged distances between the QDs are influenced by the size of the simulation boxes. In contrast, the viscosity as well as the temperature influence the mean velocity of the colloidal QDs. Since the signatures in the spectra result from taking the mean over 20 millions positions in the simulation box, the influence of the velocity disappears in the convergent average. If the trajectory includes such a high number of positions, the spatial arrangements determined by the geometry conditions of the simulation box more influences the signatures than the velocity determining how fast the particles reach all the positions. Furthermore, since the steps in the trajectory are randomly picked, the information of the path and the velocity are not accessible.

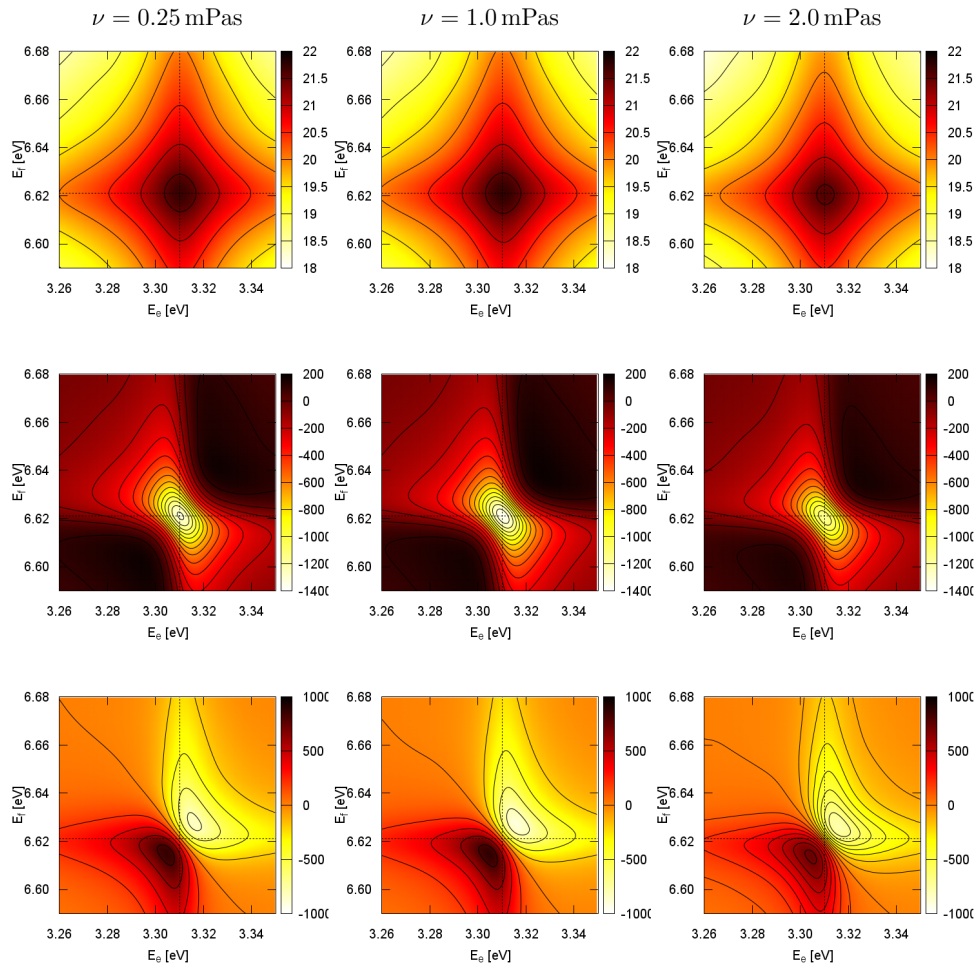


Figure 5.14 Averaged DQCS and their real and the imaginary parts calculated for different viscosities ν in a simulation box with $b = 30$ nm. The signatures for the different solvent's viscosities are generally equal. In the real and imaginary parts the symmetry as well as the phase are preserved.

In the following the interplay between the viscosity and the size of the simulation boxes shall be investigated. The calculations for Fig. 5.14 are done in a box with $b = 30$ nm. Since a phase transformation in the real and the imaginary parts occur for an increasing box size, the calculations concerning the viscosity are also done in simulation boxes with $b = 50$ nm. For bigger simulation boxes the variations in the amplitude of the signatures in the averaged DQCS in Fig. 5.15 caused by the different viscosities are increased. Again, the variation of the solvent's viscosity does not induce a phase transformation in the real or imaginary parts. In comparison to Fig. 5.14, the phases of the real and the imaginary parts are switched. Thus, the size of the simulation boxes determines the phase in the real and the imaginary parts. Furthermore, particularly visible in the imaginary parts in the bottom of Fig. 5.15, a small deviations from the symmetry perpendicular to the diagonal occur if the viscosity of the solvent differs from $\nu = 1$ mPas. For an increasing box size, the QD concentration in the solvent decreases and thus, the movement of the QDs becomes more and more freely. Therefore, the influence of the mean velocity plays a more important role, since the geometry conditions do less suppress the motion of the QDs.

To directly compare the results of the calculations concerning the solvent's viscosity done in different sized simulation boxes, 1d cuts through the absolute values, the real parts and the imaginary parts parallel to the exciton axis are done as depicted in Fig. 5.15 by the dotted lines.

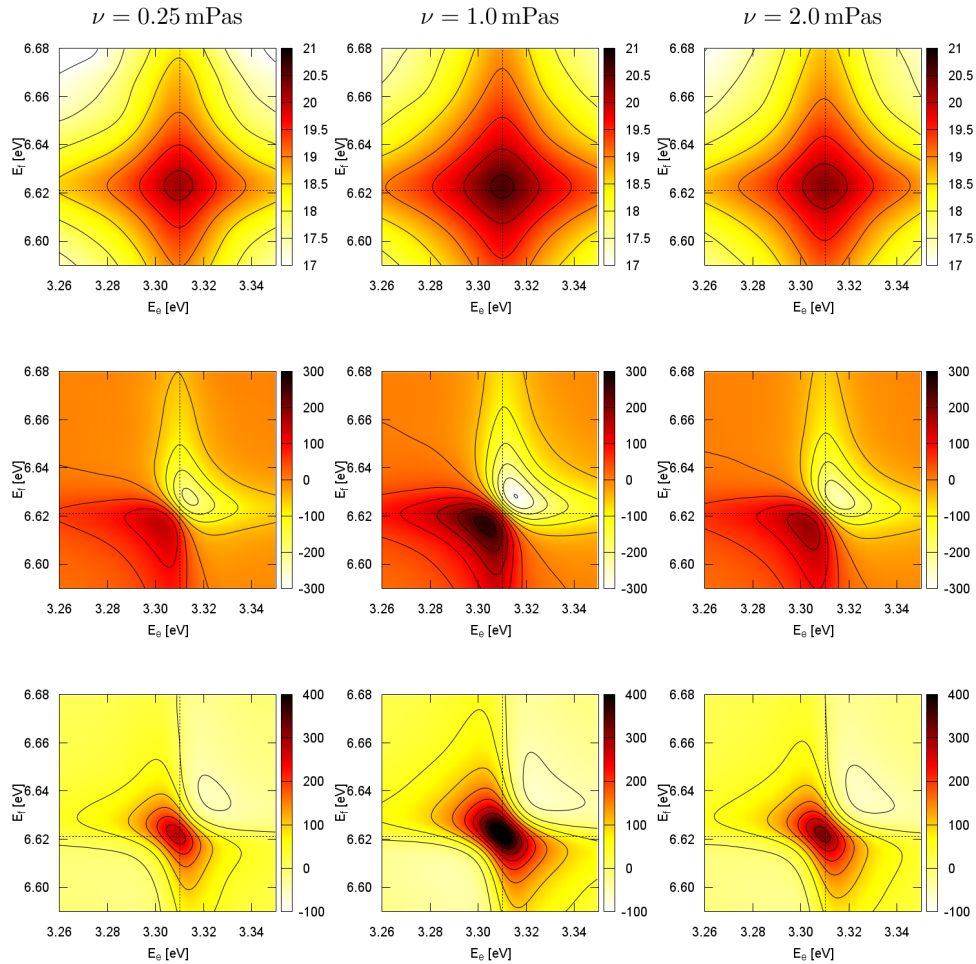


Figure 5.15 Averaged DQCS and their real and the imaginary parts calculated for different viscosities ν in a simulation box with $b = 50$ nm. Caused by the variation of the viscosity of the solvent, the amplitudes lightly changes. Although no phase transformation occurs in the real and imaginary parts, variations from the symmetry along the diagonal are visible.

Thus, the influence of the different viscosities as well as the box size is illustrated. The diagrams at the top of Fig. 5.16 results from the calculations in simulation boxes with $b = 30$ nm, while at the bottom the width of the boxes is increased to $b = 50$ nm. The cuts through the signatures of the Brownian motion inside the smaller boxes are very similar and the viscosity does lightly influences the amplitudes. For the calculations done in the boxes with an increased width, the differences in the amplitudes caused by the solvent's viscosity are more distinct. While the curves in the smaller boxes seems to be nearly convergent concerning the viscosity, the curve progressions for the calculations in the bigger simulation boxes differs from each other. The general properties, such as the phase in the real and imaginary parts are conserved in both cases. A comparison of the real and the imaginary parts resulting from the calculations done for different QD concentrations (diagrams in the middle and on right hand side) show, that the curve progressions and thus the phases are switched.

Since the concentration of the QDs in the solvent determines the strength of the Coulomb coupling between the QDs, which directly influences the signatures in the DQCS, the viscosity defines the mean velocity of the QDs in the solvent. For long trajectories in the Brownian motion, where the signatures reached their convergence, the specific trajectory does not influence the signatures in the averaged spectra. Thus, for stochastic convergent signatures in the aver-

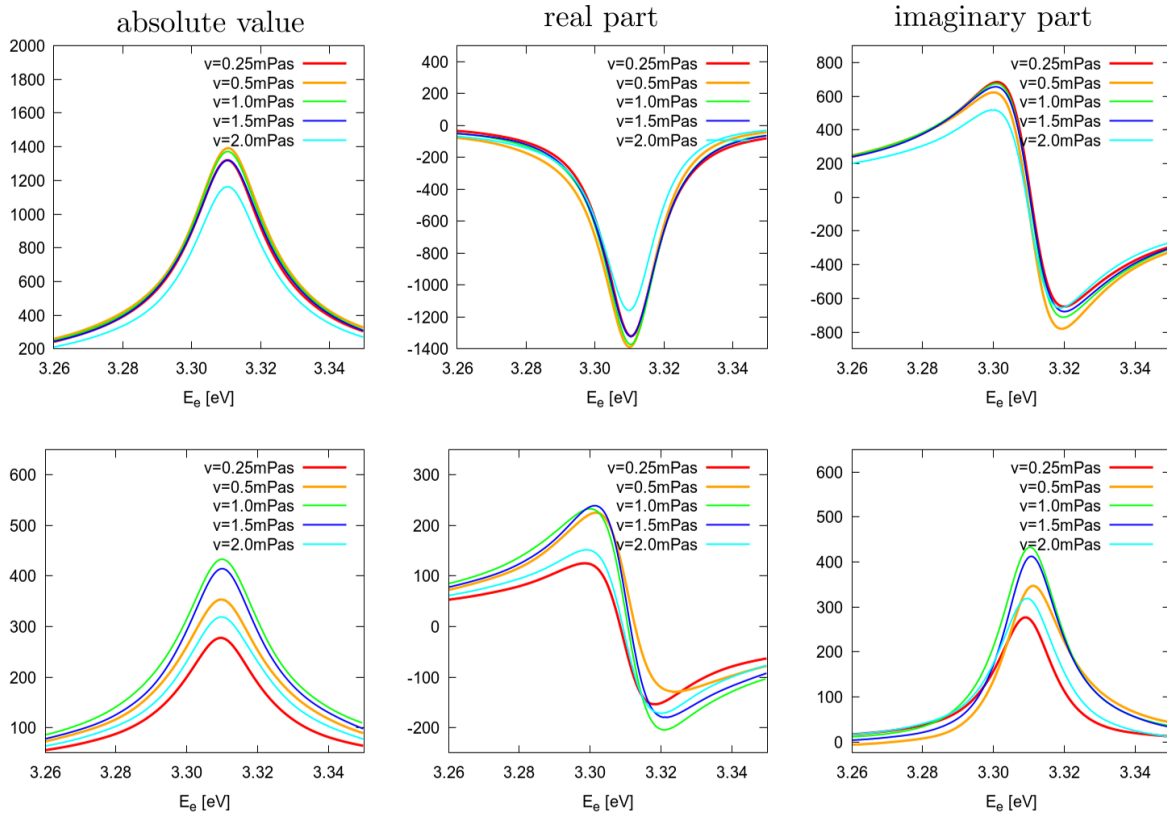


Figure 5.16 Cuts through the absolute value, the real and the imaginary part for varying viscosities. The diagrams at the top show the calculations done in a simulation box with width $b = 40$ nm, while the diagrams at the bottom are done with $b = 50$ nm. For the smaller simulation box, the motions determined by the different viscosities are very similar, while in the case of the bigger box deviations caused by the viscosity occurs. A comparison of the real and the imaginary parts calculated in the different simulation boxes shows that the phases are switched.

aged DQCS, the influence of the mean velocity determined by the solvent's viscosity and the temperature nearly vanishes.

5.4 Conclusion

The diffusion of Coulomb coupled colloidal QDs was calculated in the formalism of the Brownian motion. Since the QDs change their positions as well as their angular orientations, the trajectories were determined by the translational and the rotational diffusion. For analyzing the statistic motion of the colloidal QDs in the solvent, the DQCS was used due to the signatures in this multidimensional coherent spectroscopy are induced by the spatially depending Coulomb coupling between the QDs. Since the diffusion occurs on a different time scale than the optical processes determining the spectra, the multidimensional spectroscopy does not influence the motion of the QDs. Therefore, it presents a promising tool for visualizing the QD arrangements.

To get characteristic signatures in the averaged spectra, a huge number of QD positions was included in the trajectories of the colloidal QDs. For each step in the trajectory the strength of the Coulomb coupling as well as the spectroscopic signatures were calculated to determine the averaged DQCS. A convergence concerning the angular and the translational diffusion was reached with an estimated error of 10 %, if the trajectories includes 20 million steps, randomly and distance dependent picked, each with an own angular orientation. The calculations concerning

the Coulomb coupling are done using the point-dipole approximation adapted to the parameters given by the full calculations of the model system. If the motion of the QDs included such a high number of positions, the spectroscopic signatures were not influenced by the current trajectories but by the characteristics of the QD arrangements. Thus, the interplay between the concentration of the QDs in the solvent, given by the size of the periodic simulation boxes, and the signatures in the averaged spectra were investigated.

Since for a high QD concentration the averaged distances between the QDs are small, the high strength of the Coulomb coupling induced characteristic spectroscopic signatures. For a decreasing QD concentration, the distances decrease as well and a phase transformation in the real and imaginary part of the DQCS was investigated. Geometrically, the motion of the QDs is restricted by the concentration of the QDs in the solvent, while the mean velocity is determined by the viscosity of the solvent and the temperature. In the stochastic convergent spectra, the influence of the velocity was nearly vanished, while the QD arrangement caused specific characteristics in the spectroscopic signatures. Especially the phase of the real or imaginary parts allowed conclusions concerning accumulation of the QDs to be drawn. If the concentration of the QDs in the solvent is high, stochastically driven clusters of QDs are formed. For an decreasing concentration the occurrence of such accumulations of QDs decreases and a phase transformation in the imaginary and real parts was observed.

An analysis of the signatures in the averaged 2d spectra can be used to get information on the interplay between the spatial Coulomb depending coupling and the Brownian motion of colloidal QDs. Especially effects caused by specific averaged distances between the QDs, such as the accumulations of QDs, are accessible using multidimensional coherent spectroscopy.

Chapter 6

Conclusion

6.1 Summary

In this thesis, the double quantum coherence spectroscopy was used for the visualization and an analysis of the interplay between the Brownian motion of colloidal QDs and the arrangement-dependent Coulomb coupling.

The diffusion of the colloidal QDs in the solvent frequently induces changes in the spatial positions and the angular orientations of the QDs. Thus, in the first main part of the thesis, the influence of these changes in the QD arrangements on the Coulomb coupling was investigated. For numerical efficient calculations, the Poisson Green's function method was presented. This method reduces the number of integrals in real space and enables a fast calculation of the Coulomb coupling elements. Since the method is not restricted to specific symmetries or an explicit Green's function, it presents a very general approach for the calculation of Coulomb coupling elements. It was shown, that monopole-monopole and dipole-dipole coupling elements can be identified without a specification of the Green's function. Accordingly, the intradot as well as the interdot monopole-monopole Coulomb coupling and the Förster interaction were calculated as a function of the spatial positions and the angular orientations of two colloidal QDs respectively. While the intradot coupling elements reached a material specific saturation value, the interdot couplings decreased with increasing distance. Furthermore, the Förster elements were strongly influenced by the relative dipole-dipole orientation of the QDs.

Since the Poisson Green's function method naturally includes the influence of a spatial-dependent dielectric permittivity, the influence of the dielectric mismatch on the Coulomb coupling elements was demonstrated. Furthermore, the Coulomb coupling in a homogeneous medium was calculated. Additionally, the point-dipole approximation for a very fast calculation of a high number of dipole-dipole coupling elements was introduced in a homogeneous environment and the results were compared with the fully calculated Coulomb coupling elements. If the approximation is adapted to the results of the full calculation, the spatial- and angular-dependent dipole-dipole coupling was reproduced very well. But the point-dipole approximation suppose the environment to be homogeneous and it only includes the interdot dipole-dipole couplings. Nevertheless, for distances between the QDs which are not smaller than the QD's radius, the arrangement-dependent Förster interaction was well described in the approach of the point-dipole approximation.

Since the signatures in the double quantum coherence spectroscopy are directly determined by coupling processes, 2d spectra were calculated to analyze the correlation between the different QD arrangements and the Coulomb coupling. After the formalism was introduced in the fourth chapter, the spectroscopic signatures of QDs in different distances and with varying angular orientations were calculated. It was shown, that specific peaks and shifts occurred in the 2d

spectra dependent on the positioning of the colloidal QDs. For small distances between the QDs, the spectra showed a splitting of the signatures, while the peaks coincided with an increasing distance. If the QDs were arranged in large distances, the 2d spectra showed one exciton and two double exciton peaks. These peaks were determined by the material specific intradot couplings. This spatial-dependent behavior of the signatures in the 2d spectra was observed for the fully calculated Coulomb coupling elements and for the adapted point-dipole approximation. Furthermore, it was shown, that the occurrence of signatures was determined by a complex interplay between the angular orientations of the colloidal QDs and the polarization of the exciting laser pulses. Finally, it was demonstrated, that an increase of the temperature-dependent dephasing rate resulted in a broadening of the spectroscopic signatures. Though the 2d spectra only included one peak for all QD arrangements, arrangement-specific shifts occurred. Hence, the signatures in the 2d spectra provided information on the spatial positioning of the colloidal QDs.

In chapter five, the formalism of the Brownian motion was presented to describe the diffusion of colloidal QDs in the solvent. The approach was implemented by simulation boxes with periodic boundary conditions including two QDs. The size of these simulation boxes represented the concentration of QDs in the solvent. The Brownian motion of the QDs is given by trajectories in which the time steps are determined by the translational positions and the angular orientations for each QD respectively. It was shown, that millions of spatial positions were needed to reach a convergence concerning varying trajectories. Thus, averaged 2d spectra were determined, calculated by millions of single spectra for each of these QD arrangements. For a fast calculation of the Coulomb coupling for this huge number of QD arrangements, the point-dipole approximation was used. Since the averaged spectra resulted from stochastic convergent trajectories, characteristics of the motion, given by the viscosity of the solvent and the temperature, did not have a high impact on the spectroscopic signatures. The averaged distances, which were determined by the QD concentration, influenced the strength of the signatures. Furthermore, a phase transformation in the real and imaginary part occurred, induced by changes in the QD concentrations which were connected with the occurrence of QD accumulations.

Finally, it can be concluded, that the spatial arrangements of the colloidal QDs relative to each other strongly influenced the Coulomb coupling between them. This effect was visualized by double quantum coherence spectra which showed coupling-dependent signatures. Thus, the different QD positions resulted in characteristic signatures in the 2d spectra. For describing the Brownian motion of the colloidal QDs, these single signatures were added to get an averaged spectra. These stochastic convergent spectra provided information on the averaged distances between the QDs and therefore, they allowed conclusions concerning the QD concentration and accumulations to be drawn.

6.2 Outlook

To extend the analysis of the correlation between the Coulomb coupling and the spectroscopic signatures in the multidimensional spectra, as it was presented in this thesis, the influence of the diffusion of non-spherical QDs [138] such as nanorods [139] can be investigated. Effects and signatures caused by the relation of the axes in such ellipsoidal colloidal QDs can be analyzed. Using the Poisson Green's function method directly enables the calculation of the Coulomb coupling between non-spherical particles. The formalism of the Brownian motion can be extended to spheroids with two identical axes by introducing products of the frictional forces caused by the different axial elongation of the ellipsoids [140]. Therefore, specific signatures and shifts caused by an oblate or prolate spheroidal form of nanorod QDs can be investigated using the presented approach based on the double quantum coherence spectroscopy. Due to the Poisson Green's function method being very general, even the Coulomb coupling between arbitrarily shaped

colloidal QDs can be calculated. Therefore, the position-dependent spectroscopic signatures from non-spherical and non-ellipsoidal colloidal QDs can be calculated. Nevertheless a description of the motion of such QDs and a definition of the relative orientation will be quite difficult [131].

The relation between the stochastic accumulation of the colloidal QDs and the formation of QD clusters concerning the couplings between the QDs should be analyzed. Thus, further investigations and a quantitative description of the correlation between the spectroscopic signatures and the size of the QD clusters [135, 136] should be conducted. In particular for tracking the Brownian motion of QD clusters [135] and determining their trajectories [23], information concerning the averaged size of the clusters may be useful. Furthermore, the orientation-dependent clustering of non-spherical QDs, such as nanorods, could be investigated following the presented approach of the visualization using the 2d spectroscopy [141].

The formation of QD clusters is connected to the characteristics as well as the occurrence and thickness of ligands surrounding the QDs [137]. The QD type as well as the size of the QDs are influenced by the ligand and the shell thickness [7, 69]. Ligands surrounding the colloidal QDs create a barrier to the molecules of the solvent and therefore, they influence the QD-solvent interaction [69] and determine the strength of the Coulomb coupling. Therefore, characteristics in the 2d spectra can be used for further analyzing the correlation between the couplings and thickness of the ligands and the shell. If the barrier was compact enough, the QD-ligand interaction would dominate the observed effects caused by the dielectric environment [69]. Additionally, the influence of the size-dependent band gap and the spectroscopic signatures in the double quantum coherence spectra can be investigated and quantitatively analyzed [142].

The results of the analysis of the signatures in the double quantum coherence spectra can be compared and completed with other multidimensional spectroscopic methods. The choice of the time intervals which will be transformed into the Fourier domain and thus giving the axes and signatures in the 2d spectra, can be simply changed [80]. Accordingly exciton to biexciton coherences will occur in the spectra. Furthermore, signatures in other multidimensional coherent spectra can be calculated, such as the photo echo allowing the tracking of relaxation processes to be done [1, 118]. Combining the results from different spectroscopic methods provides further information on the correlations and electronic transitions. Thus, the interplay between the motion of colloidal QDs and the Coulomb coupling between them can be further investigated using multidimensional coherent spectroscopy.

Appendices

Appendix A

Coulomb Hamiltonian

A.1 Coulomb coupling elements determining the Hamiltonian

In this section, all Coulomb coupling elements which determine the Coulomb Hamiltonian are introduced. Thus, the total Coulomb Hamiltonian as a sum of coupling elements and electron creation and annihilation operators is formulated. The Hamiltonian is separated into the monopole-monopole and the dipole-dipole interaction part. Both are respectively divided into interdot and intradot couplings.

A.1.1 Monopole-monopole Coulomb Hamiltonian

The monopole-monopole Coulomb coupling elements for a model system of two colloidal QDs with the QD numbers $n \in \{1, 2\}$, the band index $\lambda \in \{c, v\}$ and the spin configuration $\sigma \in \{\uparrow, \downarrow\}$ are calculated as follows (A derivation of the equation is given in Sec. 3.2.2.):

$$V_{1234}^{\text{mm}} = V_{\substack{n_1 n_2 n_3 n_4 \\ \lambda_1 \lambda_2 \lambda_3 \lambda_4 \\ \sigma_1 \sigma_2 \sigma_3 \sigma_4}} = e^2 \int d^3r \int d^3r' \xi_{\lambda n}^*(\mathbf{r}) \xi_{\lambda' n'}^*(\mathbf{r}') G(\mathbf{r}, \mathbf{r}') \xi_{\lambda' n'}(\mathbf{r}') \xi_{\lambda n}(\mathbf{r}) \delta_{\sigma_1 \sigma_4} \delta_{\sigma_2 \sigma_3}. \quad (\text{A.1})$$

The Kronecker delta relations ensure the spin selection rules, since they do not appear directly. The selection rules for the QD number and the the band indices are already included in the notation. The selection rules play an important role finding all possible monopole-monopole Coulomb elements of the pure electronic Hamiltonian $H_{\text{el}} = H_0 + H_C$. For convenience, the equal quantum number indices of the monopole-monopole Coulomb coupling elements are summarized in a new notation:

$$V_{\substack{nn' n' n \\ \lambda \lambda' \lambda' \lambda \\ \sigma \sigma' \sigma' \sigma}} =: V_{\substack{nn' \\ \lambda \lambda' \\ \sigma \sigma'}}. \quad (\text{A.2})$$

Now, the monopole-monopole Coulomb coupling Hamiltonian as a summation of all coupling elements is formulated explicitly. We start with the intradot monopole-monopole elements which are given by $n = n'$. The resulting Hamiltonian of the intra-dot monopole-monopole Coulomb coupling is formulated, with respect to Pauli's exclusion principle prohibiting two fermions in

the same quantum state:

$$\begin{aligned}
H_{\text{intra}}^{\text{mm}} = & 2V_{\uparrow\downarrow}^{11} a_{v1\uparrow}^\dagger a_{v1\downarrow}^\dagger a_{v1\downarrow} a_{v1\uparrow} + 2V_{\uparrow\downarrow}^{11} a_{c1\uparrow}^\dagger a_{c1\downarrow}^\dagger a_{c1\downarrow} a_{c1\uparrow} \\
& + 2V_{\uparrow\uparrow}^{11} a_{c1\uparrow}^\dagger a_{v1\uparrow}^\dagger a_{v1\uparrow} a_{c1\uparrow} + 2V_{\downarrow\downarrow}^{11} a_{c1\downarrow}^\dagger a_{v1\downarrow}^\dagger a_{v1\downarrow} a_{c1\downarrow} \\
& + 2V_{\uparrow\downarrow}^{11} a_{c1\uparrow}^\dagger a_{v1\downarrow}^\dagger a_{v1\downarrow} a_{c1\uparrow} + 2V_{\downarrow\uparrow}^{11} a_{c1\downarrow}^\dagger a_{v1\uparrow}^\dagger a_{v1\uparrow} a_{c1\downarrow} \\
& + 2V_{\uparrow\downarrow}^{22} a_{v2\uparrow}^\dagger a_{v2\downarrow}^\dagger a_{v2\downarrow} a_{v2\uparrow} + 2V_{\uparrow\downarrow}^{22} a_{c2\uparrow}^\dagger a_{c2\downarrow}^\dagger a_{c2\downarrow} a_{c2\uparrow} \\
& + 2V_{\uparrow\uparrow}^{22} a_{c2\uparrow}^\dagger a_{v2\uparrow}^\dagger a_{v2\uparrow} a_{c2\uparrow} + 2V_{\downarrow\downarrow}^{22} a_{c2\downarrow}^\dagger a_{v2\downarrow}^\dagger a_{v2\downarrow} a_{c2\downarrow} \\
& + 2V_{\uparrow\downarrow}^{22} a_{c2\uparrow}^\dagger a_{v2\downarrow}^\dagger a_{v2\downarrow} a_{c2\uparrow} + 2V_{\downarrow\uparrow}^{22} a_{c2\downarrow}^\dagger a_{v2\uparrow}^\dagger a_{v2\uparrow} a_{c2\downarrow}. \tag{A.3}
\end{aligned}$$

Note, that all elements occur twice due to the symmetry regarding the pair-wise commutation of the indices:

$$V_{\lambda\lambda'}^{\sigma\sigma'} = V_{\lambda'\lambda}^{\sigma'\sigma}. \tag{A.4}$$

As Eq. (A.1) shows, the strength of the monopole-monopole Coulomb coupling is not directly influenced by the spin index, since the envelope functions as well as the Green's function do not directly include the spin configuration. Therefore, the monopole elements are equal regarding the spin configuration and therefore they can be summed up as follows:

$$\begin{aligned}
H_{\text{intra}}^{\text{mm}} = & 2V_{\uparrow\downarrow}^{\text{mm}} a_{v1\uparrow}^\dagger a_{v1\downarrow}^\dagger a_{v1\downarrow} a_{v1\uparrow} \\
& + 2V_{\uparrow\downarrow}^{\text{mm}} a_{c1\uparrow}^\dagger a_{c1\downarrow}^\dagger a_{c1\downarrow} a_{c1\uparrow} \\
& + 2V_{\uparrow\downarrow}^{\text{mm}} (a_{c1\uparrow}^\dagger a_{v1\uparrow}^\dagger a_{v1\uparrow} a_{c1\uparrow} + a_{c1\downarrow}^\dagger a_{v1\downarrow}^\dagger a_{v1\downarrow} a_{c1\downarrow} + a_{v1\uparrow}^\dagger a_{v1\downarrow}^\dagger a_{v1\downarrow} a_{v1\uparrow} + a_{c1\downarrow}^\dagger a_{c1\uparrow}^\dagger a_{c1\uparrow} a_{c1\downarrow}) \\
& + 2V_{\uparrow\downarrow}^{\text{mm}} a_{v2\uparrow}^\dagger a_{v2\downarrow}^\dagger a_{v2\downarrow} a_{v2\uparrow} \\
& + 2V_{\uparrow\downarrow}^{\text{mm}} a_{c2\uparrow}^\dagger a_{c2\downarrow}^\dagger a_{c2\downarrow} a_{c2\uparrow} \\
& + 2V_{\uparrow\downarrow}^{\text{mm}} (a_{c2\uparrow}^\dagger a_{v2\uparrow}^\dagger a_{v2\uparrow} a_{c2\uparrow} + a_{c2\downarrow}^\dagger a_{v2\downarrow}^\dagger a_{v2\downarrow} a_{c2\downarrow} + a_{v2\uparrow}^\dagger a_{v2\downarrow}^\dagger a_{v2\downarrow} a_{v2\uparrow} + a_{c2\downarrow}^\dagger a_{c2\uparrow}^\dagger a_{c2\uparrow} a_{c2\downarrow}). \tag{A.5}
\end{aligned}$$

Analogously, the Hamiltonian consisting of the monopole-monopole interdot Coulomb coupling elements, which is determined with $n \neq n'$ occurs

$$\begin{aligned}
H_{\text{inter}}^{\text{mm}} = & 2V_{\uparrow\uparrow}^{12} a_{v1\uparrow}^\dagger a_{v2\uparrow}^\dagger a_{v2\uparrow} a_{v1\uparrow} + 2V_{\downarrow\downarrow}^{12} a_{v1\downarrow}^\dagger a_{v2\downarrow}^\dagger a_{v2\downarrow} a_{v1\downarrow} \\
& + 2V_{\uparrow\downarrow}^{12} a_{v1\uparrow}^\dagger a_{v2\downarrow}^\dagger a_{v2\downarrow} a_{v1\uparrow} + 2V_{\downarrow\uparrow}^{12} a_{v1\downarrow}^\dagger a_{v2\uparrow}^\dagger a_{v2\uparrow} a_{v1\downarrow} \\
& + 2V_{\uparrow\uparrow}^{12} a_{c1\uparrow}^\dagger a_{c2\uparrow}^\dagger a_{c2\uparrow} a_{c1\uparrow} + 2V_{\downarrow\downarrow}^{12} a_{c1\downarrow}^\dagger a_{c2\downarrow}^\dagger a_{c2\downarrow} a_{c1\downarrow} \\
& + 2V_{\uparrow\downarrow}^{12} a_{c1\uparrow}^\dagger a_{c2\downarrow}^\dagger a_{c2\downarrow} a_{c1\uparrow} + 2V_{\downarrow\uparrow}^{12} a_{c1\downarrow}^\dagger a_{c2\uparrow}^\dagger a_{c2\uparrow} a_{c1\downarrow} \\
& + 2V_{\uparrow\uparrow}^{12} a_{c1\uparrow}^\dagger a_{v2\uparrow}^\dagger a_{v2\uparrow} a_{c1\uparrow} + 2V_{\downarrow\downarrow}^{12} a_{c1\downarrow}^\dagger a_{v2\downarrow}^\dagger a_{v2\downarrow} a_{c1\downarrow} \\
& + 2V_{\uparrow\downarrow}^{12} a_{c1\uparrow}^\dagger a_{v2\downarrow}^\dagger a_{v2\downarrow} a_{c1\uparrow} + 2V_{\downarrow\uparrow}^{12} a_{c1\downarrow}^\dagger a_{v2\uparrow}^\dagger a_{v2\uparrow} a_{c1\downarrow} \\
& + 2V_{\uparrow\uparrow}^{12} a_{v1\uparrow}^\dagger a_{c2\uparrow}^\dagger a_{c2\uparrow} a_{v1\uparrow} + 2V_{\downarrow\downarrow}^{12} a_{v1\downarrow}^\dagger a_{c2\downarrow}^\dagger a_{c2\downarrow} a_{v1\downarrow} \\
& + 2V_{\uparrow\downarrow}^{12} a_{v1\uparrow}^\dagger a_{c2\downarrow}^\dagger a_{c2\downarrow} a_{v1\uparrow} + 2V_{\downarrow\uparrow}^{12} a_{v1\downarrow}^\dagger a_{c2\uparrow}^\dagger a_{c2\uparrow} a_{v1\downarrow}. \tag{A.6}
\end{aligned}$$

Again, terms are equal regarding the spin indices and thus, they can be combined as follows:

$$\begin{aligned}
H_{\text{inter}}^{\text{mm}} = & 2V_{vv}^{\text{mm}} \left(a_{v1\uparrow}^\dagger a_{v2\uparrow}^\dagger a_{v2\uparrow} a_{v1\uparrow} + a_{v1\downarrow}^\dagger a_{v2\downarrow}^\dagger a_{v2\downarrow} a_{v1\downarrow} + a_{v1\uparrow}^\dagger a_{v2\downarrow}^\dagger a_{v2\downarrow} a_{v1\uparrow} + a_{v1\downarrow}^\dagger a_{v2\uparrow}^\dagger a_{v2\uparrow} a_{v1\downarrow} \right) \\
& + 2V_{cc}^{\text{mm}} \left(a_{c1\uparrow}^\dagger a_{c2\uparrow}^\dagger a_{c2\uparrow} a_{c1\uparrow} + a_{c1\downarrow}^\dagger a_{c2\downarrow}^\dagger a_{c2\downarrow} a_{c1\downarrow} + a_{c1\uparrow}^\dagger a_{c2\downarrow}^\dagger a_{c2\downarrow} a_{c1\uparrow} + a_{c1\downarrow}^\dagger a_{c2\uparrow}^\dagger a_{c2\uparrow} a_{c1\downarrow} \right) \\
& + 2V_{cv}^{\text{mm}} \left(a_{c1\uparrow}^\dagger a_{v2\uparrow}^\dagger a_{v2\uparrow} a_{c1\uparrow} + a_{c1\downarrow}^\dagger a_{v2\downarrow}^\dagger a_{v2\downarrow} a_{c1\downarrow} + a_{c1\uparrow}^\dagger a_{v2\downarrow}^\dagger a_{v2\downarrow} a_{c1\uparrow} + a_{c1\downarrow}^\dagger a_{v2\uparrow}^\dagger a_{v2\uparrow} a_{c1\downarrow} \right) \\
& + 2V_{vc}^{\text{mm}} \left(a_{v1\uparrow}^\dagger a_{c2\uparrow}^\dagger a_{c2\uparrow} a_{v1\uparrow} + a_{v1\downarrow}^\dagger a_{c2\downarrow}^\dagger a_{c2\downarrow} a_{v1\downarrow} + a_{v1\uparrow}^\dagger a_{c2\downarrow}^\dagger a_{c2\downarrow} a_{v1\uparrow} + a_{v1\downarrow}^\dagger a_{c2\uparrow}^\dagger a_{c2\uparrow} a_{v1\downarrow} \right).
\end{aligned} \tag{A.7}$$

The equations Eq. (A.5) and Eq. (A.7) give the total monopole-monopole Coulomb Hamiltonian. Furthermore, they show, that the monopole-monopole Coulomb coupling between two colloidal QDs is determined by ten different monopole-monopole coupling elements. Since these elements are determined by the distance between the QDs, all of them need to be calculated for each center-to-center distance separately.

A.1.2 Dipole-dipole Coulomb Hamiltonian

In this section, we determine all elements of the dipole-dipole Coulomb Hamiltonian. The strength of the dipole-dipole coupling is given by (as calculated in Sec. 3.2.3):

$$V_{1234}^{\text{dd}} = \int d^3r \int d^3r' \nabla_{\mathbf{r}} \cdot \left(\xi_{\lambda_1 n_1}^*(\mathbf{r}) \boldsymbol{\mu}_{14} \xi_{\lambda_4 n_4}(\mathbf{r}) \right) G(\mathbf{r}, \mathbf{r}') \nabla_{\mathbf{r}'} \cdot \left(\xi_{\lambda_2 n_2}^*(\mathbf{r}') \boldsymbol{\mu}_{23} \xi_{\lambda_3 n_3}(\mathbf{r}') \right) \delta_{\sigma_1 \sigma_4} \delta_{\sigma_2 \sigma_3}. \tag{A.8}$$

The dipole-dipole coupling is the Coulomb interaction between the divergences of the microscopic dipole transitions and the overlap of the connected envelope functions. The microscopic dipole transitions

$$\boldsymbol{\mu}_{ll'} = \frac{1}{V_{\text{EZ}}} \int d^3s_i u_{\lambda_l n_l}^*(\mathbf{s}_i) \mathbf{s}_i u_{\lambda_{l'} n_{l'}}(\mathbf{s}_i) \delta_{\sigma_l \sigma_{l'}} \delta_{n_l n_{l'}} \tag{A.9}$$

occurs spin-preserving and in one QD as a material parameter. The delta conditions in Eq. (A.9) determines the spin and QD number indices preservation for the dipole-dipole Coulomb interaction. The dipole moments $\boldsymbol{\mu}_{ll'}$ vanishes for equal indices $l = l'$ leading to $\lambda_1 \neq \lambda_4$ and $\lambda_2 \neq \lambda_3$. Furthermore, the principle of energy conservation gives $\lambda_1 \neq \lambda_2$ and $\lambda_3 \neq \lambda_4$. Thus, the non-vanishing dipole-dipole coupling elements show alternating band indices. Therefore, the following notation is introduced:

$$V_{1234}^{\text{dd}} = V_{\substack{\lambda\lambda'\lambda\lambda' \\ nn'n'n \\ \sigma\sigma'\sigma'\sigma}} =: \mathcal{V}_{\substack{\lambda\lambda' \\ nn' \\ \sigma\sigma'}}. \tag{A.10}$$

Note, that this abbreviation differs from the notation used for the monopole-monopole elements in Eq. (A.2) regarding the order of the band indices.

The Förster excitation transfer between the quantum dots represents the most important dipole-dipole Coulomb coupling. As interdot coupling the QD indices needs to be different $n \neq n'$. Hence, the Hamiltonian of the Förster energy transfer reads

$$\begin{aligned}
H_{\text{C}}^{\text{F}} = & 2\mathcal{V}_{\uparrow\uparrow}^{cv} a_{c1\uparrow}^\dagger a_{v2\uparrow}^\dagger a_{c2\uparrow} a_{v1\uparrow} + 2\mathcal{V}_{\downarrow\downarrow}^{cv} a_{c1\downarrow}^\dagger a_{v2\downarrow}^\dagger a_{c2\downarrow} a_{v1\downarrow} \\
& + 2\mathcal{V}_{\uparrow\downarrow}^{cv} a_{c1\uparrow}^\dagger a_{v2\downarrow}^\dagger a_{c2\downarrow} a_{v1\uparrow} + 2\mathcal{V}_{\downarrow\uparrow}^{cv} a_{c1\downarrow}^\dagger a_{v2\uparrow}^\dagger a_{c2\uparrow} a_{v1\downarrow} \\
& + 2\mathcal{V}_{\uparrow\uparrow}^{vc} a_{v1\uparrow}^\dagger a_{c2\uparrow}^\dagger a_{v2\uparrow} a_{c1\uparrow} + 2\mathcal{V}_{\downarrow\downarrow}^{vc} a_{v1\downarrow}^\dagger a_{c2\downarrow}^\dagger a_{v2\downarrow} a_{c1\downarrow} \\
& + 2\mathcal{V}_{\uparrow\downarrow}^{vc} a_{v1\uparrow}^\dagger a_{c2\downarrow}^\dagger a_{v2\downarrow} a_{c1\uparrow} + 2\mathcal{V}_{\downarrow\uparrow}^{vc} a_{v1\downarrow}^\dagger a_{c2\uparrow}^\dagger a_{v2\uparrow} a_{c1\downarrow}.
\end{aligned} \tag{A.11}$$

Again, all elements are count twice due to the symmetry of the pair-wise commutation of all indices resulting from the symmetry of the Green's function. Respecting the symmetry condition of the Förster coupling elements regarding the change of the band index, the following spin-selective abbreviation can be introduced:

$$\mathcal{V}_{\uparrow\uparrow}^{cv} = (\mathcal{V}_{\uparrow\uparrow}^{vc})^* := \mathcal{V}_{\uparrow\uparrow}. \quad (\text{A.12})$$

Using this notation, the Hamiltonian of the Förster interactions can be simplified

$$\begin{aligned} H_C^F &= 2\mathcal{V}_{\uparrow\uparrow} a_{c1\uparrow}^\dagger a_{v2\uparrow}^\dagger a_{c2\uparrow} a_{v1\uparrow} + 2\mathcal{V}_{\downarrow\downarrow} a_{c1\downarrow}^\dagger a_{v2\downarrow}^\dagger a_{c2\downarrow} a_{v1\downarrow} \\ &+ 2\mathcal{V}_{\uparrow\downarrow} a_{c1\uparrow}^\dagger a_{v2\downarrow}^\dagger a_{c2\downarrow} a_{v1\uparrow} + 2\mathcal{V}_{\downarrow\uparrow} a_{c1\downarrow}^\dagger a_{v2\uparrow}^\dagger a_{c2\uparrow} a_{v1\downarrow} \\ &+ 2\mathcal{V}_{\uparrow\uparrow}^* a_{v1\uparrow}^\dagger a_{c2\uparrow}^\dagger a_{v2\uparrow} a_{c1\uparrow} + 2\mathcal{V}_{\downarrow\downarrow}^* a_{v1\downarrow}^\dagger a_{c2\downarrow}^\dagger a_{v2\downarrow} a_{c1\downarrow} \\ &+ 2\mathcal{V}_{\uparrow\downarrow}^* a_{v1\uparrow}^\dagger a_{c2\downarrow}^\dagger a_{v2\downarrow} a_{c1\uparrow} + 2\mathcal{V}_{\downarrow\uparrow}^* a_{v1\downarrow}^\dagger a_{c2\uparrow}^\dagger a_{v2\uparrow} a_{c1\downarrow}. \end{aligned} \quad (\text{A.13})$$

Thus, the Förster Hamiltonian H_C^F consists of spin preserving $V_{\uparrow\uparrow}$ and $V_{\downarrow\downarrow}$ Coulomb elements as well as spin flipping $V_{\uparrow\downarrow}$ and $V_{\downarrow\uparrow}$ elements.

For calculating the full Coulomb Hamiltonian, the dipole-dipole intradot Coulomb coupling elements, where both electrons are arranged in one quantum dot, need to be included

$$\begin{aligned} H_C^{\text{id}} &= 2\mathbb{V}_{\uparrow\downarrow}^{cv} a_{c1\uparrow}^\dagger a_{v1\downarrow}^\dagger a_{c1\downarrow} a_{v1\uparrow} + 2\mathbb{V}_{\uparrow\downarrow}^{cv} a_{c2\uparrow}^\dagger a_{v2\downarrow}^\dagger a_{c2\downarrow} a_{v2\uparrow} \\ &+ 2\mathbb{V}_{\downarrow\uparrow}^{cv} a_{c1\downarrow}^\dagger a_{v1\uparrow}^\dagger a_{c1\uparrow} a_{v1\downarrow} + 2\mathbb{V}_{\downarrow\uparrow}^{cv} a_{c1\downarrow}^\dagger a_{v1\uparrow}^\dagger a_{c1\uparrow} a_{v1\downarrow}. \end{aligned} \quad (\text{A.14})$$

Since the remaining dipole-dipole intradot elements can be summarized as complex conjugated numbers, the notation is simplified as:

$$\mathbb{V}_{\uparrow\downarrow}^{cv} = (\mathbb{V}_{\downarrow\uparrow}^{cv})^* := \mathbb{V}_1. \quad (\text{A.15})$$

Thus, the intradot dipole-dipole Coulomb Hamiltonian occurs as follows:

$$\begin{aligned} H_C^{\text{id}} &= 2\mathbb{V}_1 a_{c1\uparrow}^\dagger a_{v1\downarrow}^\dagger a_{c1\downarrow} a_{v1\uparrow} + 2\mathbb{V}_2 a_{c2\uparrow}^\dagger a_{v2\downarrow}^\dagger a_{c2\downarrow} a_{v2\uparrow} \\ &+ 2\mathbb{V}_1^* a_{c1\downarrow}^\dagger a_{v1\uparrow}^\dagger a_{c1\uparrow} a_{v1\downarrow} + 2\mathbb{V}_2^* a_{c1\downarrow}^\dagger a_{v1\uparrow}^\dagger a_{c1\uparrow} a_{v1\downarrow}. \end{aligned} \quad (\text{A.16})$$

Collecting all terms of the Coulomb coupling elements, the total Coulomb Hamiltonian reads

$$H_C = H_{\text{inter}}^{\text{mm}} + H_{\text{intra}}^{\text{mm}} + H_C^F + H_C^{\text{id}}. \quad (\text{A.17})$$

A.2 Hamiltonian matrix in the local exciton basis

In this section, the Coulomb Hamiltonian should be specified using the basis of localized bright exciton states. Therefore, the Hamiltonian is introduced as matrix into the four bright single exciton states as well as into the six local double exciton states. Using this representation into the localized exciton states, the Hamiltonian matrices can be transformed into a diagonal form for getting a description based on the eigenstates of the purely electronic Coulomb Hamiltonian.

A.2.1 Local single exciton basis

Respecting the bright states only, because the dark states are usually not excited due to the spin flip between electron and hole (bright states), the local single exciton states are

$$|X_1\rangle = a_{c1\uparrow}^\dagger a_{v1\uparrow} |g\rangle, \quad (\text{A.18})$$

$$|X_2\rangle = a_{c1\downarrow}^\dagger a_{v1\downarrow} |g\rangle, \quad (\text{A.19})$$

$$|X_3\rangle = a_{c2\uparrow}^\dagger a_{v2\uparrow} |g\rangle, \quad (\text{A.20})$$

$$|X_4\rangle = a_{c2\downarrow}^\dagger a_{v2\downarrow} |g\rangle. \quad (\text{A.21})$$

First, the off-diagonal matrix elements are calculated in the basis of the single exciton states. The total Coulomb Hamiltonian is given in Eq. (A.17).

$$\langle X_1 | H_C | X_2 \rangle = \langle g | a_{v1\uparrow}^\dagger a_{c1\uparrow} | H_C | a_{c1\downarrow}^\dagger a_{v1\downarrow} | g \rangle = 2\mathbb{V}_1, \quad (\text{A.22})$$

$$\langle X_1 | H_C | X_3 \rangle = \langle g | a_{v1\uparrow}^\dagger a_{c1\uparrow} | H_C | a_{c2\uparrow}^\dagger a_{v2\uparrow} | g \rangle = 2\mathcal{V}_{\uparrow\uparrow}, \quad (\text{A.23})$$

$$\langle X_1 | H_C | X_4 \rangle = \langle g | a_{v1\uparrow}^\dagger a_{c1\uparrow} | H_C | a_{c2\downarrow}^\dagger a_{v2\downarrow} | g \rangle = 2\mathcal{V}_{\uparrow\downarrow}. \quad (\text{A.24})$$

The other off-diagonal elements are calculated in an analog way. The free particle and the monopole-monopole terms of the Hamiltonian, given in Eqs. (A.5) and (A.7), determine the diagonal elements of the Hamiltonian matrix in the basis of the four local single exciton states. These diagonal matrix elements are calculated as follows:

$$\langle X_1 | H_C | X_1 \rangle = \varepsilon_{c1} + \varepsilon_{v1} + 2\varepsilon_{v2} + 2V_{cv}^{\uparrow\downarrow} + 2V_{vv}^{\downarrow\downarrow} + 2V_{vv}^{\downarrow\downarrow} + 2V_{vv}^{\downarrow\downarrow} + 2V_{cv}^{\uparrow\uparrow} + 2V_{cv}^{\uparrow\downarrow}, \quad (\text{A.25})$$

$$\langle X_2 | H_C | X_2 \rangle = \varepsilon_{c1} + \varepsilon_{v1} + 2\varepsilon_{v2} + 2V_{cv}^{\downarrow\downarrow} + 2V_{vv}^{\downarrow\downarrow} + 2V_{vv}^{\downarrow\downarrow} + 2V_{vv}^{\downarrow\downarrow} + 2V_{cv}^{\uparrow\downarrow} + 2V_{cv}^{\downarrow\downarrow}, \quad (\text{A.26})$$

$$\langle X_3 | H_C | X_3 \rangle = 2\varepsilon_{v1} + \varepsilon_{v2} + \varepsilon_{c2} + 2V_{vv}^{\uparrow\downarrow} + 2V_{cv}^{\uparrow\downarrow} + 2V_{vv}^{\downarrow\downarrow} + 2V_{vv}^{\downarrow\downarrow} + 2V_{vc}^{\uparrow\uparrow} + 2V_{vc}^{\downarrow\downarrow}, \quad (\text{A.27})$$

$$\langle X_4 | H_C | X_4 \rangle = 2\varepsilon_{v1} + \varepsilon_{v2} + \varepsilon_{c2} + 2V_{vv}^{\uparrow\downarrow} + 2V_{cv}^{\uparrow\downarrow} + 2V_{vv}^{\downarrow\downarrow} + 2V_{vv}^{\downarrow\downarrow} + 2V_{vc}^{\uparrow\downarrow} + 2V_{vc}^{\downarrow\downarrow}. \quad (\text{A.28})$$

Since the strength of the monopole-monopole Coulomb coupling elements is not determined by the spin configuration, the equations can be combined in a more simple way. Therefore, some abbreviations are introduced:

$$\mathcal{E}_0 = 2\varepsilon_{v1} + 2\varepsilon_{v2} + 2V_{vv}^{\uparrow\downarrow} + 2V_{vv}^{\uparrow\downarrow} + 8V_{vv}^{\uparrow\downarrow}, \quad (\text{A.29})$$

$$\mathcal{E}_1 = \varepsilon_{c1} - \varepsilon_{v1} - 2V_{vv}^{\uparrow\downarrow} + 2V_{vv}^{\uparrow\downarrow} - 4V_{vv}^{\uparrow\downarrow} + 4V_{cv}^{\uparrow\downarrow}, \quad (\text{A.30})$$

$$\mathcal{E}_2 = \varepsilon_{c2} - \varepsilon_{v2} - 2V_{vv}^{\uparrow\downarrow} + 2V_{vv}^{\uparrow\downarrow} - 4V_{vv}^{\uparrow\downarrow} + 4V_{vc}^{\uparrow\downarrow}. \quad (\text{A.31})$$

Now, the Coulomb Hamiltonian in the basis of the four local bright single exciton states results:

$$H_{\text{el}XX} = \begin{pmatrix} \mathcal{E}_0 + \mathcal{E}_1 & 2\mathbb{V}_1 & 2\mathcal{V}_{\uparrow\uparrow} & 2\mathcal{V}_{\uparrow\downarrow} \\ 2\mathbb{V}_1^* & \mathcal{E}_0 + \mathcal{E}_1 & 2\mathcal{V}_{\downarrow\uparrow} & 2\mathcal{V}_{\downarrow\downarrow} \\ 2\mathcal{V}_{\uparrow\uparrow}^* & 2\mathcal{V}_{\downarrow\uparrow}^* & \mathcal{E}_0 + \mathcal{E}_2 & 2\mathbb{V}_2 \\ 2\mathcal{V}_{\uparrow\downarrow}^* & 2\mathcal{V}_{\downarrow\downarrow}^* & 2\mathbb{V}_2^* & \mathcal{E}_0 + \mathcal{E}_2 \end{pmatrix}. \quad (\text{A.32})$$

A.2.2 Local double exciton basis

The six local bright biexciton states created by two excitons in a two QD system are:

$$|B_1\rangle = a_{c1\uparrow}^\dagger a_{v1\uparrow} a_{c1\downarrow}^\dagger a_{v1\downarrow} |g\rangle, \quad (\text{A.33})$$

$$|B_2\rangle = a_{c1\uparrow}^\dagger a_{v1\uparrow} a_{c2\uparrow}^\dagger a_{v2\uparrow} |g\rangle, \quad (\text{A.34})$$

$$|B_3\rangle = a_{c1\downarrow}^\dagger a_{v1\downarrow} a_{c2\uparrow}^\dagger a_{v2\uparrow} |g\rangle, \quad (\text{A.35})$$

$$|B_4\rangle = a_{c1\uparrow}^\dagger a_{v1\uparrow} a_{c2\downarrow}^\dagger a_{v2\downarrow} |g\rangle, \quad (\text{A.36})$$

$$|B_5\rangle = a_{c1\downarrow}^\dagger a_{v1\downarrow} a_{c2\downarrow}^\dagger a_{v2\downarrow} |g\rangle, \quad (\text{A.37})$$

$$|B_6\rangle = a_{c2\uparrow}^\dagger a_{v2\uparrow} a_{c2\downarrow}^\dagger a_{v2\downarrow} |g\rangle. \quad (\text{A.38})$$

The diagonal elements of the Hamiltonian include the free particle energies as well as the monopole-monopole Coulomb coupling elements, which are not dependent on the spin configurations. Therefore, the elements can be combined as follows:

$$\mathcal{E}_{11} := 2V_{11}^{mm} + 2V_{11}^{mm} - 4V_{11}^{mm}, \quad (\text{A.39})$$

$$\mathcal{E}_{12} := 2V_{12}^{mm} + 2V_{12}^{mm} - 2V_{12}^{mm} - 2V_{12}^{mm}, \quad (\text{A.40})$$

$$\mathcal{E}_{22} := 2V_{22}^{mm} + 2V_{22}^{mm} - 4V_{22}^{mm}. \quad (\text{A.41})$$

For convenience, the following abbreviations for the diagonal elements of the Hamiltonian matrix are introduced:

$$E_{011} := \mathcal{E}_0 + 2\mathcal{E}_1 + \mathcal{E}_{11}, \quad (\text{A.42})$$

$$E_{012} := \mathcal{E}_0 + \mathcal{E}_1 + \mathcal{E}_2 + \mathcal{E}_{12}, \quad (\text{A.43})$$

$$E_{022} := \mathcal{E}_0 + 2\mathcal{E}_2 + \mathcal{E}_{22}. \quad (\text{A.44})$$

The Coulomb Hamiltonian matrix in the basis of the local bright double exciton states reads:

$$H_{\text{el}BB} = \begin{pmatrix} E_{011} & 2\mathcal{V}_{\downarrow\uparrow} & 2\mathcal{V}_{\uparrow\uparrow} & 2\mathcal{V}_{\downarrow\downarrow} & 2\mathcal{V}_{\uparrow\downarrow} & 0 \\ 2\mathcal{V}_{\downarrow\uparrow}^* & E_{012} & 2\mathbb{V}_1 & 2\mathbb{V}_2 & 0 & 2\mathcal{V}_{\uparrow\downarrow} \\ 2\mathcal{V}_{\uparrow\uparrow}^* & 2\mathbb{V}_1^* & E_{012} & 0 & 2\mathbb{V}_2 & 2\mathcal{V}_{\downarrow\downarrow} \\ 2\mathcal{V}_{\downarrow\downarrow}^* & 2\mathbb{V}_2^* & 0 & E_{012} & 2\mathbb{V}_1 & 2\mathcal{V}_{\uparrow\uparrow} \\ 2\mathcal{V}_{\uparrow\downarrow}^* & 0 & 2\mathbb{V}_2^* & 2\mathbb{V}_1^* & E_{012} & 2\mathcal{V}_{\downarrow\uparrow} \\ 0 & 2\mathcal{V}_{\uparrow\downarrow}^* & 2\mathcal{V}_{\downarrow\downarrow}^* & 2\mathcal{V}_{\uparrow\uparrow}^* & 2\mathcal{V}_{\downarrow\uparrow}^* & E_{022} \end{pmatrix}. \quad (\text{A.45})$$

Appendix B

Calculation of the Coulomb potential

B.1 Multidimensional Taylor expansion

In general, a multidimensional Taylor series with N expansions points reads

$$\begin{aligned} \text{T}f(x_1, \dots, x_N)|_{\mathbf{x}=\mathbf{a}} &= \sum_{n_1}^{\infty} \cdots \sum_{n_N}^{\infty} \frac{1}{n_1! \cdots n_N!} (x_1 - a_1)^{n_1} \cdots (x_N - a_N)^{n_N} \\ &\quad \cdot \frac{\partial^{n_1}}{\partial x_1^{n_1}} \cdots \frac{\partial^{n_N}}{\partial x_N^{n_N}} f(a_1, \dots, a_N). \end{aligned} \quad (\text{B.1})$$

The Coulomb coupling is determined by a Green's function, which includes two spatial three dimensional vectors as arguments. Thus, the Taylor series of a general Green's function is formulated for two expansions points, without specifying the Green's function to an explicit analytic form:

$$\begin{aligned} &G(\mathbf{R}_n + \mathbf{s}_n, \mathbf{R}_{n'} + \mathbf{s}_{n'}) \Big|_{\substack{\mathbf{s}_n = 0 \\ \mathbf{s}_{n'} = 0}} \\ = &G(\mathbf{R}_n, \mathbf{R}_{n'}) \quad (0,0) \\ &+ \mathbf{s}_n \cdot \nabla_{\tilde{\mathbf{s}}_n} G(\mathbf{R}_n + \tilde{\mathbf{s}}_n, \mathbf{R}_{n'}) \Big|_{\tilde{\mathbf{s}}_n = 0} \quad (1,0) \\ &+ G(\mathbf{R}_n, \mathbf{R}_{n'} + \tilde{\mathbf{s}}_{n'}) \widehat{\nabla}_{\tilde{\mathbf{s}}_{n'}} \cdot \mathbf{s}_{n'} \Big|_{\tilde{\mathbf{s}}_{n'} = 0} \quad (0,1) \\ &+ \mathbf{s}_n \cdot \nabla_{\tilde{\mathbf{s}}_n} G(\mathbf{R}_n + \tilde{\mathbf{s}}_n, \mathbf{R}_{n'} + \tilde{\mathbf{s}}_{n'}) \widehat{\nabla}_{\tilde{\mathbf{s}}_{n'}} \cdot \mathbf{s}_{n'} \Big|_{\substack{\tilde{\mathbf{s}}_n = 0 \\ \tilde{\mathbf{s}}_{n'} = 0}} \quad (1,1) \\ &+ \frac{1}{2} \mathbf{s}_n \cdot \nabla_{\tilde{\mathbf{s}}_n} \left(\mathbf{s}_n \cdot \nabla_{\tilde{\mathbf{s}}_n} G(\mathbf{R}_n + \mathbf{s}_n, \mathbf{R}_{n'}) \right) \Big|_{\mathbf{s}_n = 0} \quad (2,0) \\ &+ \frac{1}{2} \left(G(\mathbf{R}_n, \mathbf{R}_{n'} + \mathbf{s}_{n'}) \widehat{\nabla}_{\tilde{\mathbf{s}}_{n'}} \cdot \mathbf{s}_{n'} \right) \widehat{\nabla}_{\tilde{\mathbf{s}}_{n'}} \cdot \mathbf{s}_{n'} \Big|_{\mathbf{s}_{n'} = 0} + \dots \quad (0,2) \end{aligned} \quad (\text{B.2})$$

The zeroth order in both arguments (0,0) gives the monopole-monopole terms, the monopole-dipole mixed terms are given by (1,0) and (0,1) and the dipole-dipole term is induced by (1,1). Terms of higher order are calculated analogously. Including the Taylor series of the Green's function into the equation for calculating the Coulomb coupling, the different coupling elements can be identified by the related order of in the Taylor series.

B.2 Calculate mixed Coulomb terms

Mixed monopole-dipole Coulomb coupling terms are given by the (1,0) and (0,1) order in the Taylor series in Eq. (B.2). For calculating the Coulomb coupling elements, first the electron wave functions are written as a product of envelope $\xi(\mathbf{r})$ and Bloch function $u(\mathbf{r})$:

$$\phi_{\lambda n \sigma}(\mathbf{r}) = \xi_{\lambda n}(\mathbf{r}) u_{\lambda n \sigma}(\mathbf{r}). \quad (\text{B.3})$$

Thus, the Coulomb coupling elements are determined as follows:

$$V_{1234} = e^2 \int d^3r \int d^3r' \xi_{\lambda_1 n_1}^*(\mathbf{r}) u_{\lambda_1 n_1 \sigma_1}^*(\mathbf{r}) \xi_{\lambda_2 n_2}^*(\mathbf{r}') u_{\lambda_2 n_2 \sigma_2}^*(\mathbf{r}') G(\mathbf{r}, \mathbf{r}') \cdot \xi_{\lambda_3 n_3}(\mathbf{r}') u_{\lambda_3 n_3 \sigma_3}(\mathbf{r}') \xi_{\lambda_4 n_4}(\mathbf{r}) u_{\lambda_4 n_4 \sigma_4}(\mathbf{r}). \quad (\text{B.4})$$

A scale separation of the space operator to the position of the n th unit cell \mathbf{R}_n and the variation inside the cell \mathbf{s}_n is conducted: $\mathbf{r} = \mathbf{R}_n + \mathbf{s}_n$. The envelope function is assumed to be constant on the size of the elementary cell: $\xi(\mathbf{R}_n + \mathbf{s}_n) \approx \xi(\mathbf{R}_n)$. Together with the periodicity of the Bloch functions $u(\mathbf{R}_n + \mathbf{s}_n) = u(\mathbf{s}_n)$, the Coulomb coupling elements read

$$V_{1234} = e^2 \sum_{n, n'} \xi_{\lambda_1 n_1}^*(\mathbf{R}_n) \xi_{\lambda_2 n_2}^*(\mathbf{R}_{n'}) \xi_{\lambda_3 n_3}(\mathbf{R}_{n'}) \xi_{\lambda_4 n_4}(\mathbf{R}_n) \quad (\text{B.5})$$

$$\cdot \int d^3s_n \int d^3s_{n'} u_{\lambda_1 n_1 \sigma_1}^*(\mathbf{s}_n) u_{\lambda_2 n_2 \sigma_2}^*(\mathbf{s}_{n'}) G(\mathbf{R}_n + \mathbf{s}_n, \mathbf{R}_{n'} + \mathbf{s}_{n'}) u_{\lambda_3 n_3 \sigma_3}(\mathbf{s}_{n'}) u_{\lambda_4 n_4 \sigma_4}(\mathbf{s}_n). \quad (\text{B.6})$$

For calculating the mixed dipole-monopole term the (1,0) order in Taylor series in Eq. (B.2) is included for the Green's function in the equation for the Coulomb coupling elements:

$$V_{1234}^{(1,0)} = e^2 \sum_{n, n'} \xi_{\lambda_1 n_1}^*(\mathbf{R}_n) \xi_{\lambda_2 n_2}^*(\mathbf{R}_{n'}) \xi_{\lambda_3 n_3}(\mathbf{R}_{n'}) \xi_{\lambda_4 n_4}(\mathbf{R}_n) \int d^3s_n \int d^3s_{n'} u_{\lambda_1 n_1 \sigma_1}^*(\mathbf{s}_n) u_{\lambda_2 n_2 \sigma_2}^*(\mathbf{s}_{n'}) \cdot \left[\mathbf{s}_n \cdot \nabla_{\tilde{\mathbf{s}}_n} G(\mathbf{R}_n + \tilde{\mathbf{s}}_n, \mathbf{R}_{n'} + \tilde{\mathbf{s}}_{n'}) \right]_{\substack{\tilde{\mathbf{s}}_n = 0 \\ \tilde{\mathbf{s}}_{n'} = 0}} u_{\lambda_3 n_3 \sigma_3}(\mathbf{s}_{n'}) u_{\lambda_4 n_4 \sigma_4}(\mathbf{s}_n). \quad (\text{B.7})$$

The differentiation of the Green's function can be transformed from the variable \mathbf{s}_n to \mathbf{R}_n due to the fact they belong to the same entry:

$$\left[\nabla_{\tilde{\mathbf{s}}_n} G(\mathbf{R}_n + \tilde{\mathbf{s}}_n, \mathbf{R}_{n'} + \tilde{\mathbf{s}}_{n'}) \right]_{\substack{\tilde{\mathbf{s}}_n = 0 \\ \tilde{\mathbf{s}}_{n'} = 0}} = \left[\nabla_{\mathbf{R}_n} G(\mathbf{R}_n + \tilde{\mathbf{s}}_n, \mathbf{R}_{n'} + \tilde{\mathbf{s}}_{n'}) \right]_{\substack{\mathbf{R}_n - \tilde{\mathbf{s}}_n \\ \mathbf{R}_{n'} - \tilde{\mathbf{s}}_{n'}}}. \quad (\text{B.8})$$

Additionally, the summation in Eq. (B.7) concerning the unit cells is transformed into an integration, due the unit cells are assumed to be densely arranged. Based on the assumption, that the Green's function does not change on the scale of the unit cells, the mixed dipole-monopole coupling elements are:

$$V_{1234}^{(1,0)} = e \int d^3r \int d^3r' \xi_{\lambda_1 n_1}^*(\mathbf{r}) \xi_{\lambda_2 n_2}^*(\mathbf{r}') \xi_{\lambda_3 n_3}(\mathbf{r}') \xi_{\lambda_4 n_4}(\mathbf{r}) \mathbf{d}_{14} \cdot \nabla_r G(\mathbf{r}, \mathbf{r}') \delta_{\lambda_2 \lambda_3} \delta_{\sigma_2 \sigma_3}. \quad (\text{B.9})$$

In analogy to the calculation of the dipole-dipole coupling, the dipole moment \mathbf{d}_{14} is defined as follows:

$$\mathbf{d}_{14} = \frac{1}{V_{\text{uc}}} \int d^3s_n u_{\lambda_1 n_1 \sigma_1}^*(\mathbf{s}_n) \mathbf{s}_n u_{\lambda_4 n_4 \sigma_4}(\mathbf{s}_n). \quad (\text{B.10})$$

Using a multidimensional integration by parts:

$$\int_{\Omega} d^3r \mathbf{r} \cdot \nabla \chi = \int_{\partial\Omega} d\mathbf{f} \cdot \mathbf{r} \chi - \int_{\Omega} d^3r \chi \nabla \cdot \mathbf{r}, \quad (\text{B.11})$$

under the assumption that the function vanish at the boundaries, the equation (B.9) reads

$$V_{1234}^{(1,0)} = -e \int d^3r \int d^3r' \nabla_{\mathbf{r}} \cdot \left(\xi_{\lambda_1 n_1}^*(\mathbf{r}) \mathbf{d}_{14} \xi_{\lambda_4 n_4}(\mathbf{r}) \right) \xi_{\lambda_2 n_2}^*(\mathbf{r}') G(\mathbf{r}, \mathbf{r}') \xi_{\lambda_3 n_3}(\mathbf{r}') \delta_{\lambda_2 \lambda_3} \delta_{\sigma_2 \sigma_3}. \quad (\text{B.12})$$

Following the approach of the PGF method introduced in Sec. 3.1, a generalized scalar potential including the Green's function as solution of the Poisson equation is introduced:

$$\Phi_{23}^{(1,0)}(\mathbf{r}) = e \int d^3r' \xi_{\lambda_2 n_2}^*(\mathbf{r}') G(\mathbf{r}, \mathbf{r}') \xi_{\lambda_3 n_3}(\mathbf{r}') = \Phi_{23}^{\text{Mo}}(\mathbf{r}). \quad (\text{B.13})$$

The generalized scalar potential $\Phi_{23}^{(1,0)}(\mathbf{r})$ in the case of the dipole-monopole mixed terms is identical with the scalar potential introduced for the monopole-monopole coupling, cf. Sec. 3.2.2. Using the scalar potential, the equation for calculating the Coulomb coupling elements can be simplified:

$$V_{1234}^{(1,0)} = - \int d^3r \nabla_{\mathbf{r}} \cdot \left(\xi_{\lambda_1 n_1}^*(\mathbf{r}) \mathbf{d}_{14} \xi_{\lambda_4 n_4}(\mathbf{r}) \right) \Phi_{23}^{(1,0)}(\mathbf{r}) \delta_{\lambda_2 \lambda_3} \delta_{\sigma_2 \sigma_3}. \quad (\text{B.14})$$

The equation for calculating the dipole-monopole mixed coupling terms seems to be identical to the equation used for the calculation of the dipole-dipole coupling given in Sec. 3.2.3. In contrast to the dipole-dipole coupling, the scalar potential $\Phi_{23}^{(1,0)}(\mathbf{r})$ used for the calculation is given by a monopole scalar potential. This characterizes the properties of the mixed terms. Terms connected with the monopole coupling and the dipole coupling occur together.

Analogously, the mixed terms of the monopole-dipole coupling given by the (0,1) order in the Taylor series in Eq. (B.2) are calculated. The expression for the Coulomb coupling elements:

$$V_{1234}^{(0,1)} = -e \int d^3r \int d^3r' \nabla_{\mathbf{r}'} \cdot \left(\xi_{\lambda_2 n_2}^*(\mathbf{r}') \mathbf{d}_{23} \xi_{\lambda_3 n_3}(\mathbf{r}') \right) \xi_{\lambda_1 n_1}^*(\mathbf{r}) G(\mathbf{r}, \mathbf{r}') \xi_{\lambda_4 n_4}(\mathbf{r}) \delta_{\lambda_1 \lambda_4} \delta_{\sigma_1 \sigma_4}, \quad (\text{B.15})$$

can be efficiently calculated following the approach of the PGF method by introducing a scalar potential as follows:

$$\Phi_{23}^{(0,1)}(\mathbf{r}) = \int d^3r' \nabla_{\mathbf{r}'} \cdot \left(\xi_{\lambda_2 n_2}^*(\mathbf{r}') \mathbf{d}_{23} \xi_{\lambda_3 n_3}(\mathbf{r}') \right) G(\mathbf{r}, \mathbf{r}'). \quad (\text{B.16})$$

This scalar potential represents the solution of the Poisson equation equally to the case of the dipole-dipole coupling. Including the scalar potential into the expression for the calculation of the monopole-dipole mixed terms yield

$$V_{1234}^{(0,1)} = -e \int d^3r \xi_{\lambda_1 n_1}^*(\mathbf{r}) \Phi_{23}^{(0,1)}(\mathbf{r}) \xi_{\lambda_4 n_4}(\mathbf{r}) \delta_{\lambda_1 \lambda_4} \delta_{\sigma_1 \sigma_4}. \quad (\text{B.17})$$

Thus, the monopole-dipole mixed terms are characterized by the dipole-dipole scalar potential and a generally similar the equation for the monopole-monopole Coulomb coupling elements.

B.3 Free particle Coulomb potential

In a spatially homogeneous medium, the Coulomb interaction is typically represented by the free space Green's function [31, 54]:

$$G(\mathbf{r}, \mathbf{r}') = \frac{qq'}{4\pi\epsilon_0\epsilon_r} \frac{1}{|\mathbf{r} - \mathbf{r}'|}. \quad (\text{B.18})$$

For identifying the terms of the Coulomb potential which are connected with the monopole and dipole Coupling, the spatial dependent term is expanded in a multidimensional Taylor series for the two expansion points.

$$\begin{aligned} \text{T} \left(\frac{1}{|\mathbf{R}_{nn'} + \mathbf{r}_n - \mathbf{r}_{n'}|} \right)_{\substack{\mathbf{r}_n = 0 \\ \mathbf{r}_{n'} = 0}} &= \frac{1}{|\mathbf{R}_{nn'}|} + \left(\frac{1}{|\mathbf{R}_{nn'} + \tilde{\mathbf{r}}_n - \tilde{\mathbf{r}}_{n'}|} \right)^{\widehat{\cdot}} \nabla_{\tilde{\mathbf{r}}_n} \cdot \mathbf{r}_n \Big|_{\substack{\tilde{\mathbf{r}}_n = 0 \\ \tilde{\mathbf{r}}_{n'} = 0}} \\ &+ \mathbf{r}_{n'} \cdot \nabla_{\tilde{\mathbf{r}}_{n'}} \left(\frac{1}{|\mathbf{R}_{nn'} + \tilde{\mathbf{r}}_n - \tilde{\mathbf{r}}_{n'}|} \right) \Big|_{\substack{\tilde{\mathbf{r}}_n = 0 \\ \tilde{\mathbf{r}}_{n'} = 0}} \\ &+ \mathbf{r}_{n'} \cdot \nabla_{\tilde{\mathbf{r}}_{n'}} \left(\frac{1}{|\mathbf{R}_{nn'} + \tilde{\mathbf{r}}_n - \tilde{\mathbf{r}}_{n'}|} \right)^{\widehat{\cdot}} \nabla_{\tilde{\mathbf{r}}_n} \cdot \mathbf{r}_n \Big|_{\substack{\tilde{\mathbf{r}}_n = 0 \\ \tilde{\mathbf{r}}_{n'} = 0}} \end{aligned} \quad (\text{B.19})$$

Since the mixed monopole-dipole terms vanish in a usual rotating wave-approximation, the mixed terms should be neglected in the following. For evaluating the Taylor series of the free particle Coulomb potential up to the dipole-dipole order, the following derivations are firstly calculated:

$$\begin{aligned} &\mathbf{r}_{n'} \cdot \nabla_{\tilde{\mathbf{r}}_{n'}} \left(\frac{1}{|\mathbf{R}_{nn'} + \tilde{\mathbf{r}}_n - \tilde{\mathbf{r}}_{n'}|} \right)^{\widehat{\cdot}} \nabla_{\tilde{\mathbf{r}}_n} \cdot \mathbf{r}_n \Big|_{\substack{\tilde{\mathbf{r}}_n = 0 \\ \tilde{\mathbf{r}}_{n'} = 0}} \\ &= \mathbf{r}_{n'} \cdot \nabla_{\tilde{\mathbf{r}}_{n'}} \left(-\frac{(\mathbf{R}_{nn'} + \tilde{\mathbf{r}}_n - \tilde{\mathbf{r}}_{n'}) \cdot \mathbf{r}_n}{|\mathbf{R}_{nn'} + \tilde{\mathbf{r}}_n - \tilde{\mathbf{r}}_{n'}|^3} \right) \Big|_{\substack{\tilde{\mathbf{r}}_n = 0 \\ \tilde{\mathbf{r}}_{n'} = 0}} \\ &= \frac{\mathbf{r}_{n'} \cdot \mathbf{r}_n}{|\mathbf{R}_{nn'} + \tilde{\mathbf{r}}_n - \tilde{\mathbf{r}}_{n'}|^3} - 3 \frac{(\mathbf{r}_{n'} \cdot (\mathbf{R}_{nn'} + \tilde{\mathbf{r}}_n - \tilde{\mathbf{r}}_{n'})) ((\mathbf{R}_{nn'} + \tilde{\mathbf{r}}_n - \tilde{\mathbf{r}}_{n'}) \cdot \mathbf{r}_n)}{|\mathbf{R}_{nn'} + \tilde{\mathbf{r}}_n - \tilde{\mathbf{r}}_{n'}|^5} \Big|_{\substack{\tilde{\mathbf{r}}_n = 0 \\ \tilde{\mathbf{r}}_{n'} = 0}} \\ &= \frac{\mathbf{r}_{n'} \cdot \mathbf{r}_n}{|\mathbf{R}_{nn'}|^3} - 3 \frac{(\mathbf{r}_{n'} \cdot \mathbf{R}_{nn'}) (\mathbf{R}_{nn'} \cdot \mathbf{r}_n)}{|\mathbf{R}_{nn'}|^5}. \end{aligned} \quad (\text{B.20})$$

Now the Taylor series of the spatial dependent part of the free particle Coulomb potential is given as follows:

$$\text{T} \left(\frac{1}{|\mathbf{R}_{nn'} + \mathbf{r}_n - \mathbf{r}_{n'}|} \right)_{\substack{\mathbf{r}_n = 0 \\ \mathbf{r}_{n'} = 0}} = \frac{1}{|\mathbf{R}_{nn'}|} + \frac{\mathbf{r}_{n'} \cdot \mathbf{r}_n}{|\mathbf{R}_{nn'}|^3} - 3 \frac{(\mathbf{r}_{n'} \cdot \mathbf{R}_{nn'}) (\mathbf{R}_{nn'} \cdot \mathbf{r}_n)}{|\mathbf{R}_{nn'}|^5}. \quad (\text{B.21})$$

B.3.1 Calculate terms of the dipole-dipole approximation

To get the Coulomb interaction in the point-dipole approximation, the two dipole-dipole terms (last two terms) in the Taylor series in Eq. (B.21) need to be evaluated. Thus, the scale separation into the QD's center position, the variation over the unit cells, and the product ansatz of the

wave functions are applied on the first dipole-dipole term in Eq. (3.38), which results in:

$$V_{1234}^{\text{pd-1}} = \sum_{i,j} \frac{q_{14}q_{23}\xi_1^*(\mathbf{R}_i^n)\xi_2^*(\mathbf{R}_j^{n'})\xi_3(\mathbf{R}_j^{n'})\xi_4(\mathbf{R}_i^n)}{4\pi\epsilon_0\epsilon_r} \cdot \int d^3r_i^n \int d^3r_j^{n'} u_1^*(\mathbf{s}_i^n)u_2^*(\mathbf{s}_j^{n'}) \left(\frac{\mathbf{R}_i^n \cdot \mathbf{R}_j^{n'}}{|\mathbf{R}_{nn'}|^3} + \frac{(\mathbf{R}_i^n \cdot \mathbf{s}_j^{n'}) + (\mathbf{s}_i^n \cdot \mathbf{R}_j^{n'})}{|\mathbf{R}_{nn'}|^3} + \frac{\mathbf{s}_i^n \cdot \mathbf{s}_j^{n'}}{|\mathbf{R}_{nn'}|^3} \right) u_3(\mathbf{s}_j^{n'})u_4(\mathbf{s}_i^n). \quad (\text{B.22})$$

With the normalization condition of the Bloch functions in Eq. (3.17) and a transformation of the summation of the unit cells into an integration, as done in Eq. (3.19), the first term in Eq. (3.41) reads:

$$V_{1234}^{\text{pd-1a}} = \frac{q_{14}q_{23}}{4\pi\epsilon_0\epsilon_r} \int d^3\tilde{r} \int d^3\tilde{r}' \xi_1^*(\tilde{r})\xi_2^*(\tilde{r}') \frac{\tilde{r} \cdot \tilde{r}'}{|\mathbf{R}_{nn'}|^3} \xi_3(\tilde{r}')\xi_4(\tilde{r})\delta_{14}^{\lambda n \sigma} \delta_{23}^{\lambda n \sigma} \quad (\text{B.23})$$

Analogously to the definition of the microscopic transition dipole moment in Eq. (3.41), a macroscopic dipole moment, dependent on the envelope functions, is introduced

$$\mathbf{D}_{ll'}^n = \int d^3\tilde{r}_n \xi_l^*(\tilde{r}_n)\tilde{r}_n \xi_{l'}(\tilde{r}_n). \quad (\text{B.24})$$

Therefore, the first term of the dipole interaction takes the form of a dipole-dipole term between the macroscopic dipole moments:

$$V_{1234}^{\text{pd-1a}} = \frac{q_{14}q_{23}}{4\pi\epsilon_0\epsilon_r} \frac{\mathbf{D}_{14}^n \cdot \mathbf{D}_{23}^{n'}}{|\mathbf{R}_{nn'}|^3} \delta_{14}^{\lambda \sigma} \delta_{23}^{\lambda \sigma}. \quad (\text{B.25})$$

An evaluation of the Kronecker deltas, which results from the normalization condition of the Bloch function introduced in Eq. (3.17), conducts equal envelope functions in the macroscopic dipole moments in Eq. (3.43). Such macroscopic dipole moment is introduced as a statical dipole moment, due the the bandindex does not change and therefore, there is no dynamical transition. Since the squared absolute values of the envelope functions ξ_l , which give the electron probability densities, represents a symmetric function in each Cartesian direction, whereas the spatial vector \tilde{r} is anti-symmetric, the product of both factors represents an anti-symmetric function. Accordingly, the integral of the statical macroscopic dipole moments, including the spatial vector with the QD's center position \mathbf{R}_n as the origin, should vanish:

$$\mathbf{D}_{ll}^n = \lim_{c \rightarrow \infty} \int_{-c}^c d^3\tilde{r} |\xi_l(\tilde{r})|^2 \tilde{r} = 0. \quad (\text{B.26})$$

Hence, the first dipole term, which shows a form of a macroscopic dipole-dipole coupling, vanishes due to the Bloch normalize condition. The second term in Eq. (3.41) presents the mixed terms, which includes the microscopic transitions moments, defined in Eq. (3.25), as well as the macroscopic dipole moments introduced in Eq. (3.43):

$$V_{1234}^{\text{pd-1b}} = \frac{q_{14}q_{23}}{4\pi\epsilon_0\epsilon_r} \frac{(\mathbf{D}_{14}^n \cdot \boldsymbol{\mu}_{23}^{n'})O_{23}^{n'}\delta_{14}^{\lambda \sigma} + (\boldsymbol{\mu}_{14}^n \cdot \mathbf{D}_{23}^{n'})O_{14}^n\delta_{23}^{\lambda \sigma}}{|\mathbf{R}_{nn'}|^3} \quad (\text{B.27})$$

Again, since the macroscopic dipole moments \mathbf{D}_{14}^n and $\mathbf{D}_{23}^{n'}$ are connected with the Kronecker deltas, they represents statical dipole moments, which include equal envelope functions. Therefore, this term equals zero. The third term, which only includes dynamic dipole transitions $\boldsymbol{\mu}^{nij}$,

is the non-vanishing term resulting from the first dipole-dipole term of the Taylor expansion in Eq. (3.38):

$$V_{1234}^{\text{pd-1c}} = \frac{q_{14}q_{23}O_{14}^n O_{23}^{n'} \boldsymbol{\mu}_{14}^n \cdot \boldsymbol{\mu}_{23}^{n'}}{4\pi\epsilon_0\epsilon_r |\mathbf{R}_{nn'}|^3}. \quad (\text{B.28})$$

Analogously, using the scale separation into the QD center positions and the positioning of the unit cells, the second dipole-dipole term of the Taylor expansion in Eq. (3.38) occurs

$$V_{1234}^{\text{pd-2}} = \sum_{i,j} \frac{qq'\xi_1^*(\mathbf{R}_i^n)\xi_2^*(\mathbf{R}_j^{n'})\xi_3(\mathbf{R}_j^{n'})\xi_4(\mathbf{R}_i^n)}{4\pi\epsilon_0\epsilon_r} \cdot \int d^3r_i^n \int d^3r_j^{n'} u_1^*(\mathbf{s}_i^n)u_2^*(\mathbf{s}_j^{n'}) \left(\frac{(\mathbf{R}_{nn'} \cdot (\mathbf{R}_i^n + \mathbf{s}_i^n))(\mathbf{R}_{nn'} \cdot (\mathbf{R}_j^{n'} + \mathbf{s}_j^{n'}))}{|\mathbf{R}_{nn'}|^5} \right) u_3(\mathbf{s}_j^{n'})u_4(\mathbf{s}_i^n). \quad (\text{B.29})$$

Including the definitions of the macroscopic and the microscopic dipole moments analogously, the second term of the dipole-dipole interaction reads:

$$V_{1234}^{\text{pd-2}} = -3 \frac{q_{14}q_{23}}{4\pi\epsilon_0\epsilon_r} \left(\frac{(\mathbf{R}_{nn'} \cdot \mathbf{D}_{14}^n)(\mathbf{R}_{nn'} \cdot \mathbf{D}_{23}^{n'})}{|\mathbf{R}_{nn'}|^5} \delta_{14}^{\lambda\sigma} \delta_{23}^{\lambda\sigma} + \frac{(\mathbf{R}_{nn'} \cdot \mathbf{D}_{14}^n)(\mathbf{R}_{nn'} \cdot \boldsymbol{\mu}_{23}^{n'})}{|\mathbf{R}_{nn'}|^5} O_{23}^{n'} \delta_{14}^{\lambda\sigma} \right. \\ \left. + \frac{(\mathbf{R}_{nn'} \cdot \boldsymbol{\mu}_{14}^n)(\mathbf{R}_{nn'} \cdot \mathbf{D}_{23}^{n'})}{|\mathbf{R}_{nn'}|^5} O_{14}^{n'} \delta_{23}^{\lambda\sigma} + \frac{(\mathbf{R}_{nn'} \cdot \boldsymbol{\mu}_{14}^n)(\mathbf{R}_{nn'} \cdot \boldsymbol{\mu}_{23}^{n'})}{|\mathbf{R}_{nn'}|^5} O_{14}^n O_{23}^{n'} \right). \quad (\text{B.30})$$

Since the normalization condition of the Bloch functions creates an integral expression in the static macroscopic dipole moments over an anti-symmetric functions (cf. Eq. (3.44)), the last term in Eq. (B.30) of the second dipole-dipole coupling term is the only non-vanishing term in the new scale transformation. Collecting all non-vanishing terms of the Taylor expansion in Eq. (3.38) on the scale of the QD's unit cells, the point-like Coulomb coupling potential reads:

$$V_{1234}^{\text{pd}} = \frac{q_{14}q_{23}O_{14}^n O_{23}^{n'}}{4\pi\epsilon_0\epsilon_r} \left(\frac{\boldsymbol{\mu}_{14}^n \cdot \boldsymbol{\mu}_{23}^{n'}}{|\mathbf{R}_{nn'}|^3} - 3 \frac{(\mathbf{R}_{nn'} \cdot \boldsymbol{\mu}_{14}^n)(\mathbf{R}_{nn'} \cdot \boldsymbol{\mu}_{23}^{n'})}{|\mathbf{R}_{nn'}|^5} \right). \quad (\text{B.31})$$

This interdot Coulomb coupling resulting from the point-like dipole approximation includes the center-to-center distance vector between the two QDs $\mathbf{R}_{nn'}$ as well as the microscopic transition dipole moments of the QDs $\boldsymbol{\mu}_{14}^n$ and $\boldsymbol{\mu}_{23}^{n'}$. The point-like approximated Coulomb coupling of the free space Coulomb potential in the dipole-dipole order does not include monopole moments. Accordingly, the point-like dipole-dipole coupling determines the Coulomb coupling in this approximation.

B.3.2 Calculate quadrupole-quadrupole correction terms

Since for the static macroscopic dipole moment D_{ll} all terms equals zero, the quadrupole terms are calculated finding the first leading non-vanishing terms for the static case (diagonal elements). Accordingly, in the Taylor expansion in Eq. (3.38) the quadrupole-quadrupole terms are calculated and then, only the static terms are taken into account. Mixed terms in the Taylor series, like monopole-quadrupole and dipole-quadrupole terms are generally neglected, since they usually vanish in a rotating wave approximation. The terms of the Taylor expansion which are connected with the quadrupole-quadrupole coupling include the second order in both expansion

points. Accordingly, the following terms of the multidimensional Taylor series in Eq. (3.14) are calculated for describing the quadrupole-quadrupole coupling:

$$T^{\text{qq}} \left(\frac{1}{|\mathbf{R}_{nn'} + \mathbf{r}_n - \mathbf{r}_{n'}|} \right)_{\substack{\mathbf{r}_n = 0 \\ \mathbf{r}_{n'} = 0}} = \frac{1}{4} \mathbf{r}_{n'} \cdot \nabla_{\tilde{\mathbf{r}}_{n'}} \left(\mathbf{r}_{n'} \cdot \nabla_{\tilde{\mathbf{r}}_{n'}} \left(\frac{1}{|\mathbf{R}_{nn'} + \tilde{\mathbf{r}}_n - \tilde{\mathbf{r}}_{n'}|} \right) \nabla_{\tilde{\mathbf{r}}_n} \cdot \mathbf{r}_n \right) \nabla_{\tilde{\mathbf{r}}_n} \cdot \mathbf{r}_n \Big|_{\substack{\tilde{\mathbf{r}}_n = 0 \\ \tilde{\mathbf{r}}_{n'} = 0}} \quad (\text{B.32})$$

$$= \frac{1}{4} \mathbf{r}_{n'} \cdot \nabla_{\tilde{\mathbf{r}}_{n'}} \left(\mathbf{r}_{n'} \cdot \nabla_{\tilde{\mathbf{r}}_{n'}} \left(-\frac{\mathbf{r}_n \cdot \mathbf{r}_n}{|\mathbf{R}_{nn'} + \tilde{\mathbf{r}}_n - \tilde{\mathbf{r}}_{n'}|^3} + 3 \frac{((\mathbf{R}_{nn'} + \tilde{\mathbf{r}}_n - \tilde{\mathbf{r}}_{n'}) \cdot \mathbf{r}_n)^2}{|\mathbf{R}_{nn'} + \tilde{\mathbf{r}}_n - \tilde{\mathbf{r}}_{n'}|^5} \right) \right)_{\tilde{\mathbf{r}}_{n'} = 0} \quad (\text{B.33})$$

$$= \frac{3}{4} \frac{\mathbf{r}_n^2 \mathbf{r}_{n'}^2}{|\mathbf{R}_{nn'}|^5} + \frac{6}{4} \frac{(\mathbf{r}_n \cdot \mathbf{r}_{n'})^2}{|\mathbf{R}_{nn'}|^5} - \frac{15}{4} \frac{(\mathbf{R}_{nn'} \cdot \mathbf{r}_{n'})^2 \mathbf{r}_n^2}{|\mathbf{R}_{nn'}|^7} - \frac{15}{4} \frac{\mathbf{r}_{n'}^2 (\mathbf{R}_{nn'} \cdot \mathbf{r}_n)^2}{|\mathbf{R}_{nn'}|^7} - \frac{60}{4} \frac{(\mathbf{R}_{nn'} \cdot \mathbf{r}_n)(\mathbf{r}_{n'} \cdot \mathbf{r}_n)(\mathbf{r}_{n'} \cdot \mathbf{R}_{nn'})}{|\mathbf{R}_{nn'}|^7} + \frac{105}{4} \frac{(\mathbf{r}_{n'} \cdot \mathbf{R}_{nn'})^2 (\mathbf{R}_{nn'} \cdot \mathbf{r}_n)^2}{|\mathbf{R}_{nn'}|^9}. \quad (\text{B.34})$$

Now the same scale separation as done for the point-like dipole terms in the section 3.5.2 is used: the vector from the QD center \mathbf{r}_n is separated into a vector to the i th unit cell center \mathbf{R}_i^n and a vector located inside the unit cell \mathbf{s}_i^n , as illustrated in Fig. 3.26(b). Again, the wave functions are written as product of an envelope function and a Bloch part. Then, only the statical term without any dynamical transition moments is considered. Since the lower ordered mixed terms of statical and dynamical transitions vanish and the dynamical transitions are described by the point-like dipole-dipole approximation, only the statical term of the Coulomb coupling elements is transformed to the quadrupole-quadrupole order.

$$V_{1234}^{\text{qqstatic}} = \frac{q_{14} q_{23}}{16\pi\epsilon_0\epsilon_r} \int d^3\tilde{\mathbf{r}} \int d^3\tilde{\mathbf{r}}' \xi_1^*(\tilde{\mathbf{r}}) \xi_2^*(\tilde{\mathbf{r}}') \left(3 \frac{\tilde{\mathbf{r}}^2 \tilde{\mathbf{r}}'^2}{|\mathbf{R}_{nn'}|^5} + 6 \frac{(\tilde{\mathbf{r}} \cdot \tilde{\mathbf{r}}')^2}{|\mathbf{R}_{nn'}|^5} - 15 \frac{(\mathbf{R}_{nn'} \cdot \tilde{\mathbf{r}}')^2 \tilde{\mathbf{r}}^2}{|\mathbf{R}_{nn'}|^7} - 15 \frac{\tilde{\mathbf{r}}'^2 (\mathbf{R}_{nn'} \cdot \tilde{\mathbf{r}})^2}{|\mathbf{R}_{nn'}|^7} - 60 \frac{(\mathbf{R}_{nn'} \cdot \tilde{\mathbf{r}})(\tilde{\mathbf{r}}' \cdot \tilde{\mathbf{r}})(\tilde{\mathbf{r}}' \cdot \mathbf{R}_{nn'})}{|\mathbf{R}_{nn'}|^7} + 105 \frac{(\tilde{\mathbf{r}}' \cdot \mathbf{R}_{nn'})^2 (\mathbf{R}_{nn'} \cdot \tilde{\mathbf{r}})^2}{|\mathbf{R}_{nn'}|^9} \right) \xi_3(\tilde{\mathbf{r}}') \xi_4(\tilde{\mathbf{r}}) \delta_{14}^{\lambda n \sigma} \delta_{23}^{\lambda n \sigma}. \quad (\text{B.35})$$

In a description of components, the Coulomb coupling elements read: (Note: the center-to-center distance vector $\mathbf{R}_{nn'}$ is written as \mathbf{R} for simplifying the component description)

$$V_{1234}^{\text{qqstatic}} = \frac{q_{14} q_{23}}{16\pi\epsilon_0\epsilon_r} \int d^3\tilde{\mathbf{r}} \int d^3\tilde{\mathbf{r}}' \xi_1^*(\tilde{\mathbf{r}}) \xi_2^*(\tilde{\mathbf{r}}') \sum_{ijk} \left(3 \frac{\tilde{\mathbf{r}}^2 \tilde{\mathbf{r}}'^2}{|\mathbf{R}|^5} + 6 \frac{(\tilde{r}_i \tilde{r}'_i)(\tilde{r}_j \tilde{r}'_j)}{|\mathbf{R}|^5} - 15 \frac{(R_i \tilde{r}'_i)(R_j \tilde{r}'_j) \tilde{\mathbf{r}}^2}{|\mathbf{R}|^7} - 15 \frac{\tilde{\mathbf{r}}'^2 (R_j \tilde{r}_j)(R_k \tilde{r}_k)}{|\mathbf{R}|^7} - 60 \frac{(R_i \tilde{r}_i)(\tilde{r}'_j \tilde{r}_j)(\tilde{r}'_k R_k)}{|\mathbf{R}|^7} + 105 \sum_l \frac{(\tilde{r}'_i R_i)(\tilde{r}'_j R_j)(R_k \tilde{r}_k)(R_l \tilde{r}_l)}{|\mathbf{R}|^9} \right) \xi_3(\tilde{\mathbf{r}}') \xi_4(\tilde{\mathbf{r}}) \delta_{14}^{\lambda n \sigma} \delta_{23}^{\lambda n \sigma}. \quad (\text{B.36})$$

Analog to the definition of the macroscopic dipole moment in Eq. (3.43), a macroscopic quadrupole moment is introduced:

$$Q_{ij}^{ll'} = \int d^3\tilde{\mathbf{r}} \xi_l^*(\tilde{\mathbf{r}}) (3\tilde{r}_i \tilde{r}_j - \tilde{\mathbf{r}}^2 \delta_{ij}) \xi_{l'}(\tilde{\mathbf{r}}_n). \quad (\text{B.37})$$

For identifying terms connected to the quadrupole-quadrupole coupling, the product of two macroscopic quadrupole moments is calculated:

$$Q_{ij}^{14} Q_{jk}^{23} = \int d^3 \tilde{r} \int d^3 \tilde{r}' \xi_1^*(\tilde{r}) \xi_2^*(\tilde{r}') \left(9 \tilde{r}_i \tilde{r}_j \tilde{r}'_j \tilde{r}'_k - 3 \tilde{r}^2 \tilde{r}'_j \tilde{r}'_k \delta_{ij} - 3 \tilde{r}_i \tilde{r}_j \tilde{r}'^2 \delta_{ij} + \tilde{r}^2 \tilde{r}'^2 \delta_{ij} \delta_{jk} \right) \xi_3(\tilde{r}') \xi_4(\tilde{r}). \quad (\text{B.38})$$

For formulating the correction terms to the quadrupole-quadrupole coupling, we introduce a scalar term for the diagonal elements:

$$m^{ll'} = \int d^3 \tilde{r} \xi_l^*(\tilde{r}) \tilde{r}^2 \xi_{l'}(\tilde{r}_n), \quad (\text{B.39})$$

and a tensor term

$$M_{ij}^{ll'} = \int d^3 \tilde{r} \xi_l^*(\tilde{r}) \tilde{r}_i \tilde{r}_j \xi_{l'}(\tilde{r}_n). \quad (\text{B.40})$$

Including this quadrupole-quadrupole product into the equation of the Coulomb coupling elements and using these definitions, the static quadrupole-quadrupole Coulomb interaction in a point-like approximation results in:

$$V_{1234}^{\text{qqstatic}} = \frac{q_{14} q_{23}}{16 \pi \epsilon_0 \epsilon_r} \sum_{ijk} \left(\frac{Q_{ij}^{14} Q_{ij}^{23}}{|\mathbf{R}|^5} + 4 \frac{R_i Q_{ij}^{14} Q_{jk}^{23} R_k}{|\mathbf{R}|^7} - 2 \frac{m^{14} m^{23}}{|\mathbf{R}|^5} - 3 \frac{M_{ij}^{14} M_{ij}^{23}}{|\mathbf{R}|^5} - 24 \frac{R_i M_{ij}^{14} M_{jk}^{23} R_k}{|\mathbf{R}|^7} + 105 \sum_l \frac{R_i R_j M_{ij}^{23} M_{kl}^{14} R_k R_l}{|\mathbf{R}|^9} \right) \delta_{14}^{\lambda n \sigma} \delta_{23}^{\lambda n \sigma}. \quad (\text{B.41})$$

The first non-vanishing order of the interdot diagonal elements of the Coulomb coupling in the point-like approximation is given by the static quadrupole-quadrupole coupling, together with correction terms to the quadrupole-quadrupole coupling.

Appendix C

Formalism of the coherent optical spectroscopy

Typically, in the linear spectroscopy, ultrafast dynamics are observed as changes in the transmission or absorption spectra [118]. Thus, the calculation of the induced polarization provides indirect information on the electronic populations.

The induced polarization used to calculate the linear spectrum is given by:

$$\mathbf{P}^{(1)}(t) = \text{tr} \left(\mathbf{d}\rho^{(1)}(t) \right). \quad (\text{C.1})$$

The linear term of the density operator is determined by

$$\rho^{(1)}(t) = \mathcal{U}^{(1)}(t, t_0)\rho^{(0)}(t_0) = \mathcal{U}^{(1)}(t, t_0)|g\rangle\langle g| \quad (\text{C.2})$$

including the first term of the time evolution operator of the Liouville space:

$$\mathcal{U}^{(1)}(t, t_0) = -\frac{i}{\hbar} \int_{t_0}^t d^3\tau \mathcal{U}_0(t, \tau) \mathcal{L}_{e-1}(\tau) \mathcal{U}_0(\tau, t_0). \quad (\text{C.3})$$

That leads to the following presentation of the linear density operator:

$$\rho^{(1)}(t) = -\frac{i}{\hbar} \int_{t_0}^t d^3\tau \mathcal{U}_0(t, \tau) \mathcal{L}_{e-1}(\tau) \mathcal{U}_0(\tau, t_0) |g\rangle\langle g|. \quad (\text{C.4})$$

In the equation (C.4), it is visible that firstly the influence of the free part of the time evolution operator to the basis of the ground state needs to be calculated

$$\mathcal{U}_0(\tau, t_0) |g\rangle\langle g| = e^{-\frac{i}{\hbar} \mathcal{L}_{e-1}(\tau-t_0)} |g\rangle\langle g| = |g\rangle\langle g|. \quad (\text{C.5})$$

Evaluating this expression, the effect of the electronic part of the Liouville operator on the ground state propagator is used

$$\mathcal{L}_{e-1} |g\rangle\langle g| = [H_{e-1}, |g\rangle\langle g|] = E_g |g\rangle\langle g| - E_g |g\rangle\langle g| = 0. \quad (\text{C.6})$$

In the following the influence of the electron-light interaction part is investigated

$$\mathcal{L}_{e-1} |g\rangle\langle g| = H_{e-1} |g\rangle\langle g| - |g\rangle\langle g| H_{e-1}. \quad (\text{C.7})$$

Using the formulation of the dipole operator (2.48) leads to the following equation of the electron-light interaction Hamiltonian:

$$H_{e-1}(t) = - \sum_e \left(\mathbf{d}_{eg} \cdot \mathbf{E}(t) |e\rangle\langle g| + \mathbf{d}_{ge} \cdot \mathbf{E}(t) |g\rangle\langle e| \right). \quad (\text{C.8})$$

Inserting this relation into the equation (C.7) to evaluate the influence of this interaction part and use the orthonormal condition of the basis states leads to:

$$\mathcal{L}_{e-1}|g\rangle\langle g| = - \sum_e \left(\mathbf{d}_{eg} \cdot \mathbf{E}(t)|e\rangle\langle g| - \mathbf{d}_{ge} \cdot \mathbf{E}^*(t)|g\rangle\langle e| \right). \quad (\text{C.9})$$

Finally, the effect of the free part of the time evolution operator on this new propagations is investigated

$$\mathcal{L}_{e1}(t, \tau)|e\rangle\langle g| = H_{e1}|e\rangle\langle g| - |e\rangle\langle g|H_{e1} = (E_e - E_g)|e\rangle\langle g|. \quad (\text{C.10})$$

Introducing the transition frequency

$$\omega_{eg} := \frac{1}{\hbar}(E_e - E_g), \quad (\text{C.11})$$

the influence of the free propagation on the transitions can be formulated:

$$\mathcal{U}_0(t, \tau)|e\rangle\langle g| = e^{-i\omega_{eg}(t-\tau)}|e\rangle\langle g| \quad (\text{C.12})$$

$$\mathcal{U}_0(t, \tau)|g\rangle\langle e| = e^{-i\omega_{ge}(t-\tau)}|g\rangle\langle e|. \quad (\text{C.13})$$

Collecting all terms leads to the equation of the linear part of the density matrix added by a phenomenological damping rate γ :

$$\rho^{(1)}(t) = \frac{i}{\hbar} \int_{t_0}^t d^3\tau \sum_e \left(\mathbf{d}_{eg} \cdot \mathbf{E}(\tau) e^{(-i\omega_{eg}-\gamma)(t-\tau)} |e\rangle\langle g| - \mathbf{d}_{ge} \cdot \mathbf{E}^*(\tau) e^{(-i\omega_{ge}-\gamma)(t-\tau)} |g\rangle\langle e| \right). \quad (\text{C.14})$$

To get the induced linear polarization the trace over the delocalized states is calculated:

$$\begin{aligned} \mathbf{P}^{(1)}(t) = \text{tr} \left(\sum_{e'} \left(\mathbf{d}_{ge'} |g\rangle\langle e'| + \mathbf{d}_{e'g} |e'\rangle\langle g| \right) \right. \\ \left. \cdot \frac{i}{\hbar} \int_{t_0}^t d^3\tau \sum_e \left(\mathbf{d}_{eg} \cdot \mathbf{E}(\tau) e^{(-i\omega_{eg}-\gamma)(t-\tau)} |e\rangle\langle g| - \mathbf{d}_{ge} \cdot \mathbf{E}^*(\tau) e^{(-i\omega_{ge}-\gamma)(t-\tau)} |g\rangle\langle e| \right) \right). \end{aligned} \quad (\text{C.15})$$

Using the condition of the orthonormal basis the equation can be written as:

$$\begin{aligned} \mathbf{P}^{(1)}(t) = \frac{i}{\hbar} \text{tr} \left(- \int_{t_0}^t d^3\tau \sum_{e'e} \mathbf{d}_{e'g} \mathbf{d}_{ge} \cdot \mathbf{E}^*(\tau) e^{(-i\omega_{ge}-\gamma)(t-\tau)} |e'\rangle\langle e| \right. \\ \left. + \int_{t_0}^t d^3\tau \sum_{e'e} \mathbf{d}_{ge'} \mathbf{d}_{eg} \cdot \mathbf{E}(\tau) e^{(-i\omega_{eg}-\gamma)(t-\tau)} \delta_{ee'} |g\rangle\langle g| \right) \end{aligned} \quad (\text{C.16})$$

$$\begin{aligned} \mathbf{P}^{(1)}(t) = \frac{i}{\hbar} \text{tr} \left(\int_{t_0}^t d^3\tau \sum_e \mathbf{d}_{ge} \mathbf{d}_{eg} \cdot \mathbf{E}(\tau) e^{(-i\omega_{eg}-\gamma)(t-\tau)} |g\rangle\langle g| \right. \\ \left. - \int_{t_0}^t d^3\tau \sum_{e'e} \mathbf{d}_{e'g} \mathbf{d}_{ge} \cdot \mathbf{E}^*(\tau) e^{(-i\omega_{ge}-\gamma)(t-\tau)} |e'\rangle\langle e| \right). \end{aligned} \quad (\text{C.17})$$

Evaluating the trace as follows

$$\text{tr}(\dots) = \langle g| \dots |g\rangle + \sum_e \langle e| \dots |e\rangle, \quad (\text{C.18})$$

leads to:

$$\mathbf{P}^{(1)}(t) = \frac{i}{\hbar} \int_{t_0}^t d^3\tau \sum_e \left(\mathbf{d}_{ge} \mathbf{d}_{eg} \cdot \mathbf{E}(\tau) e^{(-i\omega_{eg} - \gamma)(t - \tau)} - \mathbf{d}_{eg} \mathbf{d}_{ge} \cdot \mathbf{E}^*(\tau) e^{(i\omega_{eg} - \gamma)(t - \tau)} \right). \quad (\text{C.19})$$

The pulse and the exponential function present a convolution. Due to that fact the induced polarization can be expressed in the frequency domain using the theorem of convolution for a Fourier transformation $\mathcal{F}(f) := f(\omega) = \int dt f(t) e^{i\omega t}$ and $\mathcal{F}(f * g) = \mathcal{F}(f) \cdot \mathcal{F}(g)$

$$\mathbf{P}^{(1)}(\omega) = \frac{i}{\hbar} \sum_e \left(\mathbf{d}_{ge} \mathbf{d}_{eg} \cdot \mathbf{E}(\omega) \int_0^\infty dt e^{-(i\omega_{eg} - \gamma)t} e^{i\omega t} - \mathbf{d}_{eg} \mathbf{d}_{ge} \cdot \mathbf{E}^*(\omega) \int_0^\infty dt e^{(i\omega_{eg} - \gamma)t} e^{-i\omega t} \right) \quad (\text{C.20})$$

$$= \frac{i}{\hbar} \sum_e \left(\mathbf{d}_{ge} \mathbf{d}_{eg} \cdot \mathbf{E}(\omega) \frac{1}{\gamma + i(\omega_{eg} - \omega)} - \mathbf{d}_{eg} \mathbf{d}_{ge} \cdot \mathbf{E}^*(\omega) \frac{1}{\gamma - i(\omega_{eg} + \omega)} \right) \quad (\text{C.21})$$

$$= \frac{i}{\hbar} \sum_e \left(\mathbf{d}_{ge} \mathbf{d}_{eg} \cdot \mathbf{E}(\omega) \frac{\gamma - i(\omega_{eg} - \omega)}{\gamma^2 + (\omega_{eg} - \omega)^2} - \mathbf{d}_{eg} \mathbf{d}_{ge} \cdot \mathbf{E}^*(\omega) \frac{\gamma + i(\omega_{eg} + \omega)}{\gamma^2 - (\omega_{eg} + \omega)^2} \right). \quad (\text{C.22})$$

To get the characteristic signatures of the linear spectra the absorption coefficient is calculated

$$\alpha(\omega) = \frac{\omega}{n(\omega)\varepsilon_0 c} \text{Im} \left(\frac{P^{(1)}(\omega)}{E(\omega)} \right). \quad (\text{C.23})$$

With respect to the direction of polarization the electrical field can be written as:

$$\mathbf{E}(\omega) = E(\omega) \mathbf{e}_p. \quad (\text{C.24})$$

Accordingly the induced polarization can be expressed in the same way. That leads to the following absorption coefficient:

$$\alpha(\omega) = \frac{\omega}{n(\omega)\varepsilon_0 c \hbar} \sum_e |\mathbf{d}_{eg} \cdot \mathbf{e}_p|^2 \left(\frac{\gamma}{\gamma^2 + (\omega_{eg} - \omega)^2} - \frac{\gamma}{\gamma^2 + (\omega_{eg} + \omega)^2} \right). \quad (\text{C.25})$$

If the light is left polarized the vector reads $\mathbf{e}_l = \frac{1}{\sqrt{2}}(\mathbf{e}_x - \mathbf{e}_y)$ and if it is right polarized $\mathbf{e}_r = \frac{1}{\sqrt{2}}(\mathbf{e}_x + \mathbf{e}_y)$. While the optical pumping, the angular momentum of the photons is transferred to the excitons of the electronic system related to the orientation of the crystal lattice [3]. If the energy levels of the QDs are degenerated with different angular momentums, circularly polarized light can excite these states separately. Linear spectroscopy cannot be used for selecting the different orientations in the angular momentum [3]. Therefore, the multidimensional spectroscopy is introduced.

Appendix D

Mode of the program

The program calculates the trajectories of the Brownian motion of two colloidal QDs storing the positions and as well as the quaternions giving the orientations of the two QDs for each time step. The time steps should be in the order of nanoseconds according to the mean squared displacement of the QDs less than one nanometer. Therefore, the program determines the new QD positions (solution of the Langevin equation) together with the quaternions for the angular orientation. Then the program checks if they are arranged inside the boundaries of a box and if they do not overlap each other, since tunneling processes are not included in the model system. Accordingly, for calculating the trajectories of the QDs, they are viewed as inelastic spherical symmetric objects. For calculating the center-to-center distance between the QDs, the periodic boundary conditions are included and therefore, the program takes the smallest distance respecting the virtual positions of the QDs in the nearby boxes (in a stencil ordering).

In the second part, the program calculates the Coulomb coupling elements. Therefore, first the Schrödinger equation needs to be solved to determine the eigenfunction and eigenvalues of the QD two level system consisting of a valence band and a conduction band. The calculations are done by introducing a grid for the QD system and then, the eigenproblem is solved by using the Slep library. For solving the eigenproblem the potential for the electrons and holes needs to be determined. Here, a spherical symmetric box potential for core/shell colloidal QDs is used, but it can easily be replaced by other potentials.

The calculation of the Coulomb coupling elements can be based on the Poisson Green's function method to numerical efficiently calculate very general monopole-monopole and dipole-dipole interdot and intradot coupling elements. If the numerous number of positions in the walk necessitates a very fast calculation of the Coulomb coupling, the point-dipole approximation is used instead.

If calculation is based on the numerical efficient Poisson Green's function method, the six dimensional integral to get the Coulomb coupling elements is replaced by a Poisson equation and a three dimensional integral. To include the spatial positioning of the two QDs, a dynamically specified grid is introduced according to the current QD's positions (input parameters). Then, the spatially dependent dielectric function $\varepsilon(\mathbf{r})$ is determined. In the following, the Coulomb coupling elements, required for the calculation of 2d spectra, are calculated according to the indices respectively, which include the band index, the QD number and the spin configuration.

Including the Coulomb coupling elements for each time step into the trajectory, the DQCS are calculated. To get stochastically convergent spectra including a huge number of single spectra, an averaging algorithm improves the distribution of the QD positions respecting the distance. Parameters such as the temperature, the viscosity or the formalism of the spectroscopy can be easily adapted to the investigated model system.

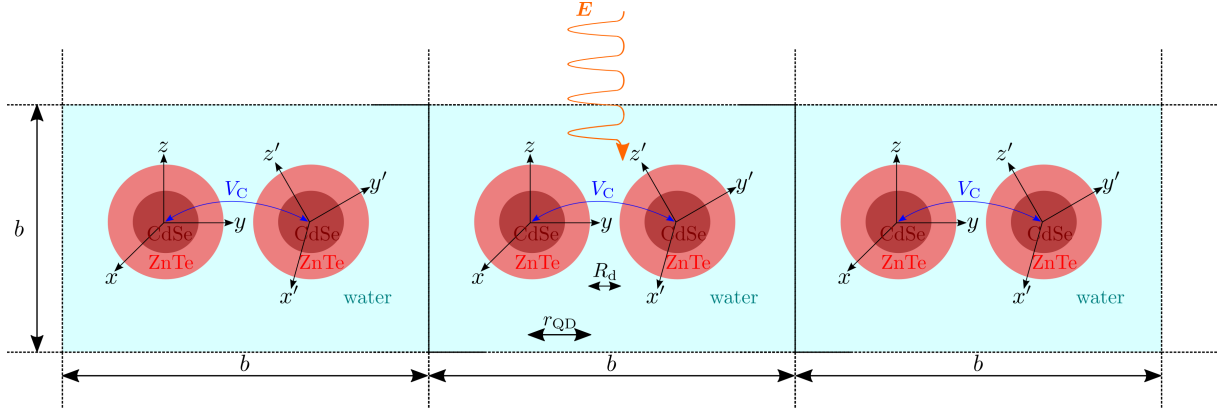


Figure D.1 Scheme of the simulation boxes which are determined by the width b with periodic boundary conditions in three dimensions (plotted are only two). Each simulation box exactly includes two colloidal CdSe/ZnTe QDs in water. Due to the Brownian motion the QDs changing their spatial positions and angular orientations. This induces a specific Coulomb coupling V_C determined by the smallest distance between the periodic QDs. Since the motion is investigated by multidimensional coherent spectra, the QDs are excited by a sequence of laser pulses E .



Figure D.2 Schematic illustration of the program mode including the input and output parameters which can be used to modify the spectra concerning the experimental setup.

Danksagung

Mein erster Dank gilt meinem Doktorvater Prof. Andreas Knorr, der diese Arbeit erst ermöglicht hat und mich in den vielen Jahren in der Arbeitsgruppe unterstützt und meine Forschung gefördert hat. In diesem Zuge möchte ich ebenfalls Dr. Marten Richter für die enge Betreuung danken. Sein Ideenreichtum zusammen mit den zahlreichen fachlichen Diskussionen über konzeptionelle Fragen bis hin zum kleinsten Detail das dennoch weitreichende Konsequenzen haben kann, haben den Verlauf dieser Arbeit erheblich bestimmt und zum Gelingen beigetragen.

Mein Dank gilt außerdem Dr. Benjamin Fingerhut, der sich so rasch als Zweitgutachter zur Verfügung gestellt hat. Bei Prof. Birgit Kanngießer möchte ich mich für die sehr freundliche Übernahme des Prüfungsvorsitzes bedanken.

Der Deutschen Forschungsgemeinschaft danke ich für die Finanzierung dieser Arbeit und das ermöglichen interessanter und abwechslungsreicher Konferenzbesuche.

Außerdem danke ich der gesamten Arbeitsgruppe für das Schaffen einer tollen Arbeitsatmosphäre und die stetige Bereitschaft Fragestellungen jeglicher Art zu diskutieren. Dies ermöglichte jederzeit einen breiten wissenschaftlichen und sonstigen Austausch. Mein besonderer Dank geht dabei an Sandra Kuhn und Judith Specht für die immerwährende freundschaftliche Unterstützung in sämtlichen fachlichen und sonstigen Belangen und natürlich für die tolle Mensagruppe. Für das Korrekturlesen und die hilfreichen Kommentare und Anmerkungen geht ein besonderer Dank an Sandra Kuhn, Falk Zimmermann und Andreas Ginter.

Ein herzliches Dankeschön geht auch an alle Sekretärinnen des Instituts, ohne deren Hilfe bei sämtlichen Verwaltungsaufgaben und darüber hinaus wohl nichts laufen würde. Ein besonderer Dank geht dabei an Andrea Schulze für die langjährige stetige Hilfsbereitschaft und das entgegengebrachte Vertrauen. Ich danke ebenfalls Peter Orłowski und Marten Richter für ihre Hilfe bei Computerbelangen aller Art.

Ein besonderer Dank geht an meine Schwiegereltern für die verständnisvolle Unterstützung und vor allem für die absolut zuverlässige und immer einsatzbereite Kinderbetreuung. Meinen Eltern möchte ich an dieser Stelle für den immerwährenden und unermüdlichen Beistand in sämtlichen Belangen über all die Jahre hinweg ein herzliches Dankeschön sagen. Meinem Bruder Falk danke ich dafür, dass er immer da ist wenn es wirklich darauf ankommt und natürlich auch für die zahlreichen physikalischen Diskussionen. Meinem lieben Arne danke ich dafür, dass er das Leben so lebenswert macht und mir stets aufs Neue den wahren Forschergeist zeigt. Zuletzt und im Besonderen möchte ich mich bei meinem Mann Andreas dafür bedanken, dass er wirklich immer für mich da ist und mir das Gefühl gibt, dass wir gemeinsam alles packen werden was da noch so auf uns zukommen mag. Worauf es wirklich ankommt hat uns der unglaublich tapfere Kämpfer Arik gezeigt.

Bibliography

- [1] Benjamin P. Fingerhut, Marten Richter, Jun-Wei Luo, Alex Zunger, and Shaul Mukamel. 2d optical photon echo spectroscopy of a self-assembled quantum dot. *Ann. Phys.*, 525(1-2):31–42, 2013.
- [2] Darius Abramavicius, Benoit Palmieri, Dmitri V. Voronine, František Šanda, and Shaul Mukamel. Coherent multidimensional optical spectroscopy of excitons in molecular aggregates; quasiparticle versus supermolecule perspectives. *Chem. Rev.*, 109(6):2350–2408, 2009.
- [3] Gregory D. Scholes and David L. Andrews. Resonance energy transfer and quantum dots. *Phys. Rev. B*, 72:125331, Sep 2005.
- [4] Judith F. Specht, Andreas Knorr, and Marten Richter. Two-dimensional spectroscopy: An approach to distinguish förster and dexter transfer processes in coupled nanostructures. *Phys. Rev. B*, 91:155313, Apr 2015.
- [5] Dirk Ziemann and Volkhard May. Distant- and shape-dependent excitation energy transfer in nanohybrid systems: Computation on a pheophorbide- α cdse nanocrystal complex. *J. Phys. Chem. Lett.*, 5:1203–1209, Mar 2014.
- [6] Yaroslav Zelinsky, Yuan Zhang, and Volkhard May. Supramolecular complex coupled to a metal nanoparticle: Computational studies on the optical absorption. *J. Phys. Chem. A*, 116(46):11330–11340, 2012.
- [7] Krishna P. Acharya, Hue M. Nguyen, Melissa Paulite, Andrei Piryatinski, Jun Zhang, Joanna L. Casson, Hongwu Xu, Han Htoon, and Jennifer A. Hollingsworth. Elucidation of two giants: Challenges to thick-shell synthesis in cdse/zns and zns/cds core/shell quantum dots. *J. Am. Chem. Soc.*, 137(11):3755–3758, 2015.
- [8] B. O. Dabbousi, J. Rodriguez-Viejo, F. V. Mikulec, J. R. Heine, H. Mattoussi, R. Ober, K. F. Jensen, and M. G. Bawendi. (CdSe)ZnS core/shell quantum dots: Synthesis and characterization of a size series of highly luminescent nanocrystallites. *J. Phys. Chem. B*, 101(46):9463–9475, 1997.
- [9] Francesco Masia, Nicolò Accanto, Wolfgang Langbein, and Paola Borri. Spin-flip limited exciton dephasing in CdSe/ZnS colloidal quantum dots. *Phys. Rev. Lett.*, 108:087401, Feb 2012.
- [10] G. Cantele, D. Ninno, and G. Iadonisi. Calculation of the infrared optical transitions in semiconductor ellipsoidal quantum dots. *Nano Lett.*, 1(3):121–124, 2001.
- [11] Jonathan Owen and Louis Brus. Chemical synthesis and luminescence applications of colloidal semiconductor quantum dots. *J. Am. Chem. Soc.*, 139(32):10939–10943, 2017.

- [12] Zhengtao Deng, Li Cao, Fangqiong Tang, and Bingsuo Zou. A new route to zinc-blende cdse nanocrystals: Mechanism and synthesis. *J. Phys. Chem. B*, 109(35):16671–16675, 2005.
- [13] Alexander Nemchinov, Maria Kirsanova, Nishshanka N. Hewa-Kasakarage, and Mikhail Zamkov. Synthesis and characterization of Type II ZnSe/CdS core/shell nanocrystals. *J. Phys. Chem. C*, 112(25):9301–9307, 2008.
- [14] Liang-shi Li, Jiangtao Hu, Weidong Yang, and A. Paul Alivisatos. Band gap variation of size- and shape-controlled colloidal cdse quantum rods. *Nano Lett.*, 1(7):349–351, 2001.
- [15] Sotirios Baskoutas and Andreas F. Terzis. Size-dependent band gap of colloidal quantum dots. *J. Appl. Phys.*, 99(1):013708, 2006.
- [16] Colonna Anne E., Yang Xiujuan, and Scholes Gregory D. Photon echo studies of biexcitons and coherences in colloidal cdse quantum dots. *phys. status solidi (b)*, 242(5):990–1000, 2005.
- [17] Jingbo Li and Lin-Wang Wang. Band-structure-corrected local density approximation study of semiconductor quantum dots and wires. *Phys. Rev. B*, 72:125325, Sep 2005.
- [18] Sergei A. Ivanov, Andrei Piryatinski, Jagjit Nanda, Sergei Tretiak, Kevin R. Zavadil, William O. Wallace, Don Werder, and Victor I. Klimov. Type-II Core/Shell CdS/ZnSe nanocrystals: Synthesis, electronic structures, and spectroscopic properties. *J. Am. Chem. Soc.*, 129(38):11708–11719, 2007.
- [19] Andrei Piryatinski, Sergei A. Ivanov, Sergei Tretiak, and Victor I. Klimov. Effect of quantum and dielectric confinement on the exciton-exciton interaction energy in type II core/shell semiconductor nanocrystals. *Nano Lett.*, 7(1):108–115, 2007.
- [20] Liselotte Jauffred, Andrew C. Richardson, and Lene B. Oddershede. Three-dimensional optical control of individual quantum dots. *Nano Lett.*, 8(10):3376–3380, 2008.
- [21] Hui Li, Shuo-Xing Dou, Yu-Ru Liu, Wei Li, Ping Xie, Wei-Chi Wang, and Peng-Ye Wang. Mapping intracellular diffusion distribution using single quantum dot tracking: Compartmentalized diffusion defined by endoplasmic reticulum. *J. Am. Chem. Soc.*, 137(1):436–444, 2015.
- [22] Robert Zwanzig. *Nonequilibrium Statistical Mechanics*. 2001.
- [23] Li Tongcang and Raizen Mark G. Brownian motion at short time scales. *Ann. Phys.*, 525(4):281–295, 2013.
- [24] Kevin McHale, Andrew J. Berglund, and Hideo Mabuchi. Quantum dot photon statistics measured by three-dimensional particle tracking. *Nano Lett.*, 7(11):3535–3539, 2007.
- [25] Igor L. Medintz, H. Tetsuo Uyeda, Ellen R. Goldman, and Hedi Mattoussi. Quantum dot bioconjugates for imaging, labelling and sensing. *Nat. Mater.*, 4:435–446, 2005.
- [26] S. A. Crooker, J. A. Hollingsworth, S. Tretiak, and V. I. Klimov. Spectrally resolved dynamics of energy transfer in quantum-dot assemblies: Towards engineered energy flows in artificial materials. *Phys. Rev. Lett.*, 89:186802, Oct 2002.
- [27] C. R. Kagan, C. B. Murray, M. Nirmal, and M. G. Bawendi. Electronic energy transfer in cdse quantum dot solids. *Phys. Rev. Lett.*, 76:1517–1520, Feb 1996.

- [28] Walter Hoyer, Mackillo Kira, and Stephan W. Koch. Influence of coulomb and phonon interaction on the exciton formation dynamics in semiconductor heterostructures. *Phys. Rev. B*, 67:155113, Apr 2003.
- [29] Marten Richter, Felix Schlosser, Mario Schoth, Sven Burger, Frank Schmidt, Andreas Knorr, and Shaul Mukamel. Reconstruction of the wave functions of coupled nanoscopic emitters using a coherent optical technique. *Phys. Rev. B*, 86:085308, Aug 2012.
- [30] Sandra C. Kuhn and Marten Richter. Excitonic effects in intraband quantum dot spectroscopy: Formation of bound continuum excitons. *Phys. Rev. B*, 90:125308, Sep 2014.
- [31] Ahsan Nazir, Brendon W. Lovett, Sean D. Barrett, John H. Reina, and G. A. Briggs. Anticrossings in förster coupled quantum dots. *Phys. Rev. B*, 71:045334, Jan 2005.
- [32] T. Sverre Theuerholz, Alexander Carmele, Marten Richter, and Andreas Knorr. Influence of förster interaction on light emission statistics in hybrid systems. *Phys. Rev. B*, 87:245313, Jun 2013.
- [33] Chun-Hsiung Wang, Chih-Wei Chen, Chih-Ming Wei, Yang-Fang Chen, Chih-Wei Lai, Mei-Lin Ho, and Pi-Tai Chou. Resonant energy transfer between CdSe/ZnS type I and CdSe/ZnTe type II quantum dots. *J. Phys. Chem. C*, 113(35):15548–15552, 2009.
- [34] Roi Baer and Eran Rabani. Theory of resonance energy transfer involving nanocrystals: The role of high multipoles. *J. Chem. Phys.*, 128(18):184710, 2008.
- [35] Brendon W. Lovett, John H. Reina, Ahsan Nazir, and G. Andrew D. Briggs. Optical schemes for quantum computation in quantum dot molecules. *Phys. Rev. B*, 68:205319, Nov 2003.
- [36] Dmitri Nikonov, Ataç Imamoglu, Leonid Butov, and Holger Schmidt. Collective intersubband excitations in quantum wells: Coulomb interaction versus subband dispersion. *Phys. Rev. Lett.*, 79:4633–4636, Dec 1997.
- [37] T. R. Nielsen, P. Gartner, M. Lorke, J. Seebeck, and F. Jahnke. Coulomb scattering in nitride-based self-assembled quantum dot systems. *Phys. Rev. B*, 72:235311, Dec 2005.
- [38] D. Reuter, P. Kailuweit, A. D. Wieck, U. Zeitler, O. Wibbelhoff, C. Meier, A. Lorke, and J. C. Maan. Coulomb-interaction-induced incomplete shell filling in the hole system of inas quantum dots. *Phys. Rev. Lett.*, 94:026808, Jan 2005.
- [39] V. A. Fonoberov, E. P. Pokatilov, and A. A. Balandin. Exciton states and optical transitions in colloidal cds quantum dots: Shape and dielectric mismatch effects. *Phys. Rev. B*, 66:085310, Aug 2002.
- [40] Krzysztof Gawarecki, Michał Pochwała, Anna Grodecka-Grad, and Paweł Machnikowski. Phonon-assisted relaxation and tunneling in self-assembled quantum dot molecules. *Phys. Rev. B*, 81:245312, Jun 2010.
- [41] Paweł Machnikowski and Emil Rozbicki. Phonon-assisted excitation transfer in quantum dot molecules: from quantum kinetics to transfer rates. *phys. status solidi (b)*, 246(2):320–324, 2009.
- [42] W. W. Chow, H. C. Schneider, and M. C. Phillips. Theory of quantum-coherence phenomena in semiconductor quantum dots. *Phys. Rev. A*, 68:053802, Nov 2003.

- [43] Igor F. Herbut, Vladimir Juričić, and Oskar Vafek. Coulomb interaction, ripples, and the minimal conductivity of graphene. *Phys. Rev. Lett.*, 100:046403, Jan 2008.
- [44] Ermin Malic, Torben Winzer, Evgeny Bobkin, and Andreas Knorr. Microscopic theory of absorption and ultrafast many-particle kinetics in graphene. *Phys. Rev. B*, 84:205406, Nov 2011.
- [45] Takashi Kitae, Takayoshi Nakayama, and Koji Kano. Chiral recognition of [small alpha]-amino acids by charged cyclodextrins through cooperative effects of coulomb interaction and inclusion. *J. Chem. Soc., Perkin Trans. 2*, pages 207–212, 1998.
- [46] Matthew C. Strain, Gustavo E. Scuseria, and Michael J. Frisch. Achieving linear scaling for the electronic quantum coulomb problem. *Science*, 271:51, Jan 1996.
- [47] H. C. Schneider, W. W. Chow, and S. W. Koch. Many-body effects in the gain spectra of highly excited quantum-dot lasers. *Phys. Rev. B*, 64:115315, Aug 2001.
- [48] Alberto Franceschetti and Alex Zunger. Pseudopotential calculations of electron and hole addition spectra of inas, inp, and si quantum dots. *Phys. Rev. B*, 62:2614–2623, Jul 2000.
- [49] Anke Zimmermann, Sandra Kuhn, and Marten Richter. Poisson Green’s function method for increased computational efficiency in numerical calculations of Coulomb coupling elements. *Phys. Rev. B*, 93:035308, Jan 2016.
- [50] Takashi Miyake and F. Aryasetiawan. Screened coulomb interaction in the maximally localized wannier basis. *Phys. Rev. B*, 77:085122, Feb 2008.
- [51] N. Baer, S. Schulz, P. Gartner, S. Schumacher, G. Czycholl, and F. Jahnke. Influence of symmetry and coulomb correlation effects on the optical properties of nitride quantum dots. *Phys. Rev. B*, 76:075310, Aug 2007.
- [52] C. Sieh, T. Meier, F. Jahnke, A. Knorr, S. W. Koch, P. Brick, M. Hübner, C. Ell, J. Prineas, G. Khitrova, and H. M. Gibbs. Coulomb memory signatures in the excitonic optical stark effect. *Phys. Rev. Lett.*, 82:3112–3115, Apr 1999.
- [53] J. Wühr, V. M. Axt, and T. Kuhn. Nonperturbative coulomb correlations generated by simultaneous excitation of excitonic and band-to-band continuum transitions. *Phys. Rev. B*, 70:155203, Oct 2004.
- [54] Alberto Franceschetti and Alex Zunger. Direct pseudopotential calculation of exciton coulomb and exchange energies in semiconductor quantum dots. *Phys. Rev. Lett.*, 78:915–918, Feb 1997.
- [55] Piotr Kowalski, Łukasz Marcinowski, and Paweł Machnikowski. Coulomb matrix elements for the impact ionization process in nanocrystals: An envelope function approach. *Phys. Rev. B*, 87:075309, Feb 2013.
- [56] Anne Myers Kelley. Electron-phonon coupling in CdSe nanocrystals. *J. Phys. Chem. Lett.*, 1(9):1296–1300, 2010.
- [57] Celso de Mello Donega. Synthesis and properties of colloidal heteronanocrystals. *Chem. Soc. Rev.*, 40:1512–1546, 2011.
- [58] Moonsub Shim and Philippe Guyot-Sionnest. Permanent dipole moment and charges in colloidal semiconductor quantum dots. *J. Chem. Phys.*, 111(15):6955–6964, 1999.

- [59] Patrick Reberstrost, Michael Stopa, and Alán Aspuru-Guzik. Förster Coupling in Nanoparticle Excitonic Circuits. *Nano Lett.*, 10(8):2849–2856, 2010.
- [60] A. P. Alivisatos. Semiconductor clusters, nanocrystals, and quantum dots. *Science*, 271(5251):933–937, 1996.
- [61] V. I. Klimov, A. A. Mikhailovsky, D. W. McBranch, C. A. Leatherdale, and M. G. Bawendi. Quantization of multiparticle auger rates in semiconductor quantum dots. *Science*, 287(5455):1011–1013, 2000.
- [62] J. Danckwerts, K. J. Ahn, J. Förstner, and A. Knorr. Theory of ultrafast nonlinear optics of coulomb-coupled semiconductor quantum dots: Rabi oscillations and pump-probe spectra. *Phys. Rev. B*, 73:165318, Apr 2006.
- [63] P. Paiano, P. Prete, N. Lovergine, and A. M. Mancini. Effect of precursors stoichiometry on morphology, crystallinity and electrical properties of znTe epilayers grown on (100)GaAs by movpe. *Cryst. Res. Technol.*, 40(10-11):1011–1017, 2005.
- [64] D. T. F. Marple. Refractive index of ZnSe, ZnTe, and CdTe. *J. Appl. Phys.*, 35(3):539–542, 1964.
- [65] D. Schooss, A. Mews, A. Eychmüller, and H. Weller. Quantum-dot quantum well CdS/HgS/CdS: Theory and experiment. *Phys. Rev. B*, 49:17072–17078, Jun 1994.
- [66] Vicente Hernandez, Jose E. Roman, and Vicente Vidal. SLEPc: A scalable and flexible toolkit for the solution of eigenvalue problems. *ACM Trans. Math. Software*, 31(3):351–362, 2005.
- [67] S. Abdullah, J. P. Coe, and I. D’Amico. Effect of confinement potential geometry on entanglement in quantum dot-based nanostructures. *Phys. Rev. B*, 80:235302, Dec 2009.
- [68] Dan Oron, Miri Kazes, and Uri Banin. Multiexcitons in type-II colloidal semiconductor quantum dots. *Phys. Rev. B*, 75:035330, Jan 2007.
- [69] C. A. Leatherdale and M. G. Bawendi. Observation of solvatochromism in CdSe colloidal quantum dots. *Phys. Rev. B*, 63:165315, Apr 2001.
- [70] M. Reichelt, B. Pasenow, T. Meier, T. Stroucken, and S. W. Koch. Spatially inhomogeneous optical gain in semiconductor photonic-crystal structures. *Phys. Rev. B*, 71:035346, Jan 2005.
- [71] Werner Vogel, Dirk-Gunnar Welsch, and Sascha Wallentowitz. *Quantum Optics An Introduction*. WILEY-VCH, 2001.
- [72] Martijn Wubs, L. G. Suttorp, and A. Lagendijk. Multipole interaction between atoms and their photonic environment. *Phys. Rev. A*, 68:013822, Jul 2003.
- [73] B. Pasenow, M. Reichelt, T. Stroucken, T. Meier, and S. W. Koch. Excitonic wave packet dynamics in semiconductor photonic-crystal structures. *Phys. Rev. B*, 71:195321, May 2005.
- [74] A. Tip. Canonical formalism and quantization for a class of classical fields with application to radiative atomic decay in dielectrics. *Phys. Rev. A*, 56:5022–5041, Dec 1997.

- [75] A. J. Williamson, L. W. Wang, and Alex Zunger. Theoretical interpretation of the experimental electronic structure of lens-shaped self-assembled InAs/GaAs quantum dots. *Phys. Rev. B*, 62:12963–12977, Nov 2000.
- [76] I. V. Solovyev and M. Imada. Screening of coulomb interactions in transition metals. *Phys. Rev. B*, 71:045103, Jan 2005.
- [77] A. M. Kapitonov, A. P. Stupak, S. V. Gaponenko, E. P. Petrov, A. L. Rogach, and A. Eychmüller. Luminescence properties of thiol-stabilized cdte nanocrystals. *J. Phys. Chem. B*, 103(46):10109–10113, 1999.
- [78] Sean A. Blanton, Robert L. Leheny, Margaret A. Hines, and Philippe Guyot-Sionnest. Dielectric dispersion measurements of cdse nanocrystal colloids: Observation of a permanent dipole moment. *Phys. Rev. Lett.*, 79:865–868, Aug 1997.
- [79] Xingcan Dai, Marten Richter, Hebin Li, Alan D. Bristow, Cyril Falvo, Shaul Mukamel, and Steven T. Cundiff. Two-dimensional double-quantum spectra reveal collective resonances in an atomic vapor. *Phys. Rev. Lett.*, 108:193201, May 2012.
- [80] Benjamin P. Fingerhut, Marten Richter, Jun-Wei Luo, Alex Zunger, and Shaul Mukamel. Dissecting biexciton wave functions of self-assembled quantum dots by double-quantum-coherence optical spectroscopy. *Phys. Rev. B*, 86:235303, Dec 2012.
- [81] Felix Schlosser, Andreas Knorr, Shaul Mukamel, and Marten Richter. Using localized double-quantum-coherence spectroscopy to reconstruct the two-exciton wave function of coupled quantum emitters. *New J. Phys.*, 15:025004, Feb 2013.
- [82] Thomas G. Mayerhöfer. Symmetric euler orientation representations for orientational averaging. *Spectrochimica Acta Part A: Molecular and Biomolecular Spectroscopy*, 61(11):2611–2621, 2005.
- [83] Gwyn Skone, Stephen Cameron, and Irina Voiculescu. Doing a good turn: The use of quaternions for rotation in molecular docking. *J. Chem. Inf. Model.*, 53(12):3367–3372, 2013.
- [84] Steven S. Andrews. Using rotational averaging to calculate the bulk response of isotropic and anisotropic samples from molecular parameters. *J. Chem. Ed.*, 81(6):877, 2004.
- [85] Charles F. F. Karney. Quaternions in molecular modeling. *J. Mol. Graph. Model.*, 25:595–604, 2007.
- [86] Jack B. Kuipers. Quaternions and rotation sequences. In *Proceedings of the International Conference on Geometry, Integrability and Quantization*, pages 127–143, Sofia, Bulgaria, 2000. Coral Press Scientific Publishing.
- [87] G. Cantele, D. Ninno, and G. Iadonisi. Shape effects on the one- and two-electron ground state in ellipsoidal quantum dots. *Phys. Rev. B*, 64:125325, Sep 2001.
- [88] J. M. Daniels, P. Machnikowski, and T. Kuhn. Excitons in quantum dot molecules: Coulomb coupling, spin-orbit effects, and phonon-induced line broadening. *Phys. Rev. B*, 88:205307, Nov 2013.
- [89] Leslie F. Greengard and Jingfang Huang. Excitons in quantum dot molecules: Coulomb coupling, spin-orbit effects, and phonon-induced line broadening. *J. Comput. Phys.*, 180:642, Aug 2002.

- [90] R Ferreira and G Bastard. Unbound states in quantum heterostructures. *Nanoscale Res. Lett.*, 1:120–136, 2006.
- [91] Sandra C. Kuhn and Marten Richter. Hybrid density matrix approach as a factorization scheme for many-body systems: Illustrated by a quantum dot-continuum system. *Phys. Rev. B*, 91:155309, Apr 2015.
- [92] Alexander Steinhoff, Paul Gartner, Matthias Florian, and Frank Jahnke. Treatment of carrier scattering in quantum dots beyond the boltzmann equation. *Phys. Rev. B*, 85:205144, May 2012.
- [93] T. R. Nielsen, P. Gartner, and F. Jahnke. Many-body theory of carrier capture and relaxation in semiconductor quantum-dot lasers. *Phys. Rev. B*, 69:235314, Jun 2004.
- [94] L. D. Hallam, J. Weis, and P. A. Maksym. Screening of the electron-electron interaction by gate electrodes in semiconductor quantum dots. *Phys. Rev. B*, 53:1452–1462, Jan 1996.
- [95] Satish Balay, Shrirang Abhyankar, Mark F. Adams, Jed Brown, Peter Brune, Kris Buschelman, Lisandro Dalcin, Victor Eijkhout, William D. Gropp, Dinesh Kaushik, Matthew G. Knepley, Dave A. May, Lois Curfman McInnes, Richard Tran Mills, Todd Munson, Karl Rupp, Patrick Sanan, Barry F. Smith, Stefano Zampini, Hong Zhang, and Hong Zhang. PETSc users manual. Technical Report ANL-95/11 - Revision 3.9, Argonne National Laboratory, 2018.
- [96] Yvan Notay and Artem Napov. A massively parallel solver for discrete poisson-like problems. *J. Comput. Phys.*, 281:237, 2015.
- [97] Thomas Guillet and Romain Teyssier. A simple multigrid scheme for solving the poisson equation with arbitrary domain boundaries. *J. Comput. Phys.*, 230:4756, 2011.
- [98] M. Stopa. Fluctuations in quantum dot charging energy. *Physica B:*, 249-251:228–232, 1998.
- [99] Johann Sée, Philippe Dollfus, and Sylvie Galdin. Comparison of a density functional theory and a hartree treatment of silicon quantum dot. *J. Appl. Phys.*, 92(6):3141–3146, 2002.
- [100] A. Franceschetti, A. Williamson, and A. Zunger. Addition spectra of quantum dots: the role of dielectric mismatch. *J. Phys. Chem. B*, 104(15):3398–3401, 2000.
- [101] Mark A. Watson, Yuki Kurashige, Takahito Nakajima, and Kimihiko Hirao. Linear-scaling multipole-accelerated gaussian and finite-element coulomb method. *J. Chem. Phys.*, 128(5):054105, 2008.
- [102] F. R. Manby and P. J. Knowles. Poisson equation in the kohn-sham coulomb problem. *Phys. Rev. Lett.*, 87:163001, Sep 2001.
- [103] Victor I. Klimov, Sergei A. Ivanov, Jagjit Nanda, Marc Achermann, Ilya Bezel, John A. McGuire, and Andrei Piryatinski. Single-exciton optical gain in semiconductor nanocrystals. *Nature*, 447:441, May 2007.
- [104] Mark I. Stockman, David J. Bergman, and Takayoshi Kobayashi. Coherent control of nanoscale localization of ultrafast optical excitation in nanosystems. *Phys. Rev. B*, 69:054202, Feb 2004.

- [105] Steven R. White, John W. Wilkins, and Michael P. Teter. Finite-element method for electronic structure. *Phys. Rev. B*, 39:5819–5833, Mar 1989.
- [106] Edwin Antillon, Birgit Wehefritz-Kaufmann, and Sabre Kais. Finite-size scaling for quantum criticality using the finite-element method. *Phys. Rev. E*, 85:036706, Mar 2012.
- [107] Y. Nishimura, Z. Lin, J.L.V. Lewandowski, and S. Ethier. A finite element poisson solver for gyrokinetic particle simulations in a global field aligned mesh. *J. Comput. Phys.*, 214(2):657 – 671, 2006.
- [108] E. L. Briggs, D. J. Sullivan, and J. Bernholc. Real-space multigrid-based approach to large-scale electronic structure calculations. *Phys. Rev. B*, 54:14362–14375, Nov 1996.
- [109] Orlando Ayala and Lian-Ping Wang. Parallel implementation and scalability analysis of 3d fast fourier transform using 2d domain decomposition. *Parallel Comput.*, 39(1):58 – 77, 2012.
- [110] László Füsti-Molnár. New developments in the fourier transform coulomb method: Efficient and accurate localization of the filtered core functions and implementation of the coulomb energy forces. *J. Chem. Phys.*, 119(21):11080–11087, 2003.
- [111] Jochen Heyd, Gustavo E. Scuseria, and Matthias Ernzerhof. Hybrid functionals based on a screened coulomb potential. *J. Chem. Phys.*, 118(18):8207–8215, 2003.
- [112] S. A. Khrapak, A. V. Ivlev, G. E. Morfill, and S. K. Zhdanov. Scattering in the attractive yukawa potential in the limit of strong interaction. *Phys. Rev. Lett.*, 90:225002, Jun 2003.
- [113] Sandra C. Kuhn, Andreas Knorr, Marten Richter, Nina Owschimikow, Mirco Kolarczik, Yücel I. Kaptan, and Ulrike Woggon. All-optical approach to determine the spatial shape of nanoscale electron wave functions using intraband spectroscopy. *Phys. Rev. B*, 89:201414, May 2014.
- [114] Huynh Thanh Duc, Jens Förstner, and Torsten Meier. Microscopic analysis of charge and spin photocurrents injected by circularly polarized one-color laser pulses in gaas quantum wells. *Phys. Rev. B*, 82:115316, Sep 2010.
- [115] Ian Affleck and Pascal Simon. Detecting the kondo screening cloud around a quantum dot. *Phys. Rev. Lett.*, 86:2854–2857, Mar 2001.
- [116] H. J. Krenner, M. Sabathil, E. C. Clark, A. Kress, D. Schuh, M. Bichler, G. Abstreiter, and J. J. Finley. Direct observation of controlled coupling in an individual quantum dot molecule. *Phys. Rev. Lett.*, 94:057402, Feb 2005.
- [117] Gerold Kvas and Volkhard May. Density matrix based microscopic theory of molecule metal-nanoparticle interactions: Linear absorbance and plasmon enhancement of intermolecular excitation energy transfer. *J. Chem. Phys.*, 134(3):034701, 2011.
- [118] Thi Uyen-Khanh Dang, Carsten Weber, Sebastian Eiser, Andreas Knorr, and Marten Richter. Two-dimensional fourier spectroscopy applied to electron-phonon correlations in quantum well intersubband systems. *Phys. Rev. B*, 86:155306, Oct 2012.
- [119] Jeongho Kim, Shaul Mukamel, and Gregory D. Scholes. Two-dimensional electronic double-quantum coherence spectroscopy. *Acc. Chem. Res.*, 42(9):1375–1384, 2009.

- [120] Martin Richter and Benjamin P. Fingerhut. Simulation of multi-dimensional signals in the optical domain: Quantum-classical feedback in nonlinear exciton propagation. *J. Chem. Theory Comput.*, 12(7):3284–3294, 2016.
- [121] Zhenyu Li, Darius Abramavicius, and Shaul Mukamel. Probing electron correlations in molecules by two-dimensional coherent optical spectroscopy. *J. Am. Chem. Soc.*, 130(11):3509–3515, 2008.
- [122] Shaul Mukamel, Rafał Oszwaldowski, and Lijun Yang. A coherent nonlinear optical signal induced by electron correlations. *J. Chem. Phys.*, 127(22):221105, 2007.
- [123] Franz Milota, Jaroslaw Sperling, Alexandra Nemeth, Tomáš Mančal, and Harald F. Kauffmann. Two-dimensional electronic spectroscopy of molecular excitons. *Acc. Chem. Res.*, 42(9):1364–1374, 2009.
- [124] Mayrose R Salvador, Matthew W Graham, and Gregory D Scholes. Exciton-phonon coupling and disorder in the excited states of CdSe colloidal quantum dots. *J. Chem. Phys.*, 125(18):184709, November 2006.
- [125] D. Valerini, A. Cretí, M. Lomascolo, L. Manna, R. Cingolani, and M. Anni. Temperature dependence of the photoluminescence properties of colloidal CdSe/ZnS core/shell quantum dots embedded in a polystyrene matrix. *Phys. Rev. B*, 71:235409, Jun 2005.
- [126] Ling Xu, Jun Xu, Zhongyuan Ma, Wei Li, Xinfan Huang, and Kunji Chen. Direct observation of resonant energy transfer between quantum dots of two different sizes in a single water droplet. *Appl. Phys. Lett.*, 89(3):033121, 2006.
- [127] Andreas Zöttl. *Hydrodynamics of Microswimmers in Confinement and in Poiseuille Flow*. PhD thesis, Technische Universität Berlin, Jan 2014.
- [128] D. A. Weitz, D. J. Pine, P. N. Pusey, and R. J. A. Tough. Nondiffusive brownian motion studied by diffusing-wave spectroscopy. *Phys. Rev. Lett.*, 63:1747–1750, Oct 1989.
- [129] P. N. Segrè, O. P. Behrend, and P. N. Pusey. Short-time brownian motion in colloidal suspensions: Experiment and simulation. *Phys. Rev. E*, 52:5070–5083, Nov 1995.
- [130] J. X. Zhu, D. J. Durian, J. Müller, D. A. Weitz, and D. J. Pine. Scaling of transient hydrodynamic interactions in concentrated suspensions. *Phys. Rev. Lett.*, 68:2559–2562, Apr 1992.
- [131] Ayan Chakrabarty, Andrew Konya, Feng Wang, Jonathan V. Selinger, Kai Sun, and Qi-Huo Wei. Brownian motion of arbitrarily shaped particles in two dimensions. *Langmuir*, 30(46):13844–13853, 2014.
- [132] P. Borri, W. Langbein, S. Schneider, U. Woggon, R. L. Sellin, D. Ouyang, and D. Bimberg. Ultralong dephasing time in InGaAs quantum dots. *Phys. Rev. Lett.*, 87:157401, Sep 2001.
- [133] M. H. Kao, A. G. Yodh, and D. J. Pine. Observation of brownian motion on the time scale of hydrodynamic interactions. *Phys. Rev. Lett.*, 70:242–245, Jan 1993.
- [134] Nathan P. Wells, Guillaume A. Lessard, and James H. Werner. Confocal, three-dimensional tracking of individual quantum dots in high-background environments. *Anal. Chem.*, 80(24):9830–9834, 2008.

- [135] Leonard F. Pease, De-Hao Tsai, Joshua L. Hertz, Rebecca A. Zangmeister, Michael R. Zachariah, and Michael J. Tarlov. Packing and size determination of colloidal nanoclusters. *Langmuir*, 26(13):11384–11390, 2010.
- [136] HyeongGon Kang, Matthew L. Clarke, Silvia H. De Paoli Lacerda, Alamgir Karim, Leonard F. Pease, and Jeeseong Hwang. Multimodal optical studies of single and clustered colloidal quantum dots for the long-term optical property evaluation of quantum dot-based molecular imaging phantoms. *Biomed. Opt. Express*, 3(6):1312–1325, Jun 2012.
- [137] Gregory Von White, Fiaz S. Mohammed, and Christopher L. Kitchens. Small-angle neutron scattering investigation of gold nanoparticle clustering and ligand structure under antisolvent conditions. *J. Phys. Chem. C*, 115(38):18397–18405, 2011.
- [138] Mingdong Li, George W. Mulholland, and Michael R. Zachariah. Understanding the mobility of nonspherical particles in the free molecular regime. *Phys. Rev. E*, 89:022112, Feb 2014.
- [139] Luigi Carbone, Concetta Nobile, Milena De Giorgi, Fabio Della Sala, Giovanni Morello, Pierpaolo Pompa, Martin Hytch, Etienne Snoeck, Angela Fiore, Isabella R. Franchini, Monica Nadasan, Albert F. Silvestre, Letizia Chiodo, Stefan Kudera, Roberto Cingolani, Roman Krahne, and Liberato Manna. Synthesis and micrometer-scale assembly of colloidal CdSe/CdS nanorods prepared by a seeded growth approach. *Nano Lett.*, 7(10):2942–2950, 2007.
- [140] Yilong Han, Ahmed Alsayed, Maurizio Nobili, and Arjun G. Yodh. Quasi-two-dimensional diffusion of single ellipsoids: Aspect ratio and confinement effects. *Phys. Rev. E*, 80:011403, Jul 2009.
- [141] Franklin Kim, Serena Kwan, Jennifer Akana, and Peidong Yang. Langmuir-blodgett nanorod assembly. *J. Am. Chem. Soc.*, 123(18):4360–4361, 2001.
- [142] Samuel D. Park, Dmitry Baranov, Jisu Ryu, Byungmoon Cho, Avik Halder, Sönke Seifert, Stefan Vajda, and David M. Jonas. Bandgap inhomogeneity of a PbSe quantum dot ensemble from two-dimensional spectroscopy and comparison to size inhomogeneity from electron microscopy. *Nano Lett.*, 17(2):762–771, 2017.